Study of unipolar and ambipolar phthalocyanine- and porphyrin-based heterojunction devices through external triggers and gas sensing

Sujithkumar Ganesh Moorthy

THESE de DOCTORAT de l' UNIVERSITE BOURGOGNE FRANCHE-COMTE

Préparée à l'UNIVERSITE de BOURGOGNE

Ecole doctorale n° ED 553

Carnot-Pasteur

Doctorat de Physique

Par

GANESH MOORTHY Sujithkumar

Study of Unipolar and Ambipolar Phthalocyanine- and Porphyrin-Based Heterojunction Devices Through External Triggers and Gas Sensing

Thèse présentée et soutenue à Dijon le 21 octobre 2024.

Composition du Jury :

Pr. LESNIEWSKA, Eric	Université de Bourgogne	Président
Dr. LENFANT, Stéphane	Université de Lille	Rapporteur
Dr. RIEU, Mathilde	Ecole des Mines de Saint-Étienne	Rapporteur
Pr. Di NATALE, Corrado	Università di Roma Tor Vergata	Examinateur
Dr. TOURNILHAC, François	ESPCI – Paris	Examinateur
Pr. BOUVET, Marcel	Université de Bourgogne	Directeur de thèse

Dedicated

To my parents, to my sister Sujithra

To all the persons who stood by my side during tough times

Vote of Thanks

– தினைத்துணை நன்றி செயினும் பனைத்துணையாக்
கொள்வர் பயன்தெரி வார். குறள் – 104

– Le bienfait reçu ne serait-il gros que comme un grain de mil, ceux qui en connaissent la valeur, le considèrent comme aussi gros que le fruit du palmier. Kural – 104

– Even if the benefit received is only as big as a grain of millet, those who know its value consider it as big as the fruit of the palm tree. Kural – 104

First and foremost, I express my sincere gratitude to Dr. Stephane Lenfant and Dr. Mathilde Rieu for their courage in agreeing to be the reviewers of my thesis. I extend special thanks to my jury members, Prof. Corrado Di Natale, Prof. Eric Lesniewska and Dr. François Tournilhac, for graciously accepting our invitation to serve as examiners. I am indeed grateful to all the honourable members of the committee.

According to ancient Indian tradition, success in life is believed to be impossible without the blessings from four great personalities. This concept is beautifully articulated in both Tamil and Sanskrit phrases: *மாதா, பிதா, குரு, தெய்வம்* and ॥ माता पिता गुरु दैवम् ॥, respectively, which means Mother, Father, Teacher, and God. Mother, who gives birth to us, comes first. She is followed by the Father, who together with the Mother, nurtures and introduces us to the world. The teacher helps us to become a responsible person with all good qualities. Tamil classic Thirukkural emphasizes the importance of education in the verse: "*எண்ணென்ப ஏனை எழுத்தென்ப இவ்விரண்டும் கண்ணென்ப வாழும் உயிர்க்கு*"; it means, "Letters and numbers are the two eyes of humans," underscoring the essential role of education. Hence, the Teacher, who imparts knowledge, comes third. Finally, with the guidance of these three personalities, one can understand the knowledge of God, thereby realizing the ultimate purpose of life.

Therefore, I sincerely thank and bow my head to these four personalities for their blessings and tremendous support throughout my life. Specifically, I express my utmost respect and gratitude to my thesis supervisor, Prof. Marcel Bouvet, for accepting me into his team and for his full-time dedication to high-quality scientific supervision. From my interview for this PhD position to the present, I have always admired his leadership qualities, especially in handling difficult tasks. On the day we signed the working contract, he said that "we will work all together", and he has kept that promise till this moment. The working autonomous, enamours resources and unwavering guidance he provided are the reasons for my numerous publications and the successful completion of this thesis. A leader is one who knows the way, goes the way,

and shows the way. He is a leader. Once again, I express my heartfelt thanks to my supervisor for his valuable knowledge and guidance.

Very next, I would like to express my sincere thanks to my secondary school physics teacher Mrs. Uma Maheshwari. At the age of 12, she was the first person to plant a seed in my heart that I should pursue a PhD in physics. My love for physics was inspired by her, and I am indeed grateful for the spark she ignited in me. I also extend my special thanks to Assoc. Prof. Pradhabhan Durairaj, my B.Sc. physics tutor for his unwavering support and guidance till now. No matter how big the problem is, he has always helped me find solutions. I am indebted to him for the knowledge and encouragement that have shaped who I am today.

Throughout my research career, many noble individuals have held a special place in my heart. Among them, Prof. Daniel Muthiah, Dr. Arun Rajasekaran, Dr. Bharathikannan Rajakannu, Dr. Joseph Chandrasekaran, Dr. Rita Meunier-Prest, Prof. Dominique Lucas, Prof. Charles Devillers, Dr. Jean-Moïse Suisse, Mr. Didier Poinsot, and Mrs. Sophie Dalmolin stand at the top. I had valuable and productive discussions with these individuals on both scientific and common topics. Whenever I approached them, they welcomed me warmly and with great attitude. Their humanity and humour always brightened my days, and whenever I was in need, they were the first to extend a helping hand. I express my heartfelt thanks to all these remarkable individuals for their tremendous support throughout my PhD journey.

I extend my sincere thanks to the members of my thesis monitoring committee Dr. François Tournilhac along with Prof. Eric Lesniewska, a dynamic and open-minded person, I also thank him for the acquisition of AFM data and the priceless time he devoted to me. I thank both of them for their valuable advice and support. I cannot forget my precious collaborators Prof. Benoît H. Lessard (Canada), Prof. Corrado Di Natale (Italy), Prof. Hong Wang (US), Dr. Seydou Ouedraogo (Burkina Faso), Dr. Nicolas Boscher (Luxembourg) and Dr. Lydie Viau (France), who taught me several scientific aspects and new techniques, which helps me to grow.

The time I spent at the Luxembourg Institute of Science and Technology with Prof. Nicola Boscher remains one of the evergreen moments and a significant milestone in my scientific career. I am indeed grateful to all my collaborators for their immense support and guidance.

Beyond scientific aspects, the life of the doctorate student is filled with adventures and trilling moments. Even after many years if we recall our PhD days it will always put a big smile in our face. The 4th floor of ICMUB is like a garden consisting of various flowers. Among them, Fatima Akhssas, Nesrine Amiri, Emmanuel Lerayer, Nada Alami Mejjati, Abhishek Kumar, Fatima Awada, Petr Bečvář and Barbora Jansová rose above and we made a great team. How can I forget Lorena Di Zazzo and Rongning Lin! Three of us often synchronized and shared a similar mindset. Lorena teasingly calls me "my son," and I respond with "mamma." To her, I am an immature kid, and to me, she is like a mom who always disciplines the child. I was 22 when I started my PhD, knowing little about European culture. She taught me a lot, while Rongning always enjoyed spoiling me. We often fought like Tom and Jerry, with Lorena stepping in like the strong dog to separate us Haha! We travelled to many places in France, discovering new things together. We loved visiting museums, and every time the receptionist asked, "Which country are you guys from?" we sang together, "India, Italy, China together in France." Our answer always brought smiles to people's faces. I remember a stanza from the poem “The Man He Killed” by Thomas Hardy *“Had he and I but met; By some old ancient inn; We should have sat us down to wet; Right many a nipperkin!”* we may have different nationalities, but in our lab, we worked with same mentality. I was little sad when they both left the lab but then comes a new friend: Benjamin King a lover of wine and beer. We travelled to Beaune just to taste Burgundy wines. The museum receptionist presented six different wines and toasted the drinks, totally six glasses! At the end, he didn’t get drunk but we did! It was a wonderful experience and you know what they say, “For a chemist, alcohol is a solution!” Haha! There are many interesting events with other friends and colleagues from ICMUB and ICB, I can’t cite them all, but hey! I haven't forgotten any of you guys; I adore you all the same.

If I had to summarize my life in France, it was like a dream in wonderland. I made several friends who later became as close as family. Here, I would like to mention Mrs. Gloria David and Mrs. Kanchana for their love and affection. They treated me like their own son and provided strong moral support. During difficult times, they were always there to comfort me. Alongside them, my special thanks go to Mrs. Elisabeth Bouvet, a very kind and dynamic personality who always kept the surroundings filled with joy and happiness. There are no words to express my gratitude to these three individuals.

At this moment, I am willing to mention my decade-old dearest friends: Shajahan, Balaji, Kanchana, Manoj, Manimegalai, Pandialakshmi, Sathyamoorthy, Abhyuday, Arjun, Vishnu, Vizak, Isaac, Naveen, etc., who have always been there for me, offering a shoulder to lean on, encouraging me in all my endeavours, and standing by my side whenever I fell. Hey! How I can forget you, Lenny! The time I spent with you guys is incredibly precious and remains dearest to my heart. I would also like to thank all my friends from school to university who recognise themselves. Additionally, there are few more noble individuals I must mention: Dr. Sasidharan, Dr. Sonia Rajan, Mrs. Karthika and Mr. Karthikeyan for their endless support and encouragement since my childhood. Their contribution is like a matchstick that lights the lamp.

Last but not least, I am deeply indebted to my wonderful family: my amazing mom, Kalavathy; my supportive dad, Ganesh Moorthy; my sweet elder sister, Sujithra; my little niece, Keerthi; my kind aunt, Lalitha and my encouraging uncle Ravichandar. Among all, my sister Sujithra rose high. She has been the first teacher in my life, always believing in my success, both in scientific and literature. Oh! I forgot to mention that I am also a poet and orator who won multiple awards in literature. My sister had great hope in me, and I am proud to have proven her right. She is the strongest woman I have ever met in this life. The love and the bond we shared as brother and sister cannot be expressed in words. From the utmost depth of my heart, all I wanted to say to her is…, "*அக்கா*…Thank you for everything…I love you".

Table of Content – General

Table of Content – General

General Introduction

General Introduction

Air quality has emerged as a pressing global issue due to the accelerated pace of industrialization, urbanization, and the proliferation of vehicular emissions. Compounding these issues, conflicts and wars between countries have led to significant destruction of nature, causing severe damage to ecosystems. Toxic air from one region can have fatal consequences for innocent populations in another. Historically, liquid poisons were known to take lives, but in today's world, the very air we breathe is becoming increasingly toxic, leading to thousands of deaths due to the inhalation of harmful gases. The detrimental effects of poor air quality on human health are well-documented, encompassing severe conditions such as respiratory diseases, cardiovascular ailments, and cancer. The World Health Organization (WHO) attributes millions of premature deaths annually to air pollution, underscoring its status as a significant environmental health hazard[1]. In addition to human health impacts, pollutants such as volatile organic compounds (VOCs), carbon monoxide (CO), ammonia (NH_3), nitrogen oxides (NO_x), ground level ozone (O_3) and sulphur dioxide (SO_2) contribute to broader environmental problems, including acid rain, global warming, and the depletion of the ozone layer[2].

Given the profound implications of air pollution, the need for precise and continuous monitoring of air quality is paramount. Air pollution itself is a serious problem, but the real danger lies in not recognizing the levels of pollutants in the air we breathe. Effective air quality monitoring is essential for assessing pollution levels, ensuring compliance with environmental regulations, protecting public health by providing timely information during high pollution events, and informing research and policy decisions aimed at environmental protection. However, current air quality monitoring techniques, such as mass spectrometry, gas chromatography, and non-dispersive infrared (NDIR) spectroscopy, though accurate, present

significant limitations. These techniques are typically costly, requiring expensive equipment and maintenance, are bulky and non-portable, and are complex to operate. Additionally, these methods are time-consuming and do not provide real-time analysis. In today's fast-paced world, delayed information can be nearly useless.

In light of these challenges, there is an urgent need for gas sensors that are cost-effective, portable, user-friendly, and capable of providing real-time monitoring. Molecular materials, particularly organic semiconductors, offer a promising solution to these challenges. These materials possess several advantageous properties, including tuneable electronic characteristics through chemical synthesis, mechanical flexibility, lightweight nature, and the potential for low-cost production[3]. Moreover, molecular semiconductors can be designed to exhibit high sensitivity and selectivity towards specific gases, enhancing their utility in gas sensing applications[4].

In this thesis, initially, we explored the potential of silicon phthalocyanines (Cl_2-SiPc and $(345F)_2$-SiPc)[5] in a bilayer organic heterojunction device by combining it with a highly conducting molecular material ($LuPc_2$)[6] and investigated its NH_3 sensing properties to understand the interaction between gas molecules and the sensing layer. With this basic knowledge, we further explored the use of two original highly π-conjugated porphyrin complexes[7] in bilayer heterojunction devices in combination with $LuPc_2$ as the top layer and their response to ammonia under both dark and UV light. For very first time, we have demonstrated an amplification in sensing properties of an organic heterojunction device under illumination of UV light.

Most interestingly, we discovered a new type of ambipolar heterojunction device ($CoF_8Pc/LuPc_2$)[8] as well as novel external trigger (temperature variation) to inverse the nature of majority charge carriers within the device ($VOF_8Pc/LuPc_2$)[8]. CoF_8Pc-based device exhibits

n-type behaviour (current increases) under NH_3 and p-type behaviour (current increases) under NO_2 and O_3. It is surprising to observe the devices current goes up under both e^- donating and withdrawing gas species. The VOF_8Pc-based device changes its polarity upon humidity and temperature variation. Finally, we also studied the influence of the top layer on the polarity of bilayer heterojunction devices. Till now, we extensively studied the effect of sublayer in devices polarity, by employing different types of poor conductors as sublayer in bilayer heterojunction devices. For the first time, to realise the original effect of top layer in bilayer heterojunction devices, we utilised an ambipolar molecule (CuF_8Pc)[9-10] as sublayer and a series of *5,15*-diaryl Ni(II) porphyrin conjugated polymers (pNiD(Aryl)P) as top layer. Thanks to these CuF_8Pc/pNiD(Aryl)P) bilayer heterojunction devices, we report the pioneering demonstration of polarity inversion within a heterojunction device, by strategically manipulating the *meso*-substituent of the *5,15*-diaryl Ni(II) porphyrin conjugated polymer in the top layer of the heterojunction device. These findings would act as a precedent for later research works.

Globally, in this project, we focused on understanding and developing unipolar and ambipolar organic heterojunction devices based on molecular materials like phthalocyanines and porphyrins through external triggers and gas sensing. We developed different types of organic bilayer heterojunction devices. Among them, we reported several devices as very best gas sensors compared to existing gas sensors in detection of polluting gases like NH_3, NO_2 and O_3. Our main goal in this thesis is in achieving ambipolarity in molecular materials-based devices, which can replace two types of devices (p- and n-type) into single ambipolar device. Such ambipolar devices hold promise for various applications in nanotechnology, including deployment in spacecraft, satellites, and everyday electrical appliances where minimizing weight and size of the system is crucial.

Chapter 1

Introduction Bibliography

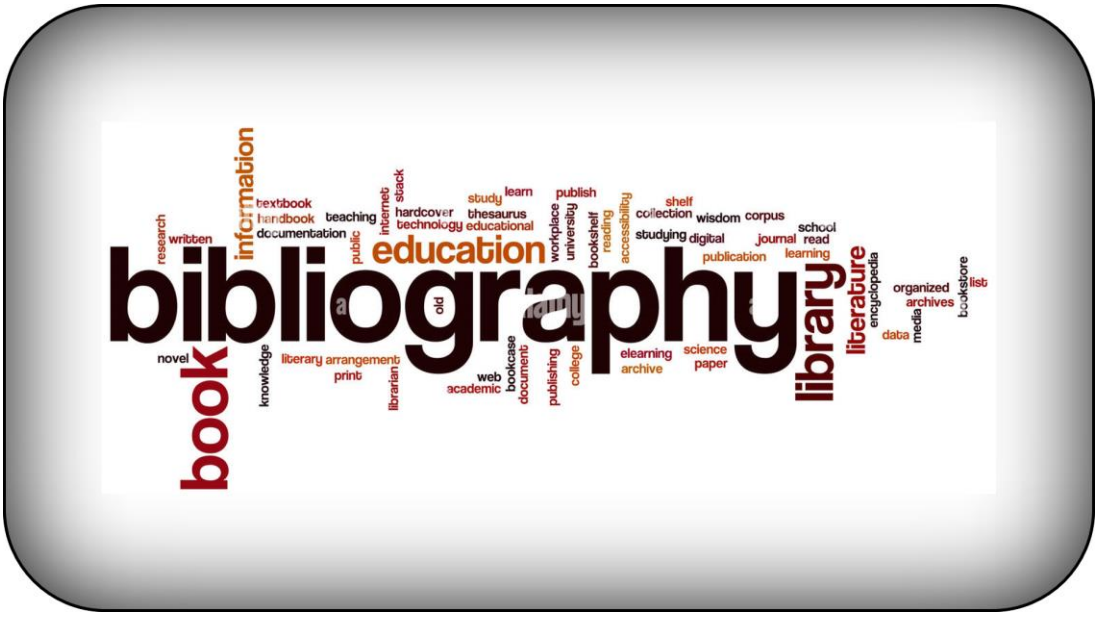

Chapter 1

Introduction Bibliography

Table of Content

Chapter 1. Introduction bibliography

1. Molecular semiconductors

In most inorganic materials, electronic wave functions are delocalized over many atoms, forming energy bands[11]. Charge carriers are generated when electrons transfer from the valence band to the conduction band, and mobility is high due to the strong overlap between atomic orbitals. However, this is not the case in molecular materials, in which conduction occurs through successive hopping of electrons from one molecule to another[12] with generally a lower conductivity compared to inorganic semiconductors. Only a few materials exhibit intrinsic electrical conductivity ranging from 10^{-6} to 10^{-1} $\Omega^{-1}cm^{-1}$ at room temperature.

The conduction process in molecular materials involves two main steps. The first step is the creation of charge carriers through the reduction of one molecular unit (A) and the oxidation of another unit. The second step involves the separation of the ion pair and the migration of the charges. Thus, the density of charge carriers is related to the oxidation and reduction potentials of the molecular unit A[12]. This process can be simply described by the following equation:

$$AAAAAA \leftrightharpoons AAA^{+}A^{-}AA \leftrightharpoons AA^{+}AAA^{-}A \qquad (1)$$

Charge carriers can also be generated through photoexcitation[13] and doping process[14]. Upon absorption of a photon, an electron is excited from the highest occupied molecular orbital (HOMO) to the lowest unoccupied molecular orbital (LUMO), creating an exciton, a Coulomb-bound electron-hole pair[15-16]. The dissociation of excitons into free charge carriers is a critical process and can be facilitated by thermal energy, electric fields, or at donor-acceptor interfaces in heterojunctions[17-18]. Doping, which involves the intentional introduction of impurities, modifies the intrinsic carrier concentration, enhancing conductivity. Molecular semiconductors

can be doped either p-type, introducing holes, or n-type, introducing electrons. Such doping phenomenon is fundamental to the development of conductometric gas sensors[19].

Among the notable molecular semiconductors, phthalocyanines have garnered significant attention. Discovered in the early 20th century, phthalocyanines are a group of macrocyclic compounds characterized by a large, planar conjugated π-system[20]. This structure, with alternating single and double bonds, creates a delocalized network of electrons over the molecule. The extended π-conjugation allows for the overlap of π-orbitals, facilitating electron mobility, which is influenced by the molecular packing, crystallinity, and purity of the material[21-23]. Overall, the unique properties of phthalocyanines, including their tuneable electronic characteristics and ability to form high-conductivity interfaces, make them highly suitable for a range of applications, especially in the realm of gas sensing, where they offer high sensitivity and selectivity.

1.1. Discrete energy levels

The electronic properties of molecular semiconductors are fundamentally determined by their energy levels, specifically the HOMO and LUMO[24]. The energy difference between these levels dictates the optical and electronic behaviour of the material[17]. Unlike inorganic semiconductors, which possess continuous energy bands, molecular semiconductors exhibit discrete energy levels[25]. In-depth, the concept of the energy gap in molecular crystals is fundamentally different from the forbidden energy gap in conventional covalent semiconductors such as germanium or silicon. However, the introduction of e^- donors or e^- acceptors substituents can lead to p-type or n-type materials, without any doping. For instance, substituting fluorine atom in copper phthalocyanine (CuPc) macrocycle, which is a p-type material, leads to the inversion in majority charge carrier densities. In CuF_0Pc, it is easy to inject an holes from Fermi energy level of the electrodes (ITO or gold) to the HOMO makes it as p-

type material. However, addition of fluorine atoms in CuF_0Pc macrocycle shifts the energy levels of the frontier orbitals. Hence it became easy to inject an electron from Fermi energy level of the electrodes to the LUMO of $CuF_{16}Pc$ making it as a n-type material. **Figure 1** displays the energy level diagram of CuF_0Pc and $CuF_{16}Pc$.

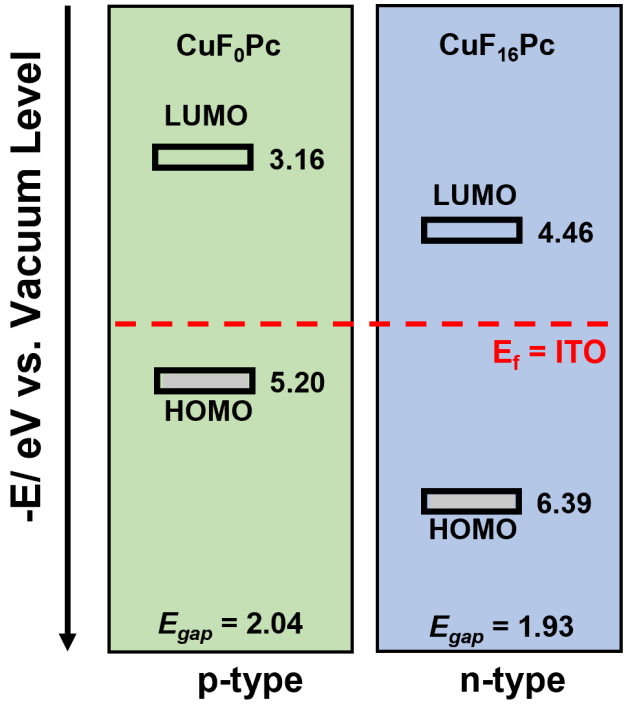

Figure 1. Energy levels of frontier orbitals: CuF_0Pc (p-type) and $CuF_{16}Pc$ (n-type).

In molecular crystals and van der Waals solids, there is a significant difference in energy between intramolecular and intermolecular interactions. The energy of an intramolecular C-C bond is about 3.6 eV (83.1 kcal/mol), whereas the intermolecular interaction energy between C atoms of neighbouring molecules is only about 4 meV (0.1 kcal/mol), which is three orders of magnitude smaller[26]. Therefore, many-electron interaction phenomena must be considered, while conventional band theory is inapplicable. In molecular crystals, charge carriers do not behave as "bare" quasi-free electrons or holes but instead form polaron-type quasi-particles, dressed “in electronic and vibronic polarization clouds[27].

1.2. Charge transport regime

Charge transport in molecular semiconductors is highly dependent on the nature of intermolecular interactions in the solid state[28-29]. These interactions, including van der Waals forces, π-π stacking, and hydrogen bonding, govern the molecular packing, crystalline order and charge transport within the material[30-32]. Efficient charge transport is often achieved in materials where strong π-π interactions lead to significant orbital overlap, facilitating coherent charge migration[28].

Understanding the frontier molecular orbitals and their alignments is pivotal for optimizing the electrical properties of the molecular semiconductor-based devices. The alignment of energy levels at interfaces, particularly in heterojunctions, critically influences charge separation and recombination processes[33]. When the work function of the electrode aligns well with the HOMO or LUMO of the semiconducting material, it can create a ohmic contact where the charges can flow through the materials without any contact resistance[34]. However, metal-semiconductor junction can exhibit rectifying behaviour due to the formation of a Schottky barrier at the interface[35]. This occurs when the semiconductor is n-type and its work function is smaller than that of the metal, or when the semiconductor is p-type and the opposite relation between work functions exists. The height of the barrier, influenced by the work functions, gives rise to Schottky diode, which has a low forward voltage drop and fast switching speeds[36]. Similarly, when p-type and n-type molecular semiconductors are engaged in a heterojunction device, it can give rise to p-n junction diode[37]. The behaviour of p-n junctions in molecular semiconductors is influenced by factors such as energy level alignment, exciton dissociation efficiency, and the quality of the interface. These diodes are essential in applications where efficient charge separation and recombination processes are crucial for device performance[38].

Beyond metal-organic semiconductor junctions, interfaces can also form in devices with bilayer or multilayer sensing active layers, creating organic-organic heterojunctions[19]. A typical p-n heterojunction, formed from p-type and n-type organic semiconductors, is characterized by the accumulation of electrons (e^-) and holes (h^+) at the interface due to differences in electron affinity and work function. These interfaces generally conduct better than the bulk of either semiconductor in the heterojunction, with carrier transport occurring along the interface. In contrast, the space charge region in conventional inorganic p-n junctions is highly resistive[39-40]. It consists of a depletion of free charge carriers exhibiting an opposite polarity to the heterojunction's built-in electric field. Charge migration in inorganic and organic heterojunction devices is shown in **Figure 2**.

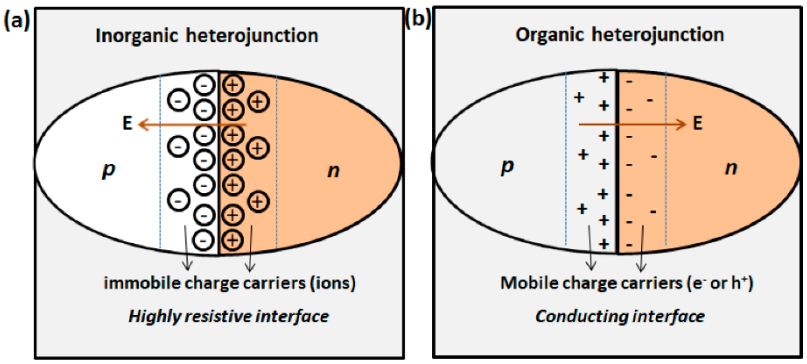

Figure 2: Typical p-n heterojunction formation and interfacial charges alignments in conventional inorganic semiconductor (a) and organic semiconductor (b). (adapted from Ref [19, 39]). The arrangements of mobile (e^- or h^+) and immobile (ions) charges at the interface and associated direction of electric field are shown.

1.3. Organic electronics

In the realm of materials science and organic electronics, the quest for efficient, flexible, and sustainable electronic devices has led to the exploration of novel materials with unique properties. Molecular semiconductors have emerged as a key class of materials, offering

promising electrical properties, making them vital components in various applications ranging from energy harvesting in solar cells[41] to light emission in organic light-emitting diodes (OLEDs)[42] and the development of organic field-effect transistors (OFETs), and organic photovoltaics (OPVs), which hold promise for flexible and wearable electronics[43].

Unlike silicon-based counterparts, organic semiconductors offer mechanical flexibility, solution processability, and potentially lower manufacturing costs[44]. These materials exhibit semiconducting behaviour through the delocalization of π-electrons across conjugated molecular structures and their electrical properties are highly tuneable by modifying molecular structure, such as varying the size and arrangement of aromatic rings, substituents, or conjugation length[45]. In recent decades, organic electronics have transitioned from the confines of research laboratories to the commercial market. A common example is OLED, which is widely used in modern displays like in televisions, computers, smartphones, and various wearable devices. Similarly, OPVs are gaining recognition as a promising alternative to traditional, costly silicon-based photovoltaic technologies[46]. Alongside these developments, chemical sensors have emerged as a significant area of research, attracting extensive studies on organic semiconductors owing to their advantages of low cost and flexibilities of chemical design, synthesis and processing.

2. Chemical Sensors

Gas sensors operate on the fundamental principle of detecting changes in the physical or chemical properties of a sensing material upon exposure to a target gas[47]. These changes, which may involve variations in electrical resistance, capacitance, or optical properties, are converted into electrical signals for measurement and analysis. The detection mechanism typically involves the adsorption of gas molecules onto the surface of the sensing material, followed by interactions that alter the material's properties and result in a measurable electrical

signal. Depending on the type of sensor and the gas involved, sorption behaviour can lead to changes in the sensor's electrical, optical or thermal properties based on the concentration of the target gas. Understanding and controlling sorption behaviour is crucial for designing effective gas sensors with high sensitivity and selectivity[47].

Various types of gas sensors have been developed, including metal-oxide semiconductor (MOS) sensors[48], electrochemical sensors[49], optical sensors[50], and molecular semiconductor-based sensors[51]. MOS sensors detect gases through changes in the resistance of metal oxide films, while electrochemical sensors measure gas concentration via redox reactions that generate a proportional current. Optical sensors utilize changes in light absorption or emission caused by gas interactions, and molecular semiconductor-based sensors leverage the unique electronic properties (delocalization of electrons) of organic semiconductors. Many different types of device architectures have been adapted in modern gas sensors. Here we discussed about the two main designs: chemiresistors and heterojunction-based gas sensors.

2.1. Chemiresistive gas sensors

Chemiresistors are nothing but conductometric sensors made up of only one layer unlike heterostructure sensors that consist of two or more different types of materials that form junctions. Schematic view of simple chemiresistive devices were shown in **scheme 1**. Over the decades, chemiresistive gas sensors have emerged as a promising technology for the simple detection of harmful gases and VOCs across various applications[52].

Scheme 1. Schematic view of simple chemiresistive devices. The arrow indicates the charge flowing pathway.

In 1960s, Seyama et al. demonstrated the effectiveness of ZnO thin films as sensing layers for propane, pioneering the development of simple electrical devices for gas sensing[53]. Since then, there has been a remarkable development in research on metal oxides-based gas sensors. For instance, tin dioxide (SnO_2)-based sensors are extensively utilized for detecting gases like methane and carbon monoxide[54]. Although, metal oxides-based sensors offer several advantages like low-power, low-cost, small-size, durability, ease of fabrication and high sensitivity, they suffer from poor selectivity in the presence of interfering gases and require high operating temperatures[55].

Throughout the 20th century and into the 21st century, research efforts focused on enhancing the sensitivity, selectivity, and stability of chemiresistive gas sensors. This involved advancements in materials science, nanotechnology, and surface chemistry, as well as the integration of sensor arrays and signal processing algorithms for improved detection and discrimination of target gases[4, 56]. In recent years, the emergence of novel materials such as carbon nanotubes, graphene, and metal-organic frameworks has opened up new possibilities for chemiresistive gas sensor technology. These materials offer advantages such as high surface area, tuneable properties, and enhanced sensing performance, driving further innovation in the field[57-58].

The development of porphyrinoids and conjugated polymers provides an effective alternative to metal oxide dominance in chemiresistive gas sensors. The tunability, durability, and their capability to operate at ambient temperature make porphyrinoids and conjugated polymers such as phthalocyanines, porphyrins, corroles, polypyrrole, polyaniline (PANI) and polythiophene attractive as chemiresistive gas sensors materials[59-60]. In particular, PANI-based materials are largely exploited for their sensing properties towards NH_3. Similarly to metal oxide-based chemiresistive gas sensors materials, the sensing properties of conjugated polymers are influenced by their structure and morphology[61-62]. For example, PANI nanowires

demonstrated excellent sensing detection limit, up to 0.5 ppm, towards NH_3, which changes to 15-120 ppb for 2D PANI films[63]. The sensing properties of conjugated polymers can be further tuned by different processes like chemical doping and composite formation with other materials, thereby amplifying the chemiresistive gas sensors' performance and selectivity.

Porphyrinoid-based chemiresistors also exhibit remarkable sensing response towards various of target gases like NH_3, Cl_2, NO_x and H_2S[64-65]. In particular, metal phthalocyanine-based chemiresistors were frequently reported for their sensing performance towards VOC[66-67]. For instance, classical NiPc-based sensor displays excellent sensitivity and stability towards NO exposure. The device exhibits sensitivity values of 0.19% ppm^{-1} and 0.42% ppm^{-1} for NO concentration in the ranges of 500–50 ppm and 50–5 ppm, respectively[66]. On other hand, Trogler et al reported the sensing performance of cobalt and metal-free phthalocyanine-based thin films under various analytes. Particularly, both CoPc and H_2Pc-based chemiresistive sensors exhibit sensitivity of 0.05% ppm^{-1} and 0.14% ppm^{-1} towards dimethyl sulfoxide (DMSO) and 0.01% ppm^{-1} and 0.1% ppm^{-1} towards dimethyl methylphosphonate (DMMP, a neurotoxin simulant), respectively[67].

Moreover, the possibility to modulate a chemical structure of porphyrinoids and polymers by introducing groups equipped with interacting sites and their adaptability in various forms like nanofibers, nanoparticles and thin films empowers scientists to tailormade sensors for desired sensing requirements[68]. However, despite several advantages, chemiresistor-based sensors face limitations in terms of slow response and long recovery times, poor thermal stability, and limited selectivity, which seldom constrained their larger utility. Today, chemiresistive gas sensors are widely used in various applications, including environmental monitoring, industrial safety, healthcare, and consumer electronics. Ongoing research aims to address remaining challenges such as selectivity, stability, and power consumption, while also

exploring new avenues for sensor integration, miniaturization, and wireless connectivity in the era of the Internet of Things (IoT)[69].

2.2. Heterojunction gas sensors

Among these, heterojunction gas sensors, which combine two different semiconductor materials, stand out for their enhanced performance[29]. The heterojunction interface creates a unique electronic environment that can significantly improve sensor sensitivity and selectivity. This improvement is due to the synergistic effects at the interface, which enhance the sensor's response to gas molecules by providing tailored interactions for specific gases and facilitating faster charge transfer processes for quicker detection. Additionally, the combination of materials can enhance the stability and durability of the sensors. This makes heterojunction gas sensors a promising solution for precise and reliable gas detection applications.

Different gas-sensitive materials engaged in heterostructures were continuously reported to offer better gas-sensing properties, in terms of sensing response, selectivity, operating temperature and reproducibility, compared to chemiresistors prepared with the same inorganic sensing materials, such as MoS_2/SnO_2[70-71]. However, the interaction between sensing materials and gas molecules is identical in heterojunction devices as in chemoresistors, but the sensing mechanisms of heterojunction devices are more complex. Indeed, after adsorption, charge transfer between target gas and sensing material can lead to doping, charge neutralization or trapping, and more important, it can modify the energy barrier at the interface between materials, which gives us astonishing results.

Numerous studies have been carried out on ZnO engaged in a heterostructure with other metal oxides, metal sulphides, quantum dots and noble metals[72-74]. Thanks to their difference in work function, each combination gives rise to different interfaces with different levels of energy barrier, which play a major role in their optical, electrical and gas sensing properties.

The improvement in gas sensing technology was attempted by changing the sensing materials, but recently a growing trend aiming to exploit organic semiconductor-based heterojunction device and the role of interface to modulate the sensing performance of the device[9, 75-76]. The interfaces between the sensing material thin film and the electrodes (typically metals) have prompted extensive research into metal-organic semiconductor junctions and their effects on chemical sensors[48]. In many sensor configurations, the interaction of target gases with either metal electrodes or the organic semiconductor thin film modulates charge carrier injection from the metal to the organic film[77]. This interaction adjusts the interfacial energy level alignment at the metal-organic junction, forming the core sensing principle[78].

Given that bulk carrier transport in organic semiconductor thin films is typically slow due to the hopping of e^- or h^+, from molecules to molecules, creating a heterojunction in organic semiconductor-based devices is highly beneficial[79]. It enhances carrier transport and thus improves device conductivity. The dynamics of interfacial alignment of free charges can be modulated by external doping, such as chemical doping by redox active gases (e.g., O_3, NO_2 or NH_3)[80-82]. This approach has been exploited to develop high-performance gas sensors.

A few years ago, M. Bouvet et al. introduced a new type of heterojunction device composed of two distinct conducting layers: a poorly conducting material as the sublayer in contact with electrodes, covered by a highly conductive molecular material as the top layer. Initially, this device was named as molecular semiconductor doped insulator (MSDI)[9, 83]. Unlike classical resistors, which exhibit linear current-voltage (I-V) characteristics in accordance with Ohm's law, this novel device displays non-linear I-V characteristics due to charge accumulation at the interface.

In this device, the poorly conducting sublayer causes injected charges to encounter significant resistance at low voltage, resulting in lower current. However, at higher biases, the

injected charges from the electrode gain sufficient energy to overcome the energy barrier, leading to higher current at higher voltages. In most of such heterojunctions reported before starting this PhD work, $LuPc_2$ was used as top layer[84] due to its high conductivity. The activation energy of $LuPc_2$ is 0.5 eV, which is very small compared to other metal phthalocyanines like CuPc (ca. 2 eV). Moreover, $LuPc_2$ has a stable radical nature and possess high density of intrinsic charge carriers with both e^- and h^+ densities near equilibrium[85]. Since the resistive sublayer is much thinner than the inter-electrode distance, when bias is applied, in order to take most conductive pathway, the charges flow through the interface between both materials. Thus, modifying the interface can lead to novel electrical and gas sensing behaviours. This idea inspired us to explore various types of poorly conducting materials as sublayers in bilayer heterojunction devices with $LuPc_2$. Additionally to $LuPc_2$, a polyporphyrin was also used as a top layer[86].

Beside double layer heterojunctions[87], another type of heterojunction was recently reported, namely double lateral heterojunctions[75]. The former is a classical heterojunction, which is fabricated by sequentially depositing two different materials over the entire surface of the substrate[9]. This method ensures complete coverage of the substrate by each material layer, one on top of the other. Typically, techniques like physical vapour deposition (PVD)[87], e.g. for phthalocyanine complexes, or chemical vapour deposition (CVD)[86] for depositing poly porphyrin, starting from porphyrin monomers are used for this purpose, allowing for precise control over the thickness and uniformity of each layer. The latter were obtained by depositing material by an electrodeposition technique, such as electropolymerization[76, 80-81, 88]. In this method, the material is deposited only on the surface of the electrodes where monomers are oxidized to form insoluble polymers. This selective deposition allows for precise patterning of the material on the electrode fingers. However, using this technique, only one material can be deposited at a time. To create a double layer heterojunction, the second layer must be deposited

using a different suitable technique after the initial electrodeposition. In this thesis, mostly we used thermal evaporation technique to deposit the top layer. Schematic view of double layer and double lateral heterojunction devices are shown in **Scheme 2**.

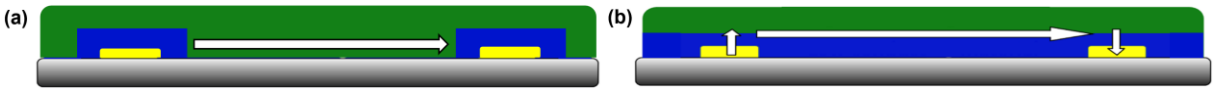

Scheme 2. Scheme of a double lateral heterojunction (a) and a double layer heterojunction (b). Arrows represent the charge transport pathways.

3. Ambipolar devices

3.1. Ambipolarity

Ambipolarity is often referred to a physical balance, characterized by an infinite number of unbalanced positions but only one stable state. It is achieved when the densities of electrons (e^-) and holes (h^+) contribute equally to electrical conduction. Theoretically, this equilibrium is realized in intrinsic semiconductors exemplified by $LuPc_2$, yet trapping effects and specific environmental interactions may impede its observation[89]. To achieve an ambipolar transport regime in organic electronic devices including gas sensors, there are two main challenges: Tuning the e^- and h^+ concentrations in the device near equilibrium to a sufficiently large level and an efficient trigger for the majority charge carrier inversion.

To achieve high densities of electrons (e^-) and holes (h^+) in equilibrium within a molecular semiconductor like metal phthalocyanines (MPcs), an appropriate combination of electron-accepting and electron-donating substituents can be grafted, and metal centres with different electron affinities can be utilized. Only a few ambipolar molecules have been previously reported. As we discussed earlier, the p-type CuPc was converted to n-type material by substituting 16 fluorine atoms ($CuF_{16}Pc$). However, optimising the degree of fluorine atoms

in CuF_xPc macrocycles gave rise to a novel electronic property. In CuF_8Pc the frontier energy levels were align well with the Fermi energy level of the electrodes that makes possible to inject charges from either to HOMO or LUMO. Hence, CuF_8Pc can exhibit both p- and n-type[90] (**Figure 3**).

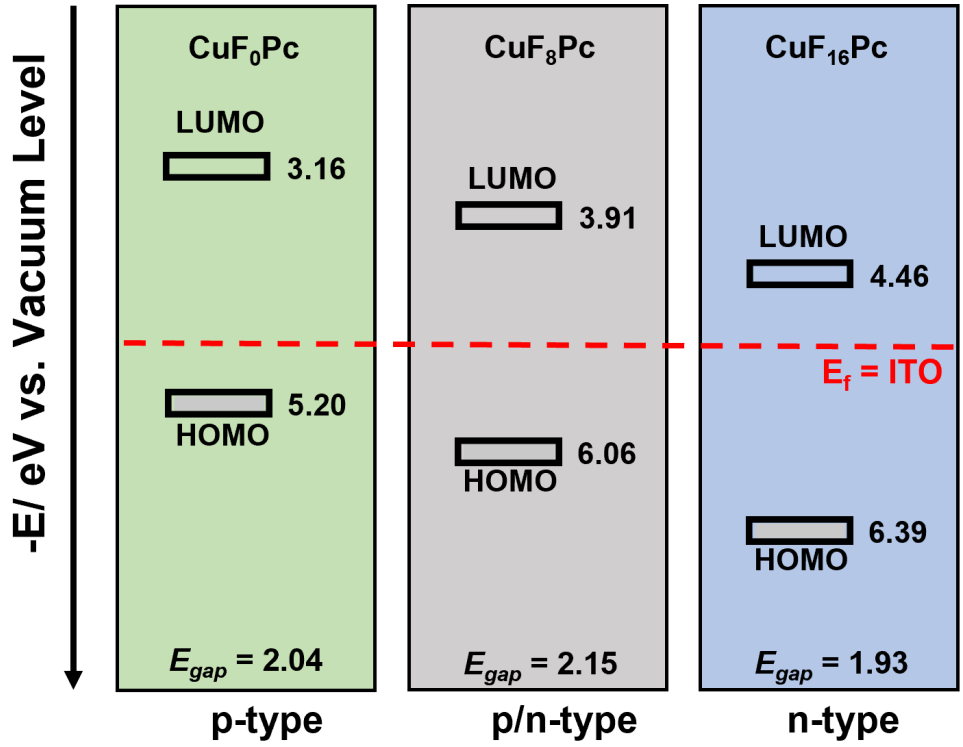

Figure 3. Comparison between frontier energy orbitals of CuF_0Pc (p-type), CuF_8Pc (p/n-type) and $CuF_{16}Pc$ (n-type).

The phenoxy and naphthoxy substitutions in europium triple-decker phthalocyanine complexes have resulted in very high and similar e^- and h^+ carrier mobilities, both exceeding 1 $cm^2\ V^{-1}\ s^{-1}$ in organic field-effect transistor (OFET) devices, thereby demonstrating air-stable ambipolar carrier transport[91-92]. However, it is important to note that not all materials with both p- and n-channels exhibit ambipolar sensing behaviour. This limitation arises due to significant differences in e- and h+ concentrations or the absence of a suitable trigger (an external stimulus) to shift the equilibrium concentration of either charge carrier.

For instance, the europium triple-decker phthalocyanine complex bearing thiohexyl groups, $Eu_2[Pc(S\text{-}hexyl)_8]_3$, in a chemiresistor configuration, exhibited n-type polarity with a current decrease under NO_2 exposure but was insensitive to NH_3 and H_2S[93]. Conversely, $LuPc_2$-based OFET shows n-type behaviour in an inert atmosphere and p-type behaviour in ambient conditions[93]. This dual behaviour is due to the equilibrium between charges densities, where specific interactions with the environment lead to polarity transformation. This example underscores the necessity of fine-tuning the molecular structure and external conditions to achieve desired ambipolar sensing characteristics.

3.2. External triggers

An external energy source such as optical, electrical or atmospheric changes, used to trigger the inversion in nature of majority charge carrier in molecular semiconductor-based devices, is often called as an external trigger. Only very few ambipolar devices have been reported in the literature, and those utilizing external triggers to control over the inversion in polarity of the device are particularly scarce. **Scheme 3** displays different external triggers used to inverse the polarity of ambipolar devices

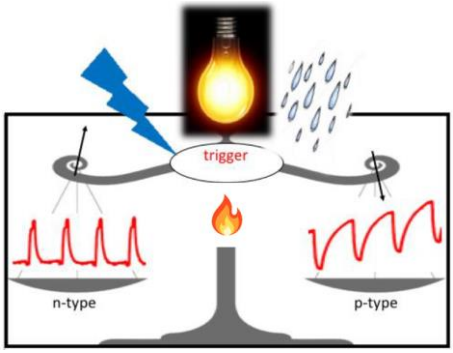

Scheme 3. Schematic view of external triggers (voltage, light, humidity and temperature) capable of inversing the polarity of an ambipolar device (modified from Ref [89]).

3.2.1. Optical trigger

It is well known that light illumination on semiconductor device can modify the density of charge carriers. However, in heterojunctions, the effect of light also depends on interfacial charge accumulation and on the work function of the materials engaged in it. A few years ago, M. Bouvet at al. demonstrated a brand-new effect on gas sensors using visible light illumination on organic heterojunction devices. They fabricated a series of bilayer semiconductor devices consisting of copper phthalocyanines with different degrees of halogenation, such as $CuF_{16}Pc$, CuF_8Pc, $CuCl_8Pc$ and CuPc as sublayers, which were commonly covered by a $LuPc_2$ as a top layer[10, 94]. The electrical and NH_3 gas sensing properties of the organic heterojunction devices were investigated both in the dark and under visible light illumination (red LED, 642 nm) at room temperature.

The $CuF_{16}Pc/LuPc_2$ device exhibits a positive response to NH_3 (**Figure 4a**), whereas the $CuCl_8Pc/LuPc_2$ device exhibits a negative response (**Figure 4c**), similar to $CuPc/LuPc_2$[10]. All three of these devices exhibit excellent observable response towards NH_3 gas at room temperature in the dark, and the response remains almost the same under visible light illumination, while a current increase was observed due to light absorption. Authors did not observe any enhancement in gas sensing properties upon illumination for the octa-fluorinated copper phthalocyanine-based heterojunction device ($CuF_8Pc/LuPc_2$). However, the most interesting phenomenon observed was the inversion in the nature of the response (**Figure 4b**)[10]. This shows that apart from charge density modification, light can induce a new phenomenon in gas sensors called the detrapping effect, which can invert the polarity of the majority charge carriers[89].

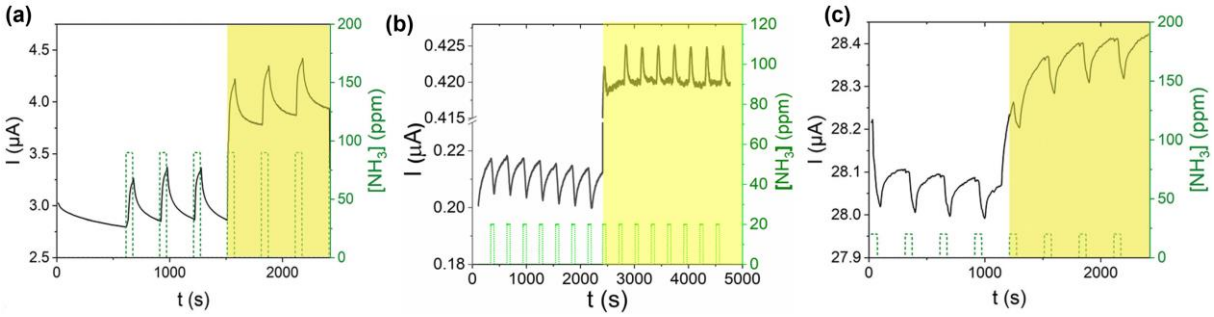

Figure 4. Response of $CuF_{16}Pc/LuPc_2$ (a), $CuF_8Pc/LuPc_2$ (b) and $CuCl_8Pc/LuPc_2$ (c) based heterojunction sensors towards 20 ppm of NH_3 under dark and light at room temperature (adapted from the Ref [10]).

Initially, the $CuF_8Pc/LuPc_2$-based heterojunction device shows a very clear negative response (with less noise) towards 20 ppm of NH_3 gas with an RR of −7%, displaying its p-type nature in the dark, but under visible light illumination, the device exhibits stable positive response with RR ca. 1.2% towards the same concentration of NH_3 gas showing n-type nature. Therefore, the $CuF_8Pc/LuPc_2$-based device changes its polarity from p- to n-type, depending on the optical external trigger, exhibiting its bistability.

This fascinating phenomenon under visible light illumination can be explained by the desorption effect of oxygen molecules. It is well known that the adsorption of oxygen molecules on semiconductor devices can decrease the density of free electrons while increasing hole density[95]. At the same time, light illumination on semiconducting devices is well known for facilitating oxygen desorption from the surface of sensing materials, which induces a detrapping of negative charges. Thus $CuF_8Pc/LuPc_2$-based device exhibits p-type behaviour towards reduction gas (NH_3) in oxygen-rich dark environmental condition. However, under red light illumination, the desorption of oxygen molecules is favoured. Hence, there is an inversion in nature of majority charge carriers, which leads to an inversion in gas response. This inversion is mainly due to the ambipolar property of CuF_8Pc, with an initial density of positive and

negative charge carriers very near to each other[10, 90]. Since the electrical properties of the semiconductor material are near equilibrium, a weak energy coming from an external trigger is sufficient to inverse its polarity. To date, this is the only report of such an astonishing effect in conductometric sensors using visible light.

3.2.2. Electrical trigger

Electrical trigger is often used in ambipolar organic field-effect transistors in the form of applying potential difference across the gate terminal of the transistor. Ambipolar transistors represent a class of transistors that facilitate the synchronous transport and accumulation of both electrons and holes within semiconductors. An ambipolar transistor typically constructed as same as classical transistors that consists of a gate electrode, a dielectric material, a semiconducting layer, and source and drain electrodes. The first three components form a metal–insulator–semiconductor architecture, which enables the accumulation of holes or electrons at the interface between the dielectric and the semiconducting layer by applying a gate bias with a specific voltage polarity, negative or positive, respectively. The source to drain voltage controls the injection of charge carriers necessary for the accumulation process in the channel at the interface between the dielectric material and the semiconductor.

The injected holes and electrons can transfer based on various bias applied at these three terminals. As a result, the amount and polarity of charge carriers within the accumulation zone vary with different gate bias: positive gate bias for electron accumulation and negative gate bias for hole accumulation. This variability in the charge carrier accumulation ultimately leads to differences in the conductivity of the transistors. In 1990, J. Simon et al. reported the first ever transistor that exhibits both p- and n-type behaviour using $LuPc_2$ as a semiconductor, depending on the direction of the gate voltage as well as the surrounding atmosphere[93]. Under vacuum, the device displayed n-type behaviour when a positive gate voltage was applied, while no transistor

effect was observed with a negative gate voltage. Conversely, in ambient conditions, the same device exhibited p-type behaviour with a negative gate voltage, while no transistor effect was observed with a positive gate voltage.

Later in 2011, Dodabalapur et al[96] reported the first ever chemical sensor based on an ambipolar transistor, consisting of two superposed semiconducting layers: zinc oxide (ZnO) as an n-type semiconductor, covered by pentacene, a p-type semiconductor. In the p-channel accumulation mode ($V_{GS} < V_{DS} < 0$), a decrease in current was observed under ethanol vapours due to positive charges being trapped in the pentacene layer. Conversely, in the n-channel linear regime ($V_{GS} > V_{DS} > 0$), an increase in current was observed. The polar ethanol molecules can act as a trap for positive charges to stabilize itself. Hence there is a shift in charge carrier equilibrium causing polarity inversion in the device. This effect is analogous to decrease in the magnitude of the gate bias, which results in an increase of the drain-source current. This sensor combines the sensitivity of organic materials to polar analytes through dipolar chemical interactions, combined with the stability of metal oxide semiconductors, which are protected from air. This ground-breaking discovery highlighted the potential of environmental conditions and electrical trigger to influence the properties of transistors, paving the way for future advancements in ambipolar transistor technology.

3.2.3. Humidity and Temperature

It is well known that variations in humidity or temperature can significantly impact the performance of conductometric transducers. Even small fluctuations can cause substantial changes in the electrical and sensing properties of these devices. Humidity, in particular, is a critical factor in real-time applications, serving as a potential external trigger that can invert the nature of the majority charge carriers in ambipolar devices. For instance, a $ZnCl_8Pc/LuPc_2$ device exhibits p-type behaviour (current decreases under NH_3 exposure) at higher humidity

levels (70%), whereas the same device shows n-type behaviour (current increases under NH_3 exposure) at lower humidity levels (20%)[97] (**Figure 5a**). On the contrary, a $CuF_8Pc/LuPc_2$ device displays p-type behaviour at lower humidity (30%) and n-type behaviour at higher humidity (70%)[94] (**Figure 5b**). Here, two different concepts were involved. Water molecules are well known for their electron-donating behaviour, but also possess the ability to trap mobile charges within the device. In heterojunction sensors, the changes in charge densities initially occur in top layer, as it is the sensor surface directly exposed to the target gas and the atmosphere. However, the diffusion of gas and water molecules into the underlying layers can subsequently influence the charge transport regime within the device[98].

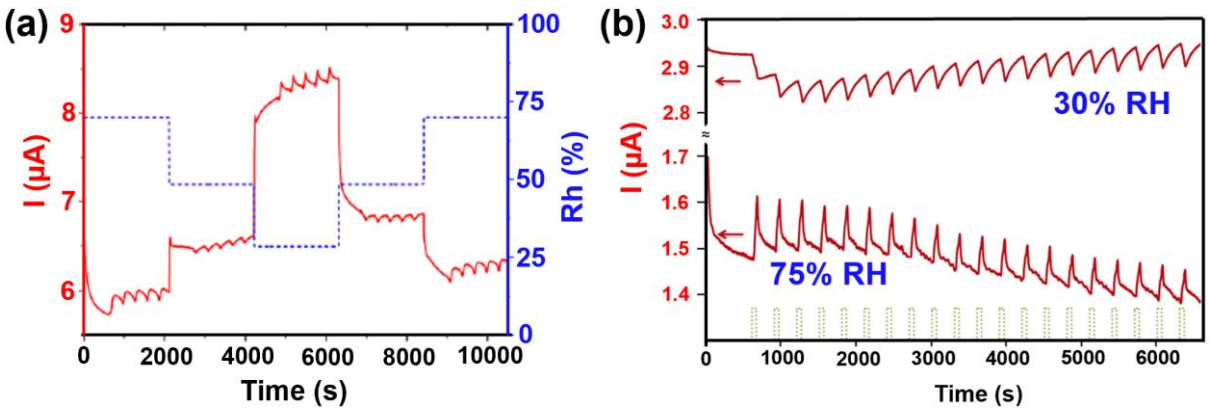

Figure 5. Response curve of $ZnCl_8Pc/LuPc_2$ (a) (adapted from the Ref [97]) and $CuF_8Pc/LuPc_2$ (b) (adapted from the Ref [94]) device towards NH_3 under different humidity level at room temperature.

Regarding temperature effect, an increase in temperature typically leads to higher current and accelerates the sorption kinetics in conductometric sensors. However, this thesis presents, for the first time, the use of temperature variation as an external trigger to invert the nature of majority charge carriers in a heterojunction device. The detailed explanation of this work is summarized in **chapter 5**.

The growing need for effective and reliable gas sensors as well as miniature electrical systems, driven by the escalating concerns about air quality and compactable devices, underscores the significance of this research. Molecular semiconductor-based heterojunction devices offer a promising approach, combining the advantageous properties of organic materials with the enhanced performance of heterojunctions. This thesis aims to explore the development and optimization of these devices, addressing current challenges and advancing the field of gas sensing and ambipolar device technologies.

Chapter 2

Experimental Descriptions and Optical Characterization of Bilayer Films

Chapter 2

Experimental Descriptions and Optical Characterization of Bilayer Films

Table of Content

Chapter 2. Experimental descriptions and optical characterization of bilayer films

1. Introduction

This chapter has been divided into two main sections: materials and methods, and optical characterization of all bilayer heterojunction devices reported in this thesis. In the first section, we discuss the molecular materials used in this work, including their synthesis and properties, as well as the various deposition techniques employed to fabricate the bilayer heterojunction devices. These techniques include physical vapour deposition (PVD), oxidative chemical vapour deposition (oCVD), electrodeposition, and the quasi-dip coating method. Additionally, we detail the different characterization techniques adopted to understand the device properties, such as electrical measurements and the setups used for studying the sensing properties of the bilayer sensors. In the second section, we focus on the optical characterization of the materials and bilayer films, presenting the ultraviolet-visible (UV-Vis) and Raman spectra of all the reported devices. The UV-Vis spectroscopy provides insights into the optical properties and electronic transitions of the materials, while the Raman spectroscopy analysis helps to understand the vibrational modes and molecular interactions within the heterojunction devices. This comprehensive approach ensures a thorough understanding of both the experimental methodologies and the optical properties of the bilayer heterojunction devices, forming a solid foundation for the subsequent analysis of their electrical and sensing performances.

2. Materials and methods

Molecular semiconductors such as dichloro silicon phthalocyanine (Cl_2SiPc) and bis(3,4,5 triflurophenoxy) silicon phthalocyanine ($(345F)_2$-SiPc) were synthesized by our collaborator Prof. Benoît H. Lessard from University of Ottawa[5]. Acenaphtho[1,2-*b*]-pentacene-9,16-dione-fused nickel porphyrin (Ace-PQ-Ni) and pentacene fused nickel porphyrin (AM6) were provided by our collaborator Prof. Hong Wang from University of North Texas[7], and different types of conjugated nickel porphyrins were obtained from our collaborator Dr. Nicolas Boscher in Luxembourg Institute of Science and Technology (LIST). Octafluoro-metallophthalocyanines (ZnF_8Pc, CoF_8Pc, VOF_8Pc) were synthesized in our laboratory by collaborating with Dr. Seydou Ouedraogo from Burkina Faso.

ZnF_8Pc, and CoF_8Pc were obtained from 4,5-difluoro-1,2-dicyanobenzene, which was reacted at 210 °C for 2.5 h in a glass tube with zinc acetate ($Zn(OAc)_2$) and cobalt acetate ($Co(OAc)_2$), respectively. VOF_8Pc was synthesized from 4,5-difluorophthalonitrile by reacting at 200 °C for 2.5 h in a glass tube with vanadyl diacetate ($VO(OAc)_2$). The obtained solids were washed with DMF and ethyl alcohol, each three times, using an ultrasonic bath for 10 min and centrifugation at 3000 rpm for 20 min. The solids were then dried at 100 °C under primary vacuum for 2 h, following a previously reported method[8].

Similarly, lutetium bisphthalocyanine ($LuPc_2$) was synthesized from o-phthalonitrile and lutetium triacetate by heating at 300 °C without any solvent for 3 h, following a previously reported method[6]. Synthesis of $Cu(F_8Pc)$ was achieved through reaction of 4,5-difluoro-1,2-dibromobenzene with copper cyanide as described in literature[9]. Chemical structure of all the molecular materials used in this thesis were shown in **scheme 4**.

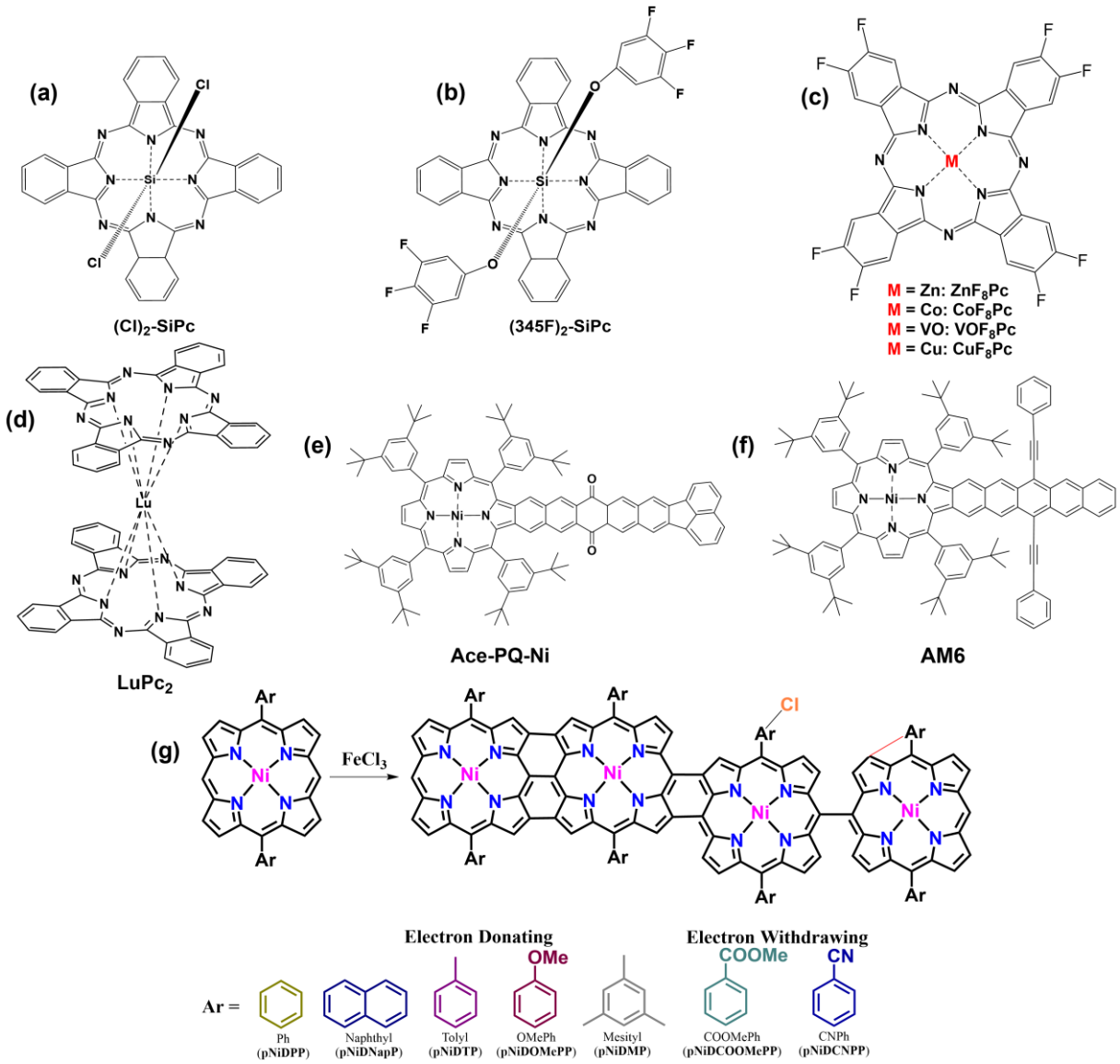

Scheme 4: Chemical structure of silicon phthalocyanine (Cl_2SiPc) (a) and bis(3,4,5-triflurophenoxy) silicon phthalocyanine ($(345F)_2$-SiPc) (b), octafluoro-metallophthalocyanines (c), lutetium bisphthalocyanine ($LuPc_2$) (d), acenaphtho[1,2-*b*]-pentacene-9,16-dione-fused nickel porphyrin (Ace-PQ-Ni) (e), pentacene fused nickel porphyrin (AM6) (f) and different substituted Ni(II) polyporphyrins (g).

3. Device fabrication techniques

The fabrication of our heterojunction devices began with the subsequent deposition of sublayer and top layer on Indium Tin Oxide (ITO) interdigitated electrodes (IDEs). These IDEs

consisted of 16 pairs of ITO digits, each with a width and spacing of 75 µm, fabricated on a glass substrate using lithography techniques. Prior to deposition, the electrodes underwent thorough cleaning with CH_2Cl_2 and EtOH through multiple stepwise ultrasonication cycles, each for 5 min, followed by drying in an oven at 100 °C for 1 h.

To fabricate bilayer heterojunction devices, we employed various deposition methods based on the solubility and thermal stability of the materials. These methods included both physical vapour deposition and oxidative chemical vapour deposition. For certain materials, the conventional drop casting method did not yield a sufficiently homogeneous surface. Therefore, we experimented different approaches and ultimately developed a novel deposition technique called quasi-dip coating method.

3.1. Physical vapour deposition

Physical Vapour Deposition (PVD) is a traditional vacuum deposition technique where material is vaporized in a vacuum environment and then deposited onto a target substrate, forming a thin film. Most of the devices reported in this thesis were fabricated using a German-made thermal evaporator, the UNIVEX 250 (Oerlikon).

The UNIVEX 250 is equipped with dual tantalum crucibles, allowing for the sequential deposition of two different materials. Additionally, a quartz crystal microbalance is mounted near the target substrate inside the instrument, enabling precise control of the deposition rate and thickness. The sublimation temperature was chosen depending on the thermal stability of the material. Moreover, the vacuum evaporation technique to deposit films is also a further purification step of the materials. Thus, on the cover of tantalum crucible, crystals are formed that are purer than the pristine material, and can be used for Raman analyses. The Cl_2-SiPc, $(345F)_2$-SiPc, MF_8Pc (Zn, Co and VO) and $LuPc_2$ were deposited using this technique. All these materials were deposited around the temperature from 400 to 450 °C with deposition rate of ca.

1 $Å s^{-1}$ except $345F_2$-SiPc. The deposition rate and sublimination temperature for $345F_2$-SiPc was maintained at ca. 0.2 $Å s^{-1}$ and 350–400 °C, respectively, due to its potential decomposition over 450 °C. To achieve a highly homogeneous surface, the samples were coated under a secondary vacuum of ca. 7 x 10^{-7} mbar. The detailed information about vacuum sublimation is given in **scheme 5**.

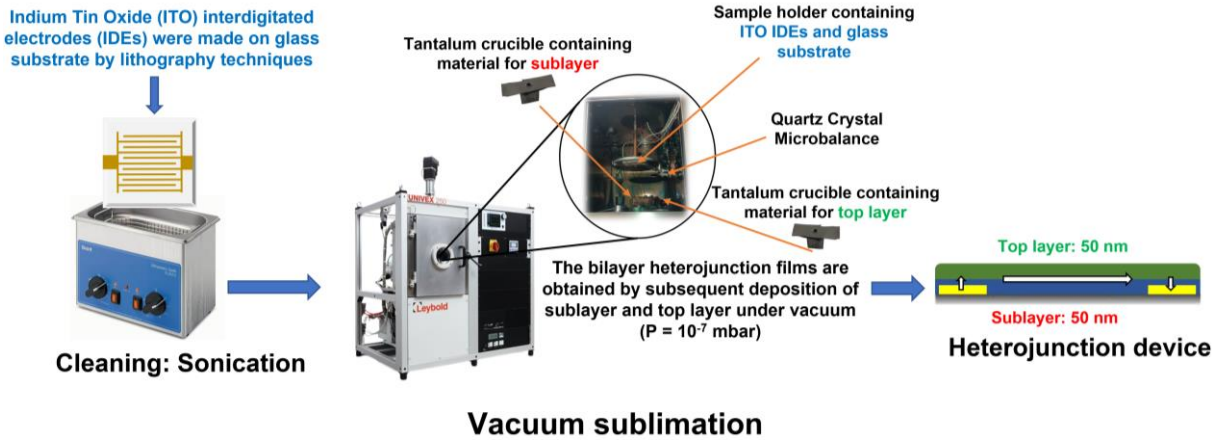

Scheme 5: Schematic view of device fabrication through physical vapour deposition using UNIVEX 250.

To attain a high vacuum, it is necessary to run the turbo molecular pump overnight, which must be maintained by a continuous flow of water (at 2 °C) provided by a cryostat cooling system to prevent heat damage to the pump. However, any failure in the water flow from the cooling system can cause significant damage to the turbo pump. To address this, we developed our own security system for the UNIVEX 250 by programming an Arduino UNO board assisted with a water flow sensor. If something goes wrong, the security system automatically turns off the pump and puts the system in safe mode.

3.2. Oxidative chemical vapour deposition

Oxidative Chemical Vapour Deposition (oCVD) has been progressively developed over the last two decades as a solvent-free (or dry) methodology for the synthesis and thin film

deposition of conjugated polymers[99]. This method offers new opportunities beyond traditional solution processing methods in the research of these materials. The general mechanism of all solvent-free methods is based on the initial oxidation of reactive monomers, similar to oxidation polymerization in the solution phase[100].

For a long time, a common practice was to first cover the substrate (to be coated) with an oxidizing agent and then expose the pre-treated substrate to vapours of monomers. In this approach, the monomers first adsorb on the surface of the substrate under reduced pressure and then are activated by interactions with the oxidant present on the substrate's surface. In oCVD both the oxidant and the monomer are vaporized and metered into a gas-phase reactor under reduced pressure. They are then adsorbed on the surface of a substrate, initiating polymerization and film formation simultaneously.

oCVD has been carried out in LIST using two types of setups called multifuser and conjugator, depending on optimization steps (**Scheme 6**). The films were prepared under 1.0 x 10^{-3} mbar and the substrate temperature has been maintained at 150 °C. Using two different crucibles porphyrin monomer and oxidant were simultaneously evaporated into the gas-phase reactor, leading to polyporphyrins. The monomers were evaporated at the temperature around 250 °C – 300 °C, while the oxidant ($FeCl_3$) was evaporated at 150 °C. By vaporizing both the monomer and oxidant and controlling their delivery into a gas-phase reactor, oCVD has become a powerful tool for creating high-quality polymer films with potential applications in electronics, sensors, and other advanced technologies[101].

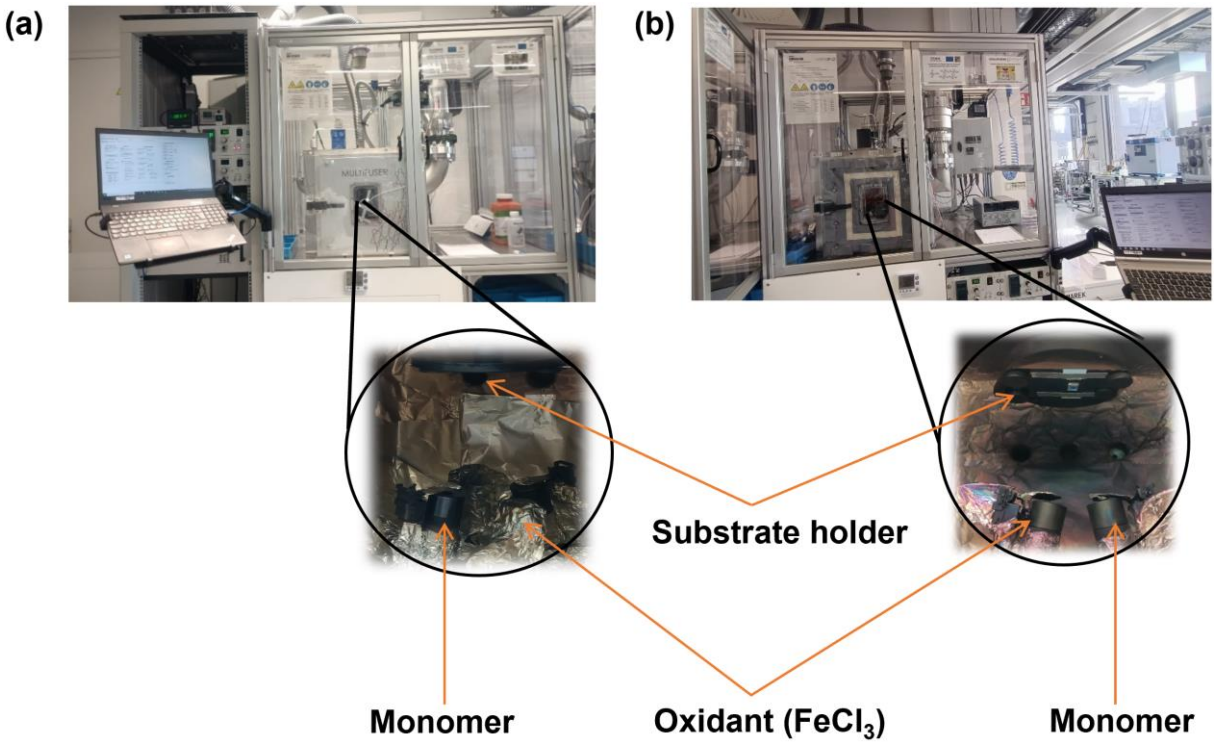

Scheme 6: Schematic view of device fabrication through oxidative chemical vapour deposition method. Evaporators: Multifuser (a) and Conjugator (b).

3.3. Quasi-dip coating method

For materials that are not suitable for thermal evaporation or electrodeposition techniques, we were compelled to use solvent casting methods. However, solvent-based deposition techniques often present challenges in achieving homogeneity. To address these issues, we experimented with several methods and accidently discover a new type of deposition technique called quasi-dip coating method.

In the classical dip coating method, the material is deposited by dipping the substrate into a solution containing the target material and then removing the substrate after a brief period, followed by drying. The quasi-dip coating method is quite different from the classical dip coating, since here the solution is poured into a Petri dish, which contains target substrate (facing upwards), until the substrate is fully submerged by solution. The solution is then slowly

sucked out by slightly tilting the Petri dish up to 45°, followed by drying at 100 °C. The detailed deposition method is shown in **scheme 7**. This technique results in a much more homogeneous surface compared to the classical solvent casting technique. The Ace-PQ-Ni and AM6 were deposited on ITO IDEs using this technique.

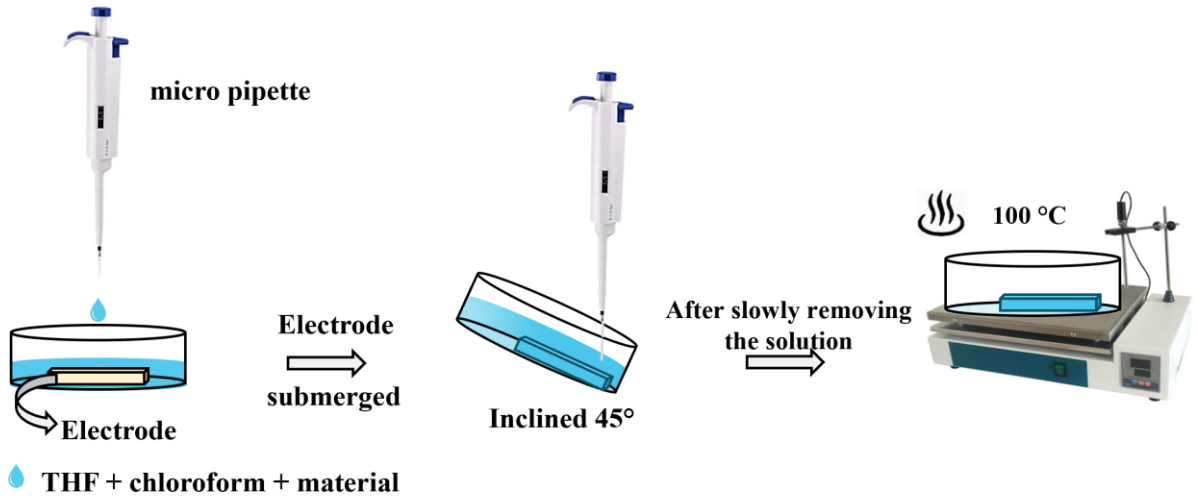

Scheme 7: Schematic view of device fabrication through homemade quasi-dip coating method.

Initially we named this method the "deep-swimming method", because of the submerging step of the substrate. We later published this technique for the first time in the journal Sensors, in 2023, under the name "quasi-dip coating method"[102].

4. Characterisation techniques

All our bilayer heterostructure films were thoroughly studied using various optical and electrical characterization techniques. These techniques included UV-Vis adsorption spectroscopy, Raman diffusion spectroscopy, current-voltage (I-V) measurements, and Impedance spectroscopy. For some specific samples, where the sensing response was significantly influenced by the surface, namely silicon phthalocyanines, we also employed Atomic Force Microscopy (AFM) to gain deeper insights into the surface morphology and its impact on the sensing performance.

4.1. Optical and topographical analyses

The optical absorption properties of the materials and bilayer devices were measured by Cary 50 (Varian) UV-vis spectrophotometer, between 300 and 1000 nm and Raman spectral measurement was conducted on the samples using a Renishaw inVia microscope at an excitation wavelength of 473 nm with ca. 1% of a 12 mW laser power, under 50x magnification. Multiple datasets were acquired for both materials and devices to derive an average representative spectrum for all normalized spectra.

The surface of the bilayer heterostructures coated on glass was evaluated by AFM imaging, on Bruker Icon 2 nano DMA equipment by employing nano DMA peak force tapping mode. Scan of the surface was performed using a silicon probe (DNP SA or ScanAsyst-HR) (tip radius<5) at a peak force frequency of 2 kHz and amplitude in the range of 50–100 nm. The images were finally analysed by Nanoscope analysis software. The measurements were carried out by Prof. E. Lesniewska in the ARCEN platform of LICB (UB) and we did the data treatment in ICMUB.

4.2. Electrical measurements

I-V measurements were conducted by Keithley 6517B electrometer by applying a bias voltage ranging from -10 to +10 V in steps of 0.1 V. In ordered to avoid any polarization effect the I-V measurements were started and ended at 0 V. Impedance measurements were carried out using a Solartron SI 1260 impedance analyser, applying a fixed AC oscillation amplitude of 0.2 V in the frequency range of 10 Hz to 10 MHz and a DC bias ranging from 0 to 10 V. All the electrical measurement were carried out under ambient conditions (20-22 °C and 45% RH), unless otherwise specified.

The experimental Nyquist plot of all heterojunction devices, which corresponds to the imaginary part of impedance as a function of the real part, presented two depressed semicircles. **Figure 6** displays an example of heterojunction's Nyquist plot. The one at high frequency (HF, left part) remains unaffected no matter the applied DC bias. It represents charge transport in bulk medium. On the other hand, the one at low frequency (LF, right part) decreases as a function of increasing DC bias from 0 to 10 V, which corresponds to interfacial charge transport at the interface of organic-organic heterojunction[103]. Obtained data were treated using commercially available Ametek's Zview software.

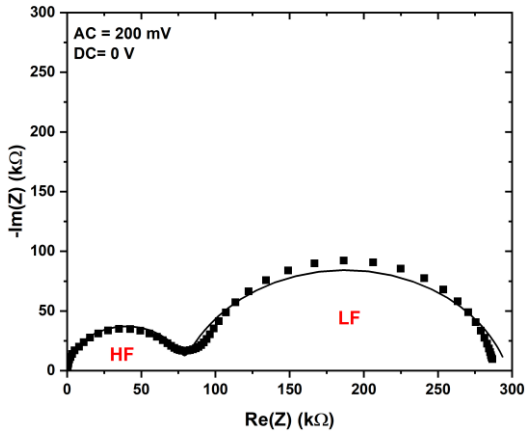

Figure 6. Example of Nyquist plot of an heterojunction device.

To quantitatively access various charge transport parameters of the devices, the experimental Nyquist plots were fitted with constant phase element (CPE)-based circuits. CPE are most often used to describe the non-ideal capacitive behaviour of a system[104]. All bilayer heterojunction devices were modelled by incorporating two CPEs connected in series, along with resistors connected in parallel to those CPEs. A contact resistor was also included to account for the resistance between the material and the electrodes. Generally, the contact resistance is very small, and in some cases, it has been completely negligible. Hence, we used two types of circuits, specifically, R1-CPE1 describes the semicircles at HF, while R2-CPE2

represents the semicircles at LF, correlating to bulk and interfacial charge transport, respectively. The impedance of the CPE is defined by **equation (2)**.

$$Z_{CPE_i}(\omega) = \frac{1}{Q_i \times (j\omega)^{\propto i}} \qquad (2)$$

where Q_i and α_i are the parameters defining the CPE and ω is pulsation (ω = 2πf, f being the frequency). Here, α_i varying between 0 to 1 as a dimensionless parameter, Q_i represents the capacity of the system in the case where $\alpha_i = 1$. It is important to note that the CPE parameter Q_i cannot represent capacitance when $\alpha_i < 1$[105-109].

Through fitting the data, we obtain R1, α1, and Q1 as parameters characterizing bulk charge transport, and R2, α2, and Q2 as parameters characterizing interfacial charge transport. In all the cases the α_i values are less than 1 for both heterojunction devices. Hence the effective capacitance (C_{eff}) is calculated using Brug's relationship (**equation 3**)[106].

$$C_{eff_i} = Q_i^{1/\alpha} R_i^{(1-\alpha)/\alpha} \qquad (3)$$

5. Sensing measurements

All gas sensing experiments were carried out using homemade gas chamber (volume 8 cm^3), which is equipped with DN505-05 controlled heater positioned at the bottom, ensuring precise temperature regulation, while three red LEDs (maximum wavelength: 642 nm) are strategically positioned 2 cm above the test sample, providing consistent illumination. Furthermore, the chamber is connected to a cooling system, facilitating rapid cooldown when necessary. The workstation was fully automated in which the gas concentration, humidity values, switching of the value, PID control, temperature regulation, light illumination and data transfer were controlled by homemade and customized software.

The detailed experimental setup utilized for electrical and gas sensing measurements under different conditions is depicted in **scheme 8**. It comprises fluidic circuits interconnected with commercial cylinders containing synthetic air, ammonia gas (with a concentration of 1000 ppm mol/mol or 100 ppm mol/mol), nitrogen dioxide (with a concentration of 10 ppm mol/mol) purchased from Air Liquide France and ozone generator (O_3 41M Environment S.A., France).

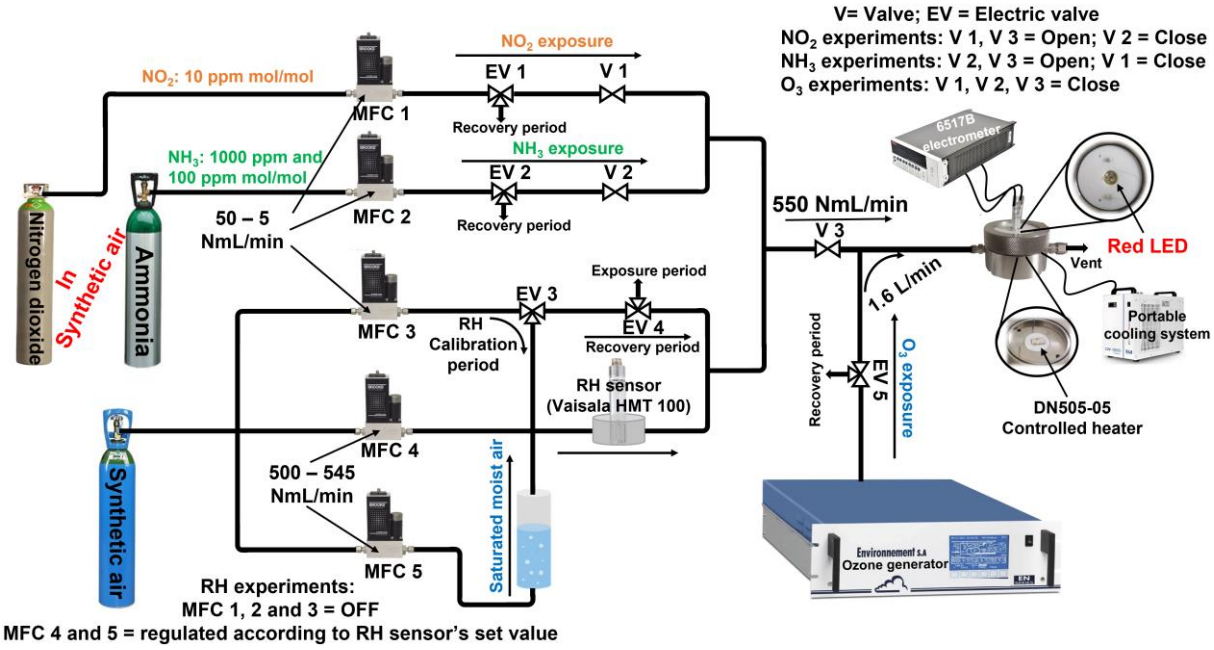

Scheme 8: Illustration of homemade device testing workstation integrating different gas sources, fluidic circuits, mass flow controllers, electronic valves, water column, humidity sensor, ozone generator, electrometer, and test chamber equipped with a controlled heater, cooling system and red LEDs.

The gas flow within the circuit is controlled as per our desired gas concentration and exposure/recovery time using various mass flow controllers (Brooks Instrument) and electric valves, respectively. Precise control over relative humidity is achieved with the help of a commercially available humidity sensor (HMT 100, Vaisala, Finland) interconnected with mass flow controllers. Both the mass flow controllers and humidity sensor are interfaced with a PID program, enabling the precise dilution of humidity saturated air from the water column with dry

air to maintain a standardized relative humidity value. A small flow of target gas (ca. 5 to 50 NmL min^{-1}) was introduced into the previous flow to generate air with controlled gas concentrations, in the range of 1 – 90 ppm and 100 – 900 ppb, depending on the concentration in the NH_3/air and NO_2/air cylinders, respectively. The total gas flow was kept constant throughout all the experiments (550 NmL min^{-1}), except for ozone experiments. For ozone experiments, a total mass flow of 1.6 L min^{-1} with desire ozone concentration (20 – 100 ppb) was generated by the ozone generator.

All the heterojunction devices were characterized under target gas for so called long and short exposure/recovery for 10 min/30 min and 1 min/4 min, respectively, at 45% RH, with recovery under clean air, except for ozone. For ozone, we followed a static recovery since ozone is self-destructive. As quantitative measurement, relative response (RR) of the heterojunction sensors was calculated using the following equation:

$$RR(\%) = \frac{I_f - I_0}{I_0} \times 100 \qquad (4)$$

where I_0 and I_f are initial and final current of an exposure period, respectively. The plot of RR (%) as a function of the gas concentration will be called as calibration curve. When it comes to conductometric sensors, limit of detection (LOD) stands out as a critical parameter, which has to be calculated with high precision. Hence the LOD was estimated for the heterojunction sensors using the following equation:

$$LOD = \frac{3N}{S * I_0} \qquad (5)$$

Here, N is the level of noise of the sensor's signal that has been measured during exposure phase, S is the sensitivity given by the slope of the sensor calibration curve and I_0 is the sensor baseline current.

6. Optical characterisation of bilayer films

6.1. UV-Vis absorption spectroscopy measurements

The normalized optical absorption spectra of each layer as well as the resulting bilayer heterostructures are displayed in **Figure 7 and 8.** The spectral region spanning between 300 and 800 nm contains some of the most representative absorption bands for both sublayer and top layer. Notably, all phthalocyanine-based heterojunction films exhibit a typical B band in the range of 300–400 nm, while Q-band appears in the range of 600–700 nm, originating from the electron transition from the HOMO to the LUMO ($\pi \rightarrow \pi^*$ transition).[110] Notably, in most of the case, the Q bands of bilayers experienced splitting into two or three sub-bands, which are ascribed to Davydov splitting, originating stronger intermolecular interactions in the thin film of MPcs heterostructures compared to solutions[111-112].

On other hand, the porphyrin-based films exhibit typical porphyrin absorption peaks from sublayer that correspond to Soret band region spanning at 428, 460, 493 and 577 nm in Ace-PQ-Ni/$LuPc_2$ and at 435 nm in AM6/$LuPc_2$. Several weaker bands of AM6 between 600 to 704 nm were overlapped with a main peak of $LuPc_2$ at 669 nm. In all bilayer films, majority of absorption peaks from sublayer were overlapped with peaks from top layer resulting in change in peak intensity and broadness, e.g. the sharp peaks at 657 and 646 nm from ZnF_8Pc and CoF_8Pc, respectively, are completely shadowed by the broad peak from $LuPc_2$ layer (650–690 nm) and appeared at 669 and 667 nm in $ZnF_8Pc/LuPc_2$ and $CoF_8Pc/LuPc_2$ heterostructures, respectively.

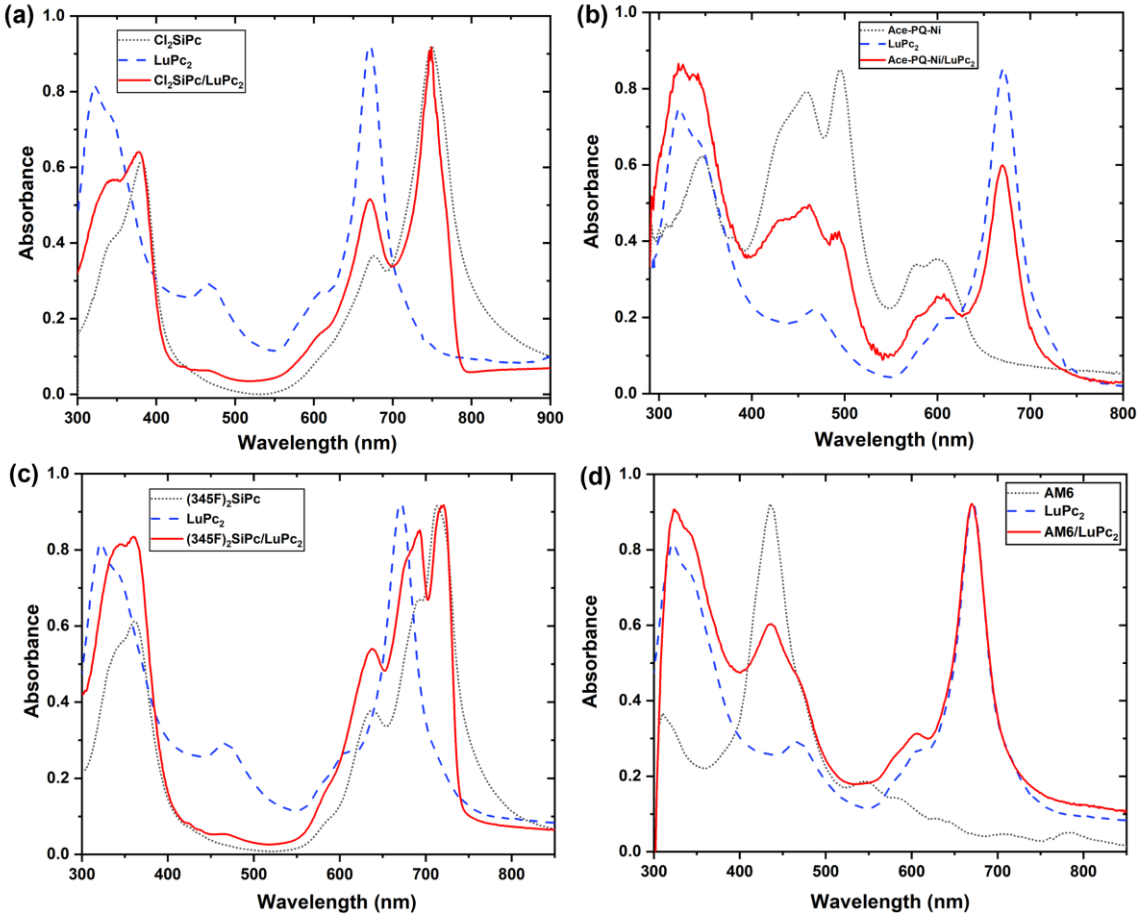

Figure 7. Absorption spectrum of $Cl_2SiPc/LuPc_2$ (a), $(345F)_2$-SiPc/$LuPc_2$ (c), Ace-PQ-Ni/$LuPc_2$ (b), and AM6/$LuPc_2$ (d) bilayer heterostructure films (red line) compared to the spectra of their corresponding sublayer (black dotted line) and top layer ($LuPc_2$) (blue dash line) in THF solutions.

Notably, while the main peak of $LuPc_2$ remains consistent in the $VOF_8Pc/LuPc_2$ heterojunction film, the main peak of the sublayer broadens into a shoulder. As previously reported by T. Basova,[8] the VOF_8Pc film exhibits a broad red-shifted Q-band. It can be correlate to J-aggregate formation, compared to its spectra in solution. Consequently, the main peak from the sublayer shifts entirely to around 750 nm and appears as a broad shoulder in the heterostructure film. It is quite particular in VOF_8Pc due to strongest interaction compared to ZnF_8Pc and CoF_8Pc, resulting from the presence of the polar vanadyl moiety. The shoulder at 608 nm in heterojunction film is significant for fluorinated compounds and similar shoulder

was observed in $MF_{16}Pc$, corresponding to H-aggregates. The UV-Vis spectra of octafluoro-metallophthalocyanines were shown in **Figure 8**. The absorption band at 470 nm in all heterostructure films is specifically associated with the Semi-Occupied Molecular Orbital (SOMO) of the $LuPc_2$ neutral radical, linked to the $e_1 \rightarrow a_2$ transition[8, 113-114].

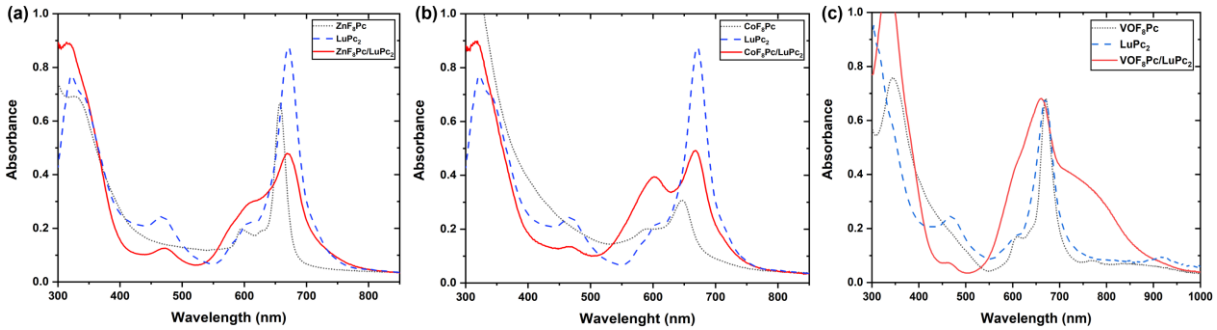

Figure 8. Absorption spectrum of $ZnF_8Pc/LuPc_2$ (a), $CoF_8Pc/LuPc_2$ (b) and $VOF_8Pc/LuPc_2$ (c) bilayer heterostructure films (red line) compared to the spectra of their corresponding sublayer (black dotted line) and top layer ($LuPc_2$) (blue dash line) in THF solutions.

6.2. Raman diffusion spectroscopy measurements

For further understanding the distinct optical properties of bilayer heterostructure films, Raman vibrational spectroscopy measurement was studied on each layer, as well as on resulting heterostructures. In the analysis of various heterostructures using Raman spectroscopy, distinct vibrational modes were identified for each sample. On bilayer films, Raman spectra reveal a combination of peaks attributed to the chemical signatures of both sublayer and top layer. In the Cl_2-SiPc/$LuPc_2$ heterostructure, the peak at 592 cm^{-1} was consistent with the Pc breathing mode, while additional peaks at 756, 965, 1005, 1048, 1188, 1525 cm^{-1}, and a strong peak at 1558 cm^{-1} belonged to Cl_2-SiPc. In the $(345F)_2$-SiPc/$LuPc_2$ heterostructure, peaks at 594 cm^{-1} and 652 cm^{-1} corresponded to Pc breathing, with peaks at 1047 and 1196 cm^{-1} attributed to C-H bending, and peaks at 1615 cm^{-1} and a strong peak at 1553 cm^{-1} belonging to $(345F)_2$-SiPc (**Figure 9**).

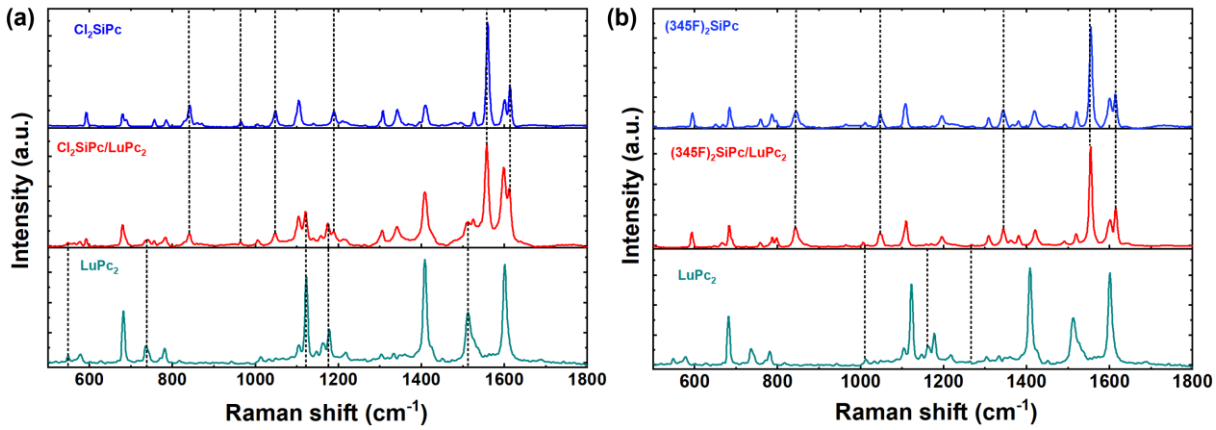

Figure 9. Superimposition of the Raman spectra of $Cl_2SiPc/LuPc_2$ (a) and $(345F)_2SiPc/LuPc_2$ (b) bilayers with the respective spectra of their constituents. Individual peaks from each layer were marked with dotted lines.

For the Ace-PQ-Ni/$LuPc_2$ heterostructure, medium intense peaks at 1270, 1352, 1381, 1429, 1568, 1589 cm^{-1}, and strong peaks at 1140 and 1658 cm^{-1} were attributed to the Ace-PQ-Ni layer. In the AM6/$LuPc_2$ heterostructure, peaks at 772, 831, 1075, 1287, 1372, 1656 cm^{-1}, and a strong peak at 1565 cm^{-1} were associated with the AM6 layer (**Figure 10**).

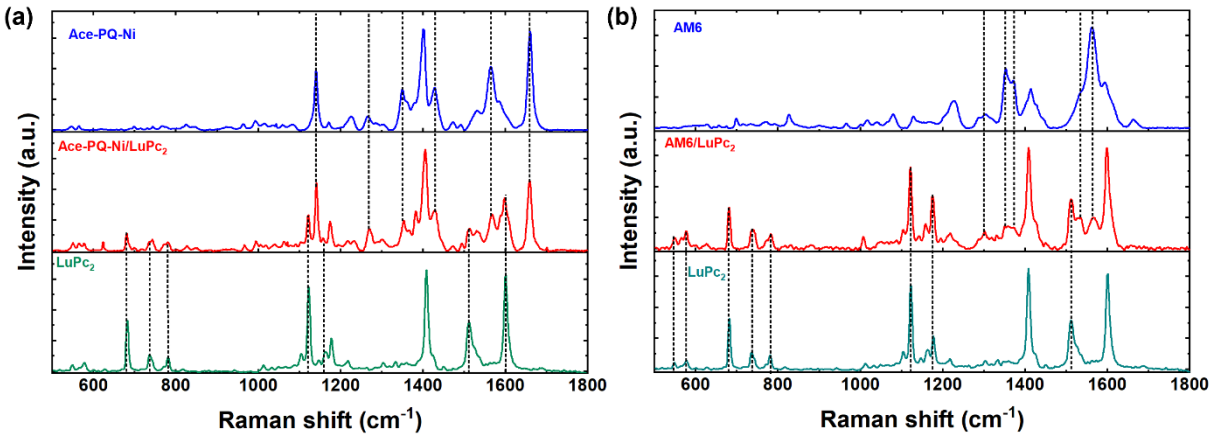

Figure 10. Superimposition of the Raman spectra of Ace-PQ-Ni /$LuPc_2$ (a) and AM6/$LuPc_2$ (b) bilayers with the respective spectra of their constituents. Individual peaks from each layer were marked with dotted lines.

The $ZnF_8Pc/LuPc_2$, $CoF_8Pc/LuPc_2$ and $VOF_8Pc/LuPc_2$ heterostructures exhibited numerous common peaks, such as those at approximately 550, 740, 1000, 1030, 1100, 1150, 1220, 1300, 1335 cm^{-1}, and a strong peak at 1405 cm^{-1}. Specifically, the main peak at 1513 cm^{-1} in ZnF_8Pc shifted to 1531 cm^{-1} in VOF_8Pc, and to 1546 cm^{-1} in CoF_8Pc, demonstrating the effect of the central metal in the octafluoro-phthalocyanine complex. The peaks at ca. 760, 880, 1190, 1360, 1470, 1530 and 1620 cm^{-1} were particularly belonging to the sublayer (ZnF_8Pc and CoF_8Pc and VOF_8Pc) (**Figure 11**)[8].

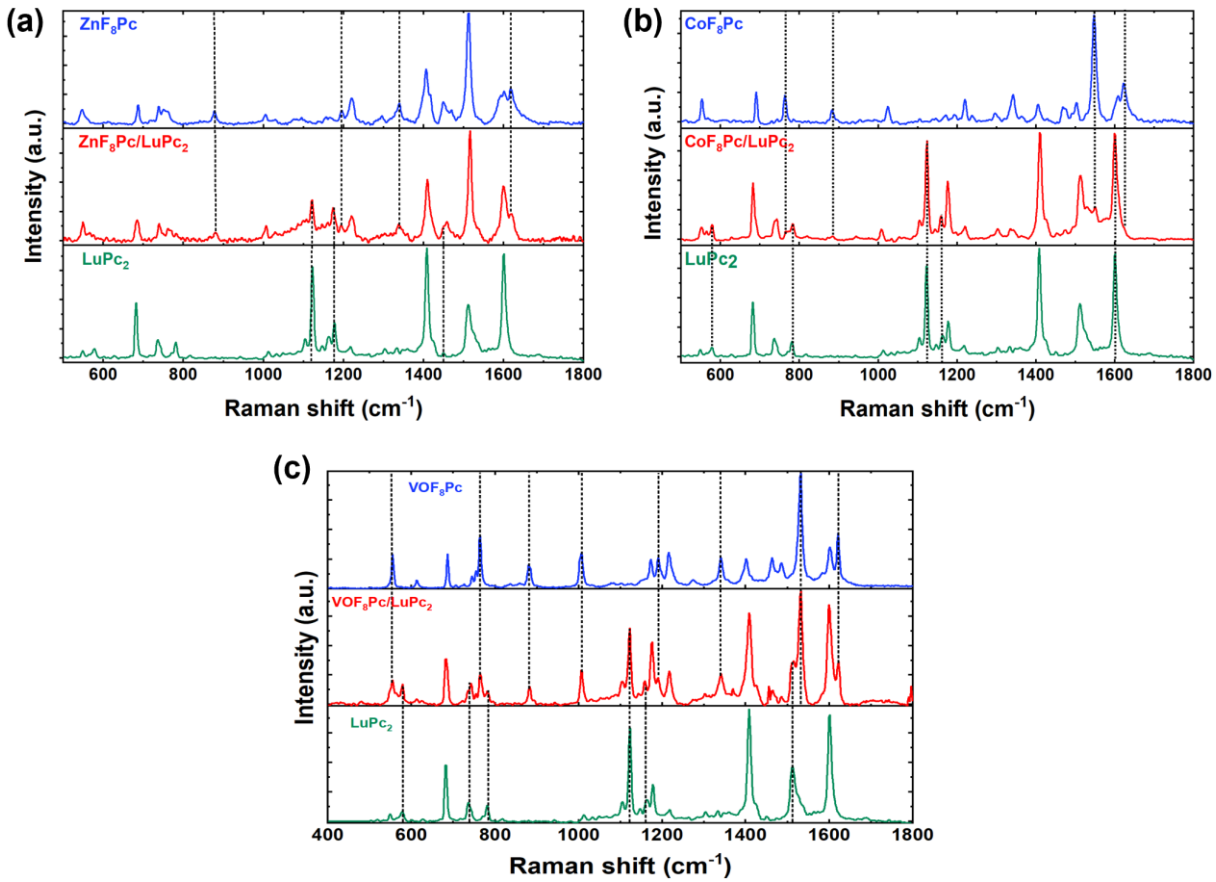

Figure 11. Superimposition of the Raman spectra of $ZnF_8Pc/LuPc_2$ (a), $CoF_8Pc/LuPc_2$ (b) and $VOF_8Pc/LuPc_2$ (c) bilayer with the respective spectra of their constituents. Induvial peaks from each layer were marked with dotted line.

Throughout all the heterostructures, most of the peaks from $LuPc_2$ overlapped with those from the sublayers, resulting in changes in peak intensity without introducing new peaks,

which indicates no degradation of the sublayer is observed with the subsequent deposition of $LuPc_2$ during the fabrication of the bilayer devices. Unique peaks such as ca. 1125, 1175, 1512 and 1598 cm^{-1} presented in bilayer heterojunction films were directly attributed to $LuPc_2$[114]. These findings underscore the importance of maintaining pristine interfaces void of molecular degradation, as charge transport primarily occurs at the bilayer interface. Globally, the UV-vis and Raman spectra of heterostructure films are the addition of the spectra of sublayers and top layers. For better understanding, the Raman data of all bilayer heterojunction films with their corresponding layers were given in **Annexed – Raman Data**.

Conclusion

In this thesis work, we engaged seven different types of molecular semiconductors such as dichloro silicon phthalocyanine (Cl_2SiPc), bis(3,4,5-triflurophenoxy) silicon phthalocyanine ($(345F)_2$-SiPc), acenaphtho[1,2-*b*]-pentacene-9,16-dione-fused nickel porphyrin (Ace-PQ-Ni), pentacene fused nickel porphyrin (AM6), and octafluoro-metallophthalocyanines such as ZnF_8Pc, COF_8Pc, VOF_8Pc, and CuF_8Pc as sublayer in bilayer heterojunction devices, which is commonly covered by LuP_2 as top layer, except in CuF_8Pc-based bilayer heterojunction devices, different types of conjugated nickel porphyrins were used as top layer for common CuF_8Pc sublayer. For fabricating these devices, we adapted three different deposition methods: physical vapour deposition, oxidative chemical vapor deposition and quasi-dip coating method to obtain highly homogeneous bilayer heterojunction device. All the bilayer films and materials reported in this work were thoroughly studied using various optical and electrical characterization techniques, including UV-Vis, Raman, impedance spectroscopies and I-V measurements. AFM measurements were also considered for some devices that have high influence of roughness and morphology on their sensing properties. All the sensing measurements were conducted on our advanced homemade work bench under different experimental conductions.

Chapter 3

Silicon Phthalocyanine-Based Ammonia Sensors

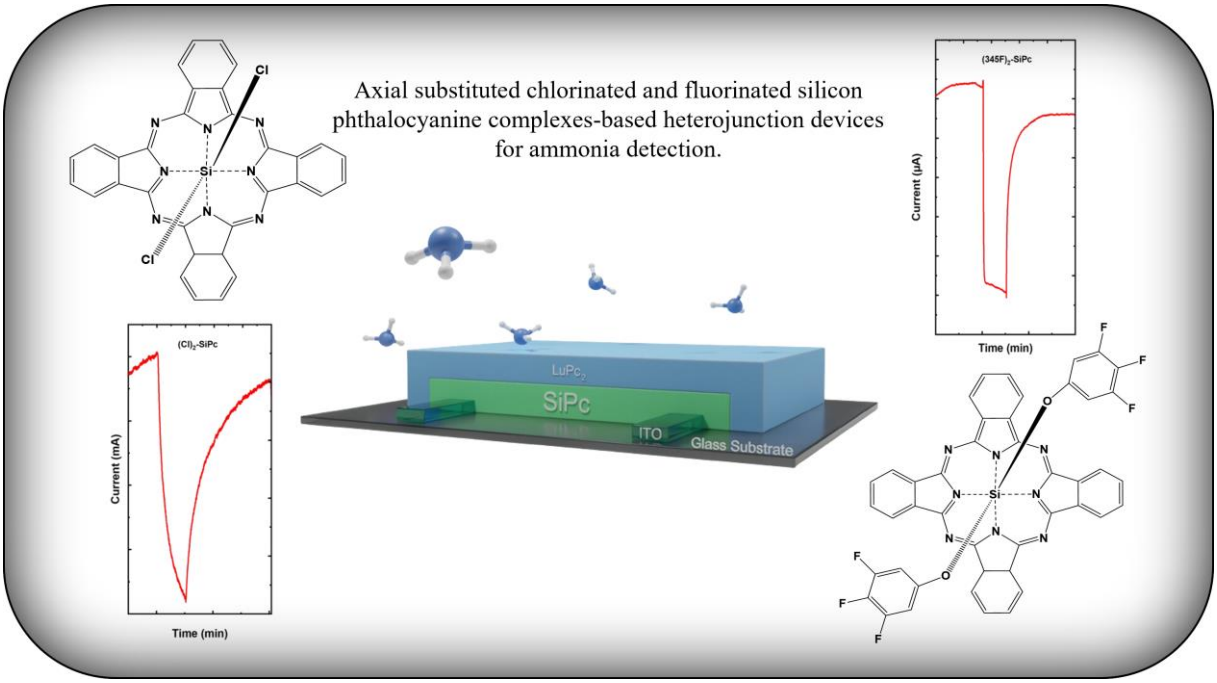

Chapter 3

Silicon Phthalocyanine-Based Ammonia Sensors

Table of Content

Chapter 3. Silicon phthalocyanine-based ammonia sensors

1. Introduction

Over 175 million tons of ammonia is produced globally every year, making it one of the most essential chemicals in industries[115]. In addition to its widespread use in agriculture, pharmaceutical development, and food processing, ammonia has received increased attention as a refrigerant, capable of replacing chlorofluorocarbons. Moreover, it is being increasingly used as a source of green hydrogen[116] and an important biomarker in disease monitoring[117-118]. Despite its widespread use, ammonia is highly toxic, corrosive and damaging to human health and the environment. Short term (10-15 min) exposure limits to ammonia are typically set at 35 parts per million (ppm) while longer (8-10 h) limits are set at 25 ppm[119]. To enable a proactive response to ammonia exposure and prevent serious negative health outcomes, ammonia sensors must have a LOD below these thresholds, with rapid response and recovery times, and with high selectivity for ammonia in environments containing other gaseous analytes, especially water vapour. Many sensing technologies have been reported previously for ammonia detection, such as chemiresistors,[120] diodes[121-122] and field-effect transistors (FET),[123-124] which revealed high sensitive to ammonia. However, conventional chemiresistors based on metal oxides often require high operating temperature (typically over 200 °C), have longer response/ recovery times and suffer from drift in the sensors signal baseline[9, 80]. On the other hand, FET-based sensors require expensive fabrication methods, such as micromachining and clean-room requirements, limiting their upscaling for large area coverage.

Silicon phthalocyanines (SiPc) are a class of MPc which have shown promising applications in n-type or ambipolar OTFTs[125-126]. Additionally, SiPcs can be functionalized with axial ligands as well as peripheral substitution, to tune their crystalline structure in thin

film, chemical affinity and electronic properties[127-128]. A large catalogue of axially substituted SiPc derivatives have been reported, which are processable into devices by physical vapour deposition,[127] solution casting[129] or both, making them suitable for applications in organic electronics. SiPcs have shown great promises in heterojunction devices, having been incorporated into both planar heterojunction (PHJ)[130] and bulk heterojunction (BHJ)[131] organic photovoltaic (OPVs) as non-fullerene acceptors. Despite exhibiting high performances in PHJ and BHJ, the use of SiPc as a sensing layer in gas sensors has been scarce. Recently, carbon nanotube cross-linked to SiPc via axial substitution was used in chemiresistive sensors for detecting NH_3 and H_2[132]. A conductometric sensor based on Langmuir-Blodgett coated SiPc, having tert-butyl moieties as peripheral substituents and ethyloxy as an axial ligand was reported to sensitively detect NO_2 at 5 ppm[133]. Elsewhere, gas sensing properties of polymeric SiPc film was investigated at high temperature to detect NO_2 and Cl_2 gases[134]. However, there is no SiPc-based heterostructure reported yet for application in gas sensors. Taking into account, fast charge conductivity, these materials demonstrated in PHJ and BHJ photovoltaic devices and their applications in chemiresistor gas sensors, they can provide tremendous opportunity in organic heterojunction gas sensors.

Accordingly, here we explored the potential of R_2-SiPcs (R= axial ligand) in a bilayer organic heterojunction device by combining it with a highly conducting material $LuPc_2$ and investigates its NH_3 sensing properties. Two different R_2-SiPc derivatives, axially substituted with chlorine and trifluorophenol, respectively (**Scheme 9**), were studied in heterostructures as the sublayer in order to modulate the interfacial charge transport and NH_3 gas sensing properties of resulting devices.

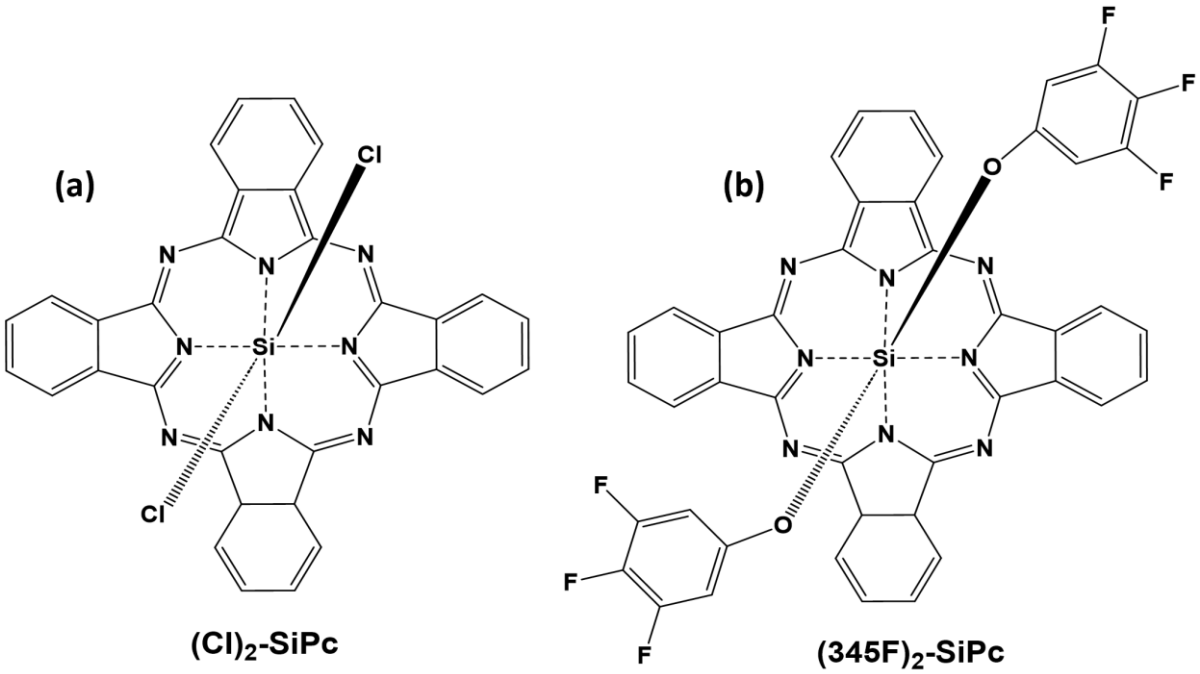

Scheme 9. Chemical structure of dichloro silicon phthalocyanine (a) and bis(3,4,5-triflurophenoxy) silicon phthalocyanine (b).

The chemical functionality and microstructure of the bilayer films are characterized by UV-Vis and Raman spectroscopies (**chapter 2**), while their surface topography is investigated by atomic force microscopy. The electrical properties of the heterojunction devices have been studied by I-V measurements, while in depth charge transfer studies have been performed by impedance spectroscopy. Ammonia sensing properties of the heterojunction sensors are finally evaluated at room temperature and different metrological characteristics are assessed.

2. Electrical properties of heterojunction devices

To investigate the electrical properties, I-V measurements were performed on both devices at applied bias in the range from -10 to +10 V. As expected for bilayer organic heterojunction devices, Cl_2-SiPc/$LuPc_2$ (**Figure 12a**) and $(345F)_2$-SiPc/$LuPc_2$ (**Figure 12b**) devices exhibit symmetric and non-linear I-V curves. The non-linearity in I-V curves is due to the difference in work functions, which leads to accumulation of mobile charges at the interface

between the two layers[40, 135]. Considering the distance between interdigitated electrodes (75 µm) and the thickness of the layers (50 nm), the horizontal resistance of the sublayer is exceptionally enormous compared to the vertical resistance. Due to the geometry of the IDE ITO electrodes, charges predominantly flow through the interface between materials to access the most conductive pathway. It is worthy to note that $LuPc_2$ resistors exhibit perfectly linear I-V curves, displaying ohmic contact between ITO and $LuPc_2$ semiconductor[80]. It confirms the presence of organic-organic interface in the organic heterojunction devices. Moreover, at lower bias current across the devices remains small, because charges experience high resistance due to the poor conducting sublayer. However, when applying higher bias, the mobile charges have enough energy to overcome the energy barrier resulting in higher current.

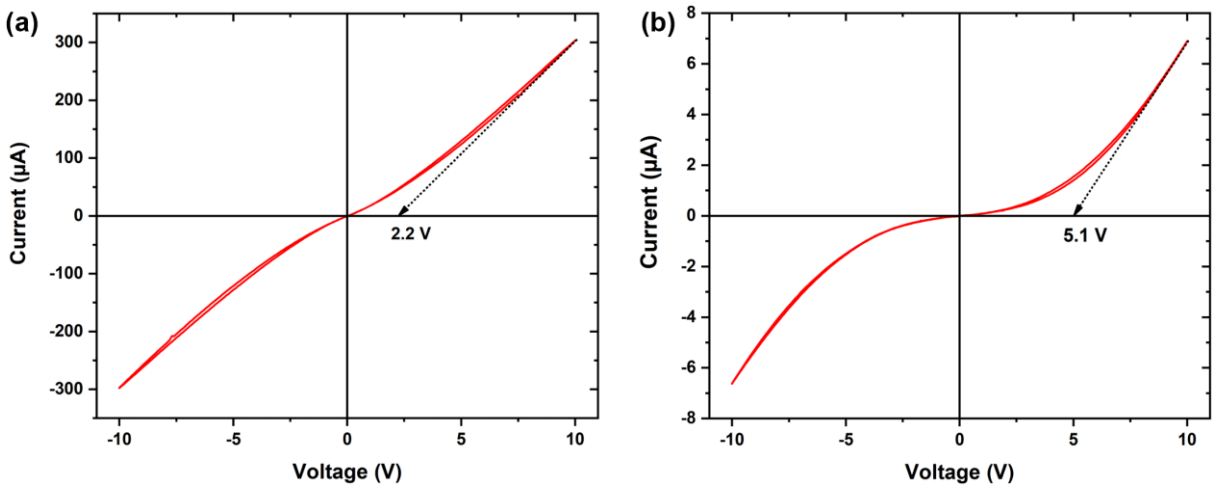

Figure 12. I-V characteristics of Cl_2-SiPc (a) and $(345F)_2$-SiPc (b) based heterojunctions.

The non-linearity in the I-V curves is quantified by the threshold voltage (U_{th}) that gives an estimation of the apparent energy barrier, through tracing a tangent on the I-V curves and extrapolating it to the X-axis. The calculated U_{th} are 2.2 and 5.1 V for Cl_2-SiPc/$LuPc_2$ and $(345F)_2$-SiPc/$LuPc_2$ devices, respectively, clearly indicating that the latter has higher energy resistance for the transport of mobile charges in the heterostructure. Although, the work function of the sublayer materials are similar (4.1 and 4.4 eV)[5].

To get in depth information about the effect of heterojunction in bilayer devices, charge transport studies were performed by impedance spectroscopy on both octafluoro-phthalocyanine-based devices, at given amplitude of 0.2 V AC signal, with a wide range of frequency, from 10 Hz to 10 MHz, superimposed by different DC bias (0 to 10 V). The Nyquist plots of the both heterojunction devices presented two depressed semicircles (**Figure 13**).

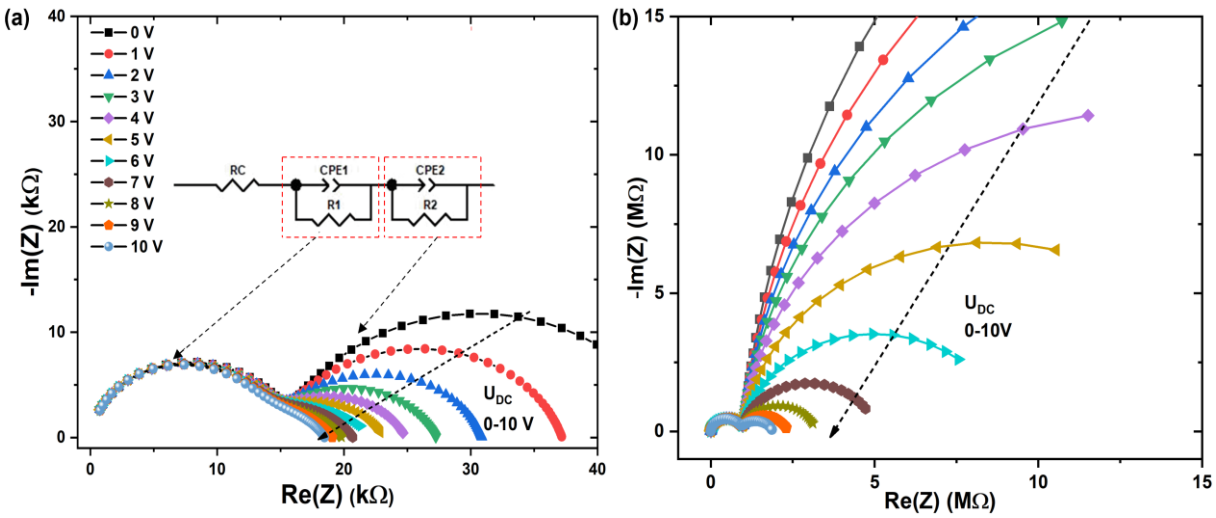

Figure 13. Nyquist plots of Cl_2SiPc (a) and $(345F)_2SiPc$ (b) based heterojunctions measured at fixed AC (0.2 V) superimposed by variable DC voltage in the range of 0-10 V. The equivalent circuit selected for fitting Nyquist plots is added in (b).

Interestingly, the magnitude of the bulk and the interfacial impedances are lower in Cl_2-SiPc/$LuPc_2$ than those of $(345F)_2$-SiPc/$LuPc_2$, implying that both bulk and interfacial charge transport are faster in the former. Using **equation (3)** Brug's relationship[106], the experimental Nyquist plots of both devices have been fitted and the variation of charge transport parameters with respect to applied bias is shown in **Figure 14**. From the variations of bulk resistance R1 (**Figure 14a**) and interfacial resistance R2 (**Figure 14b**) of the both devices as a function of DC bias, it is noted that R1 remains nearly independent of the bias, while R2 reveals an exponential decay with increasing bias. Such observation infers that interfacial charge transport gets faster,

while bulk charge transport does not change with increasing bias, which is a typical characteristic feature of bilayer heterojunction devices[10]. The rapid decrease in R2 is attributed to the arrival of injected charges from the electrode to the interface region, which further populates the interface region with mobile charges accumulation, thereby filling the traps and enhancing the charge mobility along the interface. On the other hand, mean variation of the mobile charge carriers' concentration in the large bulk region does not change significantly with changing bias, keeping charge transport unchanged. Notably, R1 and R2 of $(345F)_2$-SiPc/$LuPc_2$ are 66 times and 2760 times higher at 1 V than R1 and R2 of Cl_2-SiPc/$LuPc_2$, respectively, which are also commensurate with the higher magnitude of current and lower U_{th} of the latter in the I-V curve. Such a large R2 in $(345F)_2$-SiPc/$LuPc_2$ device can be assigned to the small number of mobile charge carriers' accumulation at the interface between $(345F)_2$-SiPc and $LuPc_2$ because of their work function differences.

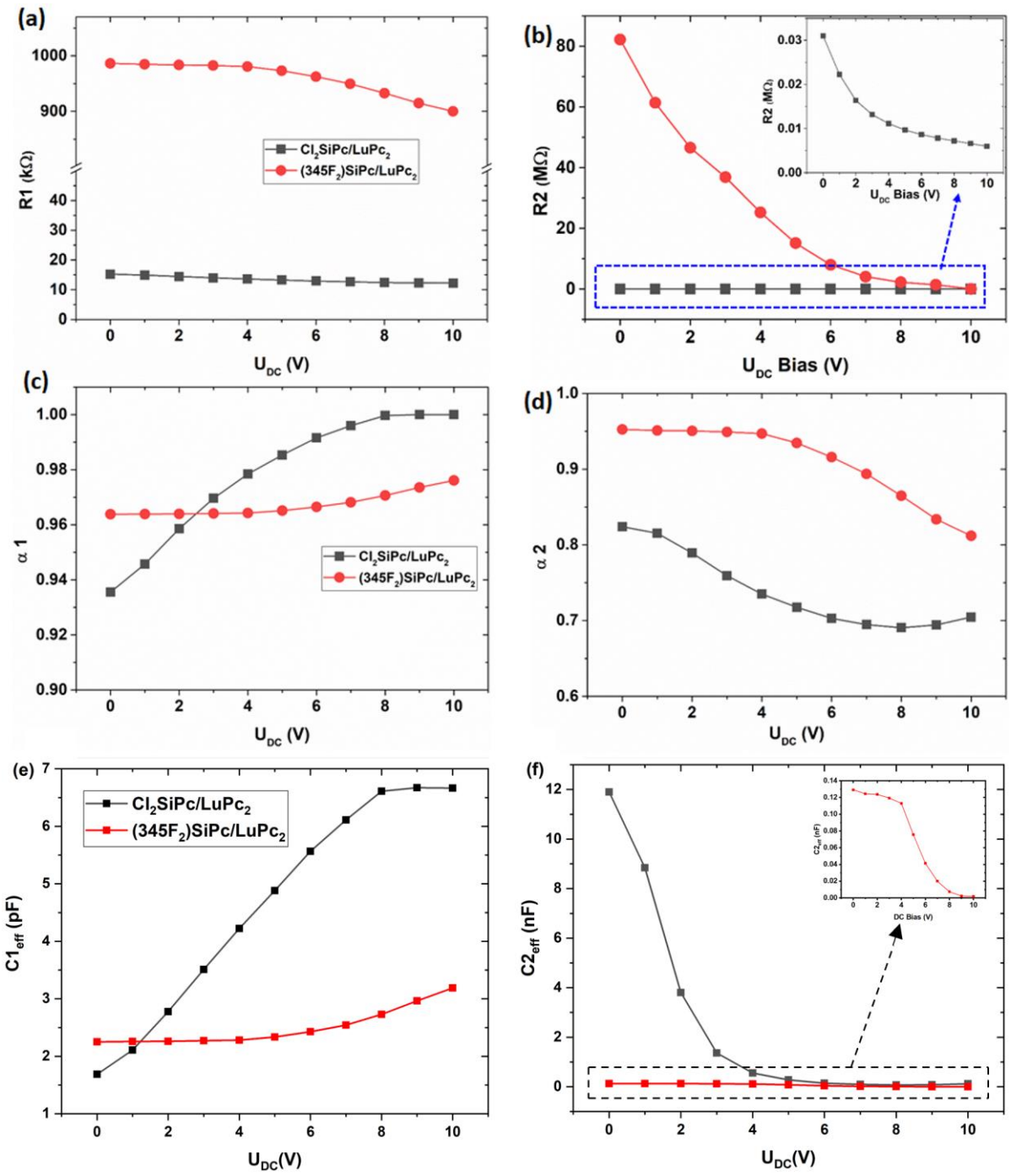

Figure 14. Variations of equivalent circuit resistances, R1 (a) and R2 (b), α1 (c) and α2 (d), effective capacitances $C_{eff}1$ (e) and $C_{eff}2$ (f), as a function of bias voltage (0-10 V) for Cl_2-SiPc/$LuPc_2$ and $(345F)_2$-SiPc/$LuPc_2$ heterojunction devices.

The α1 value of both heterojunction devices remains more than 0.93 and increases towards 1 as bias increase (**Figure 14c**). It indicates that CPE associated to bulk region is highly

homogeneous, which is consistent with the negligible variation in the electrical properties of the bulk with change in bias. On the contrary, α2 experienced a significant decrease from 0.95 to 0.81 in $(345F)_2$-SiPc/$LuPc_2$ and from 0.83 to 0.69 in Cl_2-SiPc/$LuPc_2$ heterojunction device (**Figure 14d**). It indicates that interface region is heterogeneous at higher bias in both the devices. It is attributed to the arrival of higher concentration of mobile charges at interface, thus extending the conducting networks by filling of the traps. The variations of effective capacitances of the heterojunction devices with DC bias are presented in **Figure 14e and 14f**, exhibiting the bulk capacitance ($C1_{eff}$) in the range of pF, while interfacial capacitance ($C2_{eff}$) in the range of nF. This huge difference is due to the very thin interface compared to the thickness of layers (50 nm). The calculated effective capacitance values agree with the α_i values, indicating higher capacitance as the α_i values approach 1 and vice versa.

3. Ammonia sensing performance of heterojunction sensors

Both heterojunction devices were characterized under exposure to 90 ppm of NH_3 for 10 min and recovery under clean air for 30 min. The current variations with time (i-t) (**Figure 15**) exhibits a decrease in current under exposure cycle and increase of current during the recovery cycle. Such behaviour of the heterojunction sensors suggests their p-type nature, taking into account electron donating tendency of ammonia. It is important to note here that even though $(345F)_2$-SiPc is known to exhibit n-type performance in organic thin film transistors[126], in the present experimental conditions, particularly in air and combined with $LuPc_2$ in a bilayer heterojunction, it exhibits a p-type behaviour. This can be attributed to the hole injection from the $LuPc_2$ and adsorption of O_2 and H_2O in the ambient conditions, which can neutralise negative charge carriers (**equation 6**) and act as trap for mobile electrons, respectively[136].

$$MPc^{+} + NH_3 \rightarrow MPc + NH_3^{+} \qquad (6)$$

Notably, the baseline of the both i-t curves evidenced slight drift, which is attributed to incomplete desorption of the NH_3 during the recovery step. Nonetheless, sensors recover more than 90% of their signal during the desorption cycle. Interestingly, the shapes of the response curves associated to adsorption and desorption phases present different profiles in Cl_2-SiPc/$LuPc_2$ and $(345F)_2$-SiPc/$LuPc_2$ heterojunction sensors. In the former a continuous decrease/increase in current is noticeable throughout the exposure/recovery cycles, while in the latter a plateau in the i-t curve is evidenced in the exposure/recovery steps. Such features imply that NH_3 gas diffuses within the volume of the Cl_2-SiPc/$LuPc_2$ layer, accessing adsorption sites within the bulk. On the other hand, NH_3 adsorption remains confined to the surface in $(345F)_2$-SiPc/$LuPc_2$ layer, in which limited adsorption sites are available, consequently a sorption equilibrium is attained rapidly in the exposure/recovery cycles.

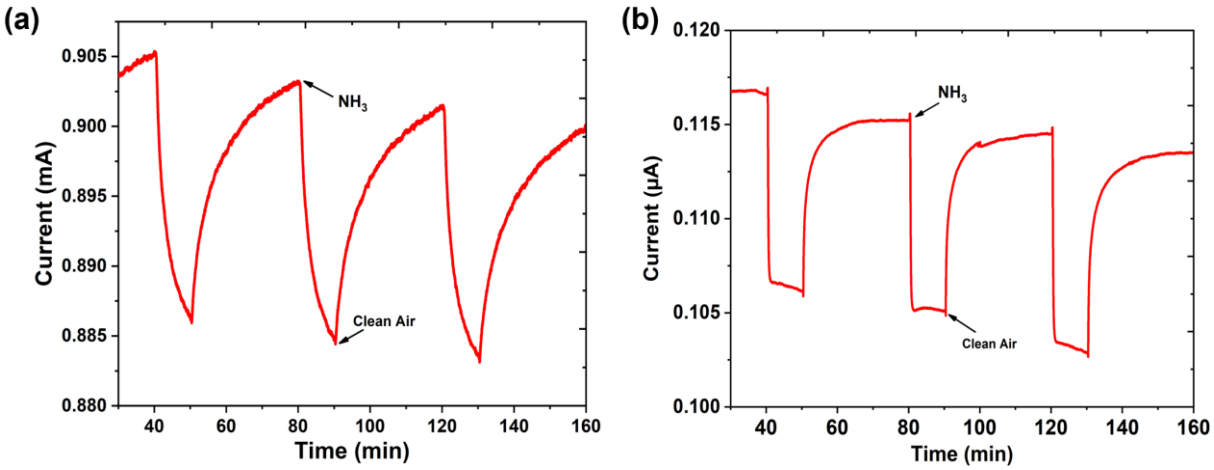

Figure 15. Response of Cl_2-SiPc/$LuPc_2$ (a) and $(345F)_2$-SiPc/$LuPc_2$ (b) heterojunction sensors under successive exposures to 90 ppm ammonia for 10 min and recovery period under clean air for 30 min at 45% relative humidity (RH) and room temperature (20–22 °C).

To understand the difference in sorption kinetics, we studied the topography analysis (AFM studies) on both bilayer heterojunction films. **Figure 16a and 16b** depicts the AFM

micrographs of Cl_2-SiPc/$LuPc_2$ and $(345F)_2$-SiPc/$LuPc_2$ bilayer heterostructure films coated on the glass substrates, respectively. The two heterostructures present a very contrasting surface topography profile, as evidenced by a highly rugged and porous film of Cl_2-SiPc/$LuPc_2$, while a compact packing of molecular crystals in $(345F)_2$-SiPc/$LuPc_2$. Taking into account the common top layer in the bilayer heterostructures, it is clear that organization of the sublayer provides a template for the subsequent growth of the top layer, thus influencing the surface topography of the bilayer film[103]. The evolution of different surface topographies of Cl_2-SiPc and $(345F)_2$-SiPc can be attributed to different sublimation temperatures, solid state stacking and evaporation sticking coefficients[5, 137], which would determine their microstructural organization in the thin film.

The distribution of surface pores of up to 50 nm in Cl_2-SiPc/$LuPc_2$ film is evident in the surface height variations profile (**Figure 16c**) deduced from a selected linescan in the image. Notably, the surface depth is similar to the thickness of the either layer, indicating that sublayer does not completely cover the substrate, leaving behind holes to be filled by $LuPc_2$ layer. Further analysis of the total image area resulted in the mean roughness (RMS) of 15.6 nm. The surface of $(345F)_2$-SiPc/$LuPc_2$ film is mainly composed of closely packed elongated grains of size ca. 160 nm, while mean roughness of the total image area is estimated as ca. 7.3 nm. The presence of a few larger grains is also noticed as bright spots in the image, which surface height increase up to 40 nm (**Figure 16d**) in the selected linescan. The different surface topographies, as confirmed by AFM images, clearly has implication on the nature of organic-organic interfaces formed within the heterostructures. Higher roughness, porous and rugged surface of Cl_2-SiPc/$LuPc_2$ film predicts a non-continuous interface between Cl_2-SiPc and $LuPc_2$ layer. On the contrary, relatively smooth and compact surface of $(345F)_2$-SiPc/$LuPc_2$ bilayer predicts a continuous interface between the constituent organic layers. Such differences in the organic-organic interface in the two heterostructures are expected to influence the electrical properties

of the devices based on them and it also explains the difference in sorption kinetics of the bilayer heterojunction devices.

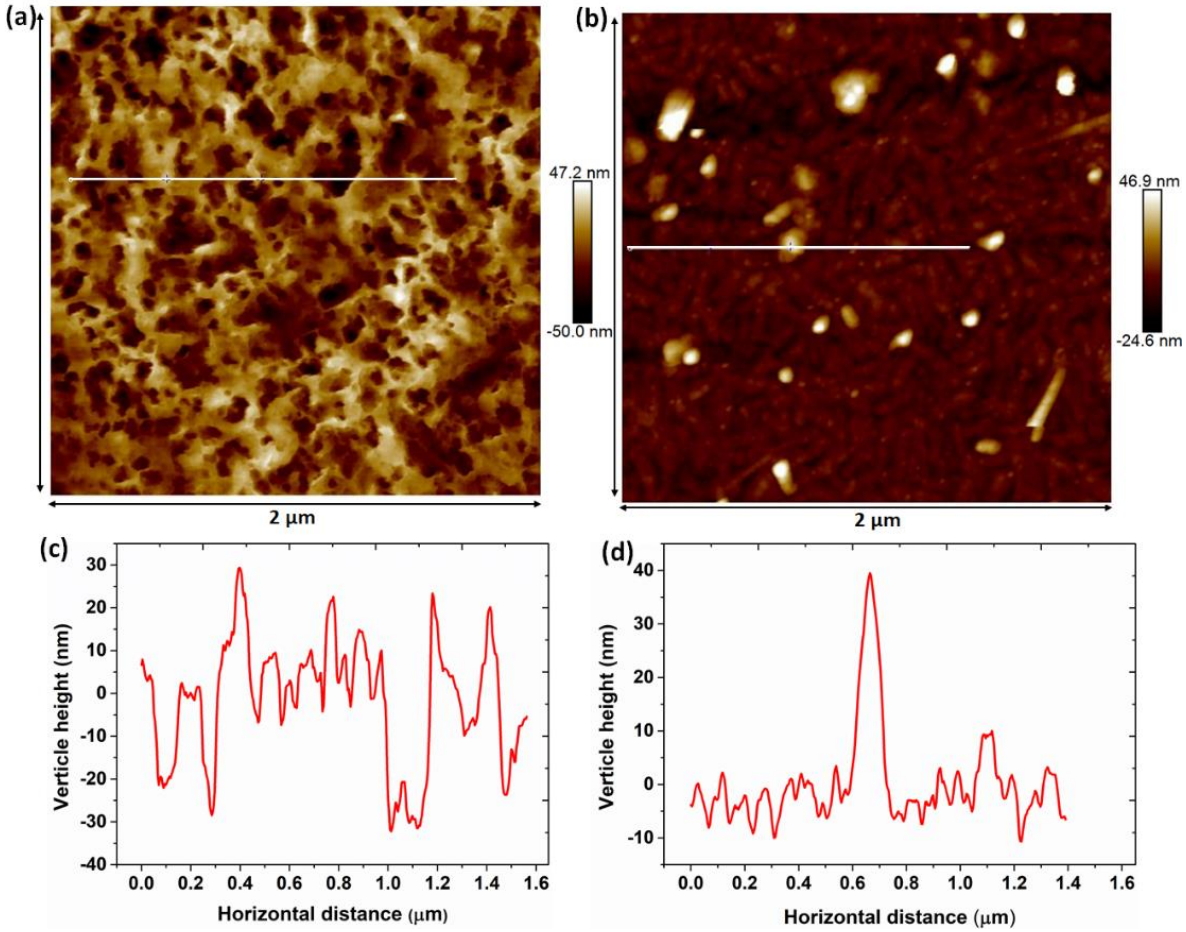

Figure 16. AFM images of Cl_2-SiPc/$LuPc_2$ (a) and $(345F)_2$-SiPc/$LuPc_2$ (b) bilayer heterostructures coated on glass substrate. The surface height variation corresponding to the linescan on both images are shown in image panel (c) and (d).

The implication of variable adsorption/desorption profiles of NH_3 on the two sensing layers is evident on the response/recovery times (time taken to change 90% of the current in respective cycle) of the two sensors, which are estimated as more than 7 min and less than 1 min for Cl_2-SiPc/$LuPc_2$ and $(345F)_2$-SiPc/$LuPc_2$, respectively. To further evaluate the NH_3 sensing performances of the two sensors in a wide concentration range, they were subjected to short exposure/recovery cycles of 1 min/4 min at different NH_3 concentration in the range of

10 to 90 ppm and 1 to 9 ppm. **Figure 17** depicts the response curves of Cl_2-SiPc/$LuPc_2$ and $(345F)_2$-SiPc/$LuPc_2$ sensors, respectively, exhibiting current decrease and increase under alternating exposure/recovery cycles. Notably, the current variations are highly reversible during the exposure and recovery cycles and increase as a function of the increasing ammonia concentration. Moreover, the sensors responses at a given NH_3 concentration are highly repeatable, as similar variation in current is observed in 4 consecutive exposure/recovery cycles recorded at each concentration. It confirms high repeatability of the two sensors in an extended range of NH_3 exposure.

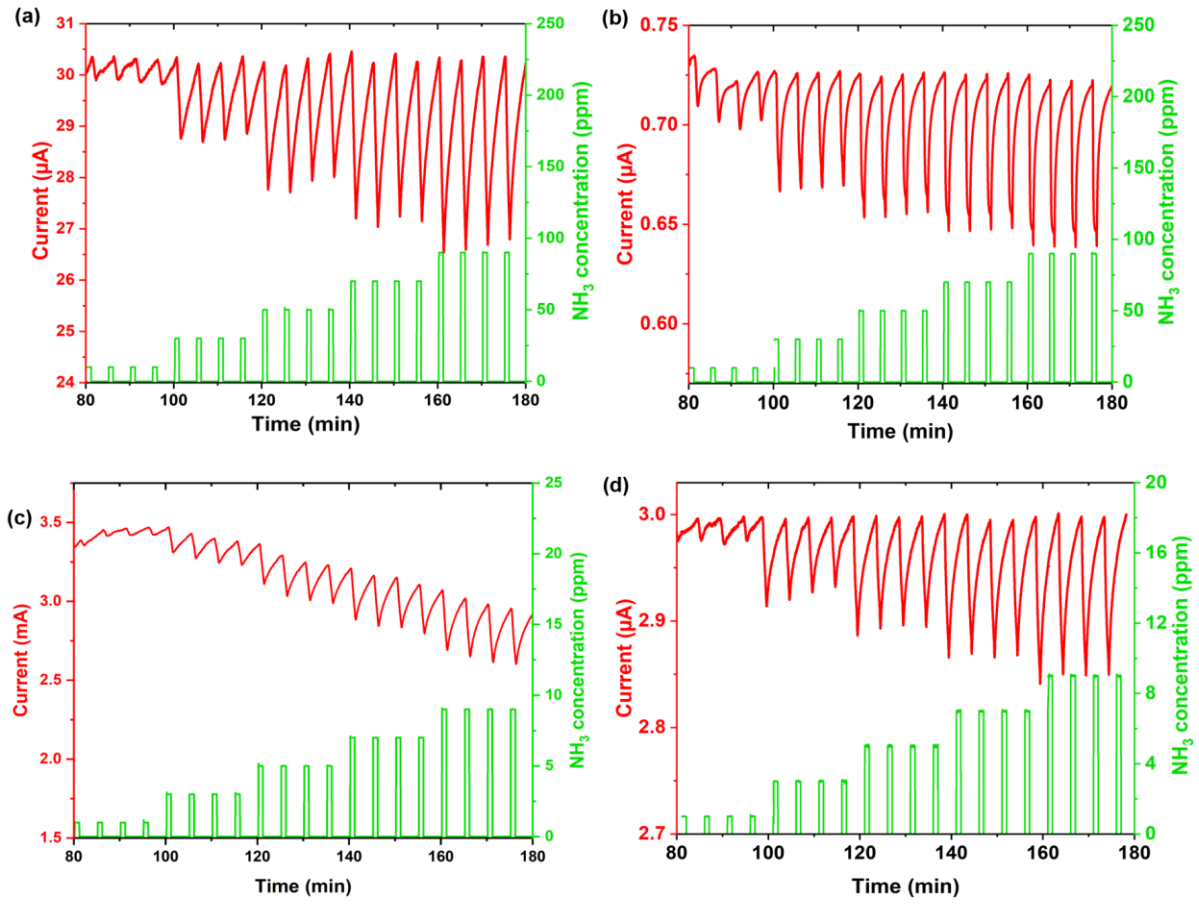

Figure 17: Response of Cl_2-SiPc/$LuPc_2$ (a, c) and $(345F)_2$-SiPc/$LuPc_2$ (b, d) heterojunction sensors under successive exposure of NH_3 for 1 min and recovery under clean air for 4 min in the range of NH_3 concentration 1 – 90 ppm at a RH of 45% and room temperature (20 – 22 °C).

The calibration curves of the two sensors present different profiles (**Figure 18**), exhibiting a linear variation in the sensors response magnitude, with RR from ca. -0.3% to -15.5% for $Cl_2SiPc/LuPc_2$, while an exponential decay in the response, with RR from ca. -0.4% to -11.4% for $(345F)_2$-$SiPc/LuPc_2$, as NH_3 concentration increases from 1 to 90 ppm. The uncertainties of the sensors are given as error bars in calibrations curves. The evolution of different calibration curves of the two sensors are attributed to different adsorption regimes, associated to surface topography of the sensing layers. The porous layer of $Cl_2SiPc/LuPc_2$ imparts access to larger adsorption sites to NH_3 molecules, as they can diffuse within its volume. Thus there is always availability of the adsorption sites for increasing number of NH_3 molecules in the range of 1 to 90 ppm. On the other hand, compact topography of $(345F)_2$-$SiPc/LuPc_2$ provides limited number of adsorption sites, mainly on the surface and restricts the NH_3 diffusion within the bulk of the sensing layer. Consequently, the surface adsorption sites, limited in number, are saturated with increasing NH_3 concentration, exhibiting a Langmuir type adsorption isotherm. The fitting parameters were given in the insets of **Figure 18**.

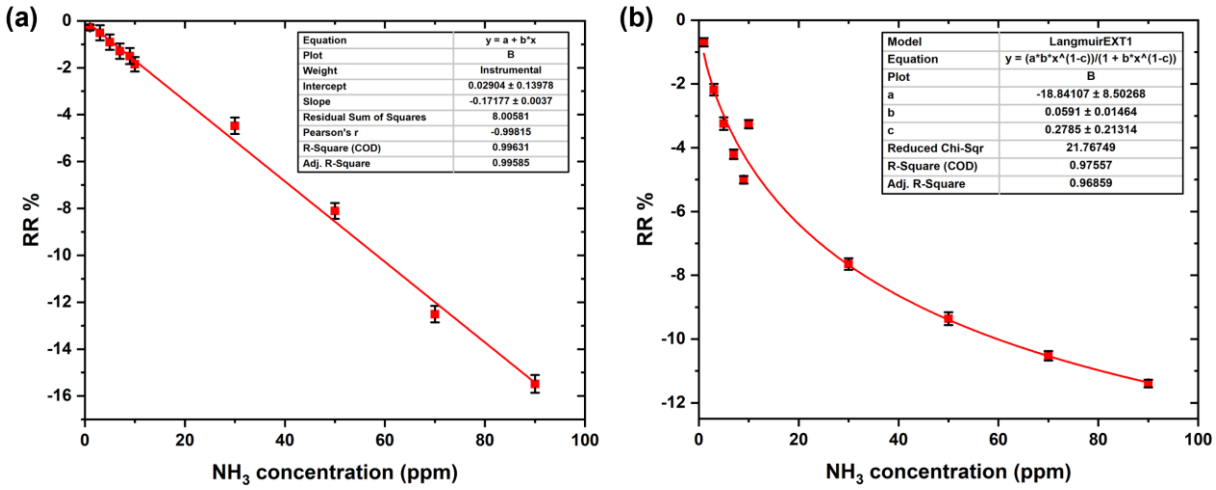

Figure 18. The variation of RR of Cl_2-$SiPc/LuPc_2$ (a) and $(345F)_2$-$SiPc/LuPc_2$ (b) as a function of NH_3 concentration.

It is worth mentioning that both heterojunction sensors can experimentally detect NH_3 at 1 ppm. Using **equation (5)**, LOD of $Cl_2SiPc/LuPc_2$ and $(345F)_2$-SiPc/$LuPc_2$ heterojunction sensors are estimated as ca. 400 ppb and 310 ppb, respectively.

4. Humidity effect

Humidity is a potential interferant in the real environment application of NH_3 sensors, which can experience variation in a wide range during a short period. Therefore, the behaviour of the two heterojunction sensors was investigated in a changing RH condition was investigated. **Figure 19** depicts the current variation of the two sensors over time as RH is increased at first from 30% to 60% and then decreased to the initial value. The i-t curves of the two sensors revealed distinct features. For $Cl_2SiPc/LuPc_2$-based sensor, current continuously increases during the monotonic increase of RH from 30 to 60% and remains constant during the monotonic decrease of RH (**Figure 19a**). The increase of the sensor current can be attributed to the trapping of mobile electron in the sensing layer, facilitating the hole transport in the sublayer[138]. On the contrary, the $(345F)_2$-SiPc/$LuPc_2$-based sensor reveals a rapid increase in current followed by a plateau like feature during step of RH increase and a similar decreasing pattern during the monotonically decreasing cycles of RH change (**Figure 19b**). Different behaviour of the two sensors towards RH can be correlated to surface topography of the respective sensing layer, imparting different adsorption of H_2O. The highly porous layer of $Cl_2SiPc/LuPc_2$ results in diffusion of H_2O molecules in the bulk of the heterostructure, causing large increase in the sensor current during monotonically increasing steps of RH change. However, H_2O molecules remain trapped in the porous morphology of the film, causing sensor current to stay constant during the decreasing cycles of RH. In the case of $(345F)_2$-SiPc/$LuPc_2$-based sensor, H_2O interaction remains confined to its surface because of its highly compact topography. Consequently, water adsorption/desorption cycles have a rapid and reversible

effect on the sensor current. Moreover, fluorination of the phenoxy groups of the $(345F)_2$-SiPc layer repulses adsorbed water molecules more easily than Cl_2SiPc, preventing H_2O molecules to diffuse in the sublayer. Thus, the results suggest that the choice of axial functional groups in SiPc play a significant role on the moisture sensitivity of the sensor. For real application of these sensors, association of a humidity sensor in the measurement system will be necessary to take into the account the humidity effect and interaction between NH_3 and H_2O molecules to minimize the interference.

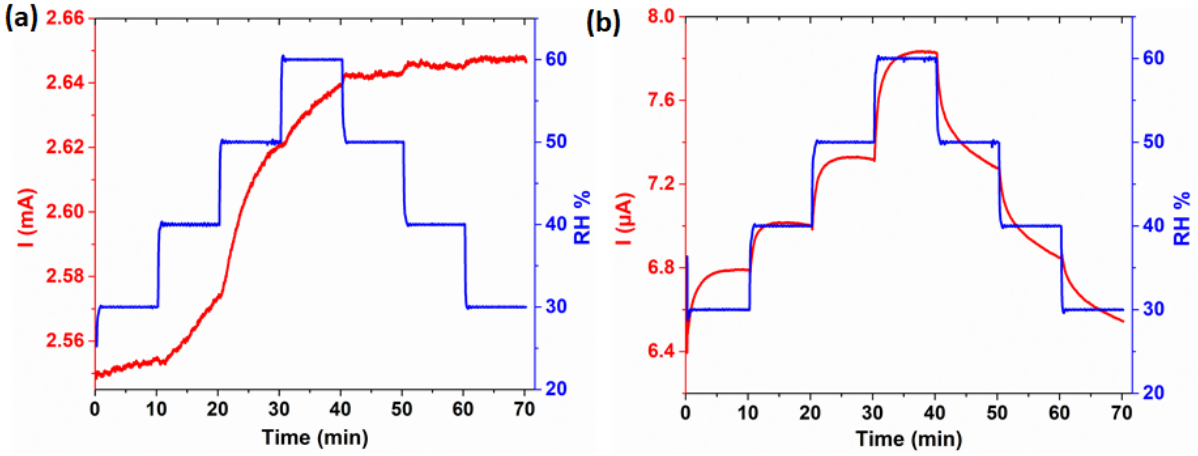

Figure 19. Response of Cl_2-SiPc/$LuPc_2$ (a) and $(345F)_2$-SiPc/$LuPc_2$ (b) heterojunctions towards the RH change in the range of 30% to 60% and then to 30%, at room temperature (20°C).

5. Conclusion

Here, we have demonstrated for the first time the application of silicon phthalocyanines (Cl_2-SiPc and $(345F)_2$-SiPc) in thin film bilayer heterojunction sensors for NH_3 detection. The choice of axial groups in SiPc imparts different thin film morphologies and electronic properties, which strongly influence the interfacial charge transport in the associated heterojunction device and finally sensing performances towards NH_3. The bilayer heterostructures of SiPc derivatives in combination with $LuPc_2$ revealed characteristics

absorption bands and vibrational Raman peaks of phthalocyanines, confirming that each macrocycle preserves its electronic identity in the heterostructures. The two heterostructures film exhibited very distinct surface topography as revealed by the AFM imaging, such that Cl_2-SiPc/$LuPc_2$ film has highly porous and rugged surface, while $(345F)_2$-SiPc/$LuPc_2$ possesses a compact surface. Different topographies of the two heterostructures has a strong impact on its electrical and charge transport properties. Accordingly, Cl_2-SiPc/$LuPc_2$ heterojunction device exhibits a smaller U_{th} and faster interfacial and bulk charge transport than $(345F)_2$-SiPc/$LuPc_2$. Both sensors exhibit p-type behaviour upon interaction to NH_3, revealing a quasi-reversible response in the alternate exposure/recovery steps. However, $(345F)_2$-SiPc/$LuPc_2$ reveals a short response/recovery time (less than 1 min), while Cl_2-SiPc/$LuPc_2$ based sensor presents a long response/recovery time (more than 7 min). Moreover, the calibration curve of the Cl_2-SiPc/$LuPc_2$-based sensor is linear, while the one of $(345F)_2$-SiPc/$LuPc_2$ is exponentially decaying, in NH_3 concentration range of 1 to 90 ppm. The different sensing properties of the two heterojunction sensors have been correlated to different regimes of surface adsorption and bulk diffusion, associated to their surface topography. Both sensors are capable to detect NH_3 in the sub-ppm range, making them suitable for application in real environmental conditions.

Chapter 4

Effect of UV Light on π-Extended Porphyrin-Phthalocyanine-Based Ammonia Sensors

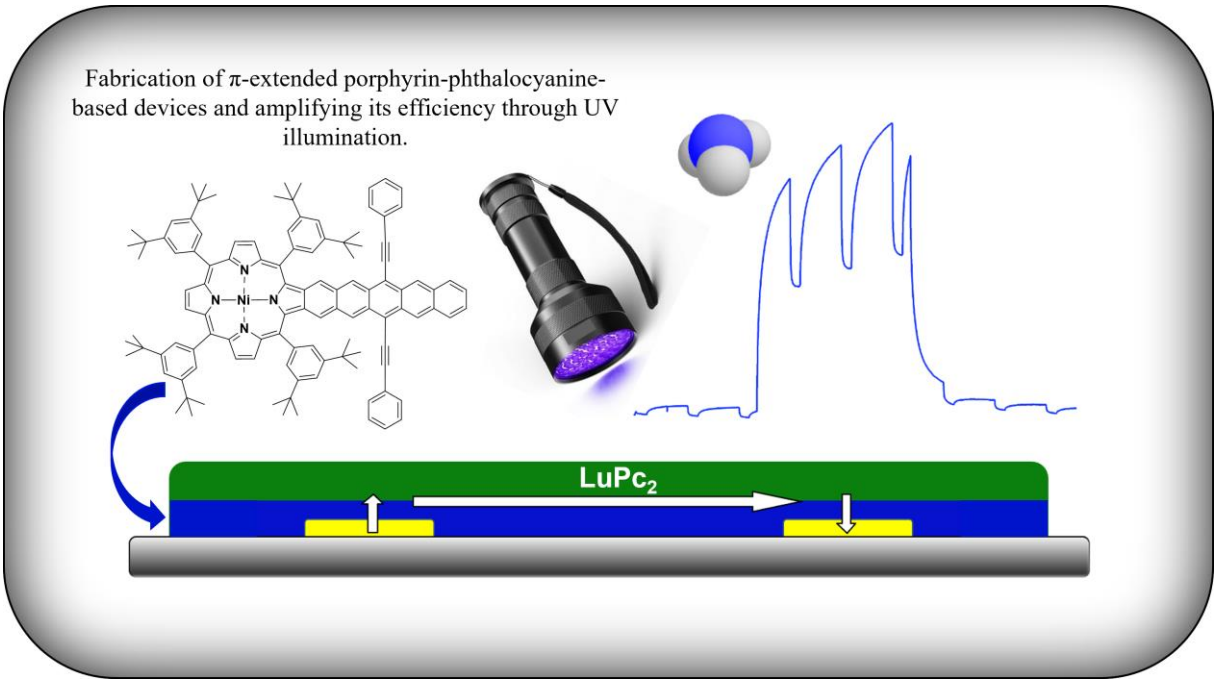

Chapter 4

Effect of UV Light on π-Extended Porphyrin-Phthalocyanine-Based Ammonia Sensors

Table of Content

Chapter 4. Effect of UV light on π-extended porphyrin-phthalocyanine-based ammonia sensors

1. Introduction

Porphyrins known as pigments of life offer a wide range of interaction mechanisms for analyte binding, mainly through Van der Waals interactions, π-π interactions and coordination to the central metal ion. The richness of their properties has been taken advantage of to develop gas sensors, associated mainly to optical[139-140] and acoustic[141-142] transducers. Due to their rather poor conducting properties, porphyrins have been rarely used directly as sensing materials in conductometric sensors[143]. However, they were more studied associated with carbonaceous materials, such as carbon nanotubes[144-146]. Recently, polyporphyrins were introduced in two types of gas sensing heterostructures including double lateral heterojunctions[147] and double layer heterojunctions[86]. In double lateral heterojunctions, polyporphyrins were electrodeposited on interdigitated electrodes, then covered by $LuPc_2$ as a molecular semiconductor. In double layer heterojunctions, polyporphyrins were synthesized and deposited by chemical vapour deposition technique, in the presence of an oxidizing species, on a poor conducting phthalocyanine material. In the former devices, electrosynthesis of zinc porphyrin – a non-substituted porphyrin – at low positive potential, to obtain a low conjugated and poor conducting polymer, allowing for the heterojunction effect to play a key role. In the latter case, polyporphyrins obtained from nickel tetraphenyl and nickel tetramesityl porphyrins were highly conjugated, leading to another type of heterojunction effect[40, 148].

It is well-known that photoexcitation can affect transport phenomena by increasing the density of free charge carriers and by decreasing the energy barrier at grain boundaries[149]. Thus, illumination can also change trapping phenomena by changing the occupancy of defects by

electrons and holes. In terms of gas sensing, relative response can be increased and response time can be shortened under light. It has been reported that the response was multiplied by ca. 6[13] upon UV irradiation on SnO_2 exposed to CO (100 ppm, RT) or NO_2 (1 ppm, 300°C). With In_2O_3, RR was multiplied by 16 at 100 ppm CO, while RR was quasi unchanged at 3 ppm NO_2, but with a better recovery and improved kinetics at RT. To explain these observations, the authors hypothesized that light helps oxygen desorption, and consequently facilitating CO adsorption. However, response can also decrease depending on light energy, even though recovery time is shortened[150], suggesting complex light effect. Improved response time by a factor of ten was reported by Llobet et al. for pulsed UV light illuminated on WO_3 nanoneedles exposed to NO_2 or NH_3[151]. Nakamura and co-workers reported an interesting p-NiO/n-ZnO heterojunction, for which sensing performances for aromatic volatile organic compounds (VOCs) were highly improved under deep UV light irradiation, as a result of an electron transfer from the photo-excited VOC adsorbates to the valence band (VB) of *p*-NiO[152]. A high sensitivity increase was also observed with visible light on inorganic halide perovskites used to detect O_2, and volatile small organic molecules including acetone and ethyl alcohol[153]. Di Natale et al. reported the use of visible light effect to tune the selectivity of porphyrin coated ZnO hybrid material towards VOCs[154-155]. In this case, light induces not only a photocurrent as in any junction-based solar cell, but also promotes the selectivity towards amines compared to alcohols. Obviously, mechanisms involved in metal oxide-based resistors or heterojunctions cannot be directly applied to molecular material-based sensors. Actually, only a few examples of light effect on molecular material-based gas sensors were reported. An increase in sensitivity towards water, ethyl alcohol and dimethyl methyl phosphonate (DMMP) was reported for graphene field-effect transistor under UV light[156].

In this work, we used two original π- extended conjugated porphyrin complexes in double layer heterojunction devices, in combination with $LuPc_2$ as a top layer and studied their

response to ammonia. π-Extended porphyrins have received particular attention due to their unique photophysical and optoelectronic properties[157-158]. Recently, H. Wang et. al reported the synthesis of unsymmetric polycyclic aromatic hydrocarbon (PAH) – fused porphyrins, i.e. pentacenequinone – fused (cross-conjugated) and pentacene – fused porphyrins (linear-conjugated)[7], which can potentially lead to original electrical properties. Despite their similar D_{2h} symmetry, they display very different optical and electronic properties, due to the type of conjugation involved. In the former, conjugation is extended on all the pentacene moiety, while in the later the quinone carbonyl fragment interrupts the π-conjugation. Precisely, the porphyrin complexes compiled in this chapter are pentacene-fused nickel porphyrin (AM6) and acenaphtho[1,2-b]pentacene-9,16-dione-fused nickel porphyrins (Ace-PQ-Ni) (**Scheme 10**). We also studied the effect of illumination on electrical and sensing responses.

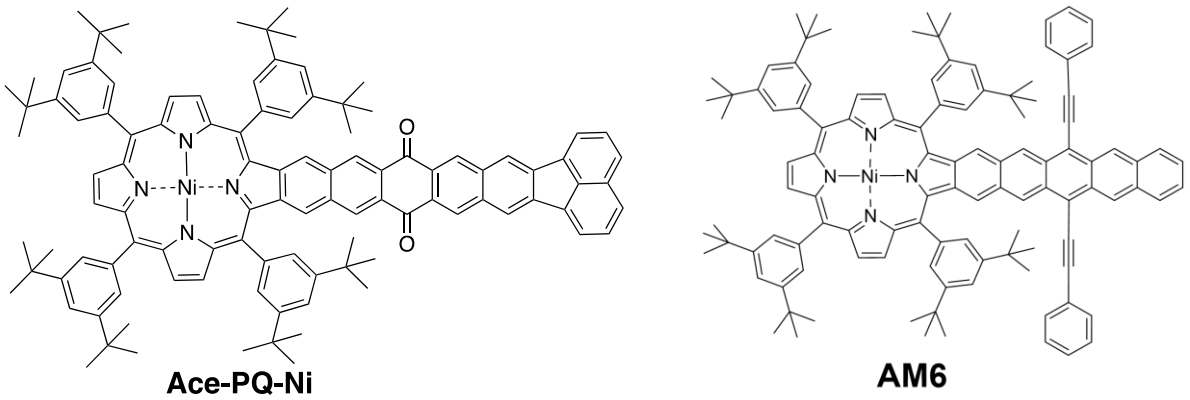

Scheme 10. Chemical structure of acenaphtho[1,2-b]pentacene-9,16-dione-fused nickel porphyrin (Ace-PQ-Ni) and pentacene-fused nickel porphyrin (AM6).

2. Electrical properties of heterojunction devices in dark and under light

Electrical properties of the Ace-PQ-Ni/$LuPc_2$ and AM6/$LuPc_2$ bilayer heterojunction devices were investigated by performing I-V measurements in the applied bias range of -10 V to +10 V in dark and under UV light (EvoluChem 365PF: 12.4 mW/cm^2) (**Figure. 20a and 20b**). Both heterojunction devices exhibit symmetric and non-linear behavior in all conditions. However, a plateau is observed only with AM6-based device.

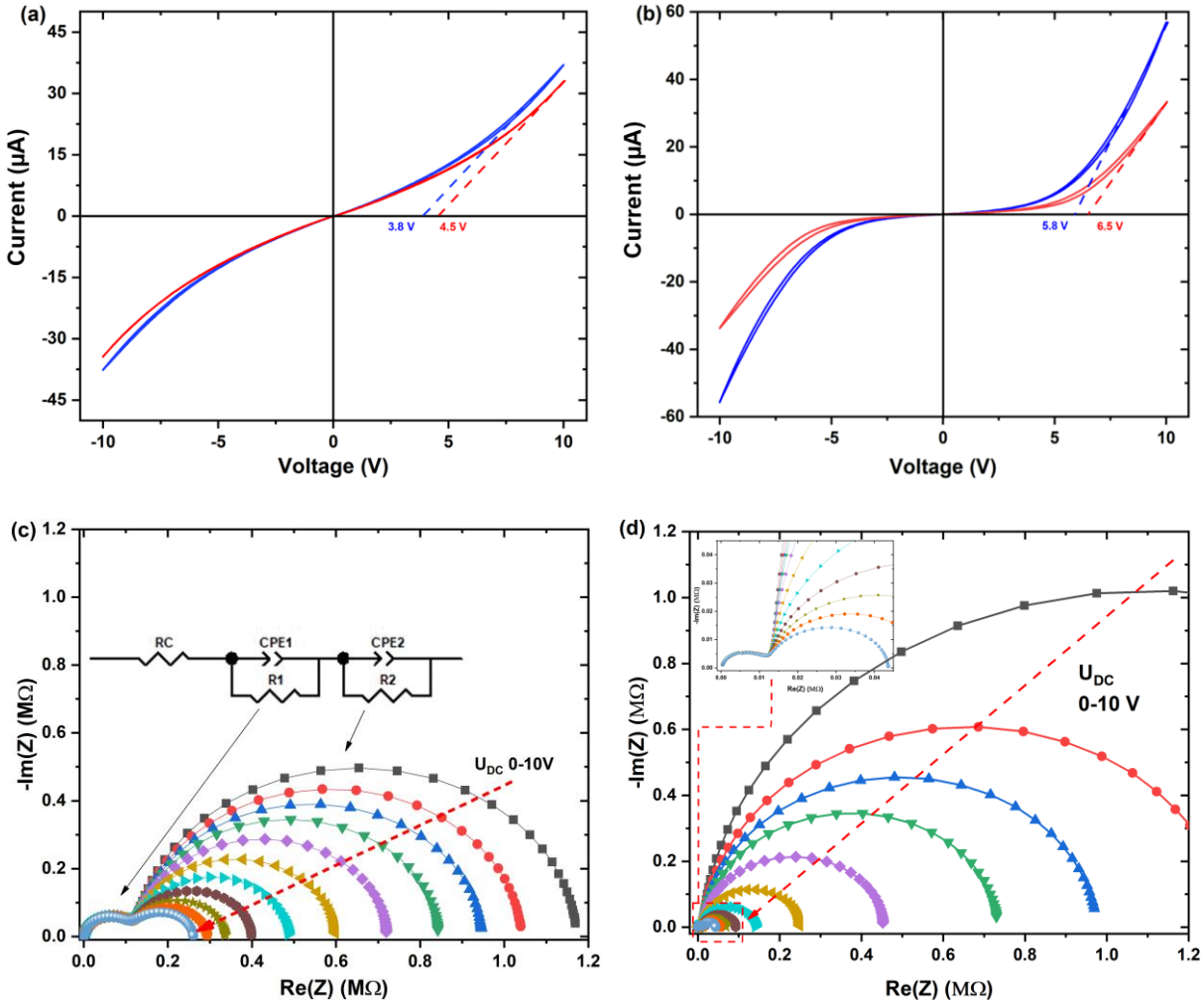

Figure 20. I-V characteristics of Ace-PQ-Ni- (a) and AM6- (b) based heterojunctions under dark (red curve) and under UV light (blue curve). Nyquist plots of Ace-PQ-Ni- (c) and AM6-

(d) based heterojunctions recorded at variable DC voltage in the range of 0-10 V. The inset of Figure (c) indicates the equivalent circuit selected for fitting Nyquist plots.

The apparent energy barrier was calculated for different conditions. The calculated U_{th} for Ace-PQ-Ni/$LuPc_2$ and AM6/$LuPc_2$ in dark was 4.5 V and 6.6 V, respectively. Under light, current increases, as expected for most of the semiconductor-based devices. Thus, current at +10 V was multiplied by 1.13 times for Ace-PQ-Ni/$LuPc_2$ and by 1.73 times for AM6/$LuPc_2$ under UV light, with U_{th} values slightly lower at 4.0 V and 6.3 V, respectively. Whatever the conditions, the energy barrier of AM6/$LuPc_2$ heterojunction is much higher compared to this of Ace-PQ-Ni/$LuPc_2$ heterojunction.

To further understand the different electrical behaviours of the two heterojunction devices, in depth charge transport studies were performed by impedance spectroscopy in a wide frequency range, from 10 Hz to 10 MHz, at different DC bias. The Nyquist plots of both Ace-PQ-Ni/$LuPc_2$ and AM6/$LuPc_2$ heterojunction devices presented two depressed semicircles (**Figure 20c and 20d**). To quantitatively determine different charge transport parameters, the experimental Nyquist plots were fitted with constant phase element (CPE) based circuits[108]. Through fitting the data using **equation (2)** and Brug's relationship[106] **equation (3)**, we obtain parameters such as R1, α1, and $C1_{eff}$ for bulk charge transport characterization, and R2, α2, and $C2_{eff}$ for interfacial charge transport characterization. R1 value is about ten times lower for AM6-based device than for Ace-PQ-Ni-based device, but R2 is ca. ten times higher, at 2.2 MW at low bias, which confirms the lower current at low bias. However, R2 diminishes with bias increase, down to a value comparable for both devices (**Figure 21a and 21b**).

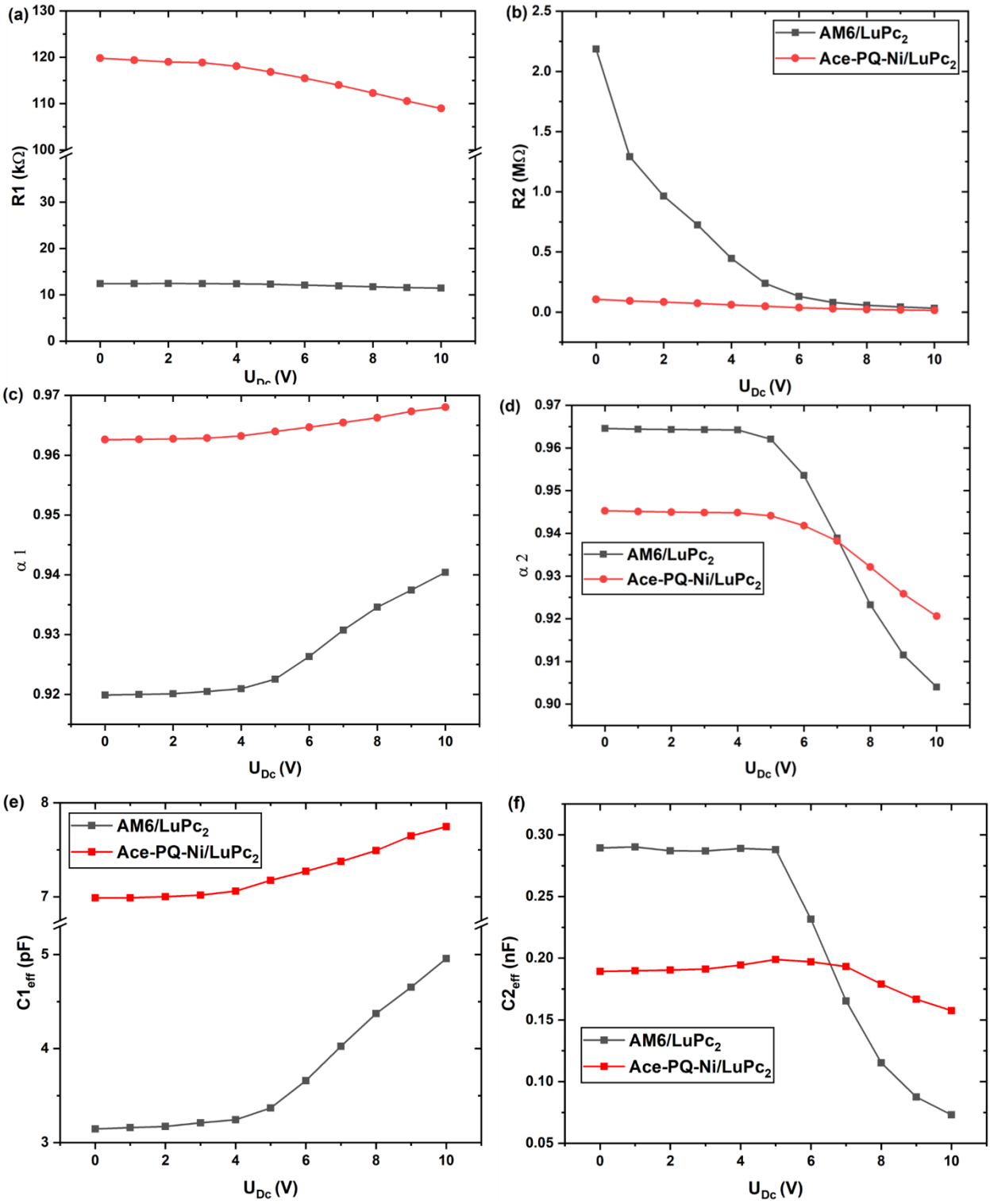

Figure 21. Variations of equivalent circuit resistances, R1 (a) and R2 (b), α 1 (c) and α 2 (d), effective capacitances $C_{eff}1$ (e) and $C_{eff}2$ (f), as a function of bias (0-10 V) for Ace-PQ-Ni/$LuPc_2$ and AM6/$LuPc_2$ heterojunction devices.

This explains why at +10 V, current value was higher for AM6-based device compared to Ace-PQ-Ni-based device. For a1 and a2, values are different for both devices, but remain in the same range, namely 0.9 – 1.0, so near 1, which confirms the existence of high capacity at the interfaces for both devices and explains the non-linearity of I-V characteristics (**Figure 21c and 21d**). This is also confirmed by the effective capacitances, in the nF range for $C2_{eff}$ and in the pF range for $C1_{eff}$, with values for AM6-based device about twice these of Ace-PQ-Ni-based device (**Figure 21e and 21f**).

3. Ammonia sensing properties

Ammonia sensing properties of the heterojunction devices were investigated under 90 ppm of NH_3 for 10 min/30 min exposure/recovery cycles. The current variation with time depicted in **Figure 22** exhibits a decrease in current under NH_3 exposure, while an increase of current was observed during the recovery period, which depicts the heterojunction's p-type nature.

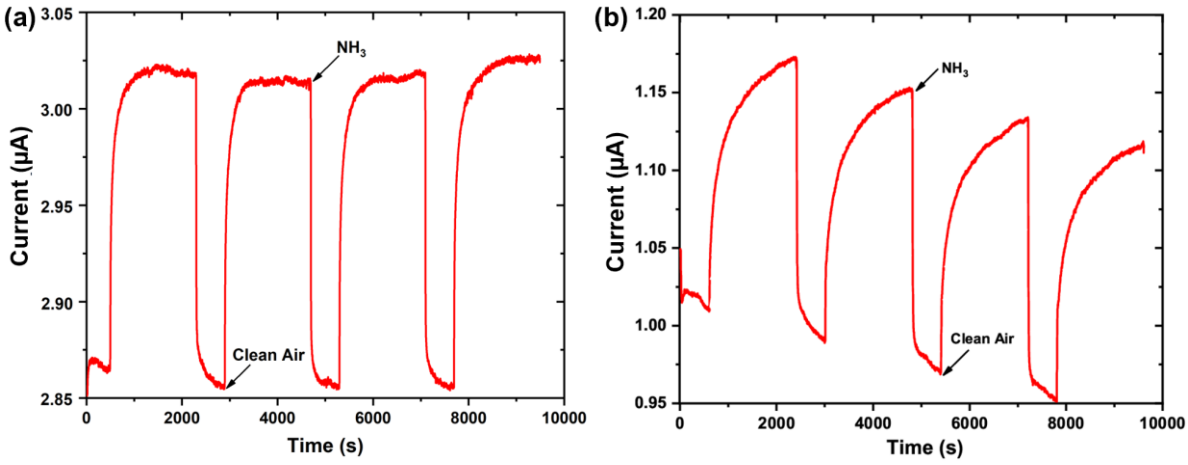

Figure 22. Response curve of Ace-PQ-Ni /$LuPc_2$ (a) and AM6/$LuPc_2$ (b) heterojunction sensors, under successive exposures to 90 ppm ammonia for 10 minutes and recovery under clean air for 30 minutes at 45% relative humidity (RH) and room temperature (18 – 21°C).

Notably, Ace-PQ-Ni/$LuPc_2$ heterojunction response curve demonstrated very stable baseline with almost complete recovery of the signal during desorption period. On the other hand, AM6/$LuPc_2$ shows slight drift in response curve, which mainly attributed to incomplete desorption of the NH_3 during recovery period. Anyhow, it is worthy to notice that the sensor recovers more than 85% of its signal during desorption period. A continuous decrease/increase of current was observed throughout exposure/recover cycles for AM6/$LuPc_2$ heterojunction sensor, while in Ace-PQ-Ni/$LuPc_2$ heterojunction sensor, a plateau in the response curve was observed during exposure/recovery period. This sorption behaviour of NH_3 in Ace-PQ-Ni/$LuPc_2$ heterojunction sensor shows that the sorption equilibrium was attained rapidly during exposure/recovery cycles.

Interestingly, different kinetics in response curves of both heterojunction sensors associated with adsorption and desorption rates was evident in response/recovery times. The time taken for both heterojunction sensors to change 90% (t_{90}) of its current during exposure period was approximately estimated as 40 s for Ace-PQ-Ni/$LuPc_2$ device and 80 s for AM6/$LuPc_2$ device. The quick response of both heterojunction sensors towards NH_3 gas were ascribed to the organic heterojunction effect in heterojunction sensors, in which interfacial accumulation of mobile charges facilitates the faster exchange of charges between NH_3 and the sensing layer[97, 147].

To further evaluate the NH_3 sensing properties, both bilayer heterojunction sensors were subjected to short exposure/recovery cycles of 1 min/4 min, under variable NH_3 concentration from 1 to 90 ppm (**Figure 23a-d**). As quantitative measurement, RR of the two sensors was calculated using **equation (4)**. The RR variation as a function of NH_3 concentration of Ace-PQ-Ni/$LuPc_2$ and AM6/$LuPc_2$ heterojunction sensors were displayed as calibration curves in **Figure 23e and 23f**, respectively. The uncertainties of the sensors were included as error bar in calibration curves.

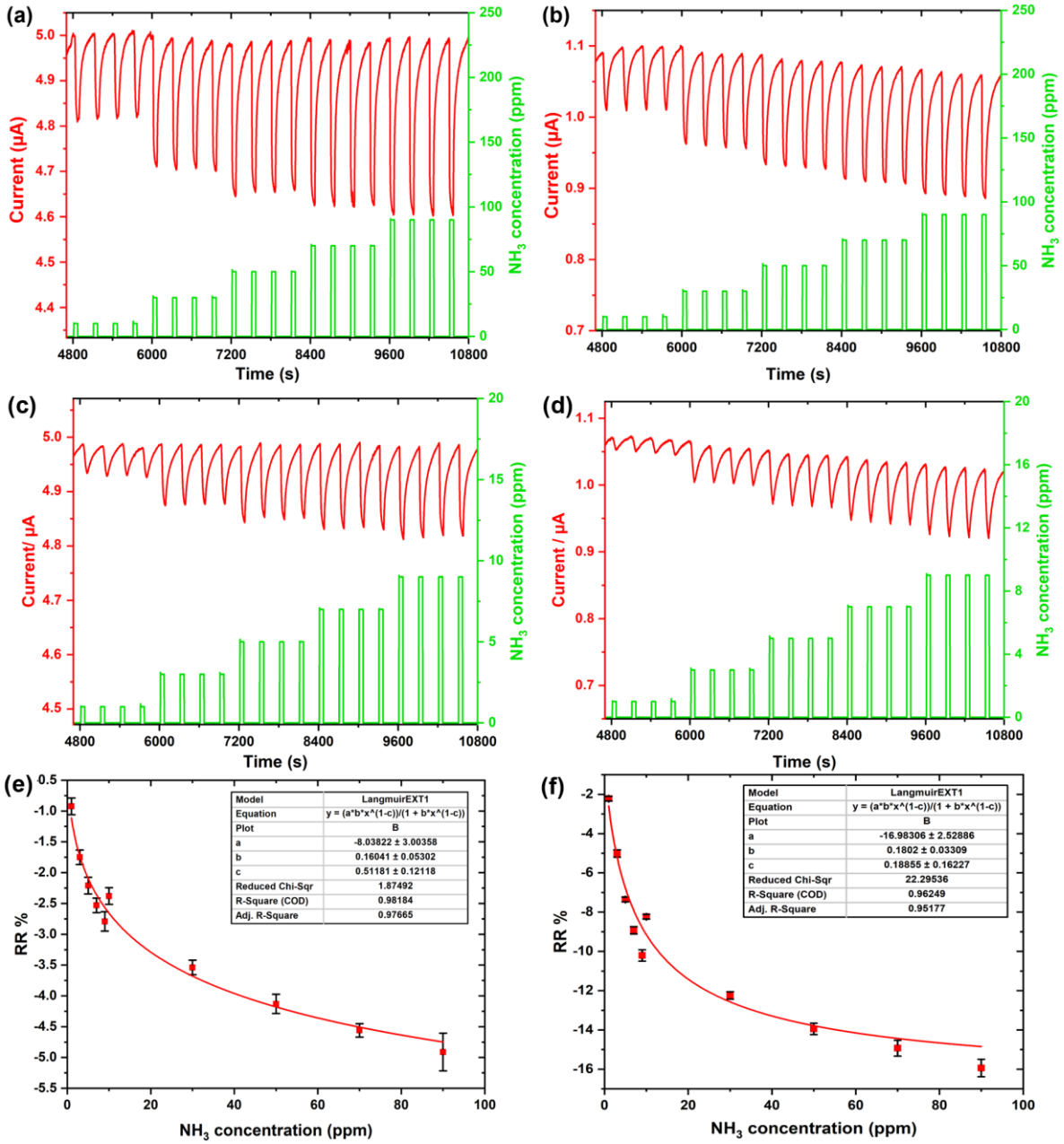

Figure 23. Response of Ace-PQ-Ni /$LuPc_2$ (a and c) and AM6/$LuPc_2$ (b and d) heterojunction sensors under NH_3 gas for 1 min and recovery under clean air for 4 min in the range of NH_3 concentration from 1 to 90 ppm at 45% of RH and room temperature (18–21 ˚C). The variation of relative response (calibration curve) of Ace-PQ-Ni /$LuPc_2$ (e) and AM6/$LuPc_2$ (f) as a function of NH_3 concentration.

RR value of AM6/$LuPc_2$ based sensor is up to 4 times higher than Ace-PQ-Ni/$LuPc_2$ sensor as evident from the calibration curve. Notably, the calibration curves are not linear and fit accurately with Langmuir's equation. The fitting parameters were given in the inserts of **Figure 23e and 23f**. Therefore, the interaction of NH_3 gas molecules on sensor's surface obeys Langmuir type adsorption. It is worth mentioning that Ace-PQ-Ni/$LuPc_2$- and AM6/$LuPc_2$-based heterojunction sensors can detect NH_3 gas experimentally even at 1 ppm with very low noise. Sensitivity of Ace-PQ-Ni/$LuPc_2$ heterojunction sensor was determined as S = -0.059% ppm^{-1} at 10 ppm and for AM6/$LuPc_2$ heterojunction sensor, S = -0.21% ppm^{-1} at 10 ppm. Limit of detection was calculated by using **equation (5)**. Such sensitivity of the sensor led us to obtain a LOD of ≈156 ppb and 115 ppb for Ace-PQ-Ni/$LuPc_2$ and AM_6/$LuPc_2$ heterojunction sensors, respectively.

4. Effect of UV light exposure in ammonia sensing

Taking into account the light effect on the electrical properties of heterojunction devices, we also carried out sensing experiments under UV light (365 nm). As expected for semiconductor-based devices, current increases under light. Surprisingly, both heterojunction sensors show different sensing responses towards NH_3 gas under UV light. Ace-PQ-Ni-based heterojunction sensor shows only a weak response to NH_3 under UV light (**Figure 24a**). In addition, we observed a continuous increase in current due to the heating effect of UV light, temperature increasing up to 55 °C, current was finally multiplied by a factor of 2 at the end of light exposure. At this stage, we cannot distinguish between thermal and pure optical effects. On the other hand, with AM6-based heterojunction sensor we observed a greater response to NH_3, with relative response multiplied by more than 3 at 90 ppm compared to dark, from -10.0% in the dark to -34.33% under light exposure (**Figure 24b, Table 1**).

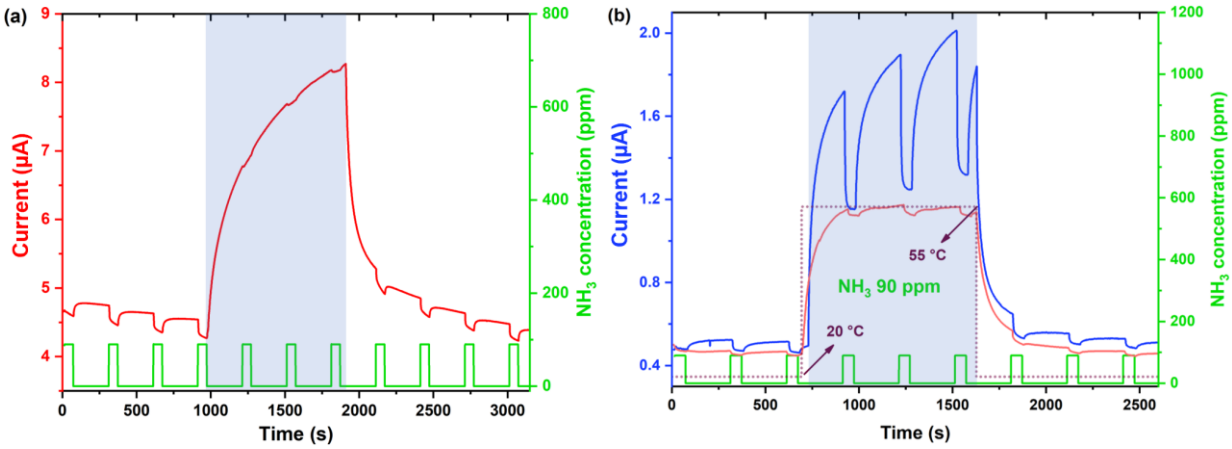

Figure 24. Response of Ace-PQ-Ni /$LuPc_2$ (a) and AM6/$LuPc_2$ (b) heterojunction sensors under NH_3 concentration of 90 ppm for 1 min/4min exposure/recovery under light exposure (365 nm) at 45% of RH. In (b), current variation was added during the same exposure/recovery cycles, but under a thermal cycle (red line), showing the programmed temperature cycle (dotted line). Blue shaded indicating illumination cycles.

This results from a huge increase of ΔI, multiplied by more than 13, while current baseline increased by only 3.9. This stronger current increase due to light effect has to be correlated with the higher energy barrier. Under light, the temperature of both samples increased up to 55 °C, while light effect is smaller in sensing response with Ace-PQ-Ni compared to AM6. We have to keep in mind that 365 nm corresponds to a minimum of absorption for both porphyrins. Actually, $LuPc_2$ is the material that absorbs the most at this wavelength through its Soret band. These results confirm that the difference between the two devices is mainly due to the interface between the two layers in each sensor. Actually, upon constant UV illumination, we can distinguish between a short time effect, which is optical in nature, and a slow kinetics effect, which can be attributed to the heating of the device. This thermal effect is visible with Ace-PQ-Ni, but is masked with AM6, due to the high response to NH_3. In addition, as soon as light is turned off, a sharp decrease is observed, followed by a slow decrease (temperature decrease).

To differentiate the light and temperature effects, we studied the AM6/$LuPc_2$ sensor under the same concentration of NH_3 gas by increasing the temperature from 20 °C to 55 °C in the dark. The baseline current was multiplied by 3, but ΔI remains almost the same from 20 °C to 55 °C, leading to a weaker RR. Even though the temperature change shows strong effect, it still has nothing to do with increasing in RR under light. It is evident that the unique increase in RR is truly because of the illumination. Sensitivity of AM6-based heterojunction sensor at 90 ppm NH_3 was increased from -0.21% ppm^{-1} in the dark to -0.56% ppm^{-1} under light exposure (**Table 1**).

To evaluate further, the AM6/$LuPc_2$ sensor was investigated under a wide range of NH_3 concentration from 10 ppm to 90 ppm under exposure to UV light. Nine cycles were recorded at each given concentration where the light was turned on after third cycle and turned off after sixth cycle, at each concentration, using a homemade software with Arduino UNO board. At all tested NH_3 concentrations, current increase and decrease under light were reversible, while the sensor response was correlated with the NH_3 concentration (**Figure 25**). Under light, the LOD became better than 100 ppb (calc. 83 ppb, **Table 1**). This value is the best we ever obtained with heterojunction devices.

Such response enhancement under light has been already reported, but only with inorganic conductometric gas sensors[159]. Two phenomena can occur in the present molecular material-based sensors. At First, light can facilitate dioxygen desorption, increasing the number of available adsorption sites for ammonia molecules. Second, by adsorption/desorption processes are generally faster under illumination.

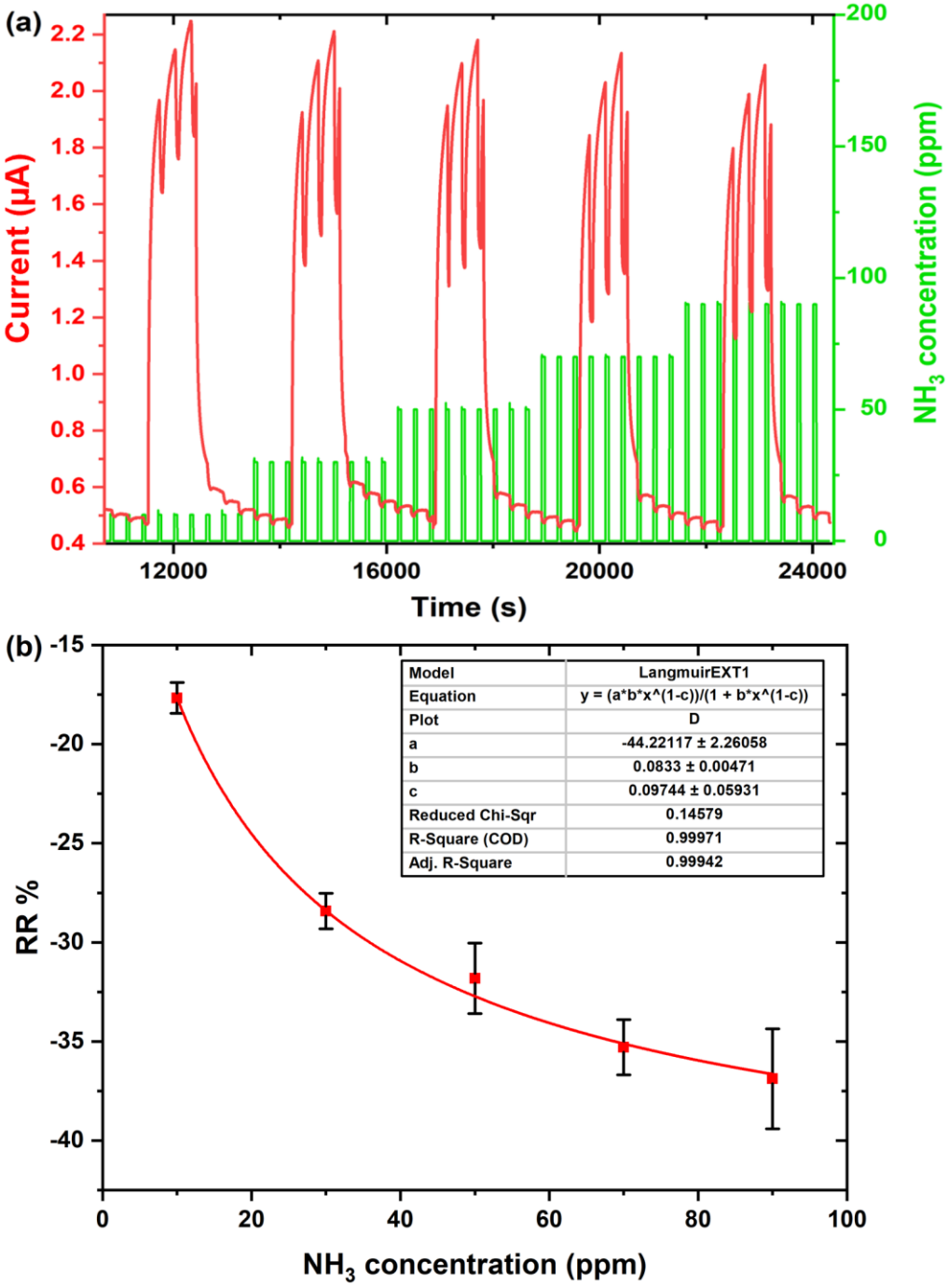

Figure 25. (a) Response of AM6/$LuPc_2$ heterojunction sensors under NH_3 gas for 1 min and recovery under clean air for 4 min in the range of NH_3 concentration from 10 to 90 ppm alternating in the dark and under UV light exposure, at 45% of RH. Calibration curve of AM6/$LuPc_2$ (b) as a function of NH_3 concentration.

Table 1. Comparison of I_0, ΔI and RR of Ace-PQ-Ni- and AM6-based heterojunction sensors in the dark and under light, as determined at 90 ppm NH_3 and LOD.

Device	Dark				UV light				Ratio UV light/Dark		
	I_0 (µA)	ΔI (µA)	RR %	LOD (ppb)	I_0 (µA)	ΔI (µA)	RR %	LOD (ppb)	I_0 (µA)	ΔI (µA)	RR %
Ace-PQ-Ni/ $LuPc_2$	4.62	-0.27	-5.95	156	-	-	-	-	-	-	-
AM6/ $LuPc_2$	0.51	-0.05	-10.0	115	2.01	-0.69	-34.3	83	3.94	13.53	3.40

The difference between the two studied heterojunctions can only come from the nature of the sub-layer. As shown in **Figure 20**, AM6/$LuPc_2$ exhibits a higher energy barrier than Ace-PQ-Ni/$LuPc_2$ and a stronger light effect. As a result, in sensing experiments, we also observed a higher current increase from dark to light. Current was multiplied by a factor of 4 with AM6 and only 2 with Ace-PQ-Ni. It means that, under light, a higher density of mobile charges is accumulated in the channel, resulting in a higher sensitivity[147].

5. Humidity effect

Both heterojunction devices were also investigated in a broad range of humidity, varying monotonically from 30% to 60%, then decreased to initial value for 10 min at each RH step. **Figure 26** depicts the current variation of the two sensors at given RH over time.

Ace-PQ-Ni/$LuPc_2$-based sensor shows increase in current during monotonically increase in RH step and decrease during monotonically decrease in RH with good reversibility. On the other hand, AM6/$LuPc_2$-based sensor reveals a continuous increase in current during steps of RH and exhibits partial recovery during RH decrease, which is attributed to incomplete

desorption of the H_2O molecules during the recovery step, which may get trapped during monotonically increase in RH. Overall, current changes by +27% for AM6/$LuPc_2$ and only +12% for Ace-PQ-Ni/$LuPc_2$, when RH varies from 30% to 60%, but with a quasi-stabilization of the current after 10 min, compared to -10% for the RR to 90 ppm NH_3 in the dark and -34% under UV light for AM6/$LuPc_2$.

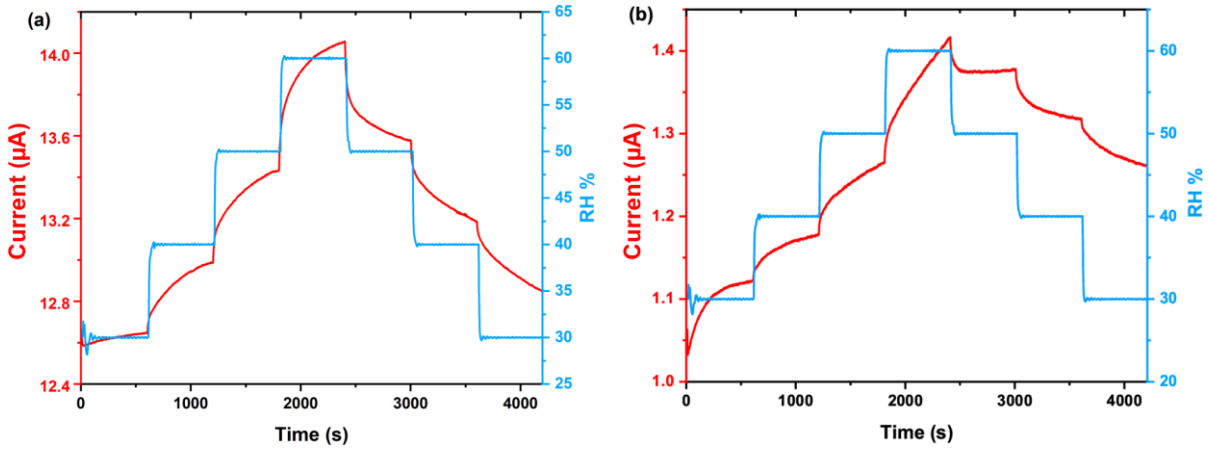

Figure 26. Response of Ace-PQ-Ni/$LuPc_2$ (a) and AM6/$LuPc_2$ (b) heterojunctions towards the RH change in the range of 30% to 60%, at room temperature (21°C).

This difference could be due to morphological differences between the heterojunctions as already demonstrated with silicon phthalocyanine-based gas sensors[160]. However, the good point is that the humidity effect is reversible, which is rarely the case, in particular when working at room temperature. So, the combination of this sensors with a humidity sensor could be used to get a corrected value of NH_3 concentration.

6. Conclusion

Cross-conjugated (Ace-PQ-Ni) and linear-conjugated (AM6) p-extended porphyrins have been introduced to construct double layer heterojunction devices. Ace-PQ-Ni and AM6 combined with $LuPc_2$ as an intrinsic semiconductor led to devices with rather high energy barriers, 4.5 and 6.5 V, respectively, as estimated from I-V characteristics. These values explain the high sensitivity towards NH_3 and the response stability compared to classical

resistors, with LOD of 156 and 115 ppb for Ace-PQ-Ni- and AM6-based sensors, respectively. In addition, although both with a current increase, the two porphyrin-based sensors show opposite sensing behaviours towards NH_3 under light illumination. Thus, for Ace-PQ-Ni/$LuPc_2$ device, the current variation under NH_3 largely decreased upon light illumination. In sharp contrast, the current variation remarkably increased by multiplication factor of 13 for AM6/$LuPc_2$ sensor under UV light illumination. This unusual behaviour observed for AM6/$LuPc_2$ sensor can be attributed to the linear conjugation in the p-extended macrocycle of AM6. In comparison, Ace-PQ-Ni is a cross-conjugated p-extended porphyrin. This work paves the way to further studies of p-extended porphyrins in organic electronics devices and gas sensors.

Chapter 5

Octafluoro-Metallophthalocyanine-Based Heterojunctions as Ambipolar Devices

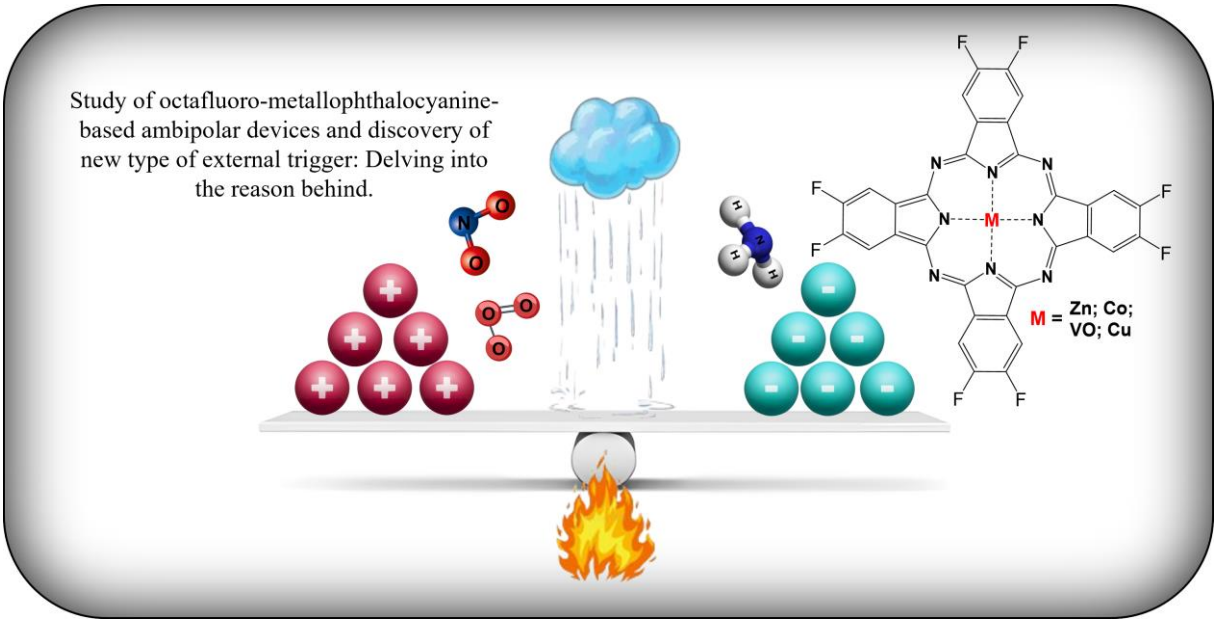

Chapter 5

Octafluoro-Metallophthalocyanine-Based Heterojunctions as Ambipolar Devices

Table of Content

Chapter 5. Octafluoro-metallophthalocyanine-based heterojunctions as ambipolar devices

1. Introduction

Optimising the frontier orbitals of a molecular semiconductor, HOMO and LUMO, relatively to the Fermi energy level of electrodes, can significantly influence the polarity of the molecular material and also facilitate ambipolar charge transport[94, 161]. Ambipolarity, as discussed earlier, refers to a physical balance where both electron (e^-) and hole (h^+) densities contribute equally to electrical conduction, achieving a stable state among infinite unbalanced positions. Although theoretically realizable in intrinsic semiconductors, practical challenges such as trapping effects and environmental interactions often hinder this equilibrium. Achieving ambipolar charge transport necessitates tuning the concentrations of e^- and h^+ near equilibrium to a sufficiently high level[10, 89]. Ambipolar materials have shown promising potential in CMOS-like inverters, where both n-type and p-type transistors can be replaced by a single ambipolar transistor[162]. This type of ambipolar device can effectively reduce the size of electronic systems, simplifying circuit designs, minimizing power dissipation, and enhances switching efficiency[163-164].

In previous work by M. Bouvet et al., ambipolar charge transport was demonstrated in various chlorinated and fluorinated metallophthalocyanine-based sensors. Notably, CuF_8Pc and $ZnCl_8Pc$-based sensors exhibited polarity switching using visible light (low power red LEDs) and humidity variation as external triggers[10, 97]. Specifically, CuF_8Pc exhibits p-type behaviour in the dark and n-type under red LED illumination. The nature of majority charge carriers underwent inversion upon exposure to light, attributed to the desorption of oxygen, which serves as a trap for mobile negative charge carriers[10]. Also humidity variation has huge effect

on the device polarity[94]. A small external trigger has the capability to reverse the nature of majority charge carrier density in a molecular semiconductor heterojunction device, thanks to the initial near-equilibrium position between charge carrier densities in the sensing layers.

In current scenario, we aimed to understand the effect of central metal atom in to the octafluoro-phthalocyanine macrocycle (**Scheme 11**). This chapter has been divided into two main sections. In the first section, we introduced a new type of ambipolar heterojunction sensor that exhibits different polarities under different gas species.

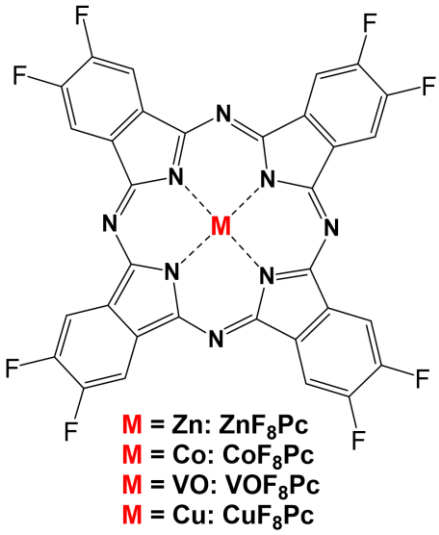

Scheme 11. Chemical structure of octafluoro-metallophthalocyanines: ZnF_8Pc, CoF_8Pc and VOF_8Pc.

Octafluoro-phthalocyanine complexes were synthesized with zinc (Zn) (**Scheme 12a and 12d**) and cobalt (Co) as metal centres (**Scheme 12b and 12e**) and engaged with $LuPc_2$ in organic-organic heterojunction devices. We investigated the sensing properties of the resulting devices towards NH_3, NO_2 and O_3 under different conditions. In the second section, with our previous experience in investigation of ambipolar devices, we delved into the ambipolar charge transport regime in bilayer heterojunction-based device to understand the effect of ambipolarity through external triggers and gas species. For this purpose, we used vanadyl (VO) as a metal

centre in octafluoro-phthalocyanine complex as a sublayer in bilayer heterojunction device covered by $LuPc_2$ as top layer and exposed to various types of gasses under different environmental conditions. The originality of VOF_8Pc is the presence of the oxygen atom that leads to a dipole moment, which induces a different crystal structure (**Scheme 12c**).

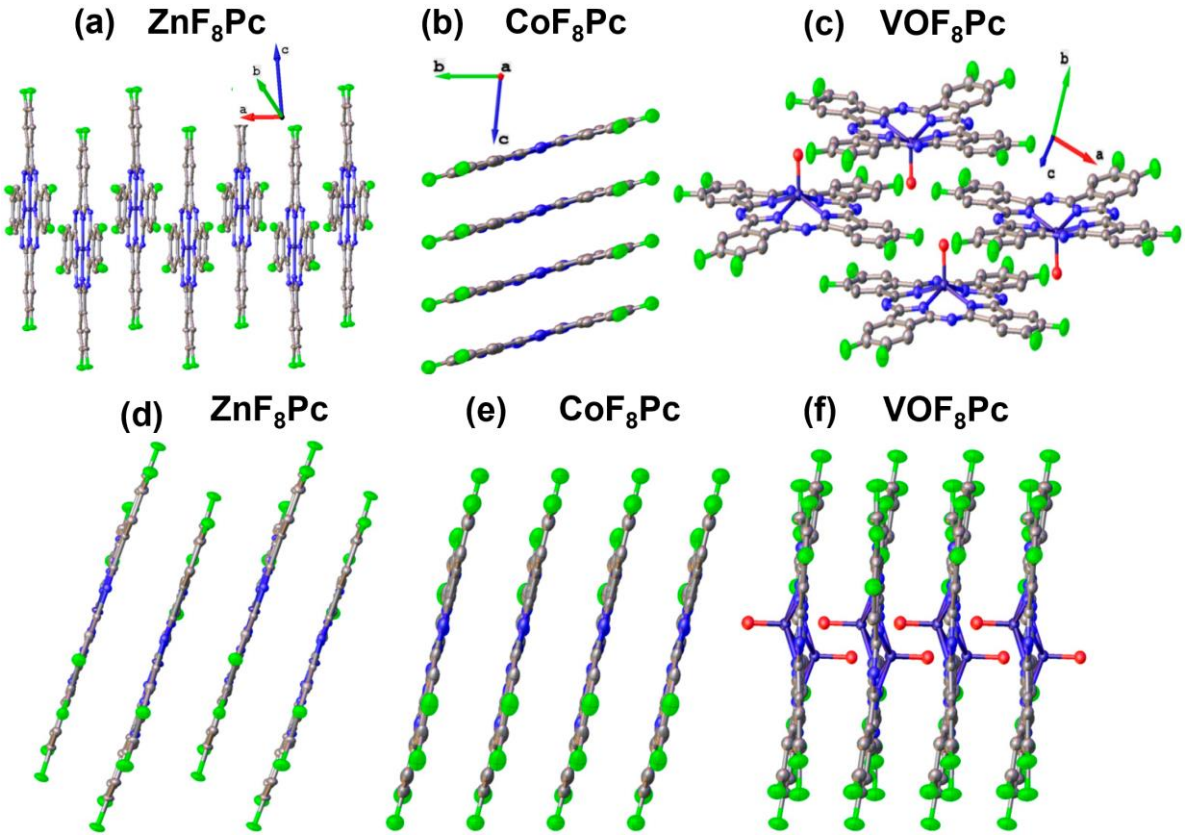

Scheme 12. Molecular packing diagram of ZnF_8Pc, CoF_8Pc, and VOF_8Pc showing their arrangement inside individual stacks (a-c). Orientation of MF_8Pc molecules in the thin films relative to the surface of the glass substrate (d-f) (adapted from ref [8]).

2. ZnF_8Pc- and CoF_8Pc-based ambipolar gas sensor – Another way to detect polluting gases

In this first section, we discussed about the electrical and sensing properties of ZnF_8Pc and CoF_8Pc-based bilayer heterojunction sensors under different gas species and experimental conditions. The main concept is to understand the effect of different metal center in octafluoro-phthalocyanine complexes and to achieve ambipolar charge transport within the device.

2.1. Electrical properties of heterojunction devices

To investigate the electrical properties, I-V measurements were performed on both devices at applied bias in the range from -10 to +10 V. As expected for bilayer organic heterojunction devices, $ZnF_8Pc/LuPc_2$ and $CoF_8Pc/LuPc_2$ devices exhibit symmetric and non-linear I-V curves (**Figure 27**).

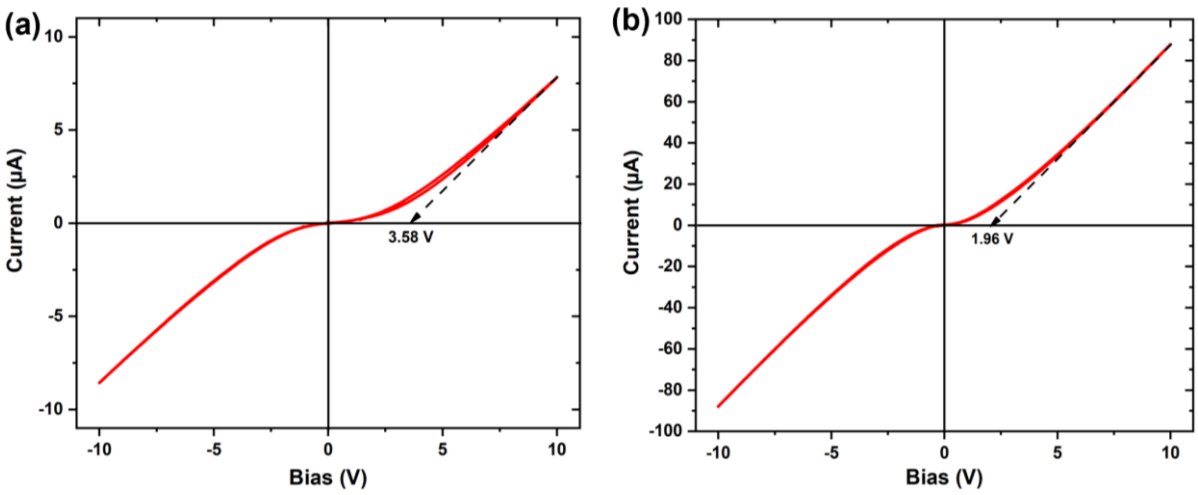

Figure 27. I-V characteristics of $ZnF_8Pc/LuPc_2$ (a) and $CoF_8Pc/LuPc_2$ (b) based heterojunction devices.

Interestingly, both heterojunction devices exhibit different electrical properties depending on central metal. Moreover, the non-linearity in I-V curve of both heterojunction devices is quantified by the threshold voltage U_{th} that gives an estimation of the energy barrier. U_{th} is 3.58 V and 1.96 V, for $ZnF_8Pc/LuPc_2$ and $CoF_8Pc/LuPc_2$, respectively, as estimated by drawing the tangent at high voltage on the I-V curves and extrapolating it to the X-axis. At +10 V, current values of $ZnF_8Pc/LuPc_2$ and $CoF_8Pc/LuPc_2$ devices are ca. +9 μA and ca. +90 μA, respectively, as a result of the higher energy barrier in $ZnF_8Pc/LuPc_2$ compared to $CoF_8Pc/LuPc_2$ device.

To get in depth information about the effect of heterojunction in bilayer devices, charge transport studies were performed by impedance spectroscopy on both octafluoro-phthalocyanine-based devices, at given amplitude of 0.2 V AC signal, with a wide range of frequency, from 10 Hz to 10 MHz, superimposed by different DC bias (0 to 10 V). The Nyquist plots that show the imaginary part of the impedance as a function of the real part exhibit different behaviours that depends on the type of metal centre in octafluoro-phthalocyanine macrocycle. Initially, both devices exhibit two depressed semicircles, which is expected for bilayer heterojunction devices (**Figure 28**).

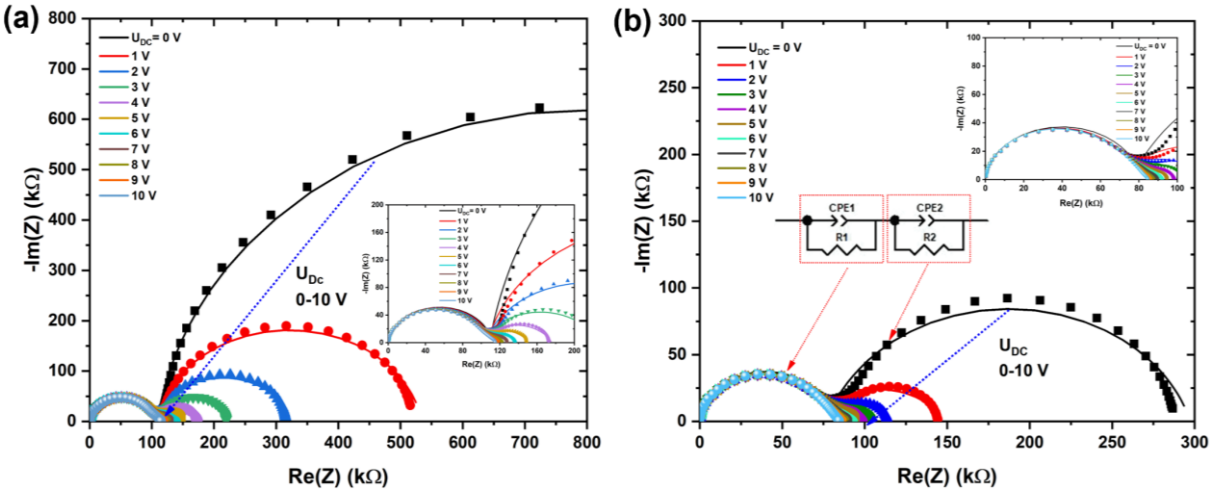

Figure 28. Nyquist plots of ZnF_8Pc (a) and CoF_8Pc (b) based heterojunctions measured at fixed AC (0.2 V) superimposed by variable DC voltage in the range of 0-10 V. The insets show the zooms at low resistance. The equivalent circuit selected for fitting Nyquist plots is added in (b).

The solely AC signal (0.2 V) is very small for both heterojunction devices compared to their apparent energy barrier. Hence the semicircle in LF region of the Nyquist plots of both devices appears larger, indicating the minimal charge injection. However, with the introduction of increasing DC voltage superimposed to the AC signal, there is a decrease in the LF semicircle due to the increasing charge density at the organic-organic interface channel. Interestingly, even at DC +10 V, $ZnF_8Pc/LuPc_2$ device exhibits two distinct semicircles, which confirms the

existence of the energy barrier even at higher bias due to the difference in work function of the materials. On the contrary, LF semicircle that belongs to $CoF_8Pc/LuPc_2$ device is almost merged with its HF semicircle at +5 V and completely collapsed at +10 V. To quantitatively determine different charge transport parameters, the experimental Nyquist plots were fitted with constant phase element (CPE)-based circuits[108] using **equation (2)** and Brug's relationship[106] **equation (3)**.

The variation in bulk charge transport (R1, α1, and $C_{eff}1$) and interfacial charge transport (R2, α2, and $C_{eff}2$) with DC bias are depicted in **Figure 29**. Similar to our previous studies, the bulk resistance (R1) demonstrates minimal dependency on applied bias, whereas the interfacial resistance (R2) exhibits an exponential decline as the DC bias increases. This indicates that the interfacial charge transport mobility increases as the DC bias increases, while bulk charge transport remains relatively stable. R1 and R2 values of Zn-based heterojunction device is ca. 1.5 and 6.5 times higher than Co-based heterojunction device at lower DC bias. The α1 values of both devices remain close to 1 and show slight increases with increasing DC bias, suggesting highly homogeneous bulk charge transport in both devices. In contrast, α2 experience relatively large variations with increasing bias, indicating heterogeneity of the interface visible when a higher density of charges arrives at the interface at higher bias. The calculated effective capacitance values agree with the αi values, indicating higher capacitance as the αi values approach 1. Additionally, the $C_{eff}2$ values were higher in magnitude compared to $C_{eff}1$ values, by a factor higher than 100, indicating that the thickness of interface is much smaller than that of bulk, which is typical for organic heterojunction devices.

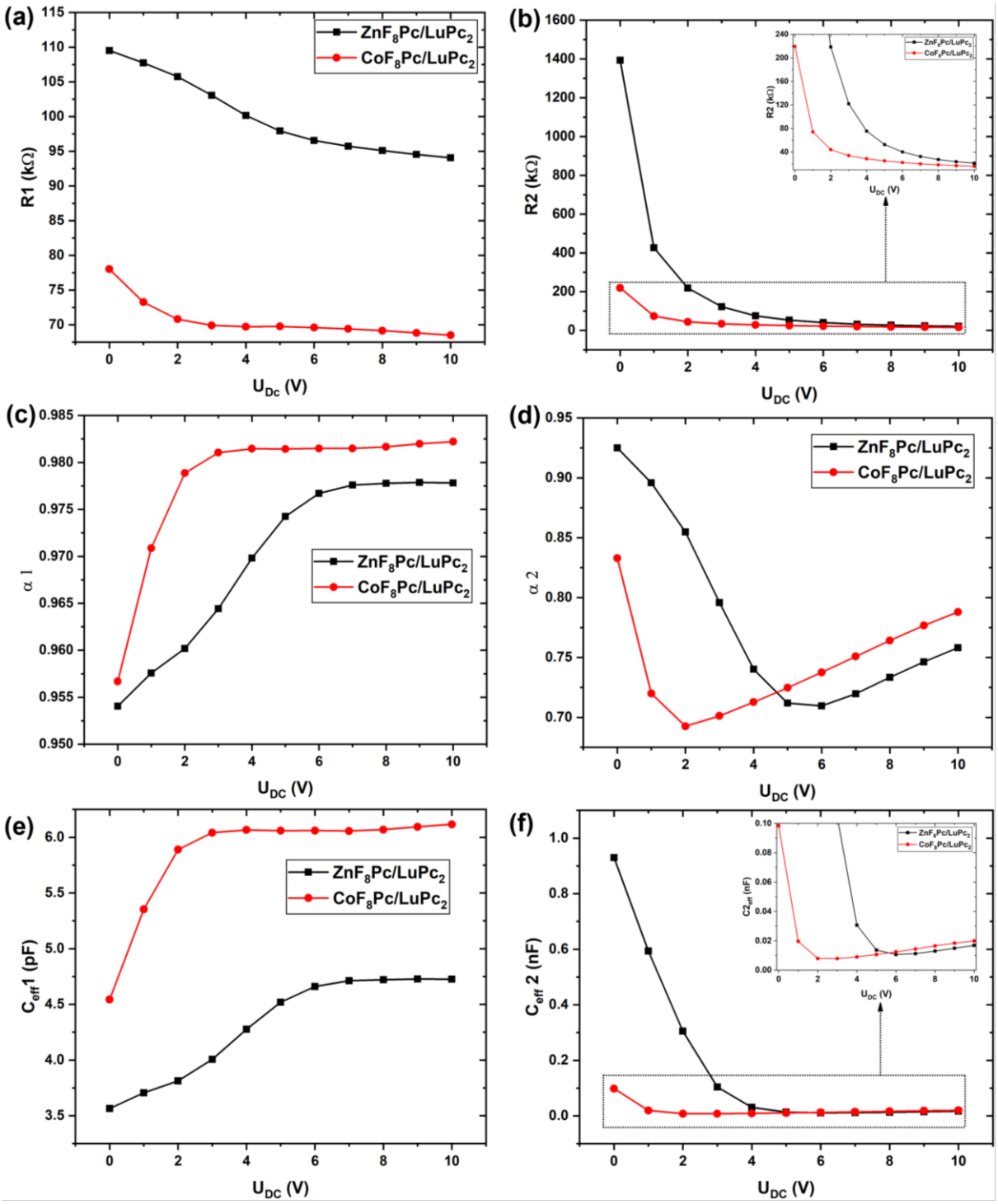

Figure 29. Variations of equivalent circuit resistances, R1 (a) and R2 (b), α1 (c) and α2 (d), effective capacitances $C_{eff}1$ (e) and $C_{eff}2$ (f), as a function of bias voltage (0-10 V) for $ZnF_8/LuPc_2$ and $CoF_8/LuPc_2$ heterojunction devices.

At lower bias levels, the $C_{eff}1$ value of Zn-based heterojunction device is ca. 1.5 times lower than that of the Co-based device. However, the $C_{eff}2$ is ca. ten times higher for Zn-based device, and this difference exponentially decreases with increasing bias until it becomes almost equal at higher bias levels. This can be attributed to the overcoming of the energy barrier at higher bias levels. These measurements further confirmed the distinct electrical properties between devices, which arise from difference in metal centre.

2.2. Gas sensing characteristics of heterojunction sensors

Sensing properties of as-prepared samples were investigated under different gases at different exposure/recovery time periods. Initially the gas sensing responses towards NH_3, NO_2 and O_3 of octafluoro-phthalocyanine-based heterojunction sensors were investigated under long dynamic exposure/recovery (10/30 min) time periods, at high gas concentration of 90 ppm, 900 ppb and 300 ppb, respectively, at room temperature. Except for ozone sensing experiments, we used dynamic exposure followed by static recovery. For O_3, since molecules are highly unstable, they can be easily destroyed by interacting with solid surface and recovery occurs by simply stopping gas flow [165].

Under exposure to NH_3, $ZnF_8Pc/LuPc_2$-based heterojunction sensor exhibits negative response (current decrease) upon NH_3 exposure, while increase in current was observed during recovery period, which depicts the heterojunction's p-type nature by considering ammonia as an electron donating species (**Figure 30a**). On the other hand, the device with Co as a central metal exhibits positive response towards NH_3 (current increase), which reveals its n-type nature (**Figure 30b**). **Equation (6)** and **(7)** explains current decrease for p-type and current increase for n-type materials, respectively.

$$MPc_2 + NH_3 \rightarrow MPc_2^{-} + NH_3^{+} \qquad (7)$$

The sensors made up of similar macrocycle organic complexes exhibit opposite sensing behaviour because of the influence of the metal centre on the electrical properties of phthalocyanine complexes.

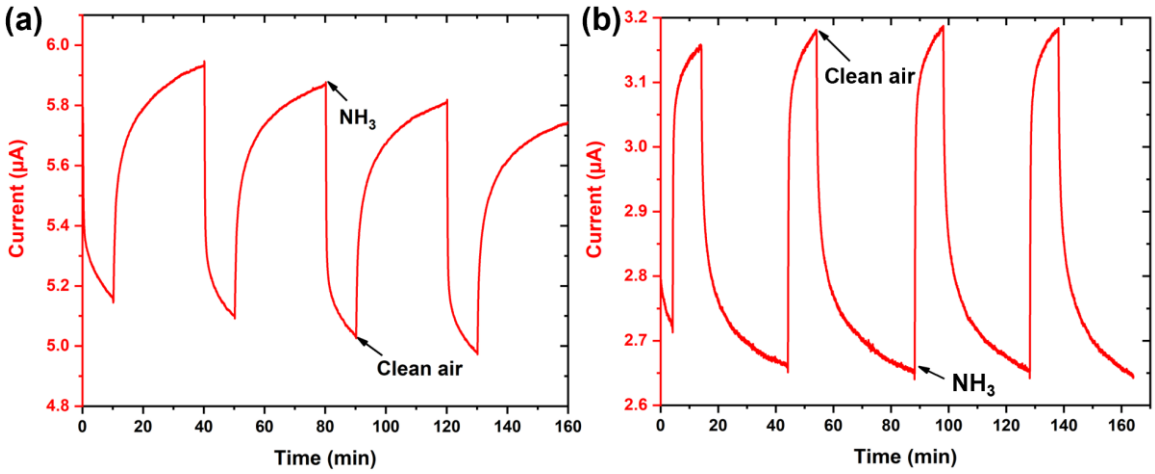

Figure 30. Response curve of $ZnF_8Pc/LuPc_2$ (a) and $CoF_8Pc/LuPc_2$ (b) heterojunction sensors, under successive exposures to 90 ppm NH_3 for 10 min and recovery under clean air for 30 min at 45% RH and room temperature (18 – 19 ˚C).

Beyond the shadow of a doubt, changing the metal centre will create a slight shift in the frontier molecular orbitals of MF_8Pc macrocycle, which greatly influences the nature of majority charge carrier density in the devices. Zinc is typically found in +2 oxidation state in coordination complexes, which has lowest electronegativity compared to Cu^{2+} and Co^{2+}. When Zn(II) coordinates with a ligand, it stabilises less the electron density in the macrocycle, which leads to the shift in HOMO to higher level. Hence it makes easier to inject an electron from HOMO to Fermi level of the electrode, exhibiting p-type behaviour. On the other hand, cobalt can typically exist in various oxidation states, most commonly in 2+ or 3+ states. Compared to ZnF_8Pc, frontier molecular orbitals are more stabilized in CoF_8Pc, which allows more easily to inject an electron from Fermi level of electrodes into the LUMO. Hence, it exhibits n-type behaviour under NH_3 exposure. At the same time, it is important to note that $LuPc_2$ is the only

common layer in both sensors that can interact with gas molecules. Thus, the electron transfer takes place between gas molecules and $LuPc_2$, which leads to a change in charge carrier density in the top layer. Moreover, $LuPc_2$ complex, due to its high conductivity, related to its radical nature, with a huge density of electrons and holes near equilibrium compared to many other MPcs. Hence, $LuPc_2$ can be oxidised and reduced quite easily depending on target gas. The unique properties of $LuPc_2$ give free access to sublayer to decide the polarity of the device [9].

When $ZnF_8Pc/LuPc_2$ heterojunction sensor is exposed to oxidation gases like NO_2 (900 ppb) and O_3 (300 ppb), which are strong oxidation gases, it shows current increase, displaying its stable p-type nature (**Figure 31a** and **31b**). Most surprisingly, when $CoF_8Pc/LuPc_2$ heterojunction sensor is exposed to oxidation gases, the device immediately changed its polarity from n- to p-type, thus exhibiting current increase under oxidizing species (**Figure 31c** and **31d**). Under both oxidizing and reducing gases, Zn complex-based sensor exhibits p-type nature, but Co complex-based sensor exhibits n-type behaviour under electron-donating gas and p-type behaviour under oxidizing gas. This change in polarity depends on the nature of the target gases, exhibiting another type of the ambipolar behaviour, compared to the light effect above mentioned for $CuF_8Pc/LuPc_2$ heterojunction. Moreover, the baseline current of both sensors is highly stable under all three gases, except for $CoF_8Pc/LuPc_2$ under NO_2 exposure, that shows a slight shift in baseline cycle after cycle. Anyhow, it is worthy to mention that the sensor recovered more than 95% of its signal during desorption period.

Under electron donating species, electrons become majority charge carriers; therefore the heterojunction sensor behaves as n-type. However, under hole donating (oxidizing) species, holes become majority charge carriers, leading to a p-type behaviour. Globally, whether it is an electron donating or withdrawing gas, $CoF_8Pc/LuPc_2$ based sensor shows current increase under exposure in the atmospheric conditions of the experiment. The quasi-equilibrium state between

positive and negative charge carriers allows for a free access to polarity change depending on external trigger that is herein the target gas[89]. This unique property is made possible because both charge carrier densities are almost equal. Very few molecular material-based gas sensors were reported in literature, with this behaviour under different gas species (**chapter 1**)[56].

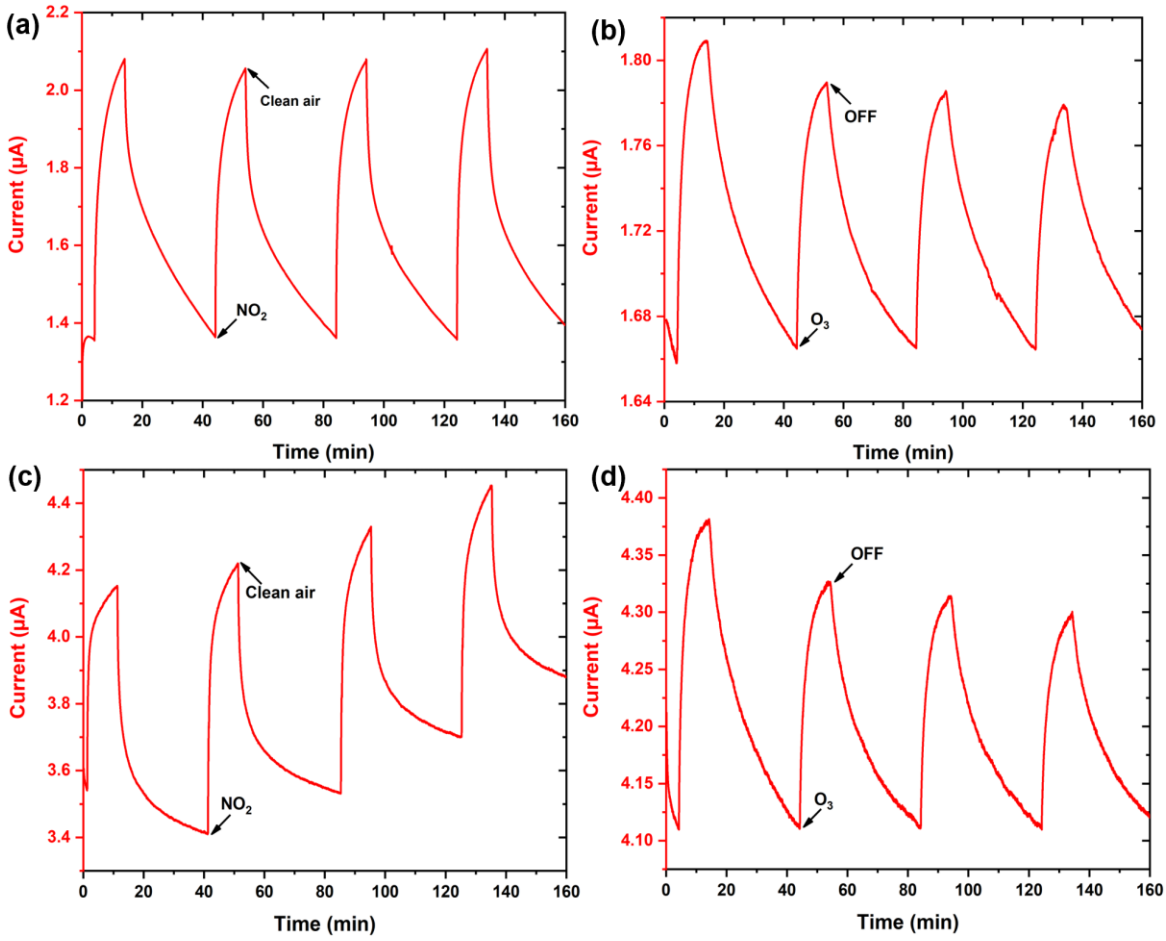

Figure 31. Response curve of $ZnF_8Pc/LuPc_2$ (a and b) and $CoF_8Pc/LuPc_2$ (c and d) heterojunction sensors under successive exposures to 900 ppb of NO_2 (a and c) and 300 ppb of O_3 (c and d) for 10 min followed by dynamic recovery (under clean air) and static recovery (without any flow) for 30 min for NO_2 and O_3, respectively, at 45% RH and room temperature (18 – 19 ˚C).

The gas sensing properties of both sensors were further studied by testing them under a wide range of gas concentration, from 90 ppm to 1 ppm, 900 to 100 ppb and 100 to 20 ppb of

NH_3, NO_2 and O_3, respectively **(Figure 32**). Both sensors exhibit clear and observable response experimentally, even at low concentration of target gases, with very low noise.

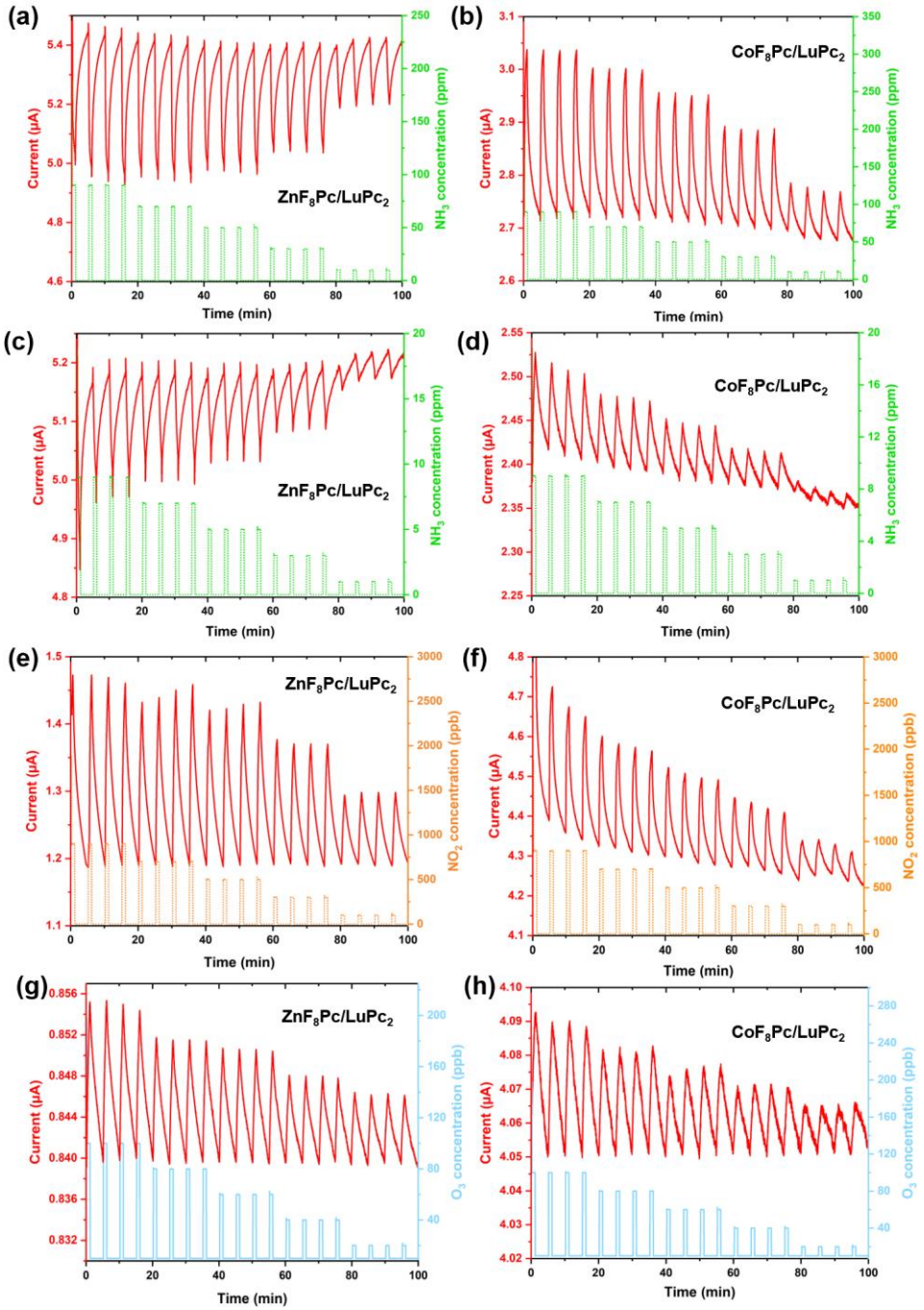

Figure 32. Response curve of $ZnF_8Pc/LuPc_2$ (a, c, e and f) and $CoF_8Pc/LuPc_2$ (b, d, g and h) heterojunction sensors under 90 to 1 ppm of NH_3, 900 to 100 ppb of NO_2 and 100 to 20 ppb of O_3, respectively, under dynamic exposure/recovery for NH_3 and NO_2 and dynamic exposure/static recovery for O_3, at 45% RH and room temperature (18 – 19 $^{\circ}$C).

The response curves of the sensors under both oxidizing and reducing gases were highly reversible and repeatable. Similar variations in current are observed in four consecutive exposure/recovery cycles recorded at each concentration. As quantitative measurement, relative response (RR) of both sensors was calculated using **equation (4)**. The RR variation as a function of gas concentration of $ZnF_8Pc/LuPc_2$ and $CoF_8Pc/LuPc_2$ heterojunction sensors was displayed as calibration curves in **Figure 33**. The uncertainties of the sensors were included as error bars in calibration curves. It is mesmerising to note the stability and reproducibility of both sensors, particularly the bistability of the CoF_8Pc-based sensor in an extended range of gas concentration.

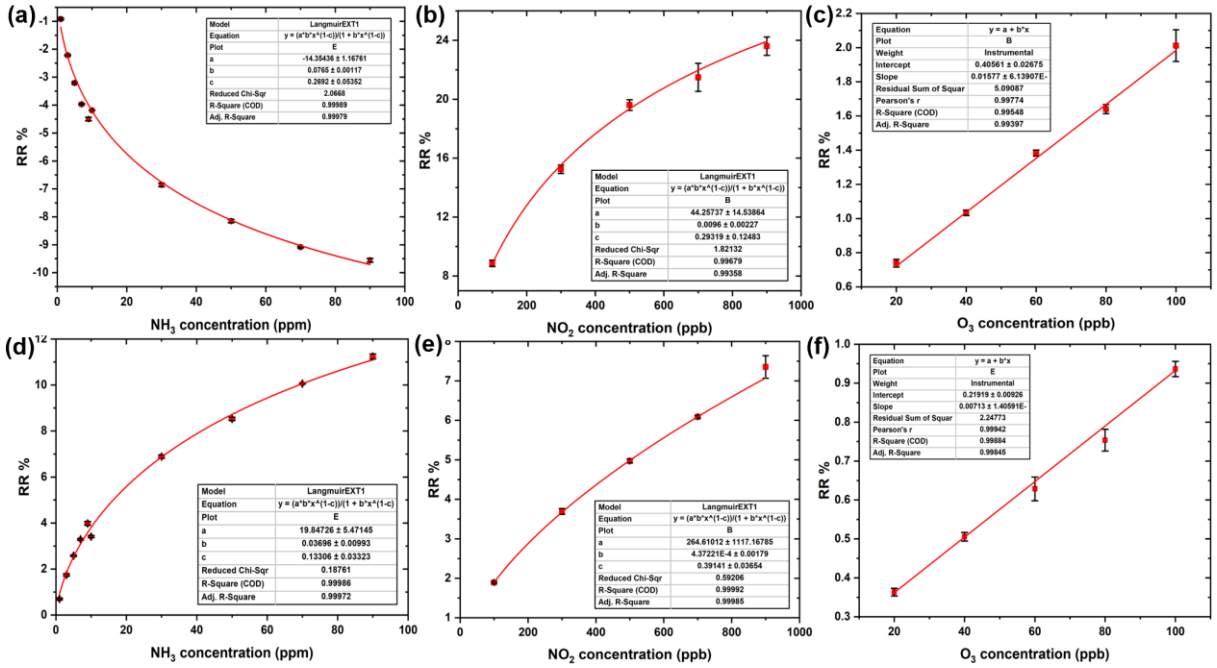

Figure 33. The variation of relative response (calibration curve) of $ZnF_8Pc/LuPc_2$ (a–c) and $CoF_8Pc/LuPc_2$ (d–f) heterojunction sensors, as a function of gas concentration, for NH_3, NO_2 and O_3.

Notably, the calibration curves show different profiles depending on the target gases. Under NH_3 and NO_2, they are not linear and fit accurately with the Langmuir's equation. Therefore, the interaction of NH_3 and NO_2 gas molecules on sensor's surface obeys Langmuir

type adsorption, in which the number of adsorption sites is limited. At high concentrations, NH_3 or NO_2 gas molecules almost occupied all the available adsorption sites leading to saturation in the sensor signal. However, the calibration curves of both devices towards O_3 show curves that are fitted precisely with linear equation. It is well known that ozone is highly unstable molecule, which can be easily destroyed at the moment it interacts with any surface. It gets destroyed into diatomic and nascent oxygen at the moment it touches the sensing material [165]. Unlike other gases, with ozone there is no such phenomenon called adsorption and diffusion. So, ozone reacts only with the surface of the top layer, and enough sites are available on the surface of the sensors for O_3 to react, so the RR linearly increases as a function of gas concentration in the studied range. Using the **equation (5)**, we estimated LOD for both the heterojunction sensors. The sensitivity of the $ZnF_8Pc/LuPc_2$-based sensor was determined as S= -0.655% ppm^{-1}, S= 0.032% ppb^{-1}, and S= 0.0767% ppb^{-1} for NH_3, NO_2, and O_3, respectively. In the case of the $CoF_8Pc/LuPc_2$-based sensor, distinct sensitivities were determined for NH_3, NO_2, and O_3 as S= 0.347% ppm^{-1}, S=0.009% ppb^{-1}, and S=0.0176% ppb^{-1}, respectively. These sensitivity values contributed to achieving a LOD of ≈330 ppb, 4.9 ppb, and 0.75 ppb for $ZnF_8Pc/LuPc_2$, and ≈200 ppb, 23 ppb, and 10 ppb for the $CoF_8Pc/LuPc_2$ under exposure to NH_3, NO_2, and O_3, respectively (**Table 2**). Both sensors displayed a LOD below daily exposure limit established by European parliament and World Health Organisation (WHO) for NH_3 (25 ppm), NO_2 (20 ppm) and O_3 (60 ppb) as long term exposure (8 h)[119, 166].

Table 2. Comparison of sensitivity and LOD of $ZnF_8Pc/LuPc_2$ and $CoF_8Pc/LuPc_2$ heterojunction devices under different target gases.

Device	NH_3			NO_2			O_3		
	S (% ppb^{-1})	LOD (ppb)	Range (ppm)	S (% ppb^{-1})	LOD (ppb)	Range (ppm)	S (% ppb^{-1})	LOD (ppb)	Range (ppm)
$ZnF_8Pc/LuPc_2$	-0.655	330	1-3	0.032	4.9	100-300	0.076	0.75	20-100
$CoF_8Pc/LuPc_2$	0.347	200	1-3	0.009	23	100-300	0.017	10	20-100

2.3. Humidity effect on electrical and sensing properties

Humidity poses a potential interference, which can highly influence the sensing and electrical properties of the devices[102]. Initially, both heterojunction sensors were investigated under changing relative humidity conditions. **Figure 34** depicts the current measurement of both sensors over time as RH increases from 30% to 60% and monotonically decreases from 60% to 30%.

Both sensors exhibit very low and highly reversible negative response to humidity change, with RR values of ca. -1.6% and –1.0% for ZnF_8Pc-and CoF_8Pc-based heterojunction sensors, respectively. Fluorinated compounds are well known for their hydrophobicity, which explains why the sensor shows reversible and very low sensitivity towards humidity change. Even though the fluorinated layers are covered by $LuPc_2$, it prevents water molecules to attain the interface, which is the main path for charge carriers.

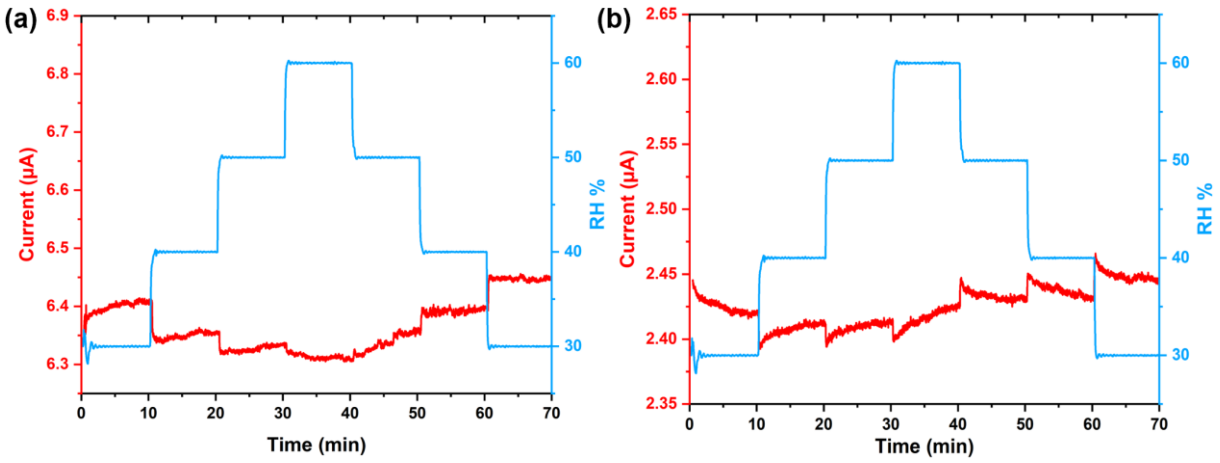

Figure 34. Response curve of $ZnF_8Pc/LuPc_2$ (a) and $CoF_8Pc/LuPc_2$ (b) heterojunction sensors towards RH change in the range of 30% to 60%, at room temperature (18 – 19°C).

It is worth mentioning that in one case (ZnF_8Pc-based sensor) the nature of the effect of humidity is the same as this of NH_3 (current decrease), but for the other (CoF_8Pc-based sensor) it is the oppositive, current increases under NH_3 and decreases when RH is increases. So, the main effect of humidity is not its electron donating effect, but rather its capability to trap the charge carriers. However, when it comes to NH_3 or NO_2 gas sensing applications in humid environment, we have to concern about the acid-base reaction between toxic gases and humidity. Therefore, investigating the response of sensors towards the target gases at different RH levels is essential.

In reality the adsorption of water molecules on the solid surface is a complex phenomenon. Indeed it is true that there is always an equilibrium between adsorbed water molecules and water molecules in environment, but the diffusion effect may differ over time. Moreover, in real environment, humidity value has huge fluctuation from morning to evening, summer to winter and sometimes even more during rainy days. Hence, the as-prepared samples and the samples that have been exposed to humidity for several times may differ in their sensing properties. Thus, prior to gas sensing investigation at different RH values, we exposed the

sensors several times from low (30%) to high (60%) RH values and back to low humidity (repeating the same humidity experiment). However, to keep the samples at ambient condition we always ended the experiments at 30% RH.

In order to study the sensors in real indoor environmental conditions, we strategically varied humidity levels from 60% to 30%. The gas sensing experiments were initiated at a RH of 60%, progressing monotonically in 10% decrements till ambient value (30%). At each humidity value, different gas concentrations (90, 60, 30 ppm of NH_3 and 900, 600, 300 ppb of NO_2) were studied (**Figure 35**). Thanks to their limited sensitivity to humidity variations, both sensors maintained a stable baseline current throughout all the experiments. However, both sensors exhibit different features in sensing properties compared to their as-prepared state.

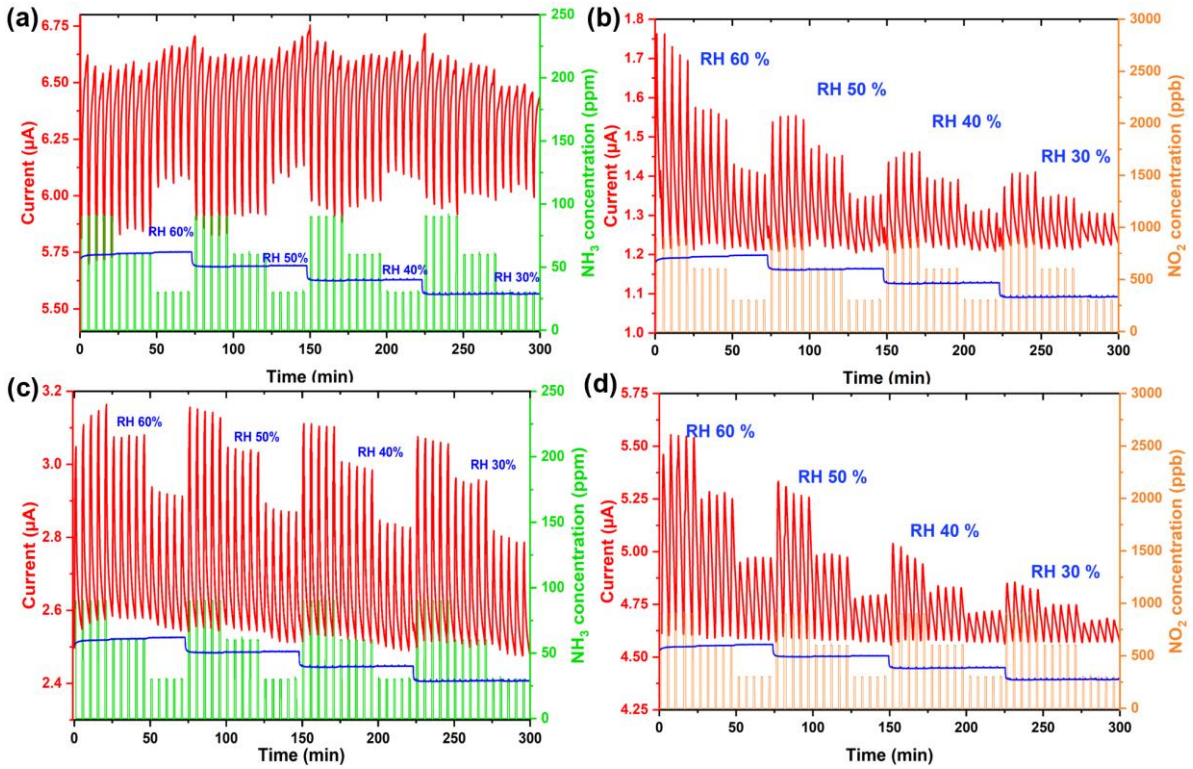

Figure 35. Response curve of $ZnF_8Pc/LuPc_2$ (a and b) and $CoF_8Pc/LuPc_2$ (c and d) heterojunction sensors under exposure of 90, 60, 30 ppm of NH_3 (a and c) and 900, 600, 300

ppb of NO_2 (b and d) in humid air, in the range of 60 to 30% RH, during 1 min exposure followed by 4 min recovery, at room temperature (18 – 19 °C)

Under NH_3, the $CoF_8Pc/LuPc_2$ heterojunction sensor exhibits slight increase in RR from ca. 22% to 23% from 30% to 40% RH change, respectively, at 90 ppm of NH_3, and became stable from 40% to 60% RH values (ca. 23%) (**Figure 36c**). However, it is multiplied by a factor of 2 when compared to its previous conditions (as-prepared samples) at 45% RH. Meanwhile, the absolute RR value of $ZnF_8Pc/LuPc_2$-based sensor increases from ca. 10% to 13% at 90 ppm with increasing humidity from 30% to 60% (**Figure 36a**), which almost agrees with RR values of it's as-prepared sample at 45% RH.

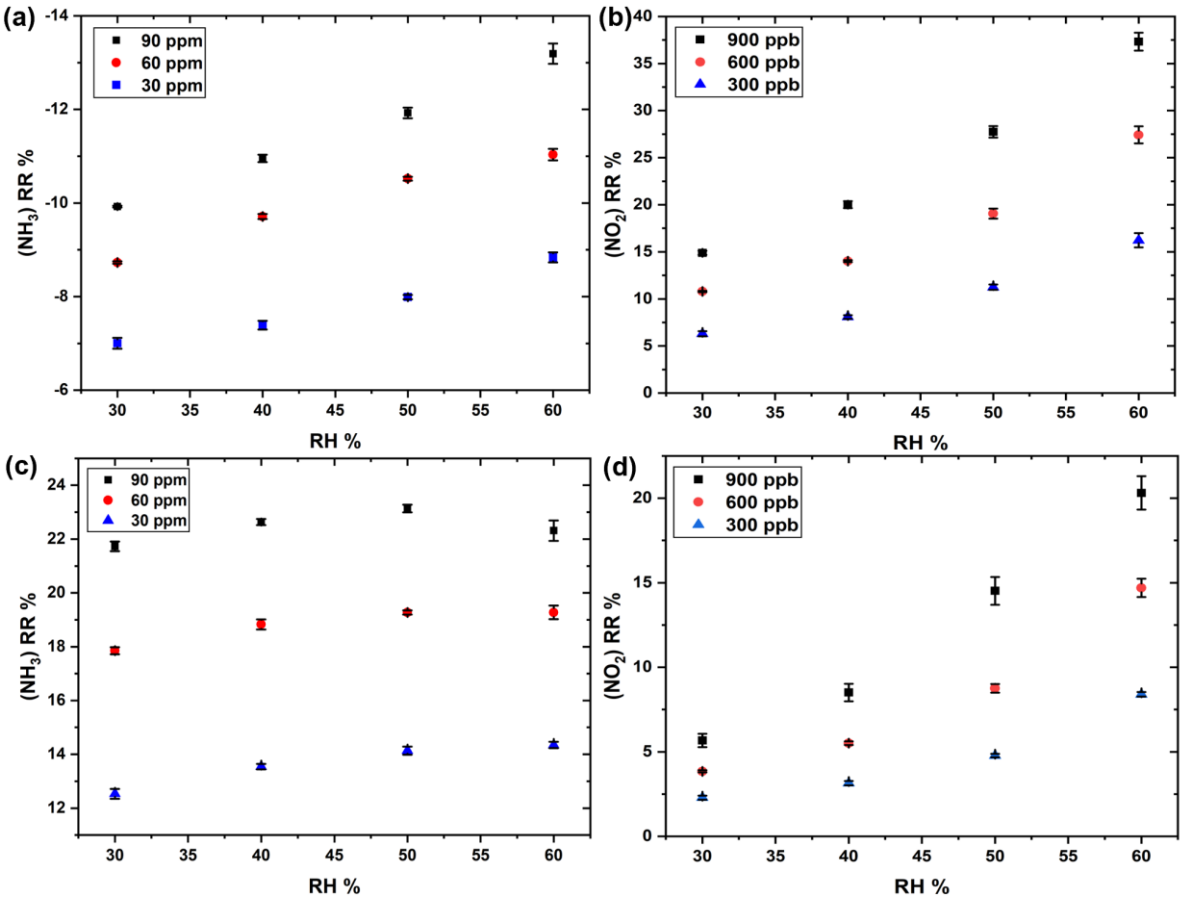

Figure 36. The variation of relative response towards NH_3 and NO_2 of $ZnF_8Pc/LuPc_2$ (a and b) and $CoF_8Pc/LuPc_2$ (c and d) heterojunction sensors as a function of gas concentration.

On the other hand, under oxidizing gas (NO_2), ZnF_8Pc- and CoF_8Pc-based sensors show an increasing in RR from ca. 14% to 38% and from ca. 5% to 20% (at 900 ppb) with increasing humidity from 30% to 60%, respectively (**Figure 36b** and **36d**). Most interestingly, these values were coexisting with the RR values of as-prepared samples at 45% RH.

Here two main concepts are involved. At first, even though the investigation of target gases were conducted on as-prepared samples at fixed RH value (45%) for long windows, the sensors properties can still experience a transition over time due to the specific interaction with fluctuating humidity, especially when it comes to ammonia sensing, due to its high solubility in water (654 L/L). This can explain why both sensor's responses towards NH_3 became higher after conditioning with varying humidity. The higher response to NH_3 at higher humidity value has been previously observed, e.g. with polypyrrole-phthalocyanine-based chemiresistors[167].

As we said before, the adsorption of water molecules on the solid surface is a complex phenomenon. At high humidity level, a molecular film of water in liquid form can develop on the surface of the sensors. The target gases are more likely to get dissolved in the molecular film of water through an acid-base reaction, generating ions, which can participate to the current in the sensing layer[168]. On the other hand, at low humidity value, hydrogen-bonded icelike network of water is formed, where there is no dissolution of gas. In the contrary, water molecules compete with target gas to occupy active adsorption sites on the sensor surface. Such event results in diminishing the RR value.

When we consider the acid-base reaction between target gases and water, most likely at high humidity level, since NH_3 has high solubility, it can easily get dissolved in H_2O molecule and forms aqueous ammonia, which is a weak base in nature. Here, the CoF_8Pc-based sensor became highly stable after humidity conditioning step, hence it is not affected anymore by this weak basic reaction, while ZnF_8Pc-based sensor shows increasing response in increasing

humidity. Meanwhile, reaction between nitrogen dioxide and water is very slow due to the weak solubility of NO_2 in water (0.27 L/L), compared to this of NH_3. This is the main reason why the RR values of as-prepared samples and the RR values of the samples, which undergoes multiple humidity testing agree with each other.

However, NO_2 is a strong oxidizing gas and even a small amount of dissolution of gas in water can influence the response of the sensors. Thus from lower (30%) to higher (60%) humidity, RR of both sensors were multiplied by ca. 3 times. It clearly shows that both sensors were highly sensitive to the small dissolution effect of NO_2 in water. It is also the reason why the sensor's uncertainties (error bars in calibration curves) were higher at high concentration of target gases and humidity, which become negligible at low concentration. Anyhow, it is noteworthy to mention that the electrical properties of the samples were preserved even after multiple exposures to NH_3 and NO_2, which confirms that no damage occurred on the device due to acid-base reaction at given concentration of target gases and humidity values. For ozone the effect is different. Ozone can react with conjugated molecules to give oxidation products. However, the previous findings show that only few Å thickness of a phthalocyanine layer, ca. 50 Å have been degraded under exposure to 1 ppm for long term (17 h)[165]. This is the reason why indigo was used as a filter in NO_2 sensors for eliminating O_3[169], to get rid of the interface between these both strong oxidizing gases. Considering the ozone sensors operate in the range 10–100 ppb, with a partial time exposure, degradation of the sensing layer should be considered only at the scale of the months.

2.4. Investigation of temperature effect around ambient condition

Much like humidity, temperature fluctuations also can significantly impact the sensing properties of gas sensors, particularly in organic semiconductors. Even minor temperature variations have the potential to alter the entire operational profile of these sensors. Therefore

gas sensors, which claimed to operate at room temperature, need a detailed investigation around the working temperature. Hence, we examined the impact of slight temperature variations around ambient conduction (19, 22, 25 and 30 °C) on both octafluoro-phthalocyanine-based gas sensors. To comprehend this influence, we exposed our sensors to a low concentration of NH_3 (20 ppm) in humid air (45% RH), at various temperatures, for 1 min/4 min exposure/recovery time periods (**Figure 37a** and **37c**).

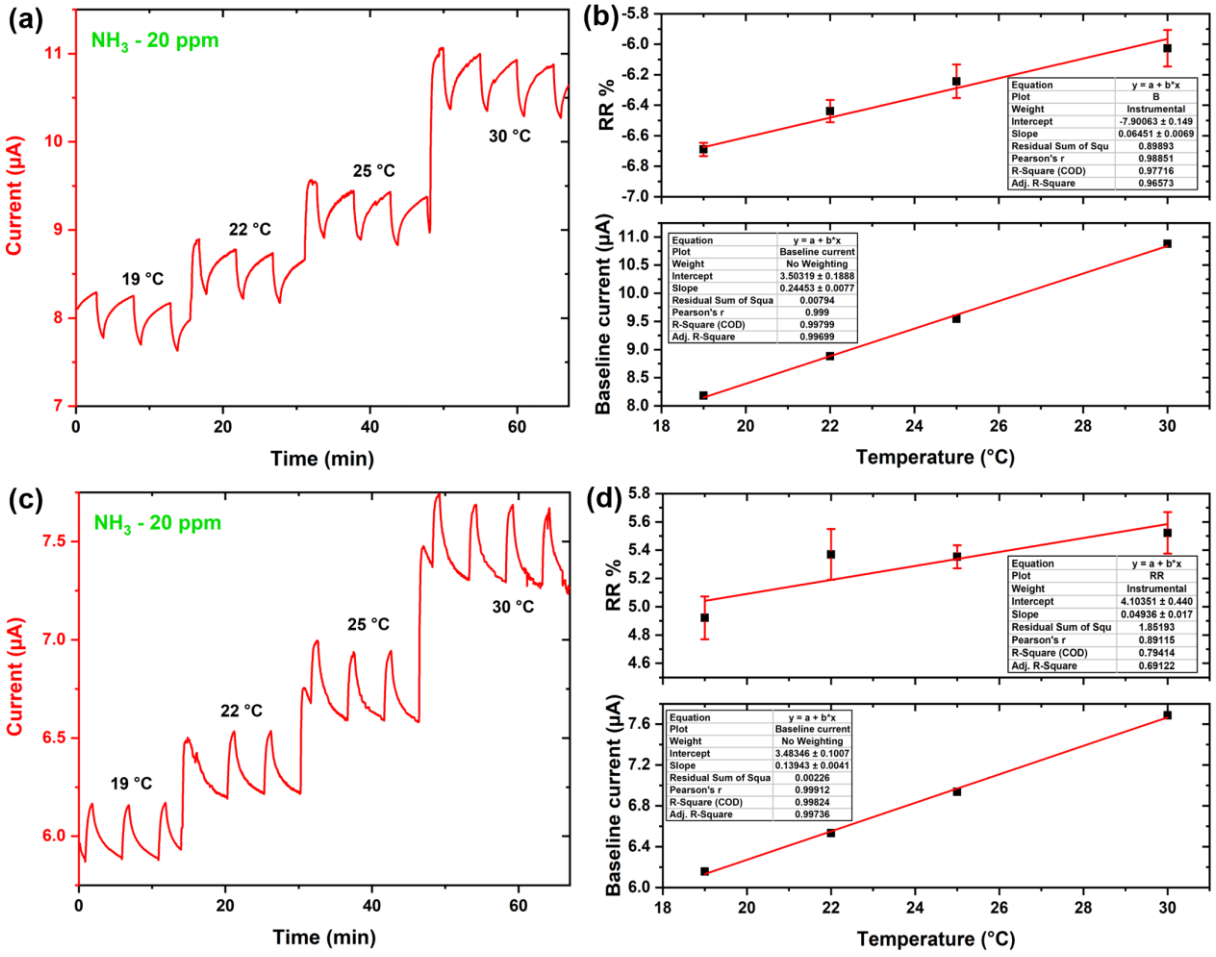

Figure 37. Response curve of $ZnF_8Pc/LuPc_2$ (a) and $CoF_8Pc/LuPc_2$ (c) heterojunction sensors under exposure of 20 ppm of NH_3 in humid air (45% RH), at different temperature, during 1 min exposure followed by 4 min recovery. The variation of relative response and baseline current of $ZnF_8Pc/LuPc_2$ (b) and $CoF_8Pc/LuPc_2$ (d) heterojunction sensors as a function of temperature.

Both heterojunction sensors show increasing in baseline current, as expected for electronic devices, with increasing in temperature from 19 to 30 °C. In $ZnF_8Pc/LuPc_2$-based sensor, baseline current and current variation were increased from +8.2 µA to ca. +11 µA and -0.55 µA to -0.64 µA, respectively. However, the absolute RR value decreases from -6.7% to -6.1% (**Figure 37b**). Meanwhile, for $CoF_8Pc/LuPc_2$-based sensor, baseline current and RR were increased from +6.2 µA to +7.8 µA and +4.9% to +5.5%, respectively (**Figure 37d)**. The baseline current of Zn and Co-based devices is multiplied by 1.4 and 1.2 times from 19 to 30 °C, respectively, and the relative thermal variation of RR of $ZnF_8Pc/LuPc_2$ and $CoF_8Pc/LuPc_2$-based sensors, in this temperature range is given by the following equation.

$$\frac{\Delta RR_T}{RR_T} = \frac{RR\ finial - RR\ initial}{RR\ initial} \qquad (7)$$

The thermal variation of RR per Celsius degree can be calculated by dividing the equation by ΔT.

$$\frac{\frac{\Delta RR}{RR} \times 100}{\Delta T}\ (in\ \%\ per\ °C) \qquad (8)$$

It is indeed true that both sensors experienced a shift in baseline current and relative response, which is often observed in conductometric gas sensors due to thermally induced charge carriers and accelerated sorption (adsorption and desorption) kinetics at higher temperature. For Co-based sensor, current variation increases more than the baseline current leading to an increase in RR, by 12% from 19 °C to 30 °C. It is opposite for Zn-based sensor, leading to a RR decrease by -9.8%. These values correspond to ca. 1% $°C^{-1}$ for both sensors.

Conducting a thorough investigation into the effect caused by humidity and temperature variations around working conditions is a very important stage in metrology that has never been reported previously. Implementing these sensors in an array, assisted with temperature and

humidity sensors, could make them suitable for real-world applications in indoor environmental monitoring. For better understanding and to take advantage of a sensor array, we also conducted NO_2 sensing experiments on a few year old $CuF_{16}Pc/LuPc_2$ sensor kept in the dark, in dry atmosphere and at room temperature, which has been already studied for NH_3 and O_3 sensing[9]. As expected, it exhibits a negative response to NO_2 and O_3 and positive response to NH_3, which indicates its stable n-type behaviour under both oxidizing and reducing species. The experimental curve of $CuF_{16}Pc/LuPc_2$ under NO_2 (200 ppb) has been shown in **Figure 38**.

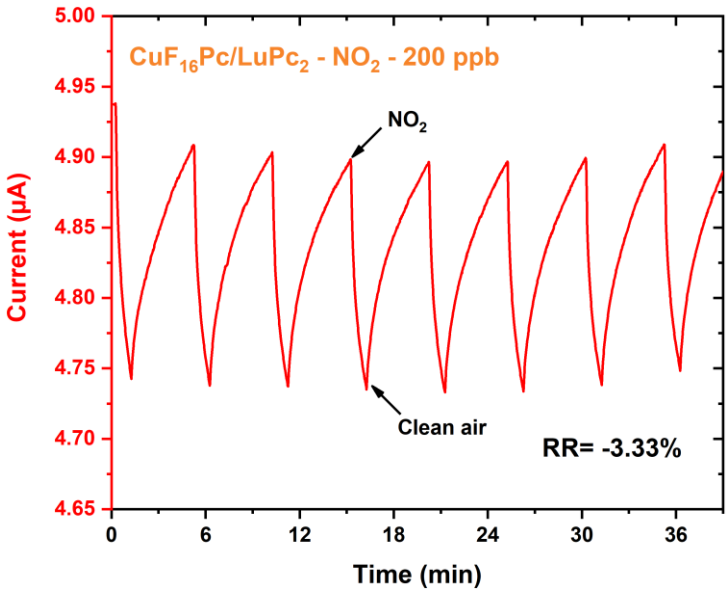

Figure 38. Response curve of $CuF_{16}Pc/LuPc_2$ heterojunction sensor under 200 ppb of NO_2, at ambient conditions (19 $^{\circ}$C and 45% RH).

Comparison table of all these sensors under different gas species is given in **Table 3**. Green colour downwards arrow indicates a negative response (current decrease) and red colour upwards arrow indicates a positive response (current increases) under target gas. Combining ZnF_8Pc (p-type) and $CuF_{16}Pc$ (n-type)-based sensors with CoF_8Pc (ambipolar)-based sensor will make a powerful tool to analysis the target gas species more accurately even in sub ppm range.

Table 3. Current change under NH_3, NO_2 and O_3. Upward arrows represent current increase and downward arrows represent current decrease.

Gas / Sensor	NH_3	NO_2	O_3	Reference
$ZnF_8Pc/LuPc_2$	▼	▲	▲	This work
$CoF_8Pc/LuPc_2$	▲	▲	▲	This work
$CuF_8Pc/LuPc_2$	▼	▲	▲	10
$CuF_{16}Pc/LuPc_2$	▲	▼	▼	9

2.5. Short conclusion

$ZnF_8Pc/LuPc_2$ sensor exhibits its stable p-type nature under both oxidizing and reducing gases, while $CoF_8Pc/LuPc_2$ sensor demonstrates n-type behaviour under reducing gas (NH_3) and p-type behaviour under oxidizing gases (NO_2 and O_3), exhibiting its ambipolar nature and bistability across a wide range of gas concentrations. Both sensors exhibit very good LOD towards all three gases. Utilizing these sensors in an array combined with a stable n-type device ($CuF_{16}Pc/LuPc_2$) will create a powerful tool for distinguishing and analysing target gases with a greater precision. However, further studies are needed to realise ambipolar devices in real life applications.

3. VOF_8Pc-based ambipolar device – In-depth study of ambipolar charge transport regime through external triggers and gas sensing

In this section, we discussed about the electrical and sensing properties of VOF_8Pc-based bilayer heterojunction sensors under different gas species and experimental conditions. The key novelty of this study lies in the in-depth examination of polarity inversion in ambipolar device from n- to p-state or vice versa, through zero state (no response) upon different external triggers, which has never been reported. Furthermore, our investigation delves into elucidating the factors influencing the polarity of the ambipolar device due to variations in humidity and temperature.

3.1. Current measurement during deposition and oxygen effect

Throughout the deposition process of both layers onto the ITO-IDE substrate, we continuously monitored the flow of electric charges across the sample by applying a voltage of 3 V. This measurement was continued from the bare ITO-IDE to the formation of the heterojunction device, aiming to understand the electrical properties of the materials and their dependency on thickness on the ITO-IDE substrate (**Figure 39**).

The sublayer exhibits poor conductivity, as evidenced by very low and noisy signal throughout its deposition process, up to a thickness of 50 nm. However, upon initiation of the $LuPc_2$ deposition over the sublayer, a notable decrease in signal noise (i.e. from A), then a sharp increase in current is observed (i.e. in B).

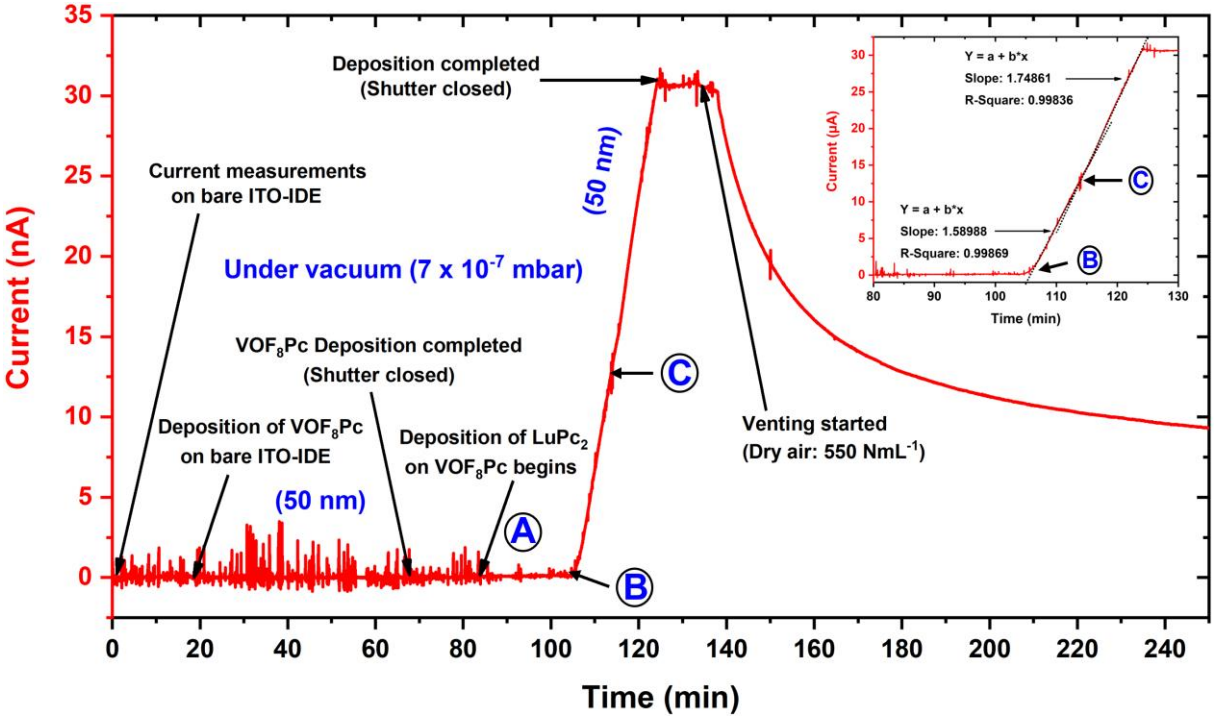

Figure 39. Current measurement during deposition process. The inset shows a zoomed view of the change in slope. The letters A, B, and C represent different singular points: A indicates a decrease in signal noise, B shows a sharp increase in current, and C denotes the change in slope.

This increase follows a linear trend during ca. 20 min of $LuPc_2$ deposition, reaching thickness around 150 to 240 Å, indicating the establishment of a conducting channel. Subsequently, above ca. 250 Å, there is a change in i(t) slope (i.e. in C phase), suggesting total surface coverage by $LuPc_2$, which continued until the shutter closed at 500 Å. A zoom was added as inset in **Figure 39** for better visibility of the change in slope.

3.2. Effect of oxygen

After the deposition process, the vacuum chamber of the thermal evaporator was vented with dry air to investigate the solely effect of oxygen without interference of humidity on the electrical properties of the resulting device. Subsequently, the current exhibited an exponential

decay upon exposure to oxygen, consistent with the n-type behaviour of the device, since oxygen neutralizes negative charge carriers. To delve into this effect, we conducted cyclically pumping and venting of the chamber while continuously measuring the current change. Notably, during the pumping phase, the heterojunction sensor demonstrated a positive response, indicative of increased conductivity, whereas a decrease in current was observed during the venting period. This experimental observation provides further confirmation of the n-type nature of the device (**Figure 40**).

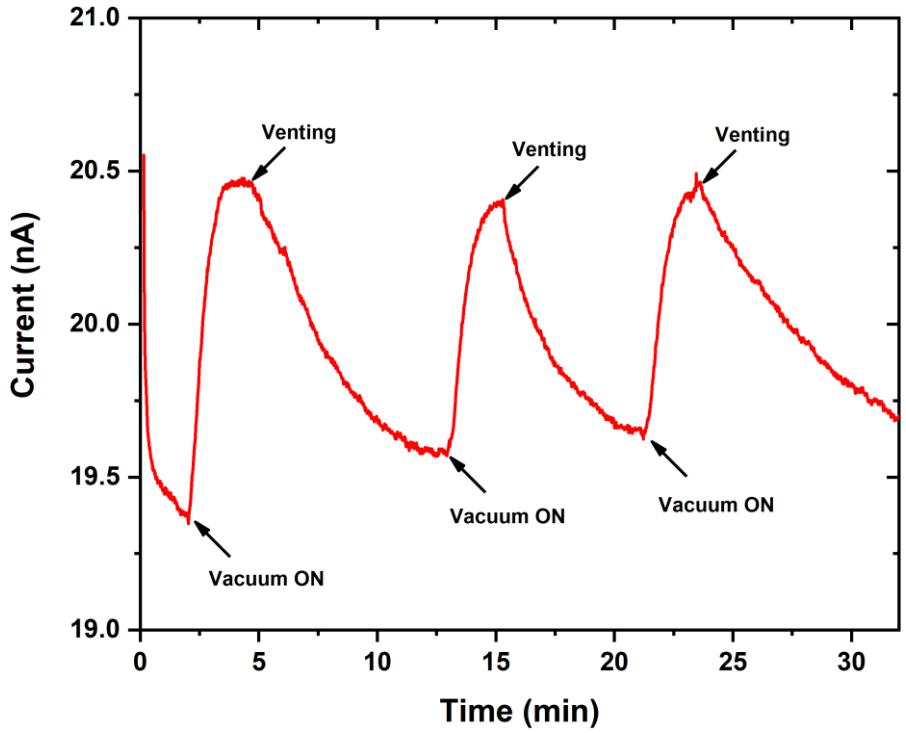

Figure 40. Effect of oxygen on $VOF_8Pc/LuPc_2$ heterojunction device.

3.3. Electrical properties of the device under different conditions.

To explore the impact of diverse atmospheric surroundings on the electrical characteristics of the heterojunction device, we performed I-V measurements by applying a potential difference across the device, varying from -10 to +10 V, under different conditions. Initially, we conducted the I-V experiments under secondary vacuum (ca. 7 x 10^{-7} mbar),

followed by exposure to 45% Relative Humidity (RH), NH_3 (90 ppm), NO_2 (900 ppm), and red-light illumination and under heating condition (80 °C) (**Figure 41**).

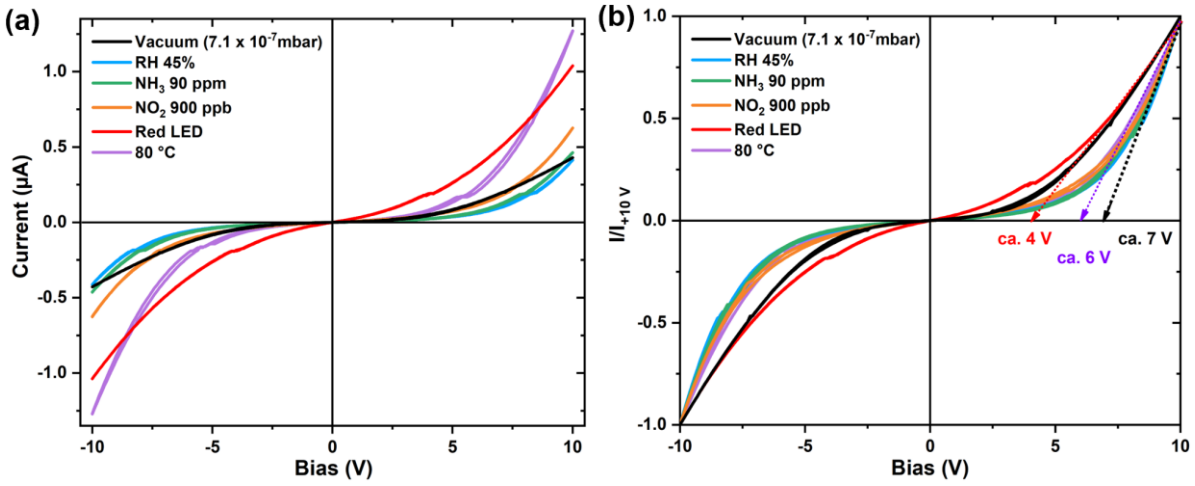

Figure 41. I-V characteristics of the heterojunction device under different atmospheric conditions (a) and their normalized view (b).

It is noteworthy that under all conditions, the device exhibits non-linear and symmetrical I-V curve. As discussed before, the non-linearity is characteristic of bilayer heterojunction devices composed of materials with different work functions, originating from the accumulation of mobile charges at the interface. However, the degree of non-linearity is intricately linked to the formation of the interface between the organic layers and to the charge transport resistance in both layers [102]. I-V curves allow comparing current values in the different conditions (**Figure 41a**). The normalized I-V characteristics, obtained by plotting I (V)/$I_{+10\ V}$ as a function of bias offer a clear perspective on realizing the apparent energy barrier of the device under various conditions (**Figure 41b**).

In current scenario, the resistivity of the sublayer is very high compared to this of $LuPc_2$, resulting in low current (ca. 0.4 µA at +10 V) and high U_{th} values (7 V) under ambient conditions. Compare to other two octafluorinated-metallophthalocyanines-based devices (Zn and Co), VOF_8Pc-based device has the highest U_{th} value in ambient conditions. When the

device is exposed to NH_3 and NO_2, the current at +10 V increases to ca. 0.45 µA and 0.6 µA, respectively. However, these gases do not affect the apparent energy barrier of the heterojunction device. Surprisingly, under secondary vacuum (ca. 7 x 10^{-7} mbar) and red-light illumination the U_{th} values roughly halved compared to other conditions. However, the current at +10 V under red-light illumination is ca. 1 µA, significantly higher than the current under secondary vacuum (ca. 0.4 µA), although they share similar U_{th} values. Interestingly, the current value at +10 V under vacuum coincides that under ambient conditions, but with a lower U_{th} value (ca. 4 V). Finally, when the device temperature is increased to 80 °C, the current at +10 V rises to ca. 1.3 µA, and the apparent energy barrier is modified to ca. 6 V. These values are summarized in the **Table 4** for better understanding.

Table 4. Comparison of current at +10 V and apparent energy barrier U_{th} under different experimental conditions.

Conditions	Current at +10 V (µA)	Apparent energy barrier U_{th} (V)
Vacuum (7.1 x 10^{-7} mbar)	0.4	4
RH 45%	0.4	7
NH_3 – 90 ppm	0.45	7
NO_2 – 900 ppb	0.6	7
Red LED	1	4
80 °C	1.3	6

To gain insights into the electrical properties of the heterojunction device and the charge transport regime at the interface, impedance spectroscopy measurements were conducted. A

fixed amplitude of 0.2 V AC signal was applied, covering a wide range of frequencies from 10 Hz to 10 MHz, under various DC bias conditions (ranging from 0 to 10 V). All the impedance spectroscopy measurements were conducted in ambient conditions. The impedance spectroscopy results, as depicted through Nyquist plots showing the imaginary part versus the real part of the impedance, offer valuable insights into the distinct charge transport characteristics observed at the interface and within the bulk of the bilayer heterojunction device (**Figure 42**). Similar to other heterojunction devices, $VOF_8Pc/LuPc_2$ devices also reveal two distinct depressed semicircles, which is a characteristic feature of typical bilayer heterojunction devices.

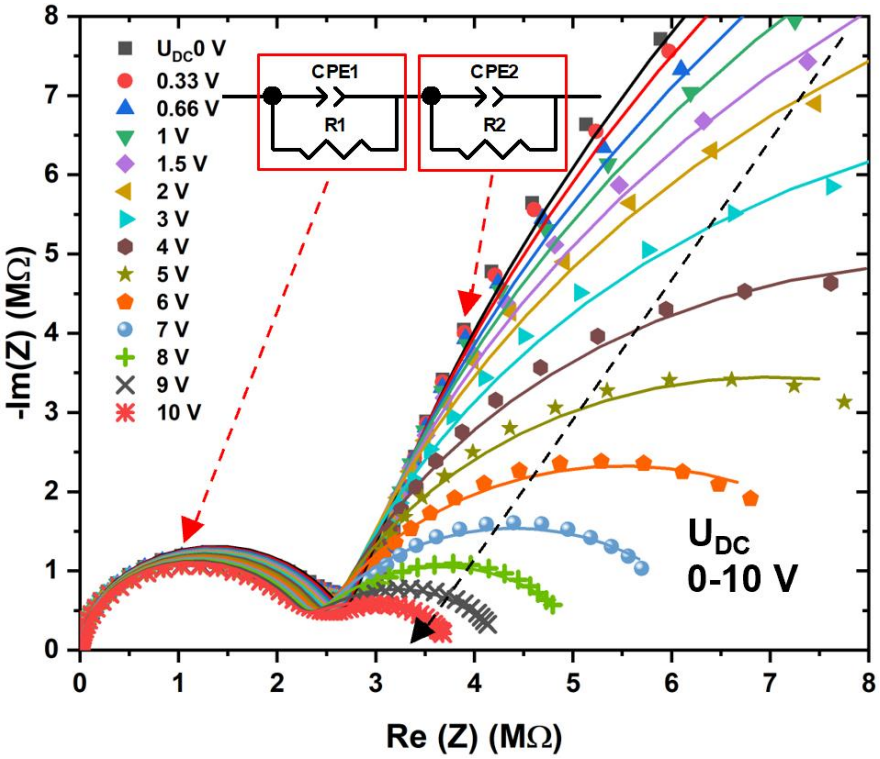

Figure 42. Nyquist plots of VOF_8Pc-based heterojunction device measured at fixed AC (0.2 V) superimposed by variable DC voltage in the range of 0-10 V. The inset shows the equivalent circuit selected for fitting Nyquist plots.

As discussed earlier, under AC mode (DC 0 V), without any steady state voltage in the circuit, the semicircle in LF region of the Nyquist plot appears larger. However, with the introduction of an increasing DC voltage superimposed to the AC signal, the injected charges started to overcome the energy barrier, because of the increasing charge density at the organic-organic interface channel. This is observable as a diminishing semicircle in the LF region of the Nyquist plot. Most interestingly, the difference in size of both semicircles continuously decreases with increasing DC bias and became almost equal between applied bias of 7 V and 8 V, indicating the arrival of equal density of mobile charges at the interface compared to the charge density within the bulk medium. However, further increases in bias lead to further decreases in LF semicircle. Notably, even at DC +10 V, the device exhibits two distinct semicircles that confirms the high value of the energy barrier, which is not totally overcome even at +10 V. As we did for other heterojunction devices, the experimental Nyquist plots were fitted with constant phase element (CPE) based circuits[108] using **equation (2)** and Brug's relationship[106] **equation (3)**. The variation in bulk charge transport (R1, α1, and $C_{eff}1$) and interfacial charge transport (R2, α2, and $C_{eff}2$) with DC bias are depicted in **Figure 43**.

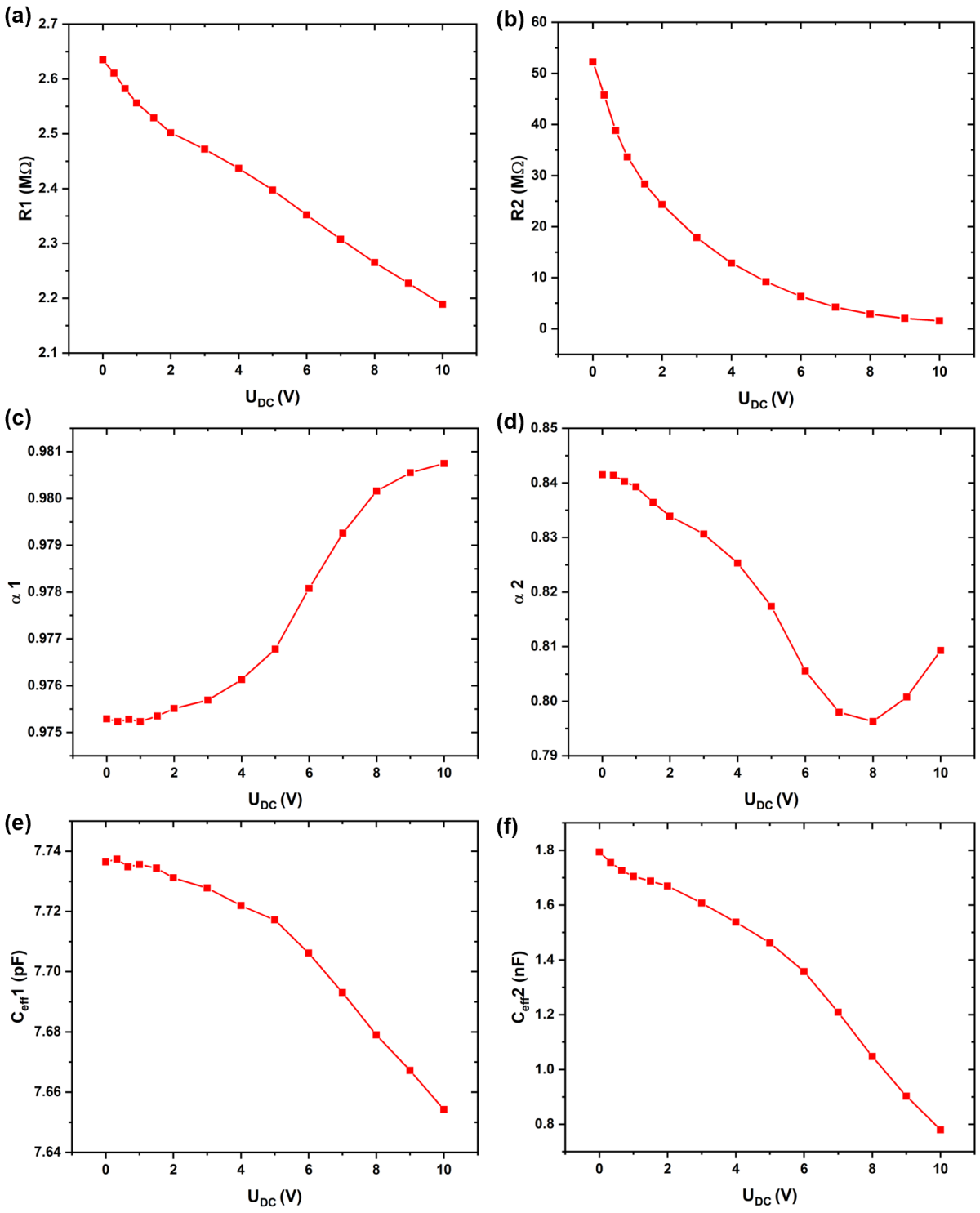

Figure 43. Variations of equivalent circuit resistances, R1 (a) and R2 (b), α1 (c) and α2 (d), effective capacitances $C_{eff}1$ (e) and $C_{eff}2$ (f), as a function of bias voltage (0-10 V).

Similar to other heterojunction devices, the bulk resistance (R1) exhibits minimal dependency on applied bias, showing a slow linear decay from ca. 2.65 to 2.15 MΩ. On the

contrary, the interfacial resistance (R2) displays significant variation, exhibiting an exponential decline, from ca. 55 to 1 MΩ, with increasing DC bias (**Figure 43a and 43b**). Notably, α1 varies with DC bias but remains very near to 1, while α2 decreases from ca. 0.84 to 0.79 when DC increases from 0 to 10 V (**Figure 43c and 43d**). Notably, the $C_{eff}2$ value decreased from ca. 1.8 to 0.78 nF as the DC bias increased from 0 to 10 V, while the $C_{eff}1$ values remained relatively stable at ca. 7.73 pF under minimal DC bias (0 to 1.5 V). Subsequently, it exhibited a quasi-linear decrease down to 7.65 pF with increasing DC bias from 2 to 10 V (**Figure 43e and 43f**).

This behaviour aligns with the fundamental principle of capacitors, where an increase in voltage does not directly change its capacitance. However, higher voltages can generate a stronger electric field at the organic-organic interface, causing the device to conduct electricity. This effect can change the device electrical properties, potentially leading to a decrease in capacitance.[170] Nevertheless, explaining the interfacial charge transport is further complex due to the play of various phenomena. As voltage increases, the density of mobile charge carriers at the interface rises, leading to decrease in heterojunction effect and consequent drops in resistance and capacitance in wide range. Furthermore, the $C_{eff}2$ values were significantly larger in magnitude compared to the $C_{eff}1$ values, ca. 100 times greater. The difference in magnitude is directly linked to the thickness of the layers, as capacitance is inversely proportional to thickness.[171] This huge difference in the capacitance values means that the interface to consider is very thin compared to the thickness of the layers (50 nm).

3.4. Exploring the ambipolarity of the bilayer device through different gaseous species

Initially, the as-prepared sample was investigated under 90 ppm of NH_3, a weak electron donating species, for time periods of 10 min exposure followed by 30 min recovery under clean

air in ambient conditions (18 °C and 45% RH). The device exhibited current increase under NH_3 exposure and decrease during recovery period, which is characteristic of an n-type device (**Figure 44a**). The relative response (RR), defined as the current variation under NH_3 divided by the current in air, was ca. 19.5%. Furthermore, it confirms the measurements recorded during oxygen exposure, when the current decreased upon air entry in the vacuum chamber.

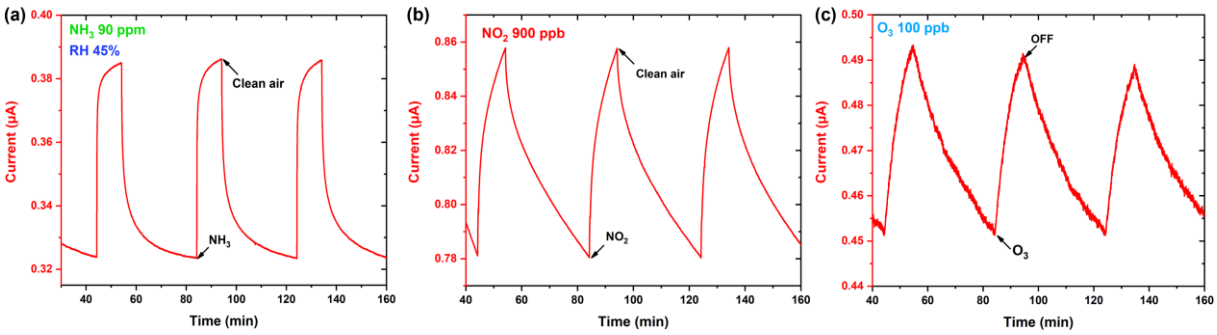

Figure 44. Response curve of $VOF_8Pc/LuPc_2$ heterojunction sensor, under successive exposures to 90 ppm NH_3 (a), 900 ppb of NO_2 (b) and 100 ppb of O_3 (c) for 10 min. This was followed by a dynamic recovery (under clean air) for NH_3 and NO_2, and a static recovery (without any flow) for O_3, each lasting 30 min at 45% RH and room temperature (18 – 19 °C).

However, under the same experimental conditions, upon exposure to 900 ppb of NO_2 and 100 ppb of O_3, both strong oxidizing species, a current increase was also observed, indicating a p-type behaviour (**Figure 44b and 44c**). This inversion of polarity from n-type under NH_3 to p-type under oxidizing species means that the density of negative charge carriers (electrons) and positive charge carriers (holes) were almost at the equilibrium in the device in air, which is similar to our previous findings with CoF_8Pc-based device. Even though it is very unusual, a few examples have already been reported by Y. Chen, with phthalocyanine-based resistors and field-effect transistors[82, 172-173]. To understand the charge ambipolar transport phenomenon in this device, we tested the device under different experimental conditions.

3.5. In-depth exploration of external triggers on ambipolar device

3.5.1. Light and temperature effects

Initially, the heterojunction device was tested under 1 min exposure to 20 ppm NH_3, followed by 4 min recovery under clean air, at 45% RH, both in dark and under red light from red LEDs (axical intensity: 700 mcd) (**Figure 45a**). As expected in organic electronics, a current increase was observed upon illumination, by slightly less than a factor of 2. Interestingly, the response to NH_3 increases under illumination. The device exhibited not only an increase in current variation under NH_3, from ca. 0.01 µA in the dark to ca. 0.05 µA under illumination, but also an increase in relative response from 3.5% in the dark to 7% under illumination. Remarkably, under light exposure, both ΔI and RR of the heterojunction device increased, by ca. 5 and 2 times, respectively, compared to the values observed in dark condition.

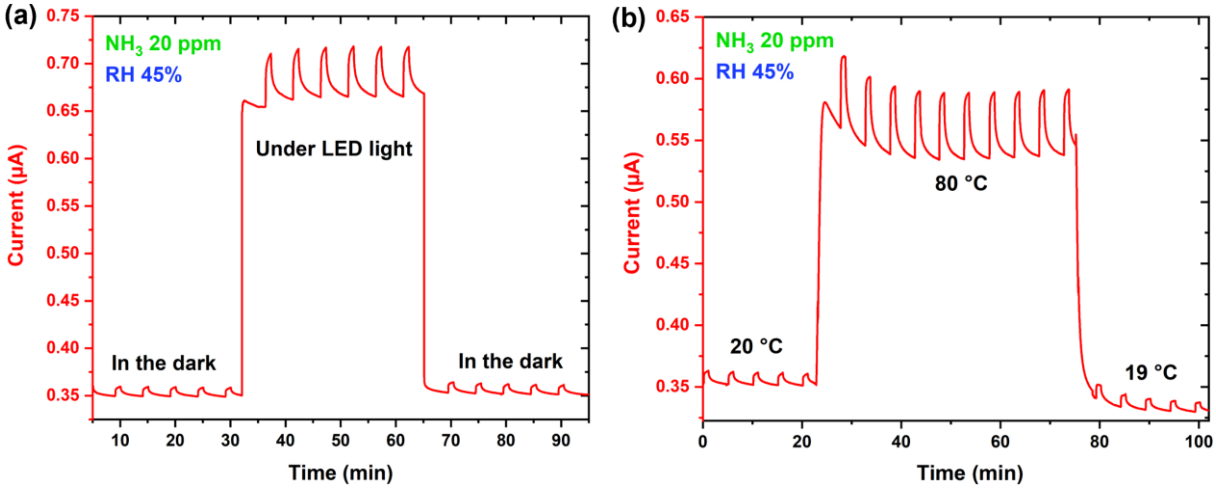

Figure 45. Response curve of $VOF_8Pc/LuPc_2$ heterojunction sensor, under successive exposures to 20 ppm NH_3 under different conditions: in the dark and under light (a), as well as in room temperature and 80 °C (b) at 45% RH.

When the device was subjected to a temperature of 80 °C in a dark environment, it displayed a higher response compared to that at room temperature (19–20 °C) and even higher

than under light exposure (**Figure 45b**). The RR increased to ca. 10.5%, roughly 5 times higher than in ambient conditions and 1.5 times higher than under light exposure. However, the current shift was higher under light exposure (ca. 0.3 μA) compared to that at 80 °C (ca. 0.2 μA). It is well known that the RR values of conductometric sensors can be influenced by changes in temperature or light exposure, because of the induced mobile charges, oxygen desorption and accelerated adsorption/desorption kinetics.[174] However, upon closer inspection, differences in sorption kinetics can be observed between light exposure and heating conditions. When the light is switched on and off, there is a sharp increase and decrease in current with a stable baseline. On the contrary, under heating conditions, there is an initial sharp increase in current, due to the activation energy of materials conductivity, followed by a decline in baseline current for the first few exposure/recovery cycles, after which it stabilised. This effect is directly linked to the desorption of water molecules from the organic layers, which influences the conductivity of the device (vide infra). However, after a few minutes, the baseline current becomes stable indicating the equilibrium state of the sensing material in terms of water contain.

To understand the solely effect of temperature on the heterojunction device, we conducted the same experiment on a freshly prepared sample under rather dry conditions (10% RH) across a wide temperature range, from 20 °C to 80 °C (**Figure 46a**). Interestingly, we observed a similar decline in baseline current as we did previously at 80 °C , but this time it occurred at 30 °C and still slightly at 40 and 50 °C. It is apparent that the device attained more easily the equilibrium state at these temperatures, as a result of its initial dry state and the rather dry experimental conditions (10% RH). At 20 °C, in this rather dry environment, the device exhibited superior RR values (ca. 12%) compared to those in a humid atmosphere (RR 3.5% at RH 45%). This can be considered as surprising, since often it is the reverse, the response to NH_3 increases when RH value increases, as a result of a higher affinity for NH_3 when sensing material is already covered by adsorbed water molecules[81, 98].

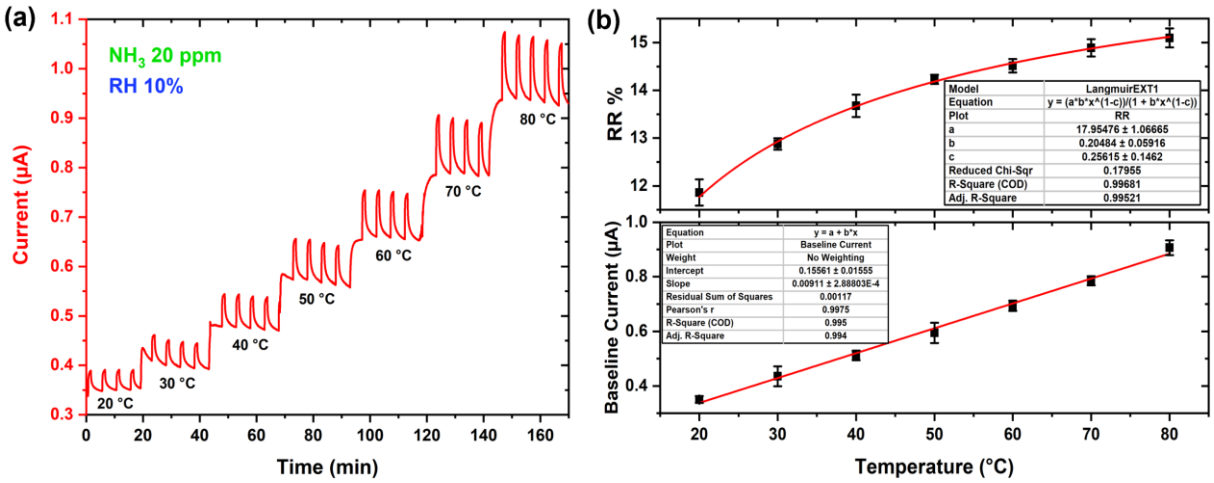

Figure 46. Response curve of $VOF_8Pc/LuPc_2$ heterojunction sensor, under successive exposures to 20 ppm NH_3 in a wide temperature range, from 20 °C to 80 °C, in rather dry experimental condition (10% RH) (a). The variation in relative response and baseline current as a function of temperature (b).

However, an opposite factor can take place. Indeed, the surface density of available adsorption sites is higher for NH_3 molecules when less water molecules are adsorbed.[98] The baseline current increased linearly with temperature, while RR values increased exponentially (**Figure 46b**). Globally, these experiments confirm that the device exhibits higher n-type nature towards electron donating gas species in rather dry experimental conditions.

3.5.2. Humidity effect on the nature of majority charge carriers

To explore the effect of humidity changes on the sensitivity towards NH_3 of the bilayer heterojunction device, we subjected a as-prepared sample to NH_3 experiments. The experiments involved stepwise increasing of the humidity level from 20% to 80% and then monotonically decreasing to 20%, all conducted for 30 min at each RH values, while maintaining a constant temperature (20 °C) (**Figure 47a**).

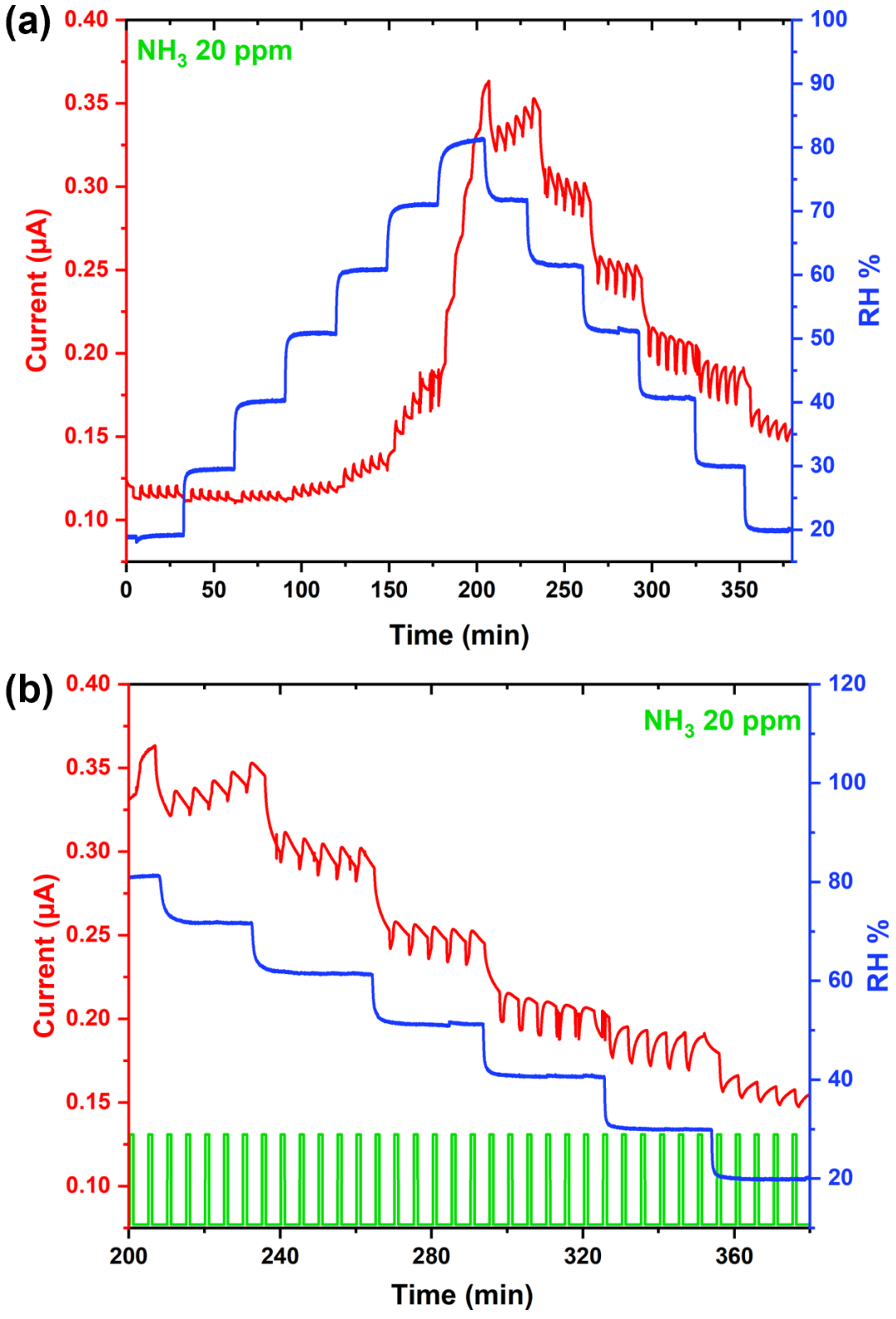

Figure 47. Response curve of $VOF_8Pc/LuPc_2$ heterojunction sensor, under successive exposures to 20 ppm NH_3 under a wide range of humidity level, from 20% to 80 %, at room temperature (a). A zoom is shown for better visibility of the polarity inversion (b).

Remarkably, during RH increasing phase, the device maintained a stable baseline current with minimal sensitivity to humidity changes and displaying n-type behaviour towards NH_3 across humidity levels from 20% to 60% RH. However, as humidity increased from 60% to 70%, the device exhibited a slight increase in baseline current (ca. 0.05 µA) with a rather noisy n-type response to NH_3. A significant current shift (ca. 0.2 µA) was observed when RH reached 80%, resulting in the disappearance of the device's gas response. Unexpectedly, as RH monotonically decreased from 70% to 50% RH, the device displayed a high transient effect during exposure/recovery cycle. The transient effect characterized by an initial sharp decrease in current followed by a small increase, or vice versa, within the same exposure/recovery cycle of NH_3. The transient effect is clearly visible around 240 min to 320 min in **Figure 47b**. Fascinatingly, the n-type behaviour of the bilayer device began to diminish, eventually transitioning to a p-type device and exhibiting a distinct negative response (current decrease) towards NH_3. Subsequently, the device stabilized into a consistent p-type behaviour. The humidity effect of $VOF_8Pc/LuPc_2$ can be directly compared to $CuF_8Pc/LuPc_2$ device, since both devices exhibit polarity inversion upon humidity change.

Remarkably, the $CuF_8Pc/LuPc_2$-based device transforms from p- to n-type, while VOF_8Pc-based device exhibits n-type behaviour at the beginning and transformed to p-type upon humidity as an external trigger. Changing the metal centre from Cu^{2+} to VO^{2+} induces modification in the organisation in the solid-state and the intermolecular interactions, due to the dipole-dipole interactions that introduce a small shift in the frontier molecular orbitals of the MF_8Pc macrocycle, but significantly impact the nature of majority charge carriers within the devices. This effect can be also correlate with the different oxidation states and electronegativity of the metal centre, as reported with metalated octachloro phthalocyanine-based heterojunctions.[114] In the current scenario, the formal oxidation state of V in VOF_8Pc is +4, the vanadyl is likely to be the dication VO^{2+}, which has higher electronegativity than Cu^{2+}, so

induces a higher stabilization of electrons of the phthalocyanine macrocycle. This is the reason why in ambient conditions VOF_8Pc leads to a n-type device, while CuF_8Pc leads to a p-type device, the injection of electrons from the Fermi level of electrodes into the LUMO of VOF_8Pc becomes feasible, contrarily to what we observe with the copper complex.

To confirm the p-type behaviour of the device, we subjected the same device, previously subjected to higher humidity levels, to 90 ppm NH_3 for an extended exposure/recovery cycle of 10 min/30 min in ambient conditions (19 °C and 45% RH). Remarkably, throughout numerous cycles, the device consistently maintained a stable p-type response over long exposure and recovery experiment (**Figure 48**).

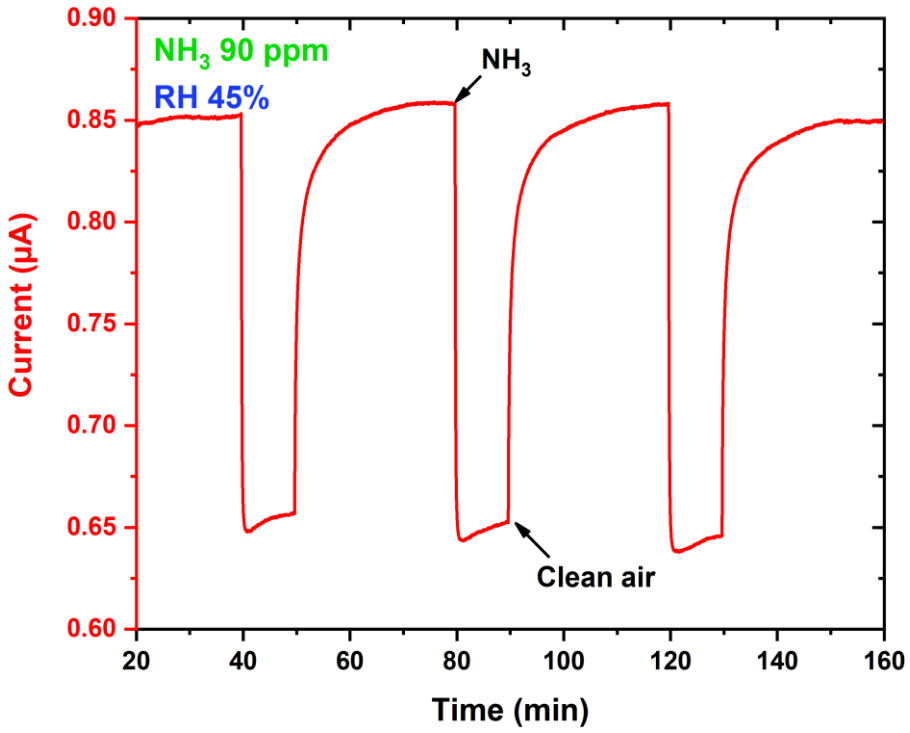

Figure 48. Response curve of $VOF_8Pc/LuPc_2$ heterojunction sensor (in p-state), under successive exposures to 90 ppm NH_3 for 10 min followed by a dynamic recovery (under clean air) for 30 min at 45% RH and room temperature (18 – 19 ˚C).

After exposure to higher humidity levels, the initially n-type device underwent a complete transformation into a stable p-type device. This transformation persisted even under

ambient conditions, with the device exhibiting RR of ca. -25%. Interestingly, the shapes of the response curves associated with adsorption and desorption phases present different profile in p-type state of the device, while comparing it to that of n-type state. When the heterojunction device was in its n-type state, a continuous increase in current was observed throughout the exposure period, while in its p-type state, a sharp current decrease followed by a plateau is observed. This difference in adsorption kinetics implies that in the n-type state, NH_3 molecules diffuse within the volume of the device and access additional sites within the bulk. On the other hand, in p-type state of the device, after adsorption, NH_3 molecules mainly neutralize positive charge carriers in the $LuPc_2$ layer, and do not diffuse anymore. After a long exposure at high humidity, limited adsorption sites are available due to the presence of water molecules. As a result, sorption equilibrium of NH_3 is attained more rapidly during exposure period in the p-state.

Further investigation into the device's behaviour involved testing it across a wide range of gas and humidity concentrations. Gas sensing experiments were conducted starting at 80% RH, decreasing incrementally in 20% steps down to RH level of 20%, with five exposure/recovery cycles at each NH_3 concentration (90, 60 and 30 ppm), at 20 °C (**Figure 49a**). Having conditioned the device at 80% RH, it consistently exhibited p-type behaviour with minimal baseline drift. The absolute value of RR linearly increased with rising humidity levels, ranging from ca. 8.5% to 13.5% at 90 ppm NH_3 under RH values from 20% to 80%, respectively (**Figure 49b**). This suggests that increasing water content in the device promotes its p-type behaviour. In other words, we can make the assumption that decreasing the water content in the device will continuously reduce the p-type behaviour and eventually it will inverse its polarity to n-type.

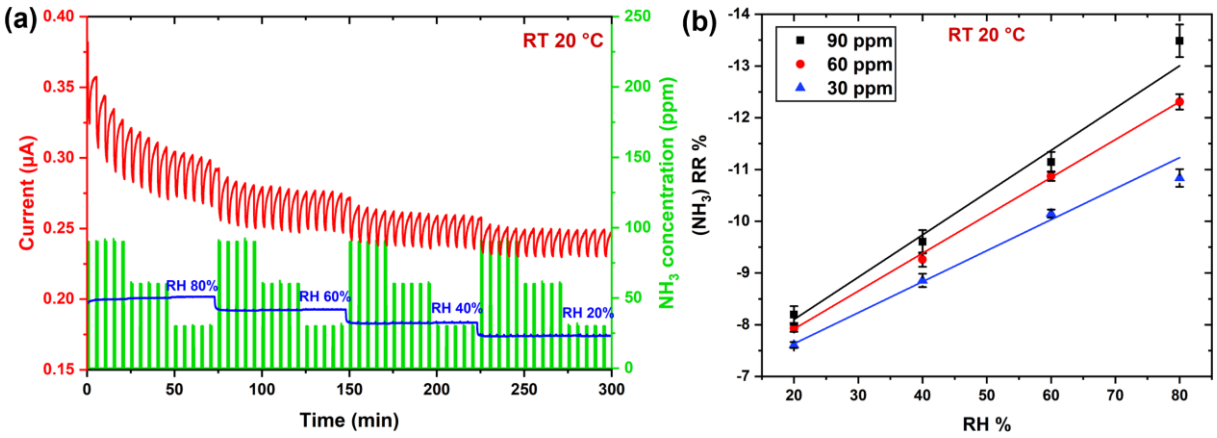

Figure 49. Response curve of $VOF_8Pc/LuPc_2$ heterojunction sensor under exposure to 90, 60, 30 ppm of NH_3 in humid air, in the range of 80 to 20% RH, during 1 min exposure followed by 4 min recovery, at 20 °C (a). The variation in relative response of the device as a function of RH (b).

This assumption was proven by repeating the experiment at 80 °C, where the device demonstrated excellent n-type behaviour, with RR from ca. 21% to 16% at 90 ppm across a wide range of humidity levels from 20% to 80%, respectively (**Figure 50**). It is mesmerising to realise the possibility of operating a single device with good stability in both polarities, regardless of the natural environmental conditions. Interestingly, in its n-state the device's response to NH_3 decreased linearly with increasing humidity levels, further confirming the influence of water molecules on the response of the bilayer heterojunction device. It means that the absolute response (|RR|) to NH_3 decreases for n-state when RH value increases, but it increases for p-state. The adsorption of water molecules onto solid surfaces is the same as explained before with Zn and Co-based devices. However, besides adsorption, water molecules can also diffuse into the materials, potentially altering the device's electrical properties depending on the exposure duration.

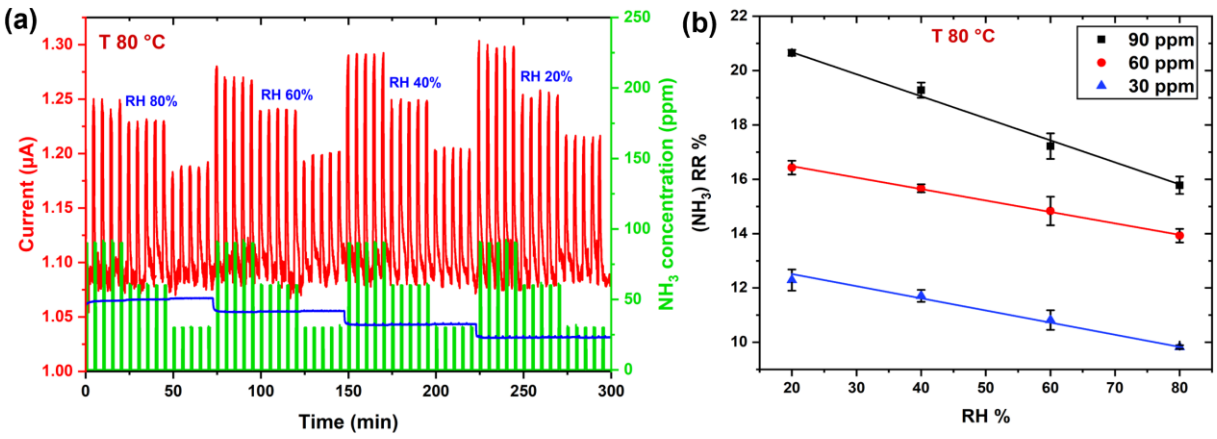

Figure 50. Response curve of $VOF_8Pc/LuPc_2$ heterojunction sensor under exposure to 90, 60, 30 ppm of NH_3 in humid air, in the range of 80 to 20% RH, during 1 min exposure followed by 4 min recovery, at 80 °C (a). The variation in relative response of the device as a function of RH (b).

To investigate this phenomenon, we investigated the bilayer heterojunction device towards 20 ppm of NH_3, under high humidity level (80%) for an extended period of approximately 7 h, at room temperature (20 °C) (**Figure 51**).

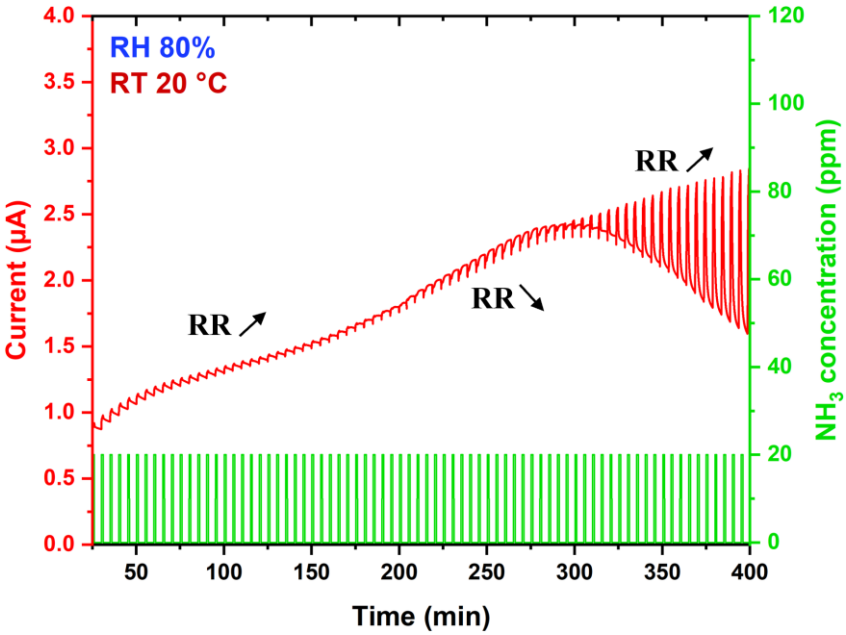

Figure 51. The original experimental curve of $VOF_8Pc/LuPc_2$ heterojunction under 20 ppm of NH_3 at 80% RH and 20 °C for 1 min/4 min exposure/recovery cycles.

Actually, the quasi-dry sample exhibits a huge drift in baseline current when it is exposed to 80% of RH. To focus on transition in the nature of majority charge carriers and to get a good visibility, we did a baseline correction and divided the single experiment into 4 graphs (labelled as 1 to 4), which are displayed in **Figure 52**.

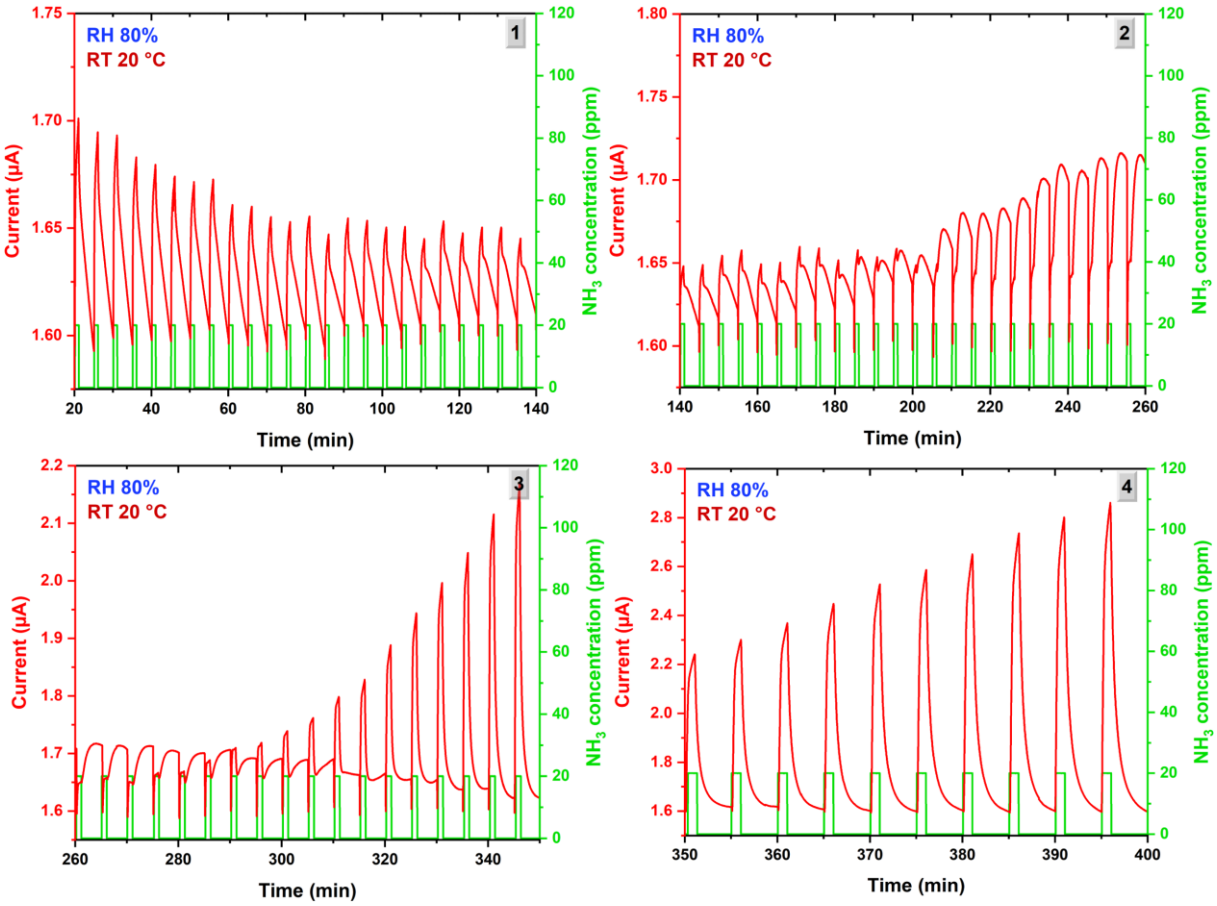

Figure 52. Response curve of $VOF_8Pc/LuPc_2$ device towards 20 ppm of NH_3 at 80% RH. A single experimental curve was divided into four parts (1, 2, 3 and 4) for better visibility.

During the investigation, we witnessed the remarkable transformation on the device's charge transport dynamics. Initially, as expected, the device exhibited n-type behaviour, with a gradually diminishing response to NH_3 over time, with an increasing transient effect during the recovery period (**Part 1** of the **Figure 52**). It is indicative of the coexistence of two phenomena involving charge carriers' density with different kinetics. We can suppose that both surface effect (fast kinetics) and diffusion (slow kinetics) phenomena coexist. During recovery periods,

a fascinating kinetic interplay unfolded: an initial sharp decline in current followed by a slower decrease (**Part 2** of the **Figure 52**). Surprisingly, subsequent cycles revealed the reversal process, with the slower decline becoming more pronounced, ultimately shifting the decrease in current entirely to the exposure phase, where a decline in current during NH_3 exposure and an increase during recovery were observed. The n-type device turned to stable p-type behaviour, after exposing it to high humidity level (80%) for approximately 210 min. The zoom has been shown in **Figure 53**.

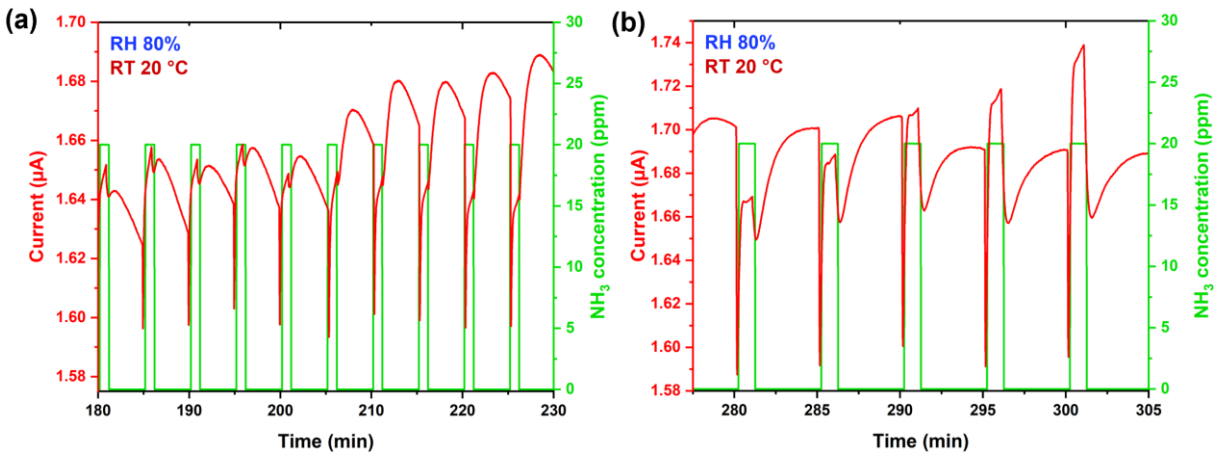

Figure 53. Zoom (from Fig. 52 part 2 and 3) in the inversion in nature of majority charge carriers from n- to p-type (a) and p- to n-type (b).

However, to our surprise, the device underwent another remarkable transformation that was occurred approximately 70 min after the initial transition (t = 280 min). The previously stable p-type behaviour began to weaken, marked by a sharp decline in current followed by a sudden increase within the same exposure period (**Part 3** of the **Figure 52**). Consequently, the device undergoes another transition and exhibits again a stable n-type behaviour (**Part 4** of the **Figure 52**). Zooming in on the data, we can clearly observe a shift in the dominance of majority charge carriers (holes) over minority charge carriers (electrons) (**Figure 53a**). Around 290 min from the beginning of the experiment, the device displayed a unique equilibrium, where both p- and n-type behaviours occur within the same exposure cycle (**Figure 53b**). This observation

underscores the intricate interplay between charge carriers and environmental factors. Anyhow, it is mesmerising to witness the inversion in device polarity and spectating the changes in nature of majority charge carriers, very closely, which to our knowledge has never reported so far.

Globally, the organic-organic bilayer heterojunction device, with a thickness of 50/50 nm, underwent two distinct episodes of polarity inversion during its ca. 7 h exposure to 80% RH at room temperature. This phenomenon is not only related to the molecular structure of the two components, but also intricately linked to the device's architecture. The initial n-type to p-type transition arises from the gradual diffusion of water into the top layer, altering charge transfer dynamics at the interface by trapping mobile charges that inverse the nature of majority charge carriers in favour of p-type. Subsequent diffusion of water till the interface and into the sublayer affecting the hole mobility, enhancing electron density and leading to the device's transformation into n-type.

3.5.3. Exploring the ambipolarity of the device under oxidating gas species

The stability of the bilayer heterojunction device's ambipolarity was further explored under the influence of strong electron withdrawing species, such as NO_2, across various conditions. Initially, the device underwent exposure to a wide range of humidity levels and gas concentrations, from 80% to 20% RH and from 900 ppb to 300 ppb of NO_2, respectively (**Figure 54**). As observed previously in ambient conditions, the device shows p-type behaviour (current increases) upon exposure to NO_2. However, it exhibited a decrease in its p-type behaviour with decreasing humidity, reflected in the decrease of RR from ca. 25% to 7.5% as humidity declined from 80% to 20% at 900 ppb of NO_2.

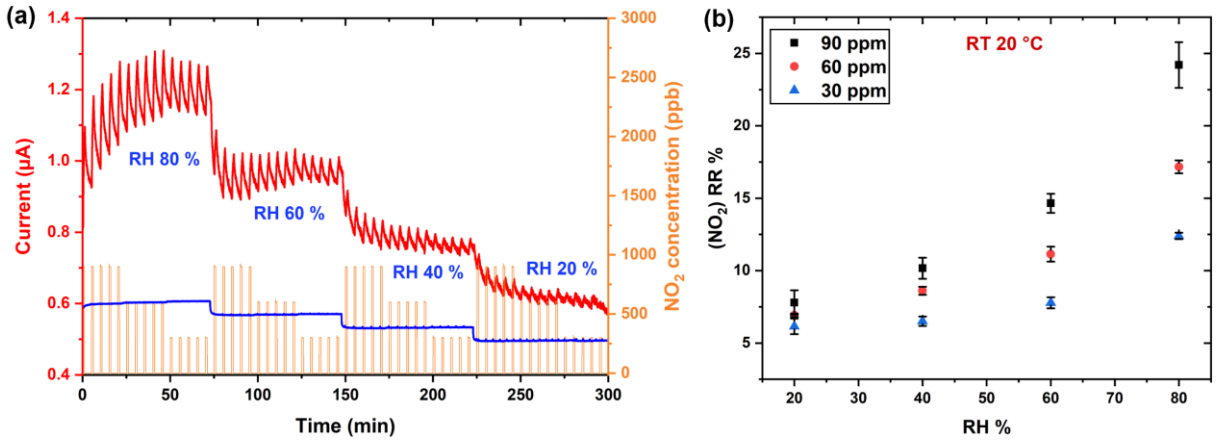

Figure 54. Response curve of $VOF_8Pc/LuPc_2$ heterojunction sensor under exposure to 900, 600, 300 ppb of NO_2 in humid air, in the range of 80 to 20% RH, during 1 min exposure followed by 4 min recovery, at 20 °C (a). The variation in relative response of the device as a function of RH (b).

This phenomenon aligns with our earlier observations and is driven by similar underlying mechanisms. However, contrarily to what happens with NH_3, the response to NO_2 is strongly affected by RH variations. To delve deeper into achieving ambipolar charge transport regimes, we investigated the heterojunction device under different temperatures at fixed NO_2 concentration of 200 ppb in a dry environmental condition (RH 10%) (**Figure 55**).

To ensure solely effect of the ambipolar device, a freshly prepared sample was utilised. In a dry environment, the device demonstrated observable p-type behaviour under NO_2, up to 30 °C. However, as the temperature increased to 40 and 50 °C, the device displayed a diminished response, with no clear polarity observed. Notably, at 60 °C, a significant inversion occurred, transitioning the device to n-type behaviour. By utilising the cooling system, within a few minutes we successfully lowered the temperature back to 30 and 20 °C, where the device returns to the p-type polarity.

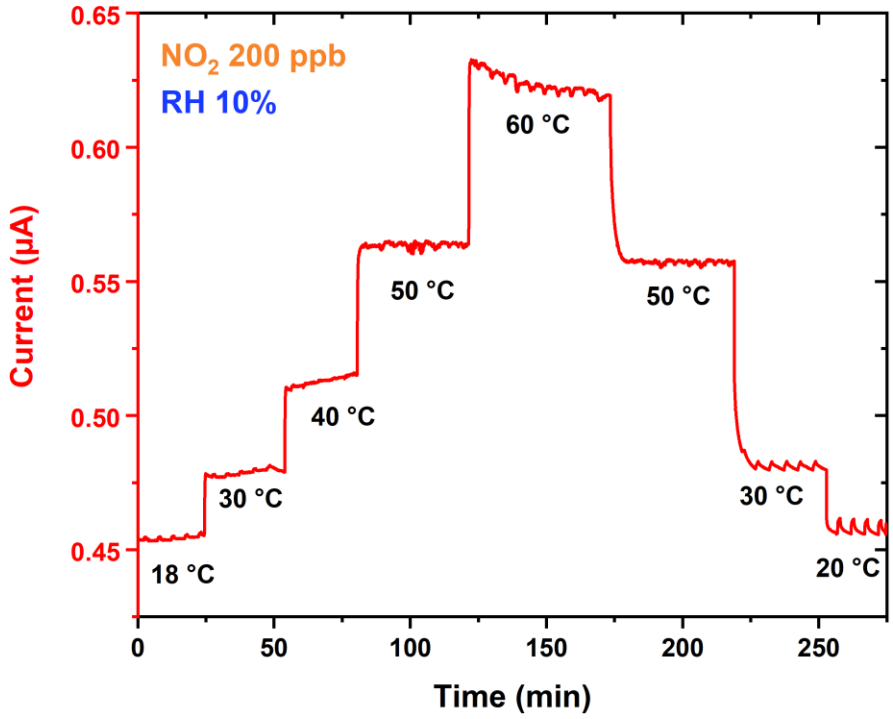

Figure 55. Response curve of $VOF_8Pc/LuPc_2$ heterojunction sensor under exposure of 200 ppb of NO_2 in dry experimental condition (10% RH), during 1 min exposure followed by 4 min recovery, under wide range of temperature from 18 °C to 60 °C.

Most interestingly, it is the very first report that observes the rather zero state (where the device exhibits no response) of the ambipolar device (at ca. 40 °C) when the domination of majority charge carrier densities goes from p- to n-state or vice versa. For better visibility, the zoom figure was displayed in **Figure 56**.

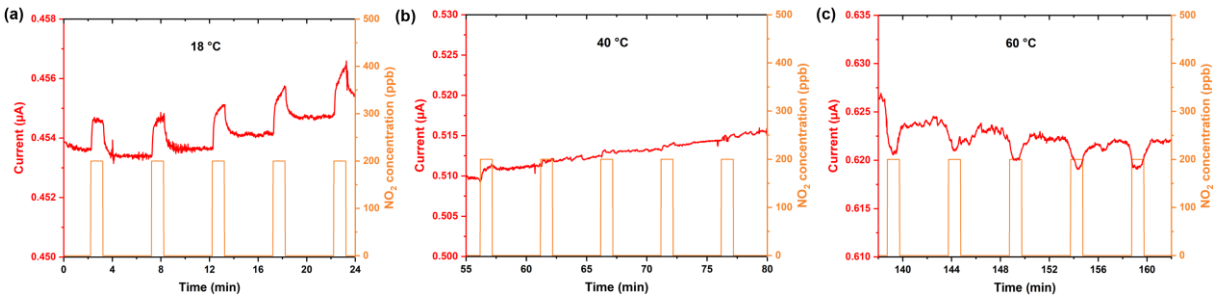

Figure 56. Zoom of Fig. 55 at different polarity state under different temperature: p-type at18 °C (a), n-type at 60 °C (b) and rather zero state (no response) at 40 °C (c).

Furthermore, the ambipolar charge transport regime was also achieved at ambient humidity level (RH 45%), by increasing the device temperature from 20 to 80 °C (**Figure 57**). As expected, the bilayer heterojunction device exhibits p-type behaviour, which shifted to n-type as the temperature raised to 80 °C. Fascinatingly, during first few cycles at 80 °C, the device exhibited a gradually increase in its n-type response, indicating the desorption of water molecules from the solid surface. Subsequently, the device's n-type response rather stabilized, suggesting a dry state and further confirmed the initial state of our ambipolar device.

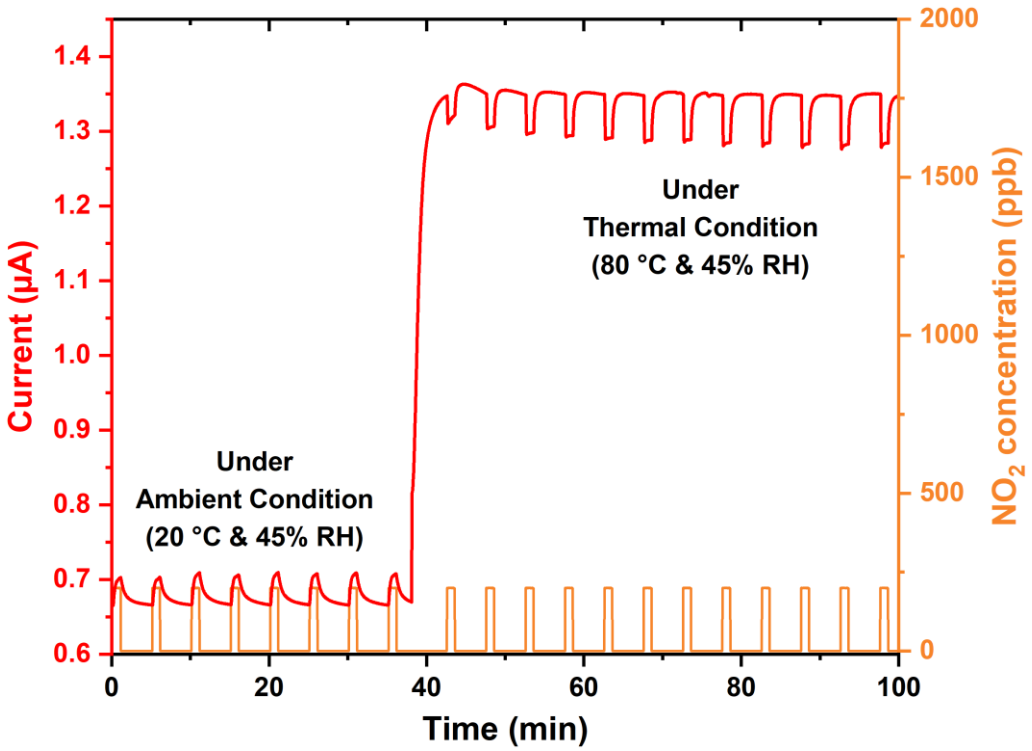

Figure 57. Response curve of $VOF_8Pc/LuPc_2$ heterojunction sensor under exposure of 200 ppb of NO_2 under 20 °C and 80 °C at 45% RH.

As we discussed earlier, the water molecules can act as a trap for positive mobile charge carriers and their desorption ultimately triggers a detrapping effect, prompting a transformation in the nature of majority charge carriers and resulting in a change in polarity. Additionally, the results aligned well with our previous experimental observations under different conditions. Particularly, it is interesting to compare these results with a previous experiment conducted

under same experimental conditions towards 20 ppm of NH_3 exposure (**Figure 45b**). In the previous case, we observed an amplification in the response at 80 °C compared to ambient conditions, whereas in the current scenario, we observed an inversion in the response. **Table 5** helps us to have a clear view on device's direction of the current change and polarity inversion under NH_3 and NO_2 with respect to the experimental conditions.

Table 5. Comparison of heterojunction device's current change direction and polarity inversion under NH_3 and NO_2 with respect to the experimental conditions. Red upward arrows represent current increase and green downward arrows represent current decrease.

Experimental conditions	Current		Polarity	
	NH_3	NO_2	NH_3	NO_2
10% RH and 20 °C	▲	▲	n-type	p-type
10% RH and 60 °C	▲	▼	n-type	n-type
45% RH and 20 °C	▲	▲	n-type*	p-type
45% RH and 80 °C	▲	▼	n-type	n-type
80% RH and 20 °C	▼	▲	p-type	n-type

*Except if the device has been conditioned in its p-type (long exposure at high humidity value).

The charge transport regime of the $VOF_8Pc/LuPc_2$ bilayer heterojunction (ambipolar) device is extensively studied by utilizing different types of external triggers under different gases. The bilayer heterojunction device demonstrates both p- and n-type behaviours under exposure to oxidation gases (NO_2 and O_3) and reducing gas species (NH_3), depending on humidity levels and temperature variations. The initial polarity of the ambipolar device is identified by observing a current decrease under oxygen exposure, indicates n-type behaviour. This is further verified by exposing freshly prepared samples to weak reducing gas (NH_3, current increase) at 20 °C and 45% RH (ambient conditions). Surprisingly, when exposed to

strong oxidation gases (NO_2 and O_3) under the same experimental conditions, the device exhibits p-type behaviour (current increases) showcasing an ambipolar behaviour. However, increasing the temperature of the device to 80 °C revealed its initial n-type polarity even under ambient conditions. Notably, the device exhibits stable response towards NO_2 and NH_3 in both polarity states.

4. Conclusion

Three different octafluoro-phthalocyanines were successfully synthesised with zinc, cobalt and vanadyl as central metal atom. By engaging these molecules as a sublayer, we fabricated bilayer heterojunction sensors with highly conducting material ($LuPc_2$) as a top layer. The change in metal centre in the octafluoro-phthalocyanine macrocycle induces a dramatic difference in the polarity of the resulting devices. Additionally, the architecture of the devices opens the gateway for ambipolar molecules (CoF_8Pc and VOF_8Pc) to decide the device polarity. For a comprehensive understanding, we summarised the polarity of all MF_8Pc under different external triggers (**Table 6**).

Table 6. Comparison of MF_8Pc-based heterojunction device's polarity under different external triggers

External trigger	$ZnF_8Pc/LuPc_2$	$CuF_8Pc/LuPc_2$	$CoF_8Pc/LuPc_2$	$VOF_8Pc/LuPc_2$
NH_3 (ambient)	⊕	⊕	⊖	⊖
NO_2 (ambient)	⊕	⊕	⊕	⊕
O_3 (ambient)	⊕	⊕	⊕	⊕
Light	⊕	⊖	⊖	⊖
Humidity	⊕	⊖	⊖	⊕⊖
Temperature	⊕	⊕	⊖	⊖

*The polarity is dependent on humidity exposure time period.

Green positive symbol has been used to represent p-type polarity of the devices, while red negative symbol indicating n-type polarity. This type of device that exhibits ambipolar behaviour has the potential to replace two different types of devices (p- and n-type) into a single ambipolar device, eventually reducing the size of the electrical system. Such ambipolar devices hold promise for various applications in nanotechnology, including deployment of spacecraft, satellites, and everyday electrical appliances where minimizing weight and size is crucial. However, achieving precise control over the inversion of majority charge carriers, which determines the device's polarity required a suitable and controllable external trigger, and it may depend on the molecular composition and the architecture of the device. It is crucial to conduct comprehensive investigations into the environmental effects such as humidity and temperature variations when working with ambipolar devices. Moreover, further research is essential before these devices can be effectively deployed in real-world applications.

Chapter 6

Controlling the Polarity of Heterojunction Devices by Manipulating the Top Layer

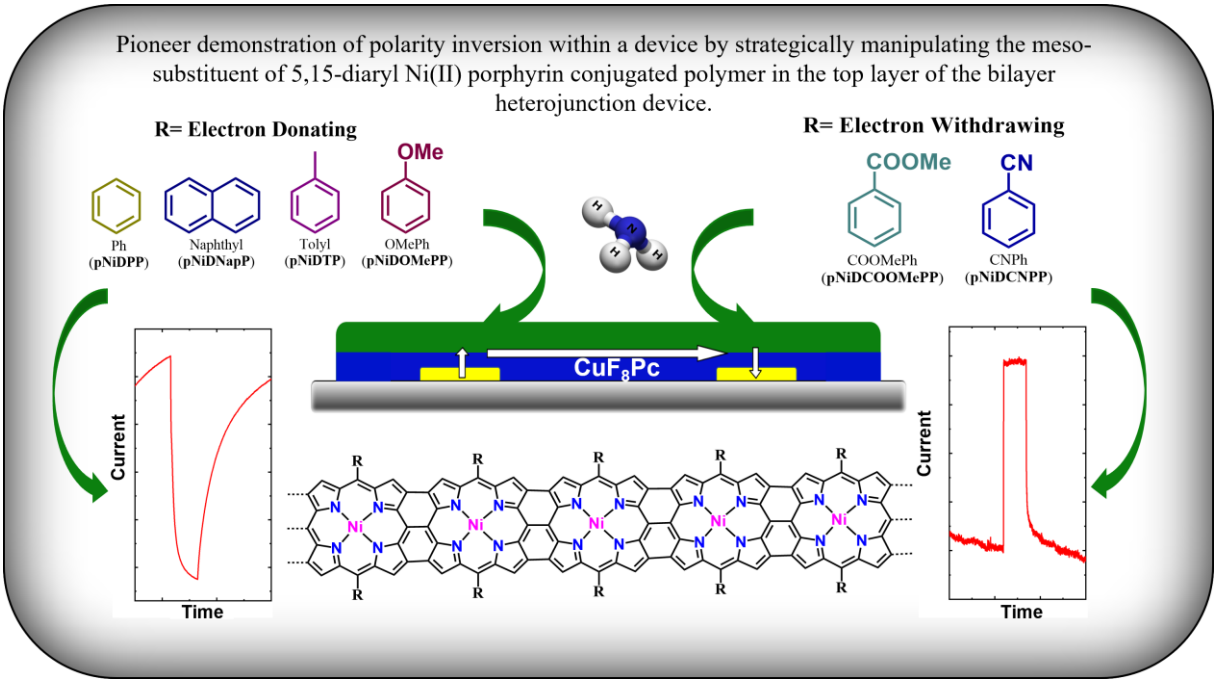

Chapter 6

Controlling the Polarity of Heterojunction Devices by Manipulating the Top Layer

Table of Content

Chapter 6. Controlling the Polarity of Heterojunction Devices by Manipulating the Top Layer

1. Introduction

The recent developments of conjugated polymers provide an effective alternative to metal oxide dominance in gas sensors[175]. The tunability, durability, and their capability to operate at ambient temperature make conjugated polymers such as polypyrrole, polyaniline (PANI), polythiophene and poly(3,4-ethylenedioxythiophene) (PEDOT) as attractive materials in gas sensing applications[176-177]. In particular, PANI-based materials are largely exploited for their sensing properties towards NH_3. Similarly to metal oxides, the sensing properties of conjugated polymers are influences by their structure and morphology[62-63, 178]. Moreover, the possibility to modulate a polymeric structure by introducing groups equipped with interacting sites and their adaptability in various forms like nanofibers, nanoparticles and thin films empower scientists to tailormade sensors for desired sensing requirements[68, 179].

Interestingly, metalloporphyrins (MPor) offer advantage to tune the electronic and optoelectronic properties of their conjugated polymer by the incorporation of substituents to one or several of the eight *β*- and four *meso*- positions of the porphyrin ring, and/or from the introduction of a cation inside the porphyrin core[86, 180-181]. Moreover, the electronic properties of the substituent on MPor directly affect the structural properties of MPor conjugated polymers, which in turn can impact the sensing response of the bilayer heterojunction devices towards ammonia. Realizing the chemistry offered by MPors and advantage of oCVD, which overcomes many of the limitations related to solution-based approaches, enable the synthesis, deposition and engineering of metalloporphyrin conjugated polymer thin films on virtually any substrate[182], herein we report the engineering of a series of multiply fused disubstituted

Ni(II)porphyrins conjugated polymer thin films containing different aryl synthons at *5,15*-positions.

Up to now we explored various types of materials engaged in our bilayer heterojunction devices as sublayer, which is commonly covered by $LuPc_2$ as top layer. Since $LuPc_2$ has huge densities of charge carriers near equilibrium, the heterojunction device's polarity is highly influenced by the sublayer. Hence, we were capable to get the desire device polarity by changing the sublayer in bilayer heterojunction devices. In current scenario, we fabricated different types of heterojunction devices that have an ambipolar material (CuF_8Pc) as common sublayer covered by different meso substituted Ni(II)porphyrins conjugated polymers, while previous works demonstrated the change in sensing response on replacing the sublayer in a bilayer heterojunction device. Goal of this work is to explore the different types of top layer on ambipolar molecule in bilayer heterojunction devices. Taking advantage of the ability of oCVD and the range of multiply fused Ni(II)porphyrin conjugated polymeric films (pNiD(Aryl)P) bearing electron donating (pNiDNapP, pNiDPP, pNiDTP and pNiDOMePP) and electron withdrawing (pNiDCOOMePP and pNiDCNPP) aryl synthons were deposited onto a CuF_8Pc thin film to form bilayer heterojunction devices for gas sensing application. Schematic representation of the oCVD reaction of *5,15*-diaryl Ni(II) porphyrins and different aryl substituents were shown in **scheme 13**.

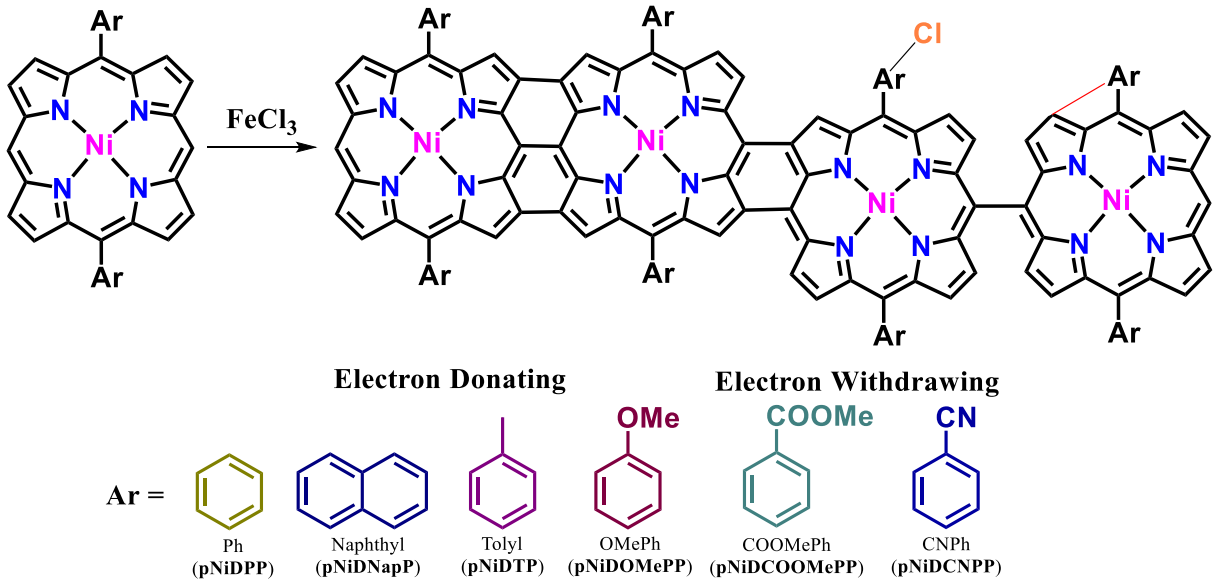

Scheme 13. Schematic representation of the oCVD reaction of *5,15*-diaryl Ni(II) porphyrins and the molecular structures of the aryl substituents used in this work.

2. Electrical properties of the heterojunction devices

Electrical properties of the resulting bilayer heterojunction sensors were studied by performing I-V measurements in the applied voltage ranging from -10 V to +10 V. As expected for bilayer heterojunction devices, all the devices exhibit symmetric and non-linear I-V curves, except CuF_8Pc/pNiDCOOMePP device, which shows huge noise, due to its very poor conducting nature (**Figure 58**). The typical non-linear I-V curve observed in other organic bilayer heterojunction devices arises from the accumulation of mobile charges at the interface as same as previous discussions. Bilayer heterojunction devices based on CuF_8Pc/pNiDNapP and CuF_8Pc/pNiDPP exhibit higher U_{th} of 2.43 V and 2.49 V with similar current at +10 V (0.32 µA and 0.29 µA), respectively. CuF_8Pc/pNiDOMePP (U_{th} = 1.97 V) and CuF_8Pc/pNiDTP (U_{th} = 1.75 V) exhibit a slightly lower apparent energy barrier, while CuF_8Pc/pNiDCNPP displays a significantly lower U_{th} value of 0.68 V.

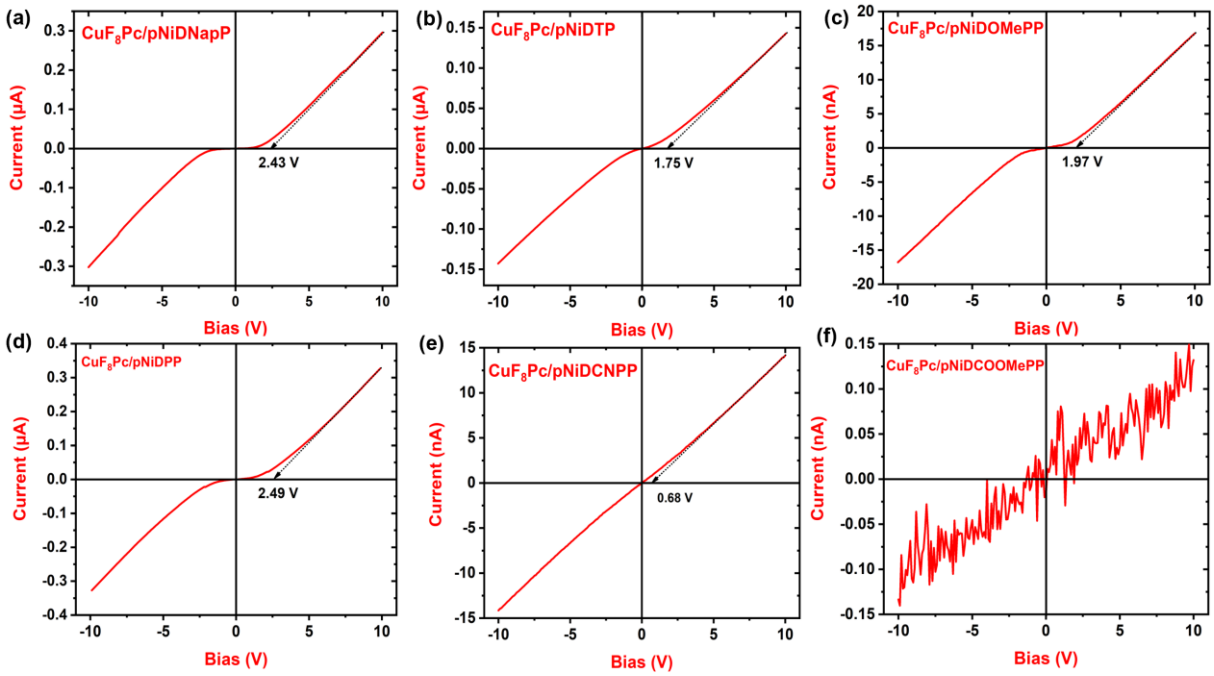

Figure 58. I-V characteristics of CuF_8Pc/pNiD(Aryl)P bilayer heterojunction devices with estimated apparent energy barrier.

3. Ammonia sensing properties

To investigate the sensing capabilities of the bilayer heterojunction devices towards ammonia, the devices were subjected to a high concentration of NH_3 (90 ppm) for 10 min/30 min exposure/recovery cycles. The bilayer heterojunction devices engaged with *5,15*-diaryl Ni(II) porphyrin conjugated polymer bearing electron-donating *meso*-substituents as top layer (pNiDNapP, pNiDTP, pNiDOMePP and pNiDPP) demonstrate a decrease in current when exposed to NH_3, while an increase in current was observed during recovery period (**Figure 59a-d**). Such behaviour of bilayer heterojunction sensors indicates their p-type behaviour, which is consistent with the electron-donating character of ammonia. Conversely, devices featuring porphyrin polymer with electron-withdrawing substituents in the top layer (pNiDCNPP and pNiDCOOMePP) exhibit an increase in current under NH_3 exposure, while a decrease in current during recovery period **(Figure 59e-f)**, showcasing their n-type nature.

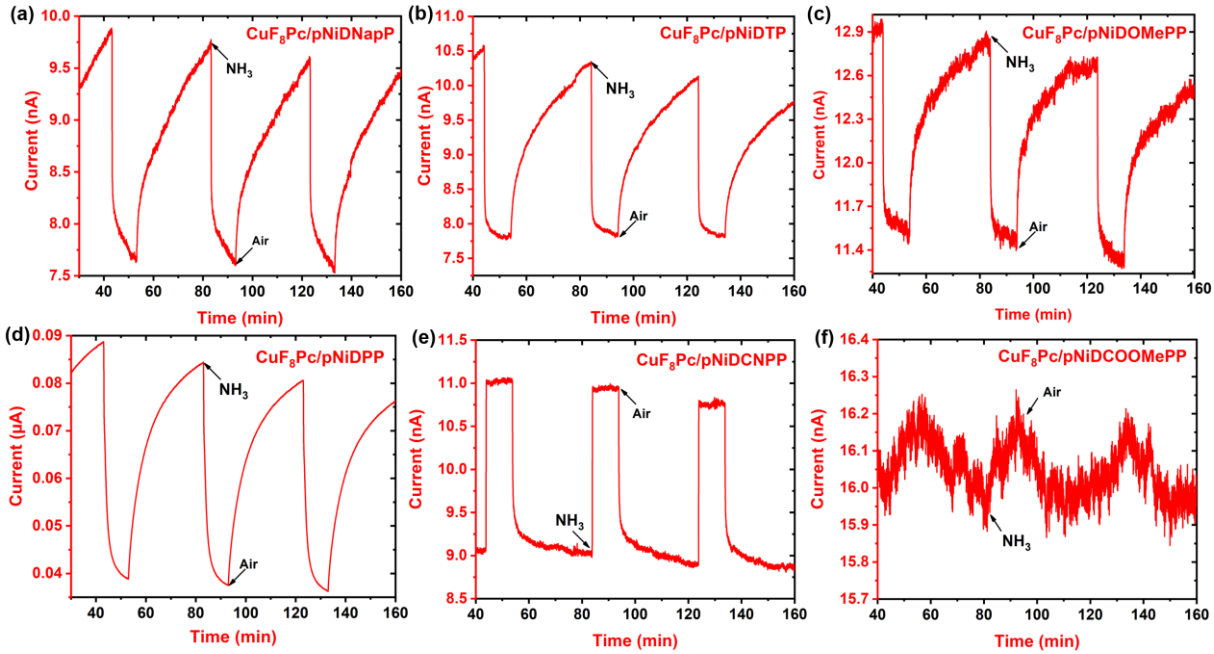

Figure 59. Response curve of CuF_8Pc/pNiD(Aryl)P bilayer heterojunction sensors, under successive exposures to 90 ppm ammonia for 10 min and recovery under air for 30 min at 45% RH and room temperature (18 – 20 °C).

In our previous studies, we extensively investigated the significant impact of the sublayer on device polarity. For the very first time, we have observed that the nature of the device is influenced by the top layer. This effect primarily arises from the equilibrium between charge carriers in the sublayer. Previously, CuF_8Pc was identified as an ambipolar molecule when combined with $LuPc_2$ in bilayer heterojunction device[10, 89, 94]. In the current scenario, owing to the ambipolarity of the sublayer, the top layer gains the ability to switch the polarity of the device according to the substituents present on their macrocycle. Notably all the bilayer heterojunction sensors demonstrated a slight drift in baseline current, which can be attributed to the incomplete desorption of NH_3 during recovery period. However, the sensors signal was recovered by more than 95% during desorption period. The relative response (RR) of the bilayer heterojunction sensors was calculated by using the **equation (4)**.

CuF_8Pc/pNiDPP shows the highest negative RR of -56% with response/recovery time (time taken to complete 90% of the final value) of 198/1170 s, respectively, whereas, CuF_8Pc/pNiDCNPP exhibits the highest positive RR of 22%, with response/recovery time of 13/255 s, respectively. Notably, this device has the fastest response/recovery kinetics among all bilayer heterojunction sensors, which makes it as highly suitable for application in emergency alert system in chemical industries and laboratories. The calculated values of RR and response/recovery time of bilayer heterojunction sensors were shown in the **Table 7**.

Table 7. Comparison of RR, Res t_{90} and Rec t_{90} of CuF_8Pc/pNiD(Aryl)P bilayer heterojunction sensors.

Sensors	$RR_{[90\ ppm]}$ (%)	Response time (t_{90}) (s)	Recovery time (t_{90}) (s)
pNiDNapP	-22.84	293	1530
pNiDTP	- 26.02	43	1383
pNiDOMePP	-11.46	64	1205
pNiDPP	-56.22	198	1170
pNiCOOMePP	2.10	519	1575
pNiDCNPP	22.11	13	255

With the exception of CuF_8Pc/pNiCOOMePP, which exhibits high noise in long exposure, all other bilayer heterojunction sensors were further evaluated under a wide range of NH_3 concentrations from 90 to 10 ppm (**Figure 60**), with dynamic cycles of 1 min exposure and 4 min recovery periods. Remarkably, the current variations observed in all sensors were highly reversible and repeatable throughout the experiments.

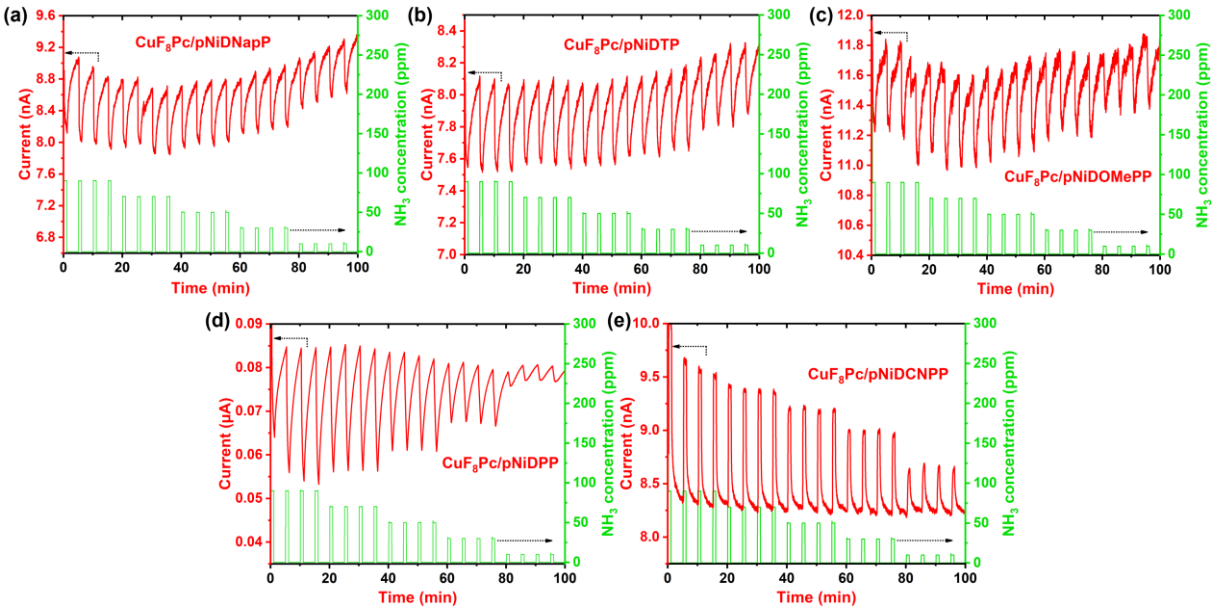

Figure 60. Response curve of CuF_8Pc/pNiD(Aryl)P bilayer heterojunction sensors, under NH_3 gas for 1 min and recovery under clean air for 4 min, in the range of NH_3 concentration from 90 to 10 ppm, at 45% of RH and room temperature (18–20 ˚C) (a–e).

All the bilayer heterojunction sensors displayed distinct gas responses down to 10 ppm. Notably, the CuF_8Pc/pNiDCNPP bilayer heterojunction sensor demonstrated a sharp and stable response without any baseline drift. Hence these sensors were further evaluated by exposing to low NH_3 concentrations, ranging from 9 to 1 ppm (**Figure 61**). Most interestingly, CuF_8Pc/pNiDNapP, CuF_8Pc/pNiDTP, CuF_8Pc/pNiDOMePP and CuF_8Pc/pNiDCNPP bilayer heterojunction sensors demonstrate observable responses even at 1 ppm experimentally (**Figure 61a-c**) and the CuF_8Pc/pNiDPP bilayer heterojunction sensor exhibits distinct gas response down to 3 ppm (**Figure 61d-e**).

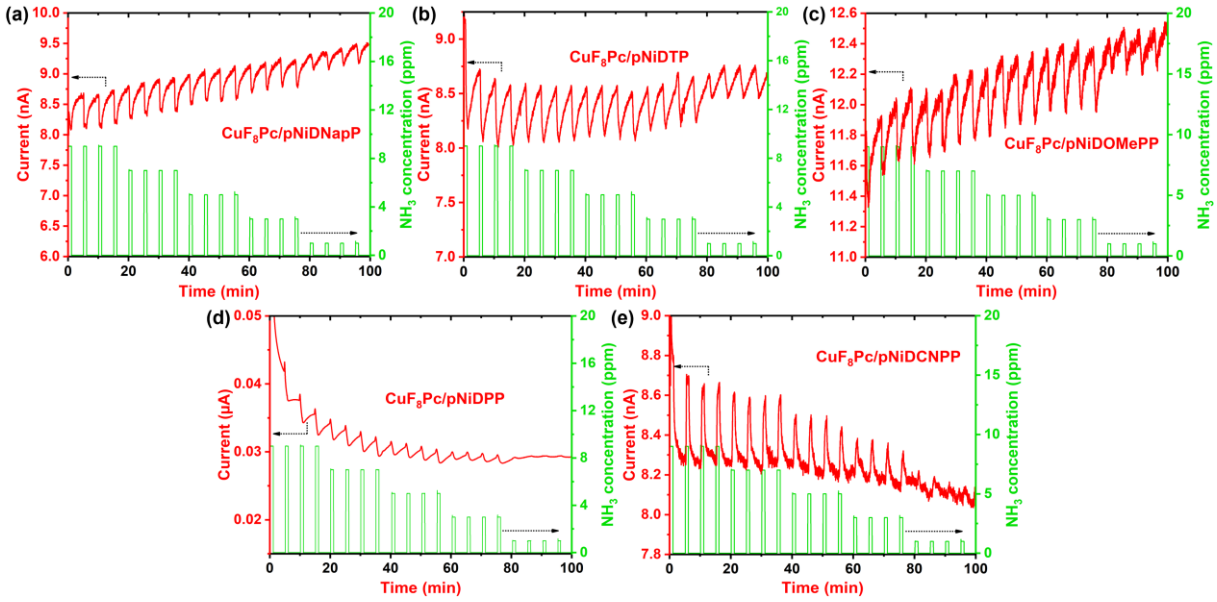

Figure 61. Response curve of CuF_8Pc/pNiD(Aryl)P bilayer heterojunction sensors, under NH_3 gas for 1 min and recovery under clean air for 4 min, in the range of NH_3 concentration from 9 to 1 ppm, at 45% of RH and room temperature (18–20 ˚C) (a–e).

To understand the variation in sensors response influenced by different top layers, we calculated the RR using the **equation (4)** and plotted them against varying NH_3 concentration, creating calibration curves. **Figure 62** illustrates these calibration curves for all five bilayer heterojunction sensors (a zoom is shown as inset for a better visibility). Notably, all curves were fitted with the Langmuir's equation, indicating that the interaction between gas molecules and solid surfaces follows Langmuir-type adsorption. This suggests the saturation of all available adsorption sites by NH_3 gas molecules at higher concentrations. This effect is particularly evident in the CuF_8Pc/pNiDTP bilayer heterojunction sensor, which almost reaches saturation between 30 to 70 ppm, displaying only a slight change in RR from -6.4% to -6.7%, respectively. Anyhow, it is important to note that this sensor shows clear distinction at low NH_3 concentrations, ranging from 5 to 1 ppm, with RR values from -4.8% to -3.5%, respectively.

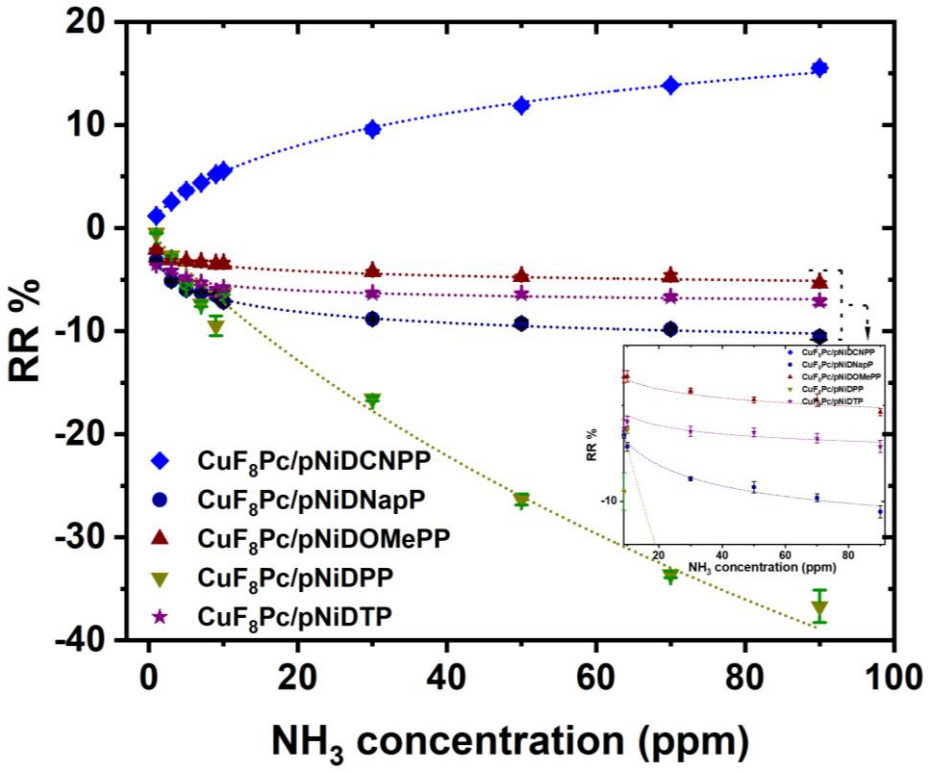

Figure 62. The variation of relative response (calibration curve) of bilayer heterojunction sensors as a function of NH_3 concentration. Inset is shown for better visibility of Langmuir's fit at low concentration.

Limit of detection was calculated for all five bilayer heterojunction devices using **equation (5)**. Among all bilayer heterojunction sensors, CuF_8Pc/pNiDPP exhibits high sensitivity (-1.17% ppm^{-1}) and CuF_8Pc/pNiDNapP exhibits the lowest LOD (190 ppb). To comprehend, the sensitivity of the sensors was increased in the order of CuF_8Pc/pNiDTP (-0.32% ppm^{-1}) < CuF_8Pc/pNiDOMePP (-0.52% ppm^{-1}) < CuF_8Pc/pNiDCNPP (-0.69% ppm^{-1}) < CuF_8Pc/pNiDNapP (-0.98% ppm^{-1}) < CuF_8Pc/pNiDPP (-1.17% ppm^{-1}) and LOD decreased in the order of CuF_8Pc/pNiDPP (2 ppm) > pNiDOMePP (508 ppb) > CuF_8Pc/pNiDTP (492 ppb) > CuF_8Pc/pNiDCNPP (199 ppb) > CuF_8Pc/pNiDNapP (190 ppb). Estimated sensitivity and LOD of the bilayer heterojunction sensors are compiled in the **Table 2**. All these sensors displayed a LOD below 20 ppm, which is the daily exposure limit established by the European Parliament. Moreover, the CuF_8Pc/pNiDNapP and CuF_8Pc/pNiDCNPP bilayer heterojunction

devices demonstrated a LOD below 200 ppb, making them exceptionally suitable for real environmental applications such as in the medical field, where concentrations of interest typically are in sub ppm range[183].

Table 8. Comparison of sensitivities (*S*) and Limit of detections (LOD) of CuF_8Pc/pNiD(Aryl)P bilayer heterojunction sensors.

Devices	S (% ppm^{-1})	LOD (ppb)	[NH_3] (ppm)
pNiDNapP	-0.98	190	3 - 1
pNiDTP	-0.32	492	9 - 1
pNiDOMePP	-0.52	508	3 - 1
pNiDPP	-1.17	2000	9 - 3
pNiDCNPP	0.69	199	3 - 1

Comparison of all these sensors polarity under NH_3 is given in **Table 9**. Green colour downwards arrow indicates a negative response (current decrease) and red colour upwards arrow indicates a positive response (current increases).

Table 9. Behaviour (n-type or p-type) of CuF8Pc/pNiD(Aryl)P bilayer heterojunction sensors upon NH_3 exposure.

Devices	Current (Under NH_3)	Polarity (Under NH_3)
CuF_8Pc/pNiDNapP	▼	p-type
CuF_8Pc/pNiDTP	▼	p-type
CuF_8Pc/pNiDOMePP	▼	p-type
CuF_8Pc/pNiDPP	▼	p-type
CuF_8Pc/pNiCOOMePP	▲	n-type
CuF_8Pc/pNiDCNPP	▲	n-type

4. Conclusion

Here we reported the direct synthesis of different *5,15*-diaryl Ni(II) porphyrin-based conjugated polymers (pNiD(Aryl)P) bearing electron donating (pNiDNapP, pNiDTP, pNiDOMePP, pNiDPP) or electron withdrawing (pNiDCOOMePP, pNiDCNPP) *meso*-substituents, and their integration, as conductive top layer, on CuF_8Pc sublayer, to construct CuF_8Pc/pNiD(Aryl)P bilayer heterojunction devices. For the first time, thanks to these devices, we report the pioneering demonstration of polarity inversion within a heterojunction device, by strategically manipulating the *meso*-substituent of the *5,15*-diaryl Ni(II) porphyrin conjugated polymer in the top layer of the heterojunction device. It is due to the ambipolarity of the sublayer, the top layer gains an access to dictate the device's polarity. This work lays a foundation for upcoming research where the top layer's participation will be crucial in device's polarities.

General Conclusion

General Conclusion

Over the three years (2021 – 2024) of research work within the team Electrochemistry, Materials, Coordination, Analysis and Porphyrinoids (EMCAP) previously knowns as Electrochemistry, Molecular Materials and Devices (EMMD) of the Institute of Molecular Chemistry of the University of Burgundy (ICMUB), we developed various types of organic bilayer heterojunction devices and investigated their electrical and sensing properties under different experimental conditions. In most of our work, we utilised a highly conducting molecular material ($LuPc_2$) as the top layer and various molecular materials as sublayer from our collaborators worldwide to fabricate novel heterojunction devices, potentially revolutionizing organic electronic applications.

Each chapter of this thesis led to new experiments, innovations, and the discovery of new phenomena. These included the pioneering demonstration of SiPc-based ammonia sensors, the introduction of a novel deposition method (Quasi-Dip Coating), and the enhancement of organic bilayer heterojunction device performance through UV light illumination. Additionally, we introduced a new type of bilayer ambipolar heterojunction device that exhibits different polarity towards different gasses, a novel external trigger (temperature variation) to invert the nature of majority mobile charge carriers within the bilayer heterojunction device, observed polarity inversion within the device through the zero state, and achieved a control of the charge transport regime through chemical engineering on the top layer of bilayer devices.

Our studies begin with the elaboration of organic heterojunction devices under different oxidizing (NO_2 and O_3) and reducing (NH_3) gases that provides insight into the charge transport properties of these devices. Initially, we explored the potential of silicon phthalocyanines (Cl_2-SiPc and $(345F)_2$-SiPc) in a bilayer organic heterojunction device by combining them with $LuPc_2$ and investigated their NH_3 sensing properties to understand the interaction between gas

molecules and the sensing layer. With this basic knowledge, we further explored two original π-extended conjugated porphyrin complexes in bilayer heterojunction devices and their response to ammonia under both dark and UV light conditions. For the first time, we demonstrated an amplification in the sensing properties of an organic heterojunction device under UV light illumination.

By changing the metal centre in octafluoro-metallophthalocyanine complexes, we achieved ambipolar charge transport regimes in organic heterojunction devices. Inversion in the nature of the majority charge carriers within the device was achieved by utilizing external triggers like humidity and temperature, as well as the nature of gas species. The CoF_8Pc-based device changed its polarity depending on the nature of the gas species, while the inversion in the nature of majority charge carriers in the VOF_8Pc-based device was achieved by varying humidity levels and temperature. These devices exhibit bistability under different experimental conditions. However, achieving precise control over the inversion of majority charge carriers, which determines the device's polarity, requires a suitable and controllable external trigger, and it may depend on the molecular composition and the architecture of the device. It is crucial to conduct comprehensive investigations into environmental effects such as humidity and temperature variations when working with ambipolar devices.

Finally, we also studied the influence of the top layer on the polarity of bilayer heterojunction devices. For the first time, we report the pioneering demonstration of polarity inversion within a heterojunction device, by strategically manipulating the *meso*-substituent of the *5,15*-diaryl Ni(II) porphyrin conjugated polymer in the top layer of the devices that contain an ambipolar molecule (CuF_8Pc) as sublayer. Globally, in this project, we focused on understanding and developing unipolar and ambipolar organic heterojunction devices based on molecular materials like phthalocyanines and porphyrins through external triggers and gas sensing.

Perspectives

Perspectives

Our fundamental research into charge transport properties of organic heterojunction devices under different experimental conditions laid a solid foundation for enhancing the device performance and achieving ambipolar charge transport regime within the device. However, to realise these types of ambipolar devices or light assisted devices in real world applications, we need to delve deeper into the underlying mechanisms of each observed effect.

Understanding the impact of light on organic heterojunction devices, such as AM6/luPc$_2$, requires an in-depth investigation into the photophysical properties of the molecules. Specifically, exploring the lifetime of excited charge carriers is crucial for understanding the amplification in device performance. This could provide insights into the mechanisms behind the observed enhancements and help optimize device designs for better efficiency and functionality.

Our findings and investigations into ambipolar molecules and the charge transport regime in ambipolar organic heterojunction-based devices can serve as a guide for future researchers in developing advanced electrical components like ambipolar organic field-effect transistors (OFETs). Our research group has already initiated efforts to realize ambipolar OFETs using octahalogeno-metallophthalocyanine complexes. These materials have promising future due to their ability to support both types of charge carriers near equilibrium, which could lead to more versatile and efficient electronic devices, with the gate voltage as external trigger.

Additionally, the work summarized in the last chapter of this thesis demonstrates that the polarity of heterojunction devices can be influenced by the top layer. This finding can be a precursor to achieve an ambipolar charge transport regime in organic heterojunction devices by modifying the substituents in the top layer while using an ambipolar molecule as the sublayer.

This approach could simplify the design and fabrication of ambipolar devices, making them more practical for widespread use.

Recommendations for Future Research

1. **Photophysical Properties:** Detailed studies on the lifetime and behaviour of excited charge carriers in light-activated devices.
2. **Ambipolar OFETs:** Investigating ambipolar molecules in OFETs.
3. **Environmental Effects:** Exploring the impact of environmental conditions such as humidity and temperature on device stability and performance.
4. **Device Architecture:** Developing new device architectures that leverage the unique properties of ambipolar materials for more efficient and multifunctional electronic components.
5. **Material Optimization:** Investigating a broader range of ambipolar materials and their interactions with different top layers to fine-tune device performance.

References – Bibliography

References:

1. World Health Organization. (2023). Air pollution: The invisible health threat. World Health Organization.https://www.who.int/news-room/feature-stories/detail/air-pollution--the-invisible-health-threat.

2. World Health Organization. (2021). WHO global air quality guidelines: particulate matter (PM2.5 and PM10), ozone, nitrogen dioxide, sulfur dioxide and carbon monoxide. World Health Organization. https://iris.who.int/handle/10665/345329. License: CC BY-NC-SA 3.0 IGO

3. Zhang, X.; Pu, Z.; Su, X.; Li, C.; Zheng, H.; Li, D., Flexible organic field-effect transistors-based biosensors: progress and perspectives. *Analytical and Bioanalytical Chemistry* **2023,** *415* (9), 1607-1625.

4. Rodriguez-Mendez, M.; de Saja, J. A., Chapter 3 - Molecular materials for gas sensors and sensor arrays. In *Advanced Nanomaterials for Inexpensive Gas Microsensors*, Llobet, E., Ed. Elsevier: 2020; pp 37-54.

5. Lessard, B. H.; Grant, T. M.; White, R.; Thibau, E.; Lu, Z.-H.; Bender, T. P., The Position and Frequency of Fluorine Atoms Changes the Electron Donor/Acceptor Properties of Fluorophenoxy Silicon Phthalocyanines Within Organic Photovoltaic Devices. *Journal of Materials Chemistry A* **2015,** *3* (48), 24512-24524.

6. Clarisse, C.; Riou, M. T., Synthesis and characterization of some lanthanide phthalocyanines. *Inorganica Chimica Acta* **1987,** *130* (1), 139-144.

7. Moss, A.; Nevonen, D. E.; Hu, Y.; Nesterov, V. N.; Nemykin, V. N.; Wang, H., Unsymmetric Pentacene- and Pentacenequinone-Fused Porphyrins: Understanding the Effect of Cross- and Linear-Conjugation. *ACS Physical Chemistry Au* **2022,** *2* (6), 468-481.

8. Sukhikh, A.; Klyamer, D.; Bonegardt, D.; Basova, T., Octafluoro-Substituted Phthalocyanines of Zinc, Cobalt, and Vanadyl: Single Crystal Structure, Spectral Study and Oriented Thin Films. *International Journal of Molecular Sciences* **2023,** *24* (3), 2034.

9. Parra, V.; Brunet, J.; Pauly, A.; Bouvet, M., Molecular semiconductor-doped insulator (MSDI) heterojunctions: an alternative transducer for gas chemosensing. *Analyst* **2009,** *134* (9), 1776-1778.

10. Loma Kikobo, G.; Kumar, A.; Vibhu, V.; Ouedraogo, S.; Deshotel, A.; Mateos, M.; Meunier-Prest, R.; Bouvet, M., Photon assisted-inversion of majority charge carriers in

molecular semiconductor-based organic heterojunctions. *Journal of Materials Chemistry C* **2021,** *9* (14), 5008-5020.

11. Gomes, W. P., Chapter 6 - Wet Etching of III—V Semiconductors. In *Semiconductors and Semimetals*, Willardson, R.; Nalwa, H. S., Eds. Elsevier: 2001; Vol. 73, pp 215-295.

12. Bouvet, M., 118 - Radical Phthalocyanines and Intrinsic Semiconduction. In *The Porphyrin Handbook*, Kadish, K. M.; Smith, K. M.; Guilard, R., Eds. Academic Press: Amsterdam, 2003; pp 37-103.

13. Wang, Z.; Park, H.; Lai, Y. H.; Xu, J.; Blaga, C. I.; Yang, F.; Agostini, P.; DiMauro, L. F., The roles of photo-carrier doping and driving wavelength in high harmonic generation from a semiconductor. *Nature Communications* **2017,** *8* (1), 1686.

14. Warren, R.; Cho, E.; Li, H.; Bredas, J.-L.; Koch, N., Understanding the Double Doping of Organic Semiconductors Via State Energy Renormalization upon Charging. *ACS Materials Letters* **2022,** *4* (10), 2051-2057.

15. Kost, A., Chapter 1 - Resonant Optical Nonlinearities in Semiconductors. In *Semiconductors and Semimetals*, Garmire, E.; Kost, A., Eds. Elsevier: 1998; Vol. 58, pp 1-53.

16. Takahashi, T., Semiconductor Devices. In *Encyclopedia of Condensed Matter Physics*, Bassani, F.; Liedl, G. L.; Wyder, P., Eds. Elsevier: Oxford, 2005; pp 264-273.

17. Pope, M.; Swenberg, C. E., *Electronic Processes in Organic Crystals and Polymers*. Oxford University Press: 1999.

18. Giebink, N. C.; Forrest, S. R., Quantum efficiency roll-off at high brightness in fluorescent and phosphorescent organic light emitting diodes. *Physical Review B* **2008,** *77* (23), 235215.

19. Kumar, A.; Meunier-Prest, R.; Bouvet, M., Organic Heterojunction Devices Based on Phthalocyanines: A New Approach to Gas Chemosensing. *Sensors* **2020,** *20* (17), 4700.

20. Kobayashi, N., Phthalocyanines. *Current Opinion in Solid State and Materials Science* **1999,** *4* (4), 345-353.

21. Ghosh, S.; Tsutsui, Y.; Kawaguchi, T.; Matsuda, W.; Nagano, S.; Suzuki, K.; Kaji, H.; Seki, S., Band-like Transport of Charge Carriers in Oriented Two-Dimensional Conjugated Covalent Organic Frameworks. *Chemistry of Materials* **2022,** *34* (2), 736-745.

22. Song, C.; Wang, Z.; Li, J.; Chen, Y.; Zhao, F.; Zhang, H., Extension of π-conjugation and enhancement of electron-withdrawing ability at terminal indenedione for A-π-D-π-A small molecules for application in organic solar cells. *Organic Electronics* **2020,** *81*, 105679.

23. Wu, W.; Liu, Y.; Zhu, D., π-Conjugated molecules with fused rings for organic field-effect transistors: design, synthesis and applications. *Chemical Society Reviews* **2010,** *39* (5), 1489-1502.

24. Silinsh, E. A., Organic Molecular Crystals. Their Electronic States. *Springer Verlag, Berlin, Heidelberg, New York* **1980**.

25. Brédas, J.-L.; Norton, J. E.; Cornil, J.; Coropceanu, V., Molecular Understanding of Organic Solar Cells: The Challenges. *Accounts of Chemical Research* **2009,** *42* (11), 1691-1699.

26. Silinsh, E. A.; Bouvet, M.; Simon, J., Determination of energy gap values in molecular crystals. *Molecular Materials* **1995,** *5* (1), 1-24.

27. Silinsh, E. A.; Capek, V., Organic Molecular Crystals. Interaction, Localization and Transport Phenomena. *AIP Press, New York* **1994**.

28. Coropceanu, V.; Cornil, J.; da Silva Filho, D. A.; Olivier, Y.; Silbey, R.; Brédas, J.-L., Charge Transport in Organic Semiconductors. *Chemical Reviews* **2007,** *107* (4), 926-952.

29. Potje-Kamloth, K., Semiconductor Junction Gas Sensors. *Chemical Reviews* **2008,** *108* (2), 367-399.

30. Sworakowski, J.; Janus, K.; Nespurek, S.; Vala, M., Local States in Organic Materials: Charge Transport and Localization. *IEEE Transactions on Dielectrics and Electrical Insulation* **2006,** *13* (5), 1001-1015.

31. Kahn, A.; Koch, N.; Gao, W., Electronic structure and electrical properties of interfaces between metals and π-conjugated molecular films. *Journal of Polymer Science Part B: Polymer Physics* **2003,** *41* (21), 2529-2548.

32. Hasegawa, T.; Takeya, J., Organic field-effect transistors using single crystals. *Science and Technology of Advanced Materials* **2009,** *10* (2), 024314.

33. Opitz, A.; Frisch, J.; Schlesinger, R.; Wilke, A.; Koch, N., Energy Level Alignment at Interfaces in Organic Photovoltaic Devices. *Journal of Electron Spectroscopy and Related Phenomena* **2013,** *190*, 12-24.

34. Liu, C.; Xu, Y.; Noh, Y.-Y., Contact engineering in organic field-effect transistors. *Materials Today* **2015,** *18* (2), 79-96.

35. Tung, R. T., The Physics and Chemistry of the Schottky Barrier Height. *Applied Physics Reviews* **2014,** *1* (1).

36. Yang, C.; Qian, J.; Jiang, S.; Wang, H.; Wang, Q.; Wan, Q.; Chan, P. K. L.; Shi, Y.; Li, Y., An Optically Modulated Organic Schottky-Barrier Planar-Diode-Based Artificial Synapse. *Advanced Optical Materials* **2020,** *8* (13), 2000153.

37. Albargi, H.; Marnadu, R.; Ganesh Moorthy, S.; Alkorbi, A. S.; Algadi, H.; Shkir, M.; Umar, A.; Sreedevi, G., Deposition of nanostructured Sn doped Co3O4 films by a facile nebulizer spray pyrolysis method and fabrication of p-Sn doped Co3O4/n-Si junction diodes for opto-nanoelectronics. *Sensors and Actuators A: Physical* **2021,** *332*, 113067.

38. Kippelen, B.; Brédas, J.-L., Organic Photovoltaics. *Energy and Environmental Science* **2009,** *2* (3), 251-261.

39. Yan, D.; Wang, H.; Du, B., Interfacial electronic structure in organic semiconductor heterojunctions. *Introduction to Organic Semiconductor Heterojunctions; Wiley: Hoboken, NJ, USA* **2010**, 87-123.

40. Wang, H.; Yan, D., Organic heterostructures in organic field-effect transistors. *NPG Asia Materials* **2010,** *2* (2), 69-78.

41. Chen, L. X., Organic Solar Cells: Recent Progress and Challenges. *ACS Energy Letters* **2019,** *4* (10), 2537-2539.

42. Stavrou, K.; Franca, L. G.; Danos, A.; Monkman, A. P., Key requirements for ultraefficient sensitization in hyperfluorescence organic light-emitting diodes. *Nature Photonics* **2024,** *18* (6), 554-561.

43. Liu, K.; Ouyang, B.; Guo, X.; Guo, Y.; Liu, Y., Advances in flexible organic field-effect transistors and their applications for flexible electronics. *npj Flexible Electronics* **2022,** *6* (1), 1.

44. Root, S. E.; Savagatrup, S.; Printz, A. D.; Rodriquez, D.; Lipomi, D. J., Mechanical Properties of Organic Semiconductors for Stretchable, Highly Flexible, and Mechanically Robust Electronics. *Chemical Reviews* **2017,** *117* (9), 6467-6499.

45. Scholz, R., Organic Semiconductors. In *Encyclopedia of Condensed Matter Physics*, Bassani, F.; Liedl, G. L.; Wyder, P., Eds. Elsevier: Oxford, 2005; pp 206-221.

46. Lizin, S.; Van Passel, S.; De Schepper, E.; Vranken, L., The future of organic photovoltaic solar cells as a direct power source for consumer electronics. *Solar Energy Materials and Solar Cells* **2012,** *103*, 1-10.

47. Singh, T.; Bonne, U., Gas Sensors. In *Reference Module in Materials Science and Materials Engineering*, Elsevier: 2017.

48. Goel, N.; Kunal, K.; Kushwaha, A.; Kumar, M., Metal oxide semiconductors for gas sensing. *Engineering Reports* **2023,** *5* (6), e12604.

49. Bakker, E.; Telting-Diaz, M., Electrochemical Sensors. *Analytical Chemistry* **2002,** *74* (12), 2781-2800.

50. Vivekanand, M.; Rashmi; Sukriti, Optical Gas Sensors. In *Metal-Oxide Gas Sensors*, Soumen, D.; Gorachand, D., Eds. IntechOpen: Rijeka, 2022; p Ch. 2.

51. Bernards, D. A.; Owens, R. M.; Malliaras, G. G. In *Organic semiconductors in sensor applications*, Springer: 2008.

52. Franco, M. A.; Conti, P. P.; Andre, R. S.; Correa, D. S., A review on chemiresistive ZnO gas sensors. *Sensors and Actuators Reports* **2022,** *4*, 100100.

53. Seiyama, T.; Kato, A.; Fujiishi, K.; Nagatani, M., A New Detector for Gaseous Components Using Semiconductive Thin Films. *Analytical Chemistry* **1962,** *34* (11), 1502-1503.

54. Nascimento, E. P.; Firmino, H. C. T.; Neves, G. A.; Menezes, R. R., A review of recent developments in tin dioxide nanostructured materials for gas sensors. *Ceramics International* **2022,** *48* (6), 7405-7440.

55. Sharma, A.; Eadi, S. B.; Noothalapati, H.; Otyepka, M.; Lee, H.-D.; Jayaramulu, K., Porous materials as effective chemiresistive gas sensors. *Chemical Society Reviews* **2024,** *53* (5), 2530-2577.

56. Duan, X.; Zhang, Y.; Wang, H.; Dai, F.; Yang, G.; Chen, Y., A phthalocyanine sensor array based on sensitivity and current changes for highly sensitive identification of three toxic gases at ppb levels. *New Journal of Chemistry* **2020,** *44* (31), 13240-13248.

57. Elakia, M.; Gobinath, M.; Sivalingam, Y.; Palani, E.; Ghosh, S.; Nutalapati, V.; Surya, V. J., Investigation on visible light assisted gas sensing ability of multi-walled carbon nanotubes coated with pyrene based organic molecules. *Physica E: Low-dimensional Systems and Nanostructures* **2020,** *124*, 114232.

58. Zhao, M.; Yan, L.; Zhang, X.; Xu, L.; Song, Z.; Chen, P.; Dong, F.; Chu, W., Room Temperature NH3 Detection of Ti/Graphene Devices Promoted by Visible Light Lllumination. *Journal of Materials Chemistry C* **2017,** *5* (5), 1113-1120.

59. Fang, Q.; Chetwynd, D. G.; Covington, J. A.; Toh, C. S.; Gardner, J. W., Micro-gas-sensor with conducting polymers. *Sensors and Actuators B: Chemical* **2002,** *84* (1), 66-71.

60. Park, S. J.; Park, C. S.; Yoon, H., Chemo-Electrical Gas Sensors Based on Conducting Polymer Hybrids. *Polymers* **2017,** *9* (5), 155.

61. Tseng, H.-R.; Wang, J.; Alam, M. M., Electrochemically Fabricated Conducting Polymer Nanoframework Electrode Junctions That Function as Resistive Sensors. *MRS Online Proceedings Library* **2004,** *828* (1), 91-96.

62. Liu, X.; Zheng, W.; Kumar, R.; Kumar, M.; Zhang, J., Conducting polymer-based nanostructures for gas sensors. *Coordination Chemistry Reviews* **2022,** *462*, 214517.

63. Sahabudeen, H.; Qi, H.; Glatz, B. A.; Tranca, D.; Dong, R.; Hou, Y.; Zhang, T.; Kuttner, C.; Lehnert, T.; Seifert, G.; Kaiser, U.; Fery, A.; Zheng, Z.; Feng, X., Wafer-Sized Multifunctional Polyimine-Based Two-Dimensional Conjugated Polymers With High Mechanical Stiffness. *Nature Communications* **2016,** *7* (1), 13461.

64. Paolesse, R.; Nardis, S.; Monti, D.; Stefanelli, M.; Di Natale, C., Porphyrinoids for Chemical Sensor Applications. *Chemical Reviews* **2017,** *117* (4), 2517-2583.

65. Saini, R.; Kaur, R.; Devi, P.; Gasso, S.; Sharma, S., Tailoring the performance of phthalocyanine-based sensor: Side chain substitution and nanofabrication. *Materials Today: Proceedings* **2023,** *92*, 574-578.

66. Ho, K.-C.; Tsou, Y.-H., Chemiresistor-type NO gas sensor based on nickel phthalocyanine thin films. *Sensors and Actuators B: Chemical* **2001,** *77* (1), 253-259.

67. Bohrer, F. I.; Sharoni, A.; Colesniuc, C.; Park, J.; Schuller, I. K.; Kummel, A. C.; Trogler, W. C., Gas Sensing Mechanism in Chemiresistive Cobalt and Metal-Free Phthalocyanine Thin Films. *Journal of the American Chemical Society* **2007,** *129* (17), 5640-5646.

68. Jang, J.; Oh, J. H., Novel crystalline supramolecular assemblies of amorphous polypyrrole nanoparticles through surfactant templating. *Chemical Communications* **2002,** (19), 2200-2201.

69. Kumar, S.; Tiwari, P.; Zymbler, M., Internet of Things is a revolutionary approach for future technology enhancement: a review. *Journal of Big Data* **2019,** *6* (1), 111.

70. Yang, Y.; Gong, W.; Li, X.; Liu, Y.; Liang, Y.; Chen, B.; Yang, Y.; Luo, X.; Xu, K.; Yuan, C., Light-assisted room temperature gas sensing performance and mechanism of direct Z-scheme MoS2/SnO2 crystal faceted heterojunctions. *Journal of Hazardous Materials* **2022,** *436*, 129246.

71. Chen, R.; Wang, J.; Luo, S.; Xiang, L.; Li, W.; Xie, D., Unraveling photoexcited electron transfer pathway of oxygen vacancy-enriched ZnO/Pd hybrid toward visible light-enhanced methane detection at a relatively low temperature. *Applied Catalysis B: Environmental* **2020,** *264*, 118554.

72. Wang, J.; Fan, S.; Xia, Y.; Yang, C.; Komarneni, S., Room-temperature gas sensors based on ZnO nanorod/Au hybrids: Visible-light-modulated dual selectivity to NO2 and NH3. *Journal of Hazardous Materials* **2020,** *381*, 120919.

73. Zhang, Q.; Xie, G.; Xu, M.; Su, Y.; Tai, H.; Du, H.; Jiang, Y., Visible light-assisted room temperature gas sensing with ZnO-Ag heterostructure nanoparticles. *Sensors and Actuators B: Chemical* **2018,** *259*, 269-281.

74. Chizhov, A. S.; Rumyantseva, M. N.; Vasiliev, R. B.; Filatova, D. G.; Drozdov, K. A.; Krylov, I. V.; Abakumov, A. M.; Gaskov, A. M., Visible Light Activated Room Temperature Gas Sensors Based on Nanocrystalline ZnO Sensitized with CdSe Quantum Dots. *Sensors and Actuators B: Chemical* **2014,** *205*, 305-312.

75. Di Zazzo, L.; Kumar, A.; Meunier-Prest, R.; Di Natale, C.; Paolesse, R.; Bouvet, M., Electrosynthesized copper polycorroles as versatile materials in double lateral heterojunctions. *Chemical Engineering Journal* **2023,** *458*, 141465.

76. Mateos, M.; Meunier-Prest, R.; Heintz, O.; Herbst, F.; Suisse, J.-M.; Bouvet, M., Comprehensive Study of Poly(2,3,5,6-tetrafluoroaniline): From Electrosynthesis to Heterojunctions and Ammonia Sensing. *ACS Applied Materials and Interfaces* **2018,** *10* (23), 19974-19986.

77. Sawatzki-Park, M.; Wang, S.-J.; Kleemann, H.; Leo, K., Highly Ordered Small Molecule Organic Semiconductor Thin-Films Enabling Complex, High-Performance Multi-Junction Devices. *Chemical Reviews* **2023,** *123* (13), 8232-8250.

78. Ellis, J. E.; Crawford, S. E.; Kim, K.-J., Metal–organic framework thin films as versatile chemical sensing materials. *Materials Advances* **2021,** *2* (19), 6169-6196.

79. Chen, W.; Qi, D.-C.; Huang, H.; Gao, X.; Wee, A. T. S., Organic–Organic Heterojunction Interfaces: Effect of Molecular Orientation. *Advanced Functional Materials* **2011,** *21* (3), 410-424.

80. Mateos, M.; Tchangaï, M.-D.; Meunier-Prest, R.; Heintz, O.; Herbst, F.; Suisse, J.-M.; Bouvet, M., Low Conductive Electrodeposited Poly(2,5-dimethoxyaniline) as a Key Material in a Double Lateral Heterojunction, for Sub-ppm Ammonia Sensing in Humid Atmosphere. *ACS Sensors* **2019,** *4* (3), 740-747.

81. Bouvet, M.; Mateos, M.; Wannebroucq, A.; Navarrete, E.; Llobet, E., A tungsten oxide–lutetium bisphthalocyanine n–p–n heterojunction: from nanomaterials to a new transducer for chemo-sensing. *Journal of Materials Chemistry C* **2019,** *7* (21), 6448-6455.

82. Wu, Y.; Ma, P.; Wu, N.; Kong, X.; Bouvet, M.; Li, X.; Chen, Y.; Jiang, J., Two-Step Solution-Processed Two-Component Bilayer Phthalocyaninato Copper-Based Heterojunctions with Interesting Ambipolar Organic Transiting and Ethanol-Sensing Properties. *Advanced Materials Interfaces* **2016,** *3* (16), 1600253.

83. Parra, V.; Bouvet, M.; Patent US8450725 B2, 2013.

84. André, J.-J.; Holczer, K.; Petit, P.; Riou, M.-T.; Clarisse, C.; Even, R.; Fourmigué, M.; Simon, J., Electrical and magnetic properties of thin films and single crystals of bis(phthalocyaninato)lutetium. *Chemical Physics Letters* **1985,** *115* (4), 463-466.

85. Bouvet, M.; Xiong, H.; Parra, V., Molecular semiconductor-doped insulator (MSDI) heterojunctions: Oligothiophene/bisphtalocyanine (LuPc2) and perylene/bisphthalocyanine as new structures for gas sensing. *Sensors and Actuators B: Chemical* **2010,** *145* (1), 501-506.

86. Bengasi, G.; Meunier-Prest, R.; Baba, K.; Kumar, A.; Pellegrino, A. L.; Boscher, N. D.; Bouvet, M., Molecular Engineering of Porphyrin-Tapes/Phthalocyanine Heterojunctions for a Highly Sensitive Ammonia Sensor. *Advanced Electronic Materials* **2020,** *6* (12), 2000812.

87. Wannebroucq, A.; Gruntz, G.; Suisse, J.-M.; Nicolas, Y.; Meunier-Prest, R.; Mateos, M.; Toupance, T.; Bouvet, M., New n-type molecular semiconductor–doped insulator (MSDI) heterojunctions combining a triphenodioxazine (TPDO) and the lutetium bisphthalocyanine (LuPc2) for ammonia sensing. *Sensors and Actuators B: Chemical* **2018,** *255*, 1694-1700.

88. Mateos, M.; Meunier-Prest, R.; Suisse, J.-M.; Bouvet, M., Modulation of the organic heterojunction behavior, from electrografting to enhanced sensing properties. *Sensors and Actuators B: Chemical* **2019,** *299*, 126968.

89. Bouvet, M.; Ouedraogo, S.; Meunier-Prest, R., Ambipolar Materials for Gas Sensing. In *Ambipolar Materials and Devices*, Zhou, Y.; Han, S.-T., Eds. The Royal Society of Chemistry: 2020; p 446.

90. Murdey, R.; Sato, N.; Bouvet, M., Frontier Electronic Structures in Fluorinated Copper Phthalocyanine Thin Films Studied Using Ultraviolet and Inverse Photoemission Spectroscopies. *Molecular Crystals and Liquid Crystals* **2006,** *455* (1), 211-218.

91. Kong, X.; Zhang, X.; Gao, D.; Qi, D.; Chen, Y.; Jiang, J., Air-Stable Ambipolar Field-Effect Transistor Based on a Solution-Processed Octanaphthoxy-Substituted Tris(phthalocyaninato) Europium Semiconductor With High and Balanced Carrier Mobilities. *Chemical Science* **2015,** *6* (3), 1967-1972.

92. Lu, G.; Chen, Y.; Zhang, Y.; Bao, M.; Bian, Y.; Li, X.; Jiang, J., Morphology Controlled Self-Assembled Nanostructures of Sandwich Mixed (Phthalocyaninato)(Porphyrinato)

Europium Triple-Deckers. Effect of Hydrogen Bonding on Tuning the Intermolecular Interaction. *Journal of the American Chemical Society* **2008,** *130* (35), 11623-11630.

93. Guillaud, G.; Al Sadoun, M.; Maitrot, M.; Simon, J.; Bouvet, M., Field-effect transistors based on intrinsic molecular semiconductors. *Chemical Physics Letters* **1990,** *167* (6), 503-506.

94. Wannebroucq, A.; Ouedraogo, S.; Meunier-Prest, R.; Suisse, J.-M.; Bayo, M.; Bouvet, M., On the interest of ambipolar materials for gas sensing. *Sensors and Actuators B: Chemical* **2018,** *258*, 657-664.

95. Nayak, P. K.; Rosenberg, R.; Barnea-Nehoshtan, L.; Cahen, D., O2 and organic semiconductors: Electronic effects. *Organic Electronics* **2013,** *14* (3), 966-972.

96. Dutta, S.; Lewis, S. D.; Dodabalapur, A., Hybrid organic/inorganic ambipolar thin film transistor chemical sensor. *Applied Physics Letters* **2011,** *98* (21).

97. Ouedraogo, S.; Meunier-Prest, R.; Kumar, A.; Bayo-Bangoura, M.; Bouvet, M., Modulating the Electrical Properties of Organic Heterojunction Devices Based On Phthalocyanines for Ambipolar Sensors. *ACS Sensors* **2020,** *5* (6), 1849-1857.

98. Kumar, A.; Meunier-Prest, R.; Lesniewska, E.; Bouvet, M., Interplay of electrode geometry and bias on charge transport in organic heterojunction gas sensors. *Sensors and Actuators B: Chemical* **2022,** *369*, 132313.

99. Dianatdar, A.; Bose, R. K., Oxidative chemical vapor deposition for synthesis and processing of conjugated polymers: a critical review. *Journal of Materials Chemistry C* **2023,** *11* (35), 11776-11802.

100. Babooram, K., Chapter 1 - Brief overview of polymer science. In *Polymer Science and Nanotechnology*, Narain, R., Ed. Elsevier: 2020; pp 3-12.

101. Heydari Gharahcheshmeh, M.; Gleason, K. K., Device Fabrication Based on Oxidative Chemical Vapor Deposition (oCVD) Synthesis of Conducting Polymers and Related Conjugated Organic Materials. *Advanced Materials Interfaces* **2019,** *6* (1), 1801564.

102. Di Zazzo, L.; Ganesh Moorthy, S.; Meunier-Prest, R.; Lesniewska, E.; Di Natale, C.; Paolesse, R.; Bouvet, M., Ammonia and Humidity Sensing by Phthalocyanine–Corrole Complex Heterostructure Devices. *Sensors* **2023,** *23* (15), 6773.

103. Yim, S.; Heutz, S.; Jones, T. S., Influence of intermolecular interactions on the structure of phthalocyanine layers in molecular thin film heterostructures. *Physical Review B* **2003,** *67* (16), 165308.

104. Hsu, C. H.; Mansfeld, F., Technical Note: Concerning the Conversion of the Constant Phase Element Parameter Y0 into a Capacitance. *Corrosion* **2001,** *57* (9), 747-748.

105. Chang, B.-Y., Conversion of a Constant Phase Element to an Equivalent Capacitor. *Journal of Electrochemical Science and Technology* **2020,** *11* (3), 318-321.

106. Brug, G. J.; van den Eeden, A. L. G.; Sluyters-Rehbach, M.; Sluyters, J. H., The analysis of electrode impedances complicated by the presence of a constant phase element. *Journal of Electroanalytical Chemistry and Interfacial Electrochemistry* **1984,** *176* (1), 275-295.

107. Scisco, G. P.; Orazem, M. E.; Ziegler, K. J.; Jones, K. S., On the rate capability of supercapacitors characterized by a constant-phase element. *Journal of Power Sources* **2021,** *516*, 230700.

108. Hirschorn, B.; Orazem, M. E.; Tribollet, B.; Vivier, V.; Frateur, I.; Musiani, M., Determination of effective capacitance and film thickness from constant-phase-element parameters. *Electrochimica Acta* **2010,** *55* (21), 6218-6227.

109. Gateman, S. M.; Gharbi, O.; Gomes de Melo, H.; Ngo, K.; Turmine, M.; Vivier, V., On the use of a constant phase element (CPE) in electrochemistry. *Current Opinion in Electrochemistry* **2022,** *36*, 101133.

110. VanCott, T. C.; Gasyna, Z.; Schatz, P. N.; Boyle, M. E., Magnetic circular dichroism and absorption spectra of lutetium bis(phthalocyanine) isolated in an argon matrix. *The Journal of Physical Chemistry* **1995,** *99* (13), 4820-4830.

111. Karan, S.; Basak, D.; Mallik, B., Copper phthalocyanine nanoparticles and nanoflowers. *Chemical Physics Letters* **2007,** *434* (4), 265-270.

112. Caplins, B. W.; Mullenbach, T. K.; Holmes, R. J.; Blank, D. A., Intermolecular Interactions Determine Exciton Lifetimes in Neat Films and Solid State Solutions of Metal-Free Phthalocyanine. *The Journal of Physical Chemistry C* **2015,** *119* (49), 27340-27347.

113. Ortí, E.; Brédas, J. L.; Clarisse, C., Electronic Structure of Phthalocyanines: Theoretical Investigation of the Optical Properties of Phthalocyanine Monomers, Dimers, and Crystals. *The Journal of Chemical Physics* **1990,** *92* (2), 1228.

114. Ouedraogo, S.; Coulibaly, T.; Meunier-Prest, R.; Bayo-Bangoura, M.; Bouvet, M., p-Type and n-type conductometric behaviors of octachloro-metallophthalocyanine-based heterojunctions, the key role of the metal. *Journal of Porphyrins and Phthalocyanines* **2020,** *24* (05n07), 750-757.

115. MacFarlane, D. R.; Cherepanov, P. V.; Choi, J.; Suryanto, B. H. R.; Hodgetts, R. Y.; Bakker, J. M.; Ferrero Vallana, F. M.; Simonov, A. N., A Roadmap to the Ammonia Economy. *Joule* **2020,** *4* (6), 1186-1205.

116. Lucentini, I.; Garcia, X.; Vendrell, X.; Llorca, J., Review of the Decomposition of Ammonia to Generate Hydrogen. *Industrial & Engineering Chemistry Research* **2021,** *60* (51), 18560-18611.

117. Shetty, S. S.; Jayarama, A.; Bhat, S.; Satyanarayan; Karunasagar, I.; Pinto, R., A review on metal-oxide based trace ammonia sensor for detection of renal disease by exhaled breath analysis. *Materials Today: Proceedings* **2022,** *55*, 113-117.

118. Kumar, A.; Vibhu, V.; Bassat, J.-M.; Nohl, L.; de Haart, L. G. J.; Bouvet, M.; Eichel, R.-A., Ammonia as a Potential Energy Vector in the Burgeoning Hydrogen Economy. *ChemElectroChem* **2024,** *11* (15), e202300845.

119. Directive 2008/50/EC of the European Parliament and of the Council of 21May 2008, on Ambient Air Quality and Cleaner Air for Europe; 2008; Vol. L 152, pp 1–44.

120. Chen, H.-I.; Hsiao, C.-Y.; Chen, W.-C.; Chang, C.-H.; Chou, T.-C.; Liu, I. P.; Lin, K.-W.; Liu, W.-C., Characteristics of a Pt/NiO Thin Film-Based Ammonia Gas Sensor. *Sensors and Actuators B: Chemical* **2018,** *256*, 962-967.

121. Tu, Y.; Kyle, C.; Luo, H.; Zhang, D.-W.; Das, A.; Briscoe, J.; Dunn, S.; Titirici, M.-M.; Krause, S., Ammonia Gas Sensor Response of a Vertical Zinc Oxide Nanorod-Gold Junction Diode at Room Temperature. *ACS Sensors* **2020,** *5* (11), 3568-3575.

122. Muzikante, I.; Parra, V.; Dobulans, R.; Fonavs, E.; Latvels, J.; Bouvet, M., A Novel Gas Sensor Transducer Based on Phthalocyanine Heterojunction Devices. *Sensors* **2007,** *7* (11), 2984-2996.

123. Yang, Y.; Zhang, G.; Luo, H.; Yao, J.; Liu, Z.; Zhang, D., Highly Sensitive Thin-Film Field-Effect Transistor Sensor for Ammonia with the DPP-Bithiophene Conjugated Polymer Entailing Thermally Cleavable tert-Butoxy Groups in the Side Chains. *ACS Applied Materials and Interfaces* **2016,** *8* (6), 3635-43.

124. Rajeev, V. R.; Paulose, A. K.; Unni, K. N. N., Ammonia Gas Detection Using Field-Effect Transistor Based on a Solution-Processable Organic Semiconductor. *Vacuum* **2018,** *158*, 271-277.

125. Melville, O. A.; Grant, T. M.; Mirka, B.; Boileau, N. T.; Park, J.; Lessard, B. H., Ambipolarity and Air Stability of Silicon Phthalocyanine Organic Thin-Film Transistors. *Advanced Electronic Materials* **2019,** *5* (8), 1900087.

126. Lessard, B. H., The Rise of Silicon Phthalocyanine: From Organic Photovoltaics to Organic Thin Film Transistors. *ACS Applied Materials and Interfaces* **2021,** *13* (27), 31321-31330.

127. King, B.; Melville, O. A.; Rice, N. A.; Kashani, S.; Tonnelé, C.; Raboui, H.; Swaraj, S.; Grant, T. M.; McAfee, T.; Bender, T. P.; Ade, H.; Castet, F.; Muccioli, L.; Lessard, B. H., Silicon Phthalocyanines for n-Type Organic Thin-Film Transistors: Development of Structure–Property Relationships. *ACS Applied Electronic Materials* **2021,** *3* (1), 325-336.

128. Melville, O. A.; Grant, T. M.; Lessard, B. H., Silicon Phthalocyanines as N-Type Semiconductors in Organic Thin Film Transistors. *Journal of Materials Chemistry C* **2018,** *6* (20), 5482-5488.

129. Cranston, R. R.; Lessard, B. H., Metal Phthalocyanines: Thin-Film Formation, Microstructure, and Physical Properties. *RSC Advances* **2021,** *11* (35), 21716-21737.

130. Grant, T. M.; Dindault, C.; Rice, N. A.; Swaraj, S.; Lessard, B. H., Synthetically facile organic solar cells with >4% efficiency using P3HT and a silicon phthalocyanine non-fullerene acceptor. *Materials Advances* **2021,** *2* (8), 2594-2599.

131. Vebber, M. C.; Rice, N. A.; Brusso, J. L.; Lessard, B. H., Variance-resistant PTB7 and axially-substituted silicon phthalocyanines as active materials for high-Voc organic photovoltaics. *Scientific Reports* **2021,** *11* (1), 15347.

132. Polyakov, M.; Ivanova, V.; Klyamer, D.; Köksoy, B.; Şenocak, A.; Demirbaş, E.; Durmuş, M.; Basova, T., A Hybrid Nanomaterial Based on Single Walled Carbon Nanotubes Cross-Linked via Axially Substituted Silicon (IV) Phthalocyanine for Chemiresistive Sensors. *Molecules* **2020,** *25* (9), 2073.

133. Fernandes, A. N.; Richardson, T. H., Conductometric gas sensing studies of tert-butyl silicon-[bis ethyloxy]-phthalocyanine LB films. *Journal of Materials Science* **2008,** *43* (4), 1305-1310.

134. Jeffery, P. D.; Burr, P. M., Gas-sensing properties of polymeric silicon and germanium phthalocyanine films. *Sensors and Actuators B: Chemical* **1989,** *17* (3), 475-480.

135. Ganesh Moorthy, S.; Arvidson, J.; Meunier-Prest, R.; Wang, H.; Bouvet, M., π-Extended Porphyrin–Phthalocyanine Heterojunction Devices Exhibiting High Ammonia Sensitivity with a Remarkable Light Effect. *ACS Sensors* **2024,** *9* (2), 883-894.

136. Quinn, J. T. E.; Zhu, J.; Li, X.; Wang, J.; Li, Y., Recent Progress in the Development of N-Type Organic semiconductors for organic Field Effect Transistors. *Journal of Materials Chemistry C* **2017,** *5* (34), 8654-8681.

137. Lessard, B. H.; White, R. T.; Al-Amar, M.; Plint, T.; Castrucci, J. S.; Josey, D. S.; Lu, Z.-H.; Bender, T. P., Assessing the Potential Roles of Silicon and Germanium Phthalocyanines in Planar Heterojunction Organic Photovoltaic Devices and How Pentafluoro Phenoxylation

Can Enhance π–π Interactions and Device Performance. *ACS Applied Materials & Interfaces* **2015,** *7* (9), 5076-5088.

138. Bouvet, M.; Gaudillat, P.; Suisse, J.-M., Lanthanide macrocyclic complexes: from molecules to materials and from materials to devices. *Journal of Porphyrins and Phthalocyanines* **2013,** *17* (08n09), 628-635.

139. Rakow, N. A.; Suslick, K. S., A Colorimetric Sensor Array for Odour Visualization. *Nature* **2000,** *406* (6797), 710.

140. Di Natale, C.; Filippini, D.; Pennazza, G.; Santonico, M.; Paolesse, R.; Bellincontro, A.; Mencarelli, F.; D'Amico, A.; Lundström, I., Sorting of Apricots with Computer Screen Photoassisted Spectral Reflectance Analysis and Electronic Nose. *Sensors and Actuators B: Chemical* **2006,** *119* (1), 70.

141. Paolesse, R.; Monti, D.; La Monica, L.; Venanzi, M.; Froiio, A.; Nardis, S.; Di Natale, C.; Martinelli, E.; D'Amico, A., Preparation and Self-Assembly of Chiral Porphyrin Diads on the Gold Electrodes of Quartz Crystal Microbalances: a Novel Potential Approach to the Development of Enantioselective Chemical Sensors. *Chemistry: A European Journal* **2002,** *8* (11), 2476.

142. Macagnano, A.; Sgreccia, E.; Zampetti, E.; Pantalei, S.; Di Natale, C.; Paolesse, R.; D'Amico, A., Potentials and Limitations of a Porphyrin-Based at-Cut Resonator for Sensing Applications. *Sensors and Actuators B: Chemical* **2008,** *130*, 411.

143. Garg, K.; Singh, A.; Debnath, A. K.; Nayak, S. K.; Chattopadhyay, S.; Aswal, D. K.; Hayakawa, Y.; Gupta, S. K.; Yakhmi, J. V., Bis-Porphyrin Films as Ppb Level Chemiresistive Sensors. *Chemical Physics Letters* **2010,** *488*, 27.

144. Penza, M.; Rossi, R.; Alvisi, M.; Signore, M. A.; Serra, E.; Paolesse, R.; Amico, A. D.; Di Natale, C., Metalloporphyrins-Modified Carbon Nanotubes Networked Films-Based Chemical Sensors for Enhanced Gas Sensitivity. *Sensors and Actuators B: Chemical* **2010,** *144* (2), 387.

145. Saxena, S.; Verma, A. L., Metal-Tetraphenylporphyrin Functionalized Carbon Nanotube Composites as Sensor for Benzene, Toluene and Xylene Vapors. *Advanced Materials Research* **2014,** *5* (8), 472.

146. Liu, S. F.; Moh, L. C. H.; Swager, T. M., Single-Walled Carbon Nanotube–Metalloporphyrin Chemiresistive Gas Sensor Arrays for Volatile Organic Compounds. *Chemistry of Materials* **2015,** *27*, 3560.

147. Kumar, A.; Meunier-Prest, R.; Herbst, F.; Heintz, O.; Lesniewska, E.; Bouvet, M., Covalent grafting of aryls to modulate the electrical properties of phthalocyanine-based heterostructures: Application to ammonia sensing. *Chemical Engineering Journal* **2022,** *436*, 135207.

148. Bouvet, M.; Gaudillat, P.; Kumar, A.; Sauerwald, T.; Schüler, M.; Schütze, A.; Suisse, J. M., Revisiting the Electronic Properties of Molecular Semiconductor – Doped Insulator (MSDI) Heterojunctions Through Impedance and Chemosensing Studies. *Organic Electronics* **2015,** *26*, 345.

149. Comini, E.; Cristalli, A.; Faglia, G.; Sberveglieri, G., Light Enhanced Gas Sensing Properties of Indium Oxide and Tin Dioxide Sensors. *Sensors and Actuators B: Chemical* **2000,** *65* (1–3), 260.

150. Comini, E.; Faglia, G.; Sberveglieri, G., UV Light Activation of Tin Oxide Thin Films for NO2 Sensing at Low Temperatures. *Sensors and Actuators B: Chemical* **2001,** *78* (1–3), 73.

151. Gonzalez, O.; Welearegay, T. G.; Vilanova, X.; Llobet, E., Using the Transient Response of WO3 Nanoneedles Under Pulsed UV Light in the Detection of NH3 and NO2. *Sensors* **2018,** *18* (5), 1346.

152. Nakamura, Y.; Ishikura, Y.; Morita, Y.; Takagi, H.; Fujitsu, S., Photo-Assisted Aromatic VOC Sensing by a P-NiO:Li/N-ZnO Transparent Heterojunction Sensor Element. *Sensors and Actuators B: Chemical* **2013,** *187*, 578.

153. Chen, H.; Zhang, M.; Bo, R.; Barugkin, C.; Zheng, J.; Ma, Q.; Huang, S.; Ho-Baillie, A. W. Y.; Catchpole, K. R.; Tricoli, A., Superior Self-Powered Room-Temperature Chemical Sensing with Light-Activated Inorganic Halides Perovskites. *Small* **2018,** *14* (7), 1702571.

154. Sivalingam, Y.; Martinelli, E.; Catini, A.; Magna, G.; Pomarico, G.; Basoli, F.; Paolesse, R.; Di Natale, C., Gas-Sensitive Photoconductivity of Porphyrin-Functionalized ZnO Nanorods. *The Journal of Physical Chemistry C* **2012,** *116* (16), 9151-9157.

155. Magna, G.; Muduganti, M.; Stefanelli, M.; Sivalingam, Y.; Zurlo, F.; Di Bartolomeo, E.; Catini, A.; Martinelli, E.; Paolesse, R.; Di Natale, C., Light-Activated Porphyrinoid-Capped Nanoparticles for Gas Sensing. *ACS Applied Nano Materials* **2021,** *4* (1), 414.

156. Alzate-Carvajal, N.; Park, J.; Pykal, M.; Lazar, P.; Rautela, R.; Scarfe, S.; Scarfe, L.; Ménard, J. M.; Otyepka, M.; Luican-Mayer, A., Graphene Field Effect Transistors: a Sensitive Platform for Detecting Sarin. *ACS Applied Materials and Interfaces* **2021,** *13* (51), 61751.

157. Carvalho, C. M. B.; Brocksom, T. J.; de Oliveira, K. T., Tetrabenzoporphyrins; Synthetic Developments and Applications. *Chemical Society Reviews* **2013,** *42* (8), 3302.

158. Roznyatovskiy, V. V.; Lee, C. H.; Sessler, J. L., Π-Extended Isomeric and Expanded Porphyrins. *Chemical Society Reviews* **2013,** *42* (5), 1921.

159. Kumar, R.; Liu, X.; Zhang, J.; Kumar, M., Room-Temperature Gas Sensors Under Photoactivation: From Metal Oxides to 2D Materials. *Nano-Micro Letters* **2020,** *12* (1), 164.

160. Ganesh Moorthy, S.; King, B.; Kumar, A.; Lesniewska, E.; Lessard, B. H.; Bouvet, M., Molecular Engineering of Silicon Phthalocyanine to Improve the Charge Transport and Ammonia Sensing Properties of Organic Heterojunction Gas Sensors. *Advanced Sensor Research* **2022,** *2* (3), 2200030.

161. Bommert, M.; Schuler, B.; Pignedoli, C. A.; Widmer, R.; Gröning, O., Ambipolar charge transfer of larger fullerenes enabled by the modulated surface potential of h-BN/Rh(111). *Carbon* **2024,** *216*, 118592.

162. Stein, E.; Nahor, O.; Stolov, M.; Freger, V.; Petruta, I. M.; McCulloch, I.; Frey, G. L., Ambipolar blend-based organic electrochemical transistors and inverters. *Nature Communications* **2022,** *13* (1), 5548.

163. Meijer, E. J.; de Leeuw, D. M.; Setayesh, S.; van Veenendaal, E.; Huisman, B. H.; Blom, P. W.; Hummelen, J. C.; Scherf, U.; Kadam, J.; Klapwijk, T. M., Solution-processed ambipolar organic field-effect transistors and inverters. *Nature materials* **2003,** *2* (10), 678-82.

164. Zeng, W.-J.; Zhou, X.-Y.; Pan, X.-J.; Song, C.-L.; Zhang, H.-L., High Performance CMOS-like Inverter Based on an Ambipolar Organic Semiconductor and Low Cost Metals. *AIP Advances* **2013,** *3* (1).

165. Bouvet, M.; Leroy, A.; Simon, J.; Tournilhac, F.; Guillaud, G.; Lessnick, P.; Maillard, A.; Spirkovitch, S.; Debliquy, M.; de Haan, A.; Decroly, A., Detection and titration of ozone using metallophthalocyanine based field effect transistors. *Sensors and Actuators B: Chemical* **2001,** *72* (1), 86-93.

166. Occupational Safety and Health Series 75 - Review report on laws and practice related to human factors/ergonomics and manual handling at the workplace, https://www.ilo.org/global/topics/safety-and-health-at-work/resources-library/publications/WCMS_906971, 2023.

167. Gaudillat, P.; Jurin, F.; Lakard, B.; Buron, C.; Suisse, J.-M.; Bouvet, M., From the Solution Processing of Hydrophilic Molecules to Polymer-Phthalocyanine Hybrid Materials for Ammonia Sensing in High Humidity Atmospheres. *Sensors* **2014,** *14* (8), 13476-13495.

168. Lechner, B. A. J.; Kim, Y.; Feibelman, P. J.; Henkelman, G.; Kang, H.; Salmeron, M., Solvation and Reaction of Ammonia in Molecularly Thin Water Films. *The Journal of Physical Chemistry C* **2015,** *119* (40), 23052-23058.

169. Viricelle, J. P.; Pauly, A.; Mazet, L.; Brunet, J.; Bouvet, M.; Varenne, C.; Pijolat, C., Selectivity improvement of semi-conducting gas sensors by selective filter for atmospheric pollutants detection. *Materials Science and Engineering: C* **2006,** *26* (2), 186-195.

170. Westerlund, S.; Ekstam, L., Capacitor theory. *IEEE Transactions on Dielectrics and Electrical Insulation* **1994,** *1* (5), 826-839.

171. Ekanayake, S. R.; Rodanski, B. S.; Cortie, M. B.; Ford, M. J. In *Quantum electrical characteristics of nanocapacitors*, 2003 Third IEEE Conference on Nanotechnology, 2003. IEEE-NANO 2003., 12-14 Aug. 2003; 2003; pp 756-759 vol. 2.

172. Kong, X.; Tarakanova, E. N.; Du, X.; Tomilova, L. G.; Chen, Y., Discrimination and detection of NO2, NH3 and H2S using sensor array based on three ambipolar sandwich tetradiazepinoporphyrazinato/phthalocyaninato europium double-decker complexes. *Materials Advances* **2023,** *4* (6), 1515-1522.

173. Liu, S.; Wang, H.; Wang, X.; Li, S.; Liu, H.; Chen, Y.; Li, X., Diverse sensor responses from two functionalized tris(phthalocyaninato)europium ambipolar semiconductors towards three oxidative and reductive gases. *Journal of Materials Chemistry C* **2019,** *7* (2), 424-433.

174. Ganesh Moorthy, S.; Bouvet, M., Effects of Visible Light on Gas Sensors: From Inorganic Resistors to Molecular Material-Based Heterojunctions. *Sensors* **2024,** *24* (5), 1571.

175. Zegebreal, L. T.; Tegegne, N. A.; Hone, F. G., Recent progress in hybrid conducting polymers and metal oxide nanocomposite for room-temperature gas sensor applications: A review. *Sensors and Actuators A: Physical* **2023,** *359*, 114472.

176. Verma, A.; Gupta, R.; Verma, A. S.; Kumar, T., A review of composite conducting polymer-based sensors for detection of industrial waste gases. *Sensors and Actuators Reports* **2023,** *5*, 100143.

177. Tran, V. V.; Lee, S.; Lee, D.; Le, T. H., Recent Developments and Implementations of Conductive Polymer-Based Flexible Devices in Sensing Applications. *Polymers (Basel)* **2022,** *14* (18).

178. Wang, J.; Chan, S.; Carlson, R. R.; Luo, Y.; Ge, G.; Ries, R. S.; Heath, J. R.; Tseng, H.-R., Electrochemically Fabricated Polyaniline Nanoframework Electrode Junctions that Function as Resistive Sensors. *Nano Letters* **2004,** *4* (9), 1693-1697.

179. Padua, L. M. G.; Yeh, J.-M.; Santiago, K. S., A Novel Application of Electroactive Polyimide Doped with Gold Nanoparticles: As a Chemiresistor Sensor for Hydrogen Sulfide Gas. *Polymers* **2019,** *11* (12), 1918.

180. Bansal, D.; Cardenas-Morcoso, D.; Boscher, N., Conjugated porphyrin polymer films with nickel single sites for the electrocatalytic oxygen evolution reaction. *Journal of Materials Chemistry A* **2023,** *11* (10), 5188-5198.

181. Cardenas-Morcoso, D.; Vey, E.; Heiderscheid, M.; Frache, G.; Boscher, N. D., Electronic and energy level engineering of directly fused porphyrin-conjugated polymers – impact of the central metal cation. *Journal of Materials Chemistry C* **2022,** *10* (6), 2194-2204.

182. Bengasi, G.; Baba, K.; Frache, G.; Desport, J.; Gratia, P.; Heinze, K.; Boscher, N. D., Conductive Fused Porphyrin Tapes on Sensitive Substrates by a Chemical Vapor Deposition Approach. *Angewandte Chemie International Edition* **2019,** *58* (7), 2103-2108.

183. Di Natale, C.; Paolesse, R.; Martinelli, E.; Capuano, R., Solid-state Gas Sensors for Breath Analysis: A Review. *Analytica Chimica Acta* **2014,** *824*, 1-17.

Annexed – Raman Data

Raman Data

Table 1. Raman data (in cm^{-1}) of $Cl_2SiPc/LuPc_2$ and $(345F)_2$-$SiPc/LuPc_2$ devices compared to these of each product as powder and their attribution (S: strong, m: medium and w: weak).

Cl_2SiPc-evaporated crystals	**Cl_2SiPc**/$LuPc_2$ heterojunction	**$(345F)_2SiPc$** evaporated crystals	**$(345F)_2$-SiPc**/ $LuPc_2$ heterojunction	$LuPc_2$ crystalline powder	Assignment
	548 w			548 w	Pc breathing
	563 w			564 w	Pc breathing
	577 w			578 w	Pc breathing
592 w	592 w	593 w	594 w		Pc breathing
		615 w			
			634 w		Pc breathing
		647 w	652 w		Pc breathing
		666 w			Pc breathing
679 m	680 m	683 m	684 m	682 S	Pc breathing
689 w					
			717 w		
			725 w		
			735 w	735 m	C-H wagging
	742 w				
756 w	756 w	757 w			
785 w	783 w	787 w	782 w	781 m	C=N aza stretching
		798 w	798 w		
842 m	840 w	843 m	843 w		
965 w	964 w				
1005 w	1005 w	1006 w	1007 w		
1016 w				1012 w	C-H bending
				1033 w	C-H bending
1048 m	1047 w	1046 w	1047 w		C-H bending
			1057 w		
1104 m	1104 m	1109 m	1108 m	1104 w	C-H bending
	1121 m		1123 m	1122 S	
	1139 w		1144 w	1147 w	pyrrole breathing
	1158 w		1159 w	1163 w	
	1174 m		1177 w	1177 m	C-H bending
1188 m	1188 w				
		1196 w	1196 w		C-H bending
			1219 w	1217 w	C-H bending
			1230 w		
1307 m	1306 m	1309 w	1309 w	1303 w	C-H bending
			1328 w	1333 w	C=C pyrrole and benzene stretching
1341 m	1341 m	1344 w	1343 w	1347 w	
		1362 w		1360 w	
		1381 w			
1409 m	1408 S		1411 m	1408 S	isoindole stretching
		1420 w			isoindole stretching
		1491 w			
	1512 m		1512 m	1512 S	Coupling of pyrrole and aza stretching
1527 m	1525 m	1519 w			
1559 S	1558 S	1554 S	1553 S	1552 w	
1601 m	1598 S	1602 m	1601 m	1601 S	benzene stretching
1613 S	1612 S	1615 m	1615 m	-	

Table 2. Raman data (in cm^{-1}) of Ace-PQ-Ni/$LuPc_2$ and AM6/$LuPc_2$ devices compared to these of each product as powder and their attribution (S: strong, m: medium and w: weak).

Ace-PQ-Ni crystalline powder	**Ace-PQ-Ni**/$LuPc_2$ heterojunction	**AM6** crystalline powder	**AM6**/$LuPc_2$ heterojunction	$LuPc_2$ crystalline powder	Assignment
547 w	549 w		549 w	549 w	Pc breathing
564 w	564 w		564 w	564 w	Pc breathing
	576 w		576 w	578 w	Pc breathing
618 w	622 w				
		628 w	625 w		
		645 w	645 w		
667 w	665 w	655 w			
680 w	680 m	675 w	680 S	682 S	Pc breathing
697 w	697 w	699 w			
714 w	717 w	714 w			
732 w	735 w	734 w	737 m	735 m	C-H wagging
744 w	742 m				
767 w	770 w	772 w	772 w		
777 w	780 w	779 w	782 m	781 m	C=N aza stretching
825 w	827 w	827 m	831 w		
843 w	848 w	848 w	843 w		
		882 w	881 w		
		900 w	899 w		
964 w	965 w	965 w			
993 w	993 w	999 w			
	1006 w		1006 m	1002 w	C-H bending
1014 w	1017 w	1016 w		1012 w	C-H bending
1036 w	1040 w	1040 w		1033 w	C-H bending
1061 w	1062 w	1064 w	1065 w		
		1080 m	1075 w		
1086 w	1091 w				
	1102 w		1104 w	1104 w	C-H bending
	1121 m	1128 w	1121 S	1122 S	
1139 S	1140 S				
			1142 w	1147 w	pyrrole breathing
		1163 w	1158 w		
1170 w	1174 m	1172 w	1175 S	1177 m	C-H bending
	1194 w		1194 w	1207 w	C-H bending
	1216 w		1218 w	1217 w	C-H bending
1226 m	1232 w	1227 m			
1265 m	1270 m				
1285 w	1288 w	1287 w	1287 w		
1302 w	1301 w	1304 m	1301 w	1303 w	C-H bending
			1330 w	1333 w	benzene stretching
1349 m	1352 m	1352 S	1351 m		
1360 m	1366 m				
		1371 m	1372 m		
1377 m	1381 m				
1402 S	1405 S		1408 S	1408 S	isoindole stretching
		1414 m			
1428 m	1429 m	1428 w			
				1451 w	
1472 w	1474 w				
1492 w	1493 w				
	1513 m		1512 S	1512 S	Coupling of pyrrole and aza stretching
1531 m	1530 m	1536 m	1534 m		C-C stretching
1565 S	1568 m	1562 S	1565 S		C-C stretching
1584 m	1589 m				
	1598 m	1593 m	1598 S	1601 S	benzene stretching
1659 S	1658 S	1662 w	1656 w	-	

Table 3. Raman data (in cm^{-1}) of $ZnF_8Pc/LuPc_2$, $CoF_8Pc/LuPc_2$ and $VOF_8Pc/LuPc_2$ devices compared to these of each product as powder and their attribution (S: strong, m: medium, w: weak and sh.: shoulder).

ZnF_8Pc crystalline powder	**ZnF_8Pc**/$LuPc_2$ heterojunction	**CoF_8Pc** crystalline powder	**CoF_8Pc**/$LuPc_2$ heterojunction	**VOF_8Pc** crystalline powder	**VOF_8Pc**/$LuPc_2$ heterojunction	**$LuPc_2$** crystalline powder	Assignment
547 m	549 m	552 m	551 m	554 m	554 m	549 w	Pc breathing
	566 w	567 m	564 m		562 w	564 w	Pc breathing
	576 w		578 m		578 m	578 w	Pc breathing
611 w				612 m	612 m		
	625 w		628 w			627 w	
687 m	684 m	690 m	682 S	685 m	682 S	682 S	Pc breathing
719 w	714 w						
		729 w		726 w	722 w		
739 m	739 m	744 w	742 m	744 w	742 m	735 m	C-H wagging
750 m				754 w	754 w		
760 m (sh.)	762 m	762 m	766 m	764 S	764 w		
	782 m	784 w	782 m		780 w	781 m	C=N aza stretching
877 m	879 w	882 m	884 w	979 m	882 m		
		953 w	944 w		943 w		
		974 w		1006 m	1006 m		
1004 w	1006 m	997 w	1007 m			1002 w	C-H bending
						1012 w	C-H bending
1030 w	1028 w	1024 m	1033 w			1032 w	C-H bending
		1046 w	1054 w				
1076 w	1070 w						
1094 w	1099 m						
1100 w	1107 m	1105 w	1104 m		1104 w	1104 w	C-H bending
	1121 m		1123 S		1121 S	1122 S	
1155 w	1144 m	1145 w	1144 w		1144 w	1147 w	pyrrole breathing
	1161 m		1159 m		1158 w	1162 m	
	1173 m	1170 w	1175 S	1172 m	1175 m	1177 m	C-H bending
1196 m	1194 m	1191 w		1189 m	1189 w		
						1207 w	C-H bending
1219 m	1219 m	1219 m	1219 m	1215 m	1216 w	1217 w	C-H bending
1296 w	1304 w	1296 w	1303 m			1303 w	C-H bending
1338 m	1338 m	1341 m	1335 m	1340 m	1340 m	1333 w	benzene stretching
1360 w	1360 w	1364 w	1362 w				
1406 S	1409 S	1405 m	1409 S	1401 m	1408 S	1408 S	isoindole stretching
1449 m	1450 m (sh.)				1455 m	1451 w	
	1458 m		1454 w				
1470 m	1473 w (sh.)	1467 m	1475 w	1463 m	1464 w		
		1502 m	1496 m (sh.)				
1513 S	1516 S		1513 S		1515 m	1512 S	Coupling of pyrrole and aza stretching
		1527 w (sh.)	1528 m			1527 w	C-C stretching
				1531 S	1531 S		C-C stretching
		1547 S	1550 m				C-C stretching
1593 S	1586 m (sh.)			1583 w	1583 w (sh.)		
1601 S	1599 S	1607 m	1599 S	1601 m	1600S	1601 S	benzene stretching
1617 S	1620 m	1622 S	1620 w (sh.)	1620S	1622 m		

List of Publications and Communications

List of Publications and Communications

Publications (In PhD):

1. **S. Ganesh Moorthy**; A. Apoubou; S. Ouedraogo; L. Vachey; M. Bayo-Bangoura; M. Bouvet; In-depth study of ambipolar charge transport regime through external triggers and gas sensing, ACS Applied Materials & Interfaces, **2024** (**Under review**).

2. **S. Ganesh Moorthy**; D. Bensal; N. Boscher; M. Bouvet, Engineering Ni(II)porphyrin conjugated polymers with different aryl meso-substituents for ammonia sensing, ACS Applied Materials & Interfaces, **2024** (**Under revision**).

3. **S. Ganesh Moorthy**; S. Ouedraogo; M. Bouvet, Ambipolar Heterojunction Sensors: Another Way to Detect Polluting Gases, *ACS Sensors* **2024**, 9 (7), 3707-3719.

4. P. Bečvář; A. Krystianiak; **S. Ganesh Moorthy**; B. Jansová; M. Kohout; R. Meunier-Prest; M. Bouvet, Electrosynthesized fluorinated polybithiophenes for ammonia sensing, *Materials Chemistry Frontiers* **2024**, *15* (8), 2666-2680.

5. **S. Ganesh Moorthy**; M. Bouvet, Effects of Visible Light on Gas Sensors: From Inorganic Resistors to Molecular Material-Based Heterojunctions, *Sensors* **2024,** *24* (5), 1571.

6. B. King; **S. Ganesh Moorthy**; E. Lesniewska; R. Meunier-Prest; M. Bouvet; B. H. Lessard, Modulating the Majority Charge Carrier Type and Performance of Organic Heterojunction Ammonia Sensors by Increasing Peripheral Fluorination of the Silicon Phthalocyanine Sublayer, *Sensors and Actuators B: Chemical* **2024**, 408, 135507.

7. **S. Ganesh Moorthy**; J. Arvidson; R. Meunier-Prest; H. Wang; M. Bouvet, π-Extended Porphyrin–Phthalocyanine Heterojunction Devices Exhibiting High Ammonia Sensitivity with a Remarkable Light Effect, *ACS Sensors* **2024,** *9* (2), 883-894.

8. L. Di Zazzo; **S. Ganesh Moorthy**; R. Meunier-Prest; E. Lesniewska; C. Di Natale; R. Paolesse; M. Bouvet, Ammonia and Humidity Sensing by Phthalocyanine–Corrole Complex Heterostructure Devices. *Sensors* **2023,** *23* (15), 6773.

9. **S. Ganesh Moorthy**; B. King; A. Kumar; E. Lesniewska; B. H. Lessard; M. Bouvet, Molecular Engineering of Silicon Phthalocyanine to Improve the Charge Transport and Ammonia Sensing Properties of Organic Heterojunction Gas Sensors, *Advanced Sensor Research* **2022,** *2* (3), 2200030.

Other Publications:

1. S. A. Adewinbi; V. Maphiri; L. O. Animasahun; M. Shkir; F. S. Khan; V. R. Minnam Reddy; **S. Ganesh Moorthy**; R. Marnadu; W. K. Kim; N. Manyala, Facile Synthesis, Enhanced Annealing-Structural Investigation and Supercapacitive Potentials of $NiFe_2O_4$ Spinel Nanopowder, *Surfaces and Interfaces* **2024,** *51*, 104737.

2. S. A. Adewinbi; V. Maphiri; R. Marnadu; M. Shkir; N. M. H. Alsdran; H. Algarni; **S. Ganesh Moorthy**; B. Taleatu; T. Niyitanga; H. Kim, Transparent, Photosensitive and Highly Efficient Pseudocapacitive Binder-free Mo-Modified NiO Thin Film Electrode for Bifunctional Optoelectronic and Energy Storage Applications, *Journal of Alloys and Compounds* **2023,** *937*, 168304.

3. R. Marnadu; S. K. Kannan; M. Vidhya; S**. Ganesh Moorthy**; K. Mohanraj; S. Maruthamuthu; A. M. Al-Enizi; M. Ubaidullah; S. Gedi, Influence of Ag+ Ions on the Physical Properties of Spray Coated CeO_2 Thin Films and Photo-response of p-Si/n-SDC Junction Diodes, *Surfaces and Interfaces* **2022,** *30*, 101866.

4. H. Albargi; R. Marnadu; **S. Ganesh Moorthy**; A. S. Alkorbi; H. Algadi; M. Shkir; A. Umar; S. Gedi, Deposition of Nanostructured Sn Doped Co_3O_4 Films by a Facile Nebulizer Spray Pyrolysis Method and Fabrication of p-Sn Doped Co_3O_4/n-Si Junction Diodes for Opto-nanoelectronics, *Sensors and Actuators A: Physical* **2021,** *332*, 113067.

5. K. Sasikumar; R. Bharathikannan; **S. Ganesh Moorthy**; S. Raja; G. J. Arputhavalli; M. Vidhya; R. Marnadu; R. Suresh, Structural, Optical, and Magnetic Properties of Mn-Doped Nickel Ferrite ($Ni1^{-x}Mn^xFe_2O_4$) Thin Films Deposited by Jet Nebulizer Spray Pyrolysis Technique, *Journal of Superconductivity and Novel Magnetism* **2021,** *34* (8), 2189-2198.

Presentations and Awards:

1. **Oral presentation:** S. Ganesh Moorthy; J. Arvidson; M. R. Meunier-Prest; H. Wang and M. Bouvet, Remarkable Effect of Light on π-extended Porphyrin-phthalocyanine – based Heterojunction devices, *XXIII^{e} Journées de l'Ecole Doctorale Carnot – Pasteur, Université de Franche-Comté, Besançon, France*, 27th June, **2024**, **Best Presentation Award** by *Réseau des Jeunes Chimistes-Société Chimique de France (RJ-SCF)*.

2. **Oral presentation:** S. Ganesh Moorthy; S. Ouedraogo; M. Bayo-Bangoura; M. Bouvet, Molecular Semiconductor Based Heterojunction Devices: Gas Sensing and Ambipolar Behavior, *XXII^{e} Journées de l'Ecole Doctorale Carnot – Pasteur*, Université de Bourgogne, *Dijon, France*, 25-26 May, **2023**.

3. **Oral presentation:** S. Ganesh Moorthy; B. King; A. Kumar; E. Lesniewska; B. H. Lessard; M. Bouvet, Molecular Engineering of Silicon Phthalocyanine to Improve the Charge Transport and Ammonia Sensing Properties of Organic Heterojunction Sensors, *Rencontres Capteurs de l'Université de Bourgogne Franche-Comté (RCUBFC), Dijon, France*, 24-25 Nov., **2022**.

4. **Poster presentation:** S. Ganesh Moorthy; M. Bouvet, Detecting Polluting Gasses Using Dyes, *28e Journée du savoir-Dijon, France*, 26th May, **2024** (**Best Poster Award**).

5. **Poster presentation:** S. Ganesh Moorthy; S. Ouedraogo; M. Bayo-Bangoura; M. Bouvet, Octahalogeno-phthalocyanine – based Heterojunctions as Ambipolar Gas Sensors, *XXXV EUROSENSORS Conference, Lecce, Italy*, 9-14 Sept., **2023** (**Best Poster Award**).

ECOLE DOCTORALE
CARNOT - PASTEUR

Titre : Etude de dispositifs à hétérojonctions unipolaires et ambipolaires à base de phtalocyanines et de porphyrines, via des stimuli externes et la détection de gaz

Mots clés : Bistabilité ; Semi-conducteur moléculaire ; Electronique organique ; Ammoniac ; Dioxyde d'azote and Ozone.

Résumé : Les dispositifs à base de semi-conducteurs organiques font l'objet de nombreuses recherches en raison de leurs propriétés électriques uniques. Il existe une forte demande pour des appareils miniatures, en particulier ceux remplissant des fonctions multiples. Ce besoin a attiré une attention particulière sur les dispositifs ambipolaires. Dans cette thèse, nous visons à utiliser des matériaux possédant des densités de porteurs de charge mobiles positives et négatives presque égales pour créer des dispositifs bipolaires (de type p et n) appelés dispositifs ambipolaires. Ce type de dispositif présentant un comportement ambipolaire a le potentiel de remplacer deux dispositifs différents (types p et n) par un seul dispositif ambipolaire, réduisant ainsi la taille du système électronique. De tels dispositifs ambipolaires sont prometteurs pour diverses applications en nanotechnologie, notamment leur déploiement dans des engins spatiaux, des satellites et des appareils électriques quotidiens où la minimisation du poids et de la taille est cruciale.

L'étude de dispositifs organiques à hétérojonction sous différents gaz oxydants (NO_2 et O_3) et réducteurs (NH_3) donne un aperçu des propriétés de transport de charge dans ces dispositifs. Initialement, nous avons exploré le potentiel des phtalocyanines de silicium (Cl_2-SiPc et $(345F)_2$-SiPc) dans un dispositif à hétérojonction organique bicouche en les combinant avec un matériau moléculaire très conducteur ($LuPc_2$) et étudié leurs propriétés de détection de NH_3 pour comprendre l'interaction entre les molécules de gaz et la couche sensible. Grâce à ces connaissances de base, nous avons exploré plus en détail deux complexes originaux de porphyrines à nuages π étendus dans des dispositifs à hétérojonction bicouche et leur réponse à l'ammoniac dans l'obscurité et sous lumière UV. Pour la première fois, nous avons démontré une amplification des propriétés de détection d'un dispositif organique à hétérojonction sous illumination UV.

En modifiant le centre métallique des complexes octafluoro-métallophtalocyanines, nous avons observé des comportements ambipolaires dans des dispositifs organiques à hétérojonction. L'inversion de la nature des porteurs de charge majoritaires au sein du dispositif a été réalisée en utilisant des stimuli externes tels que l'humidité et la température, ainsi que la nature des espèces gazeuses. Le dispositif basé sur CoF_8Pc change de polarité en fonction de la nature du gaz, tandis que l'inversion de la nature des porteurs de charge majoritaires dans le dispositif basé sur VOF_8Pc est obtenue en faisant varier les niveaux d'humidité et la température. Ces dispositifs présentent une bistabilité dans différentes conditions expérimentales. Cependant, obtenir un contrôle précis de l'inversion des porteurs de charge majoritaires, qui détermine la polarité du dispositif, nécessite un stimulus externe approprié et contrôlable, et cela peut dépendre de la composition moléculaire et de l'architecture du dispositif. Il est crucial de mener des études approfondies sur les effets environnementaux tels que les variations d'humidité et de température lorsque l'on travaille avec ce type de dispositifs ambipolaires.

Enfin, nous avons également étudié l'influence de la couche supérieure sur la polarité des dispositifs à hétérojonction bicouche. Pour la première fois, nous rapportons la démonstration pionnière de l'inversion de polarité au sein d'un dispositif à hétérojonction, en changeant stratégiquement le substituant en position méso de la porphyrine 5,15-diaryl Ni (II), dont les polymères conjugués sont utilisés comme couches supérieures dans des dispositifs utilisant CuF_8Pc comme sous-couche. Dans ce projet, nous nous sommes concentrés sur la compréhension et le développement de dispositifs à hétérojonction organiques unipolaires et ambipolaires basés sur des matériaux moléculaires tels que les phtalocyanines et les porphyrines via des stimuli externes et la détection de gaz.

ECOLE DOCTORALE
CARNOT - PASTEUR

Title : Study of unipolar and ambipolar phthalocyanine- and porphyrin-based heterojunction devices through external triggers and gas sensing

Keywords : Bistability ; Molecular semiconductor ; Organic electronics; Ammonia; Nitrogen dioxide and Ozone.

Abstract : Organic semiconductor-based devices are attracting a wide range of researchers due to their unique electrical properties. In today's advanced world, there is a high demand for miniature devices, particularly those performing multiple functions. This need has brought special attention to ambipolar devices. In this thesis, we aim to utilize materials possessing nearly equal densities of mobile charge carriers in molecular materials to create bipolar (both p- and n-type) devices known as ambipolar devices. This type of device that exhibits ambipolar behaviour has the potential to replace two different types of devices (p- and n-type) with a single ambipolar device, eventually reducing the size of the electrical system. Such ambipolar devices hold promise for various applications in nanotechnology, including deployment in spacecraft, satellites, and everyday electrical appliances where minimizing weight and size is crucial.

The study of organic heterojunction devices under different oxidizing (NO_2 and O_3) and reducing (NH_3) gases provides insight into the charge transport properties in these devices. Initially, we explored the potential of silicon phthalocyanines (Cl_2-SiPc and $(345F)_2$-SiPc) in a bilayer organic heterojunction device by combining them with a highly conducting molecular material ($LuPc_2$) and investigated their NH_3 sensing properties to understand the interaction between gas molecules and the sensing layer. With this basic knowledge, we further explored two original π-extended conjugated porphyrin complexes in bilayer heterojunction devices and their response to ammonia under both dark and UV light conditions. For the first time, we demonstrated an amplification in the sensing properties of an organic heterojunction device under UV light illumination.

By changing the metal centre in octafluoro-metallophthalocyanine complexes, we achieved ambipolar charge transport regimes in organic heterojunction devices. Inversion in the nature of the majority charge carriers within the device was achieved by utilizing external triggers like humidity and temperature, as well as the nature of gas species. The CoF_8Pc-based device changed its polarity depending on the nature of the gas species, while the inversion in the nature of majority charge carriers in the VOF_8Pc-based device was achieved by varying humidity levels and temperature. These devices exhibit bistability under different experimental conditions. However, achieving precise control over the inversion of majority charge carriers, which determines the device's polarity, requires a suitable and controllable external trigger, and it may depend on the molecular composition and the architecture of the device. It is crucial to conduct comprehensive investigations into environmental effects such as humidity and temperature variations when working with ambipolar devices.

Finally, we also studied the influence of the top layer on the polarity of bilayer heterojunction devices. For the first time, we report the pioneering demonstration of polarity inversion within a heterojunction device, by strategically manipulating the meso-substituent of the 5,15-diaryl Ni(II) porphyrin conjugated polymer in the top layer of the devices that contain an ambipolar molecule (CuF_8Pc) as sublayer. Globally, in this project, we focused on understanding and developing unipolar and ambipolar organic heterojunction devices based on molecular materials like phthalocyanines and porphyrins through external triggers and gas sensing.

UBFC
UNIVERSITE
BOURGOGNE FRANCHE-COMTE

Université Bourgogne Franche-Comté
32, avenue de l'Observatoire
25000 Besançon